Hard X-ray Phase Contrast Microscopy
- Techniques and Applications -

A Dissertation Presented

by

Christian Holzner

to

The Graduate School

in Partial Fulfillment of the Requirements

for the Degree of

Doctor of Philosophy

in

Physics

Stony Brook University

August 2010

Stony Brook University

The Graduate School

Christian Holzner

We, the dissertation committee for the above candidate for the Doctor of Philosophy degree, hereby recommend acceptance of this dissertation.

Chris Jacobsen – Dissertation Advisor
Professor, Department of Physics and Astronomy

Harold Metcalf – Chairperson of Defense
Professor, Department of Physics and Astronomy

Martin Rocek
Professor, Department of Physics and Astronomy

Jürgen Thieme
Senior Scientist, Brookhaven National Laboratory

This dissertation is accepted by the Graduate School.

Lawrence Martin
Dean of the Graduate School

Abstract of the Dissertation

Hard X-ray Phase Contrast Microscopy - Techniques and Applications -

by

Christian Holzner

Doctor of Philosophy

in

Physics

Stony Brook University

2010

In 1918, Einstein provided the first description of the nature of the refractive index for X-rays, showing that phase contrast effects are significant. A century later, most x-ray microscopy and nearly all medical imaging remains based on absorption contrast, even though phase contrast offers orders of magnitude improvements in contrast and reduced radiation exposure at multi-keV x-ray energies.

The work presented is concerned with developing practical and quantitative methods of phase contrast for x-ray microscopy. A theoretical framework for imaging in phase contrast is put forward; this is used to obtain quantitative images in a scanning microscope using a segmented detector, and to correct for artifacts in a commercial phase contrast x-ray nano-tomography system. The principle of reciprocity between scanning and full-field microscopes is then used to arrive at a novel solution: Zernike contrast in a scanning microscope. These approaches are compared on a theoretical

and experimental basis in direct connection with applications using multi-keV x-ray microscopes at the Advanced Photon Source at Argonne National Laboratory.

Phase contrast provides the best means to image mass and ultrastructure of light elements that mainly constitute biological matter, while stimulated x-ray fluorescence provides high sensitivity for studies of the distribution of heavier trace elements, such as metals. These approaches are combined in a complementary way to yield quantitative maps of elemental concentration from 2D images, with elements placed in their ultrastructural context. The combination of x-ray fluorescence and phase contrast poses an ideal match for routine, high resolution tomographic imaging of biological samples in the future. The presented techniques and demonstration experiments will help pave the way for this development.

To my parents, family and friends.

Contents

List of Figures

List of Tables

Acknowledgements

First and foremost, I would like to thank Chris Jacobsen for giving me the opportunity to be his student. He is more than an exceptional advisor. Also special thanks goes to Michael Feser who besides guiding me to become a researcher also grew a very good friend. Thanks to Martin de Jonge for exposing me to new experiments and out-of-the-ordinary ways of thinking; and Stefan Vogt for direction and support in many ways. Generally, I can say that without the guidance of the above four people I would not be where I am as a researcher today.

Furthermore, thanks goes to Benjamin Hornberger, Jan Steinbrener, Johanna Nelson, Xiaojing Huang, Simon Moser, Bjorg Larson, Huijie Miao, Holger Fleckenstein, Sol Gruner, Stephen Baines, Ben Twining, Julia Diaz, Ian McNulty, Dan Legnini, Lydia Finney, Sophie-Chalotte Gleber, Pavel Rehak, David Paterson, Sue Wirick and Janos Kirz.

Thanks to my parents, family and friends for their support and encouragement throughout this time!

Christian Holzner, August 2010.

Chapter 1

Introduction

1.1 A Foreword

The presented thesis gives an account of various advances and novel methods of phase contrast imaging in hard x-ray microscopy.

Chapter 1 introduces the basic physical concepts and techniques for imaging with X-rays with a particular focus on the most important aspects required for the main part of this work. Chapter 2 discusses the theory of image formation in scanning and full-field x-ray microscopes, and their respective equivalence through the principle of reciprocity, which signifies the foundation for a large part of the presented methods and advancements. Neither of the two chapters include any parts of original work.

In Ch. 3 we will discuss the fundamental principles of phase contrast imaging in scanning microscopes based on the far-field intensity distribution derived in Ch. 2 and arrive at the qualitative method of differential phase contrast imaging. From there we will develop two different methods of quantitative reconstruction from differential phase contrast data: the integration method and the filtering method. Each of the two approaches is discussed in detail and applications to experimental data is shown. This is followed by a detailed comparison of both methods including a potential way for their unification, upon which parts of the comparison will be based. We conclude this chapter by demonstrating an important application of quantitative phase contrast imaging in connection with x-ray fluorescence microscopy. The original parts of this work include the participation in the implementation of phase contrast for hard x-rays [1], the derivation and realization of the integration method for x-ray microscopy [2–4], the comparison of both reconstruction methods [5] and the application to elemental concentration reconstruction in x-ray fluorescence microscopy [6].

With Ch. 4 we present a novel method of phase contrast imaging for scanning microscopy. By employing the principle of reciprocity we demonstrate the first realization of Zernike phase contrast in a scanning microscope. We discuss the basic principles of the technique and show first experimental results, followed by some initial applications to biological samples. The complete chapter represents original work, of which parts are currently under review [7]; a detailed treatment of the biological applications will follow in the future.

In Ch. 5 we address the imaging artifacts common for Zernike type phase contrast, which are due to the nature of how the contrast is formed. By realizing the equivalence of full-field and scanned imaging as a result of the principle of reciprocity, it is possible to apply the filtering method of Ch. 3 to both scanning and full-field Zernike data and remove the artifacts by means of image reconstruction. A brief discussion of Zernike artifacts is followed by the necessary consideration to apply the filtering method to Zernike images.

The chapter concludes with initial and preliminary reconstruction results, as the advances have been recent. The original work includes the content of the whole chapter [8].

The Appendix includes definitions, theorems and detailed derivations.

1.2 X-rays and Their Interaction with Matter

X-rays are part of the electromagnetic spectrum of radiation with wavelengths ranging from 10 to 0.01 nm, or respective energies of 100 eV to 100 keV.

When using X-rays for imaging applications a common classification is done as follows:

- **Soft X-rays:** $E \lesssim 1\,\mathrm{keV}$; typical attenuation lengths of a few μm in biological tissue;
- **Medium-energy X-rays:** $1\,\mathrm{keV} \lesssim E \lesssim 5\,\mathrm{keV}$; attenuation length of tens to hundreds of μm;
- **Hard X-rays:** $5\,\mathrm{keV} \lesssim E \lesssim 20\,\mathrm{keV}$; attenuation length of mm and stimulated x-ray fluorescence for a wide range of elements (see Sec. 1.2.4);

Energies above 20 keV are rarely used for x-ray microscopy applications.

1.2.1 Scattering Cross Sections

The primary interactions mechanisms of X-rays with matter in the range of photon energies considered in this work are absorption, elastic (coherent or Rayleigh) scattering and inelastic (Compton) scattering [9].

In the case of absorption, an X-ray photon is fully absorbed and ejects a photo-electron from the atom in the material leaving the atom ionized; the successive filling of the vacancy results in photo-emission of a characteristic wavelength.

In elastic scattering the incident photon is deflected while preserving its initial energy.

In inelastic scattering the energy and momentum between the photon and the scattering electron is preserved. Part of the incident photon energy and momentum are transferred to the electron, which scatters the photon off at an angle with reduced energy.

The probability that an incident photon interacts with an atom in a sample material is described by its total cross section σ, which can effectively be interpreted as the target area as seen by the photon. In Fig. 1.1 we show the cross sections for the above named interactions mechanisms of X-rays with elemental carbon. Up to 10^3 eV incident x-ray energy, photo-electric absorption is the dominating process. At an energy of 284 eV we can see the characteristic K-shell absorption edge of carbon in the σ_{ab} cross section. When an incident photon exceeds the binding energy of an atomic level or shell, the electrons from that shell can be ejected resulting in a sharp increase of the absorption cross section. The study of absorption edges via spectroscopic methods provide rich information about a samples chemical structure, but are not considered in this work. We can see that Compton scattering is negligible

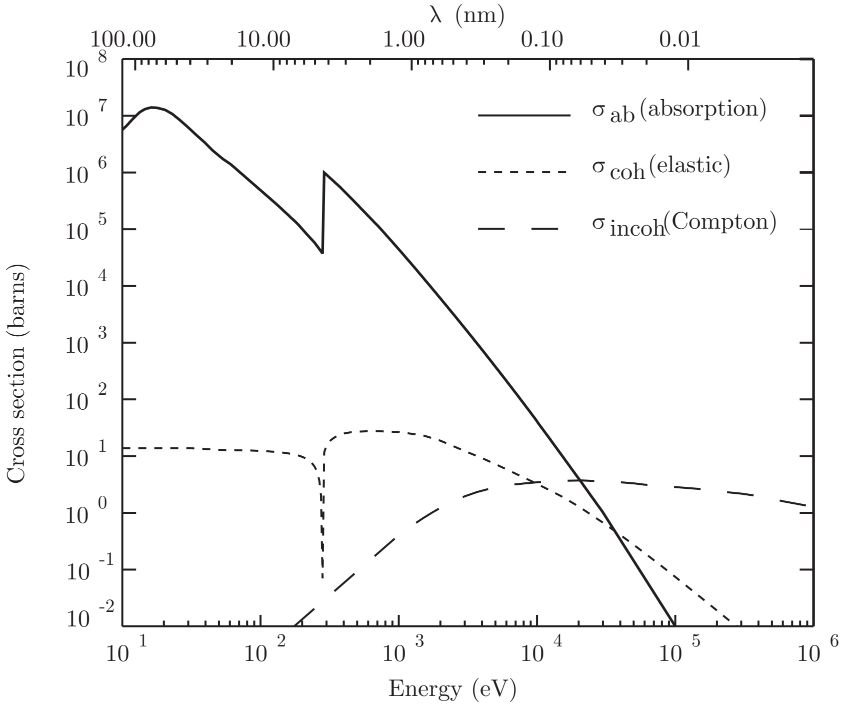

Figure 1.1: X-ray interaction cross sections with elemental carbon; figure reproduced from Kirz *et al.* [10].

in the soft X-ray region, whereas for hard X-rays, which are exclusively used in this work, it becomes more relevant for the total interaction cross section. However, it can be shown [11] that the effects of Compton scattering for x-ray transmission imaging are negligible. By considering Compton's formula for the wavelength shift through inelastic scattering [12] we can see that the relative energy change of the scattered photon is given by

$$\frac{\Delta E}{E} \approx -\frac{\Delta\lambda}{\lambda} \approx \frac{E}{mc^2}\frac{\theta^2}{2}\,, \tag{1.1}$$

where θ is the scattering angle. Considering the largest scattering angles in transmission x-ray imaging, given by the respective opening angle of the lenses used (see Sec. 1.3.3), are on the order of 1 to 50 mrad, the respective relative energy changes are on the order of 10^{-8} to 10^{-5}. Hence, the energy change in the forward direction is so small that one cannot tell the difference from elastic scattering. Therefore, we will not further consider Compton interaction for the remainder of this work.

1.2.2 Atomic Scattering Factors and Complex Index of Refraction

The complex index of refraction n for X-rays, based on the high frequency limit of classical dispersion theory, is commonly written as [13]

$$n = 1 - \delta - \mathrm{i}\beta = 1 - \frac{n_a\, r_e}{2\pi}\lambda^2(f_1 + \mathrm{i}f_2)\,, \tag{1.2}$$

where n_a is the atom number density and r_e the classical electron radius. The complex oscillator strength or atomic scattering factor is given by $(f_1 + \mathrm{i}f_2)$. Based on this the real (δ) and imaginary (β) parts of the index of refraction are given by

$$\delta = \frac{n_\mathrm{a} r_\mathrm{e}\lambda^2}{2\pi} f_1, \quad \text{and} \tag{1.3}$$

$$\beta = \frac{n_\mathrm{a} r_\mathrm{e}\lambda^2}{2\pi} f_2\,. \tag{1.4}$$

These scattering factors are related to the cross sections for absorption and elastic scattering by [10]

$$\sigma_\mathrm{abs} = 2 r_\mathrm{e}\lambda\, f_2, \quad \text{and} \tag{1.5}$$

$$\sigma_\mathrm{elastic} = \frac{8}{3}\pi r_\mathrm{e}^2\, |f_1 + \mathrm{i}f_2|^2\,, \tag{1.6}$$

which is valid for energies $\lesssim 1$ keV. For higher energies the scattering factors will depend on the scattering angle and relationships will be more complicated. The presented work only considers the forward direction, because we only consider transmission imaging.

In Fig. 1.2 we show the energy dependence of scattering factors for carbon and gold [14]. The real part of the atomic scattering factor f_1, which describes the phase shift induced on the X-ray wave field, varies slowly except near absorption edges. On the other hand the imaginary part f_2 describing absorption tends to decrease with the second power of the wavelength (λ^2). Hence, δ scales as λ^2, while β scales at λ^4. This has very practical consequences for the importance of contrast mechanisms with X-rays, as will be described in Sec. 1.4.1.

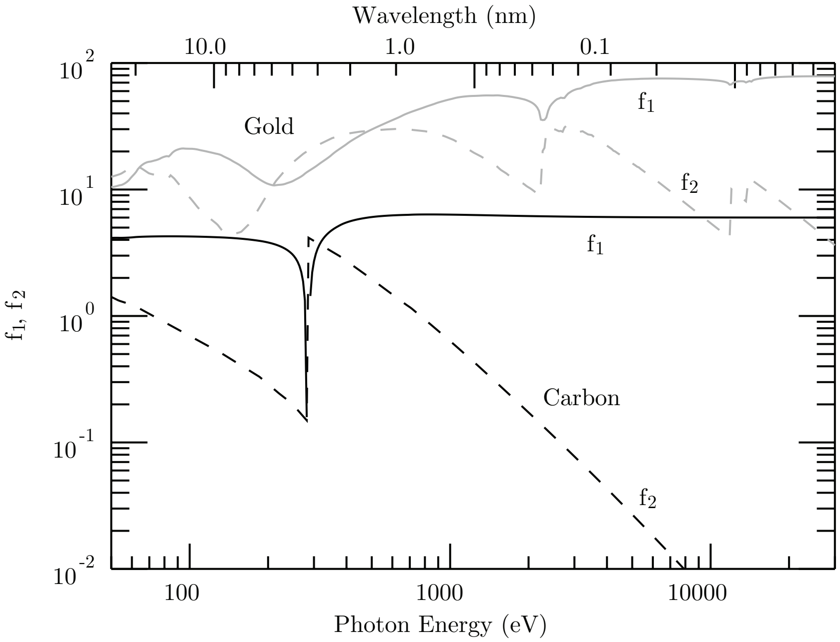

Figure 1.2: Atomic scattering factors for carbon and gold through data from [14].

An important resource for tabulated values of f_1 and f_2 is given by Henke *et al.* [14], where elements from $Z = 1$ up to 92 over an energy range of 50 eV to 30 keV are considered. The tabulated values are valid for the forward direction and away from absorption edges. While f_2 is measured directly by absorption, the values for f_1 are determined via the Kramers-Kronig relations (see *e. g.* Attwood [9])

$$f_1(\omega) = Z - \frac{2}{\pi}\mathcal{P}_\mathrm{C}\int_0^\infty \mathrm{d}u\,\frac{u f_2(u)}{u^2-\omega^2} \tag{1.7}$$

and

$$f_2(\omega) = \frac{2\omega}{\pi}\mathcal{P}_\mathrm{C}\int_0^\infty \mathrm{d}u\,\frac{f_1(u)-Z}{u^2-\omega^2}\,, \tag{1.8}$$

where ω is the radial frequency of the wave field, Z the number of electrons per atom and $\mathcal{P}_\mathrm{C}$ indicates to take the principal part of the integral after Cauchy. This means that in fact f_1 and f_2 are not independent from each other. If one is known across the whole energy range, the other can be deduced from these relations.

For compound materials consisting of different elements the atomic scattering factors are replaced by a weighted average of the constituents.

1.2.3 Wave Propagation and Specimen Function

We will describe the propagation of X-rays by considering a scalar wave field ψ. A plane wave with amplitude ψ_0 in the temporarily stationary case propagating in free space along the z-direction is written as

$$\psi(z) = \psi_0\,\exp(-\mathrm{i}kz), \tag{1.9}$$

where $k = 2\pi/\lambda$ is the wave number. In a homogeneous material with index of refraction n the propagating wave is given by

$$\psi(z) = \psi_0\,\exp(-\mathrm{i}nkz)\,. \tag{1.10}$$

With the definition of the index of refraction from Eq. 1.2 this can be expanded as

$$\psi(z) = \underbrace{\psi_0\exp(-\mathrm{i}kz)}_{\text{vacuum propagation}}\;\underbrace{\exp(+\mathrm{i}\delta kz)}_{\text{phase shift}}\;\underbrace{\exp(-\beta kz)}_{\text{amplitude attenuation}}\quad, \tag{1.11}$$

where we identify the first term as the free space propagation, the second term represents the phase shift imposed onto the wave field by the material and the third term is the amplitude attenuation. In Fig. 1.3 we compare free space propagation with the case of traversing a material with refractive index n and thickness t. Relative to the propagation in vacuum the wave field is attenuated and phase shifted. Therefore, it is suggestive to describe the interaction of X-rays with a sample by a multiplicative transmission function h which effects

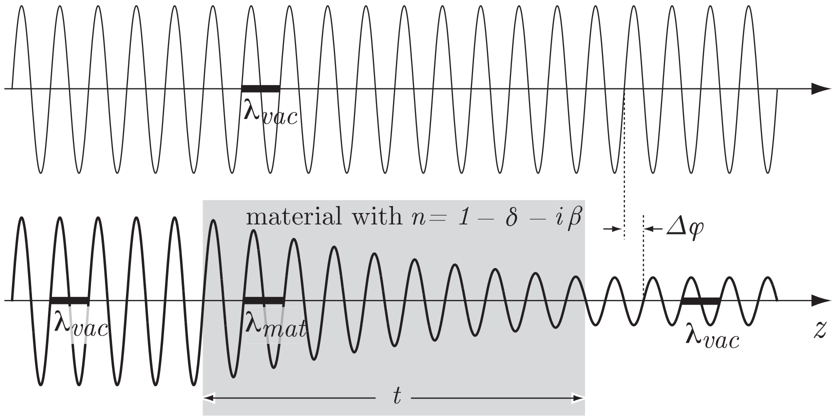

Figure 1.3: Wave propagation through vacuum and material with index of refraction $n = 1 - \delta + \mathrm{i}\,\beta$. The wavelngth inside the material is given by $\lambda_{\mathrm{mat}} = \lambda_{\mathrm{vac}}/(1-\delta)$.

an incoming wave field ψ_{in} by

$$\psi_{\mathrm{out}} = h\,\psi_{\mathrm{in}}\,, \tag{1.12}$$

to produce and outgoing wave field ψ_{out}, where the specimen function is given by

$$h = \exp(-\beta k t)\,\exp(+\mathrm{i}\delta k t)\,. \tag{1.13}$$

This will serve as a basic relation for the remainder of this work when describing the influence of samples onto the x-ray wave field. The quantity h is called the specimen (transmission) function.

1.2.4 X-ray Fluorescence

A significant application of the phase contrast techniques presented in this work is in the context of x-ray fluorescence microscopy; therefore, we will have a brief look at the basic principles of fluorescence. When an x-ray photon is absorbed it will knock-out an electron from one of the absorbing atom's orbitals. In order for this to happen, the x-ray energy needs to be larger than the binding energy of the corresponding electron. Many of elements core-shell binding energies are of comparable or lower magnitude than hard x-ray energies. The ejected electron will have a kinetic energy of the absorbed photon energy minus its binding energy. This photo-ionization process is shown in

Fig. 1.4(a).

The atom with this vacancy will relax back into its ground state through transition of an electron from an higher orbital into the vacant state. The successive release of energy will happen through one of two processes: in fluorescence the energy is released in form of a photon of the corresponding energy (Fig. 1.4(b)); instead the the energy can be transferred to a different electron, which is ejected from the atom as an Auger electron (Fig. 1.4(c)). The probability that the relaxation occurs through the process of fluorescence and not the Auger process is called fluorescence yield. In Fig. 1.5 it can be seen that the yield is low for low-Z elements and high for high-Z elements. Figure 1.6 shows a similar plot of the yield in terms of photon energy below 10 keV, in-

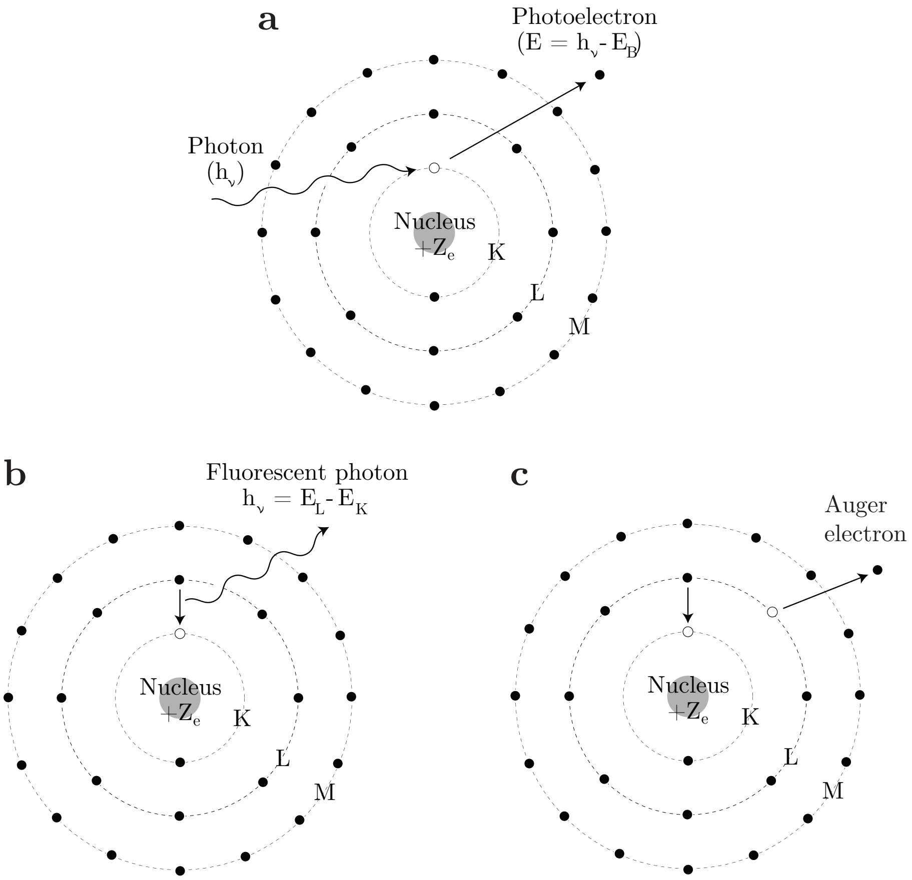

Figure 1.4: Absorption and emission process illustrated in a simplified atomic model. (**a**) Photo-ionization, (**b**) fluorescence and (**c**) Auger process.

dicating also specific elemental K and L shell photo-ionization energies. From both plots we can see that the yield for light elements, which mainly constitute biological matter such as carbon, nitrogen and oxygen, are low, making fluorescence detection of such structures challenging.

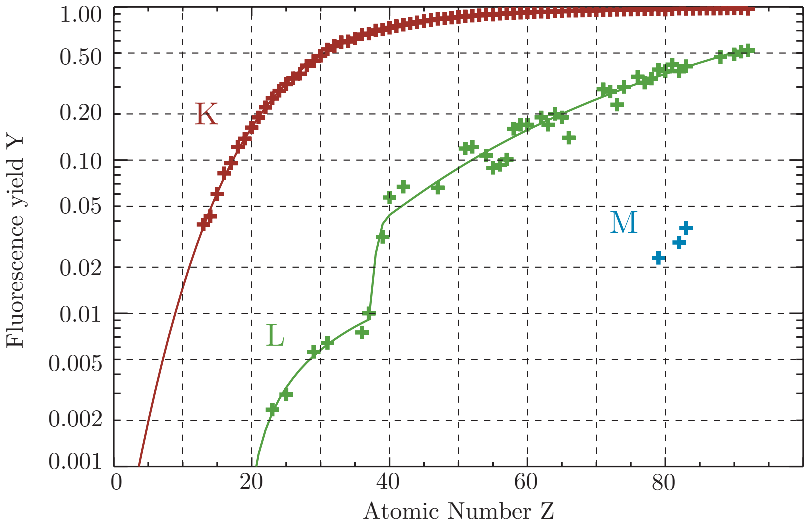

Figure 1.5: Fluorescence yields for K, L and M shells as a function of atomic number Z

The wavelength of the fluorescent lines observed from a given element is well defined by the energy states of the atom and the selection rules for successive transitions (see *e. g.* [9]). Tabulations of these values are available, such as in the X-ray Data Booklet [15]. In x-ray fluorescence microscopy the sample is irradiated with an x-ray beam and the emitted fluorescence spectrum is collected with an energy dispersive detector. The elemental content of the sample is then determined via the emission spectrum and the known and tabulated values for emission lines.

1.3 X-ray Microscopy

Microscopy with X-rays is a complementary technique to imaging with visible light and electrons. Due to its shorter wavelength, X-rays have the potential for higher spatial resolution compared to visible light. The current state-of-the-art resolution achieved with X-rays lies in the 10 nm range. At the same time, novel techniques [16] in visible light microscopy are pushing its resolution

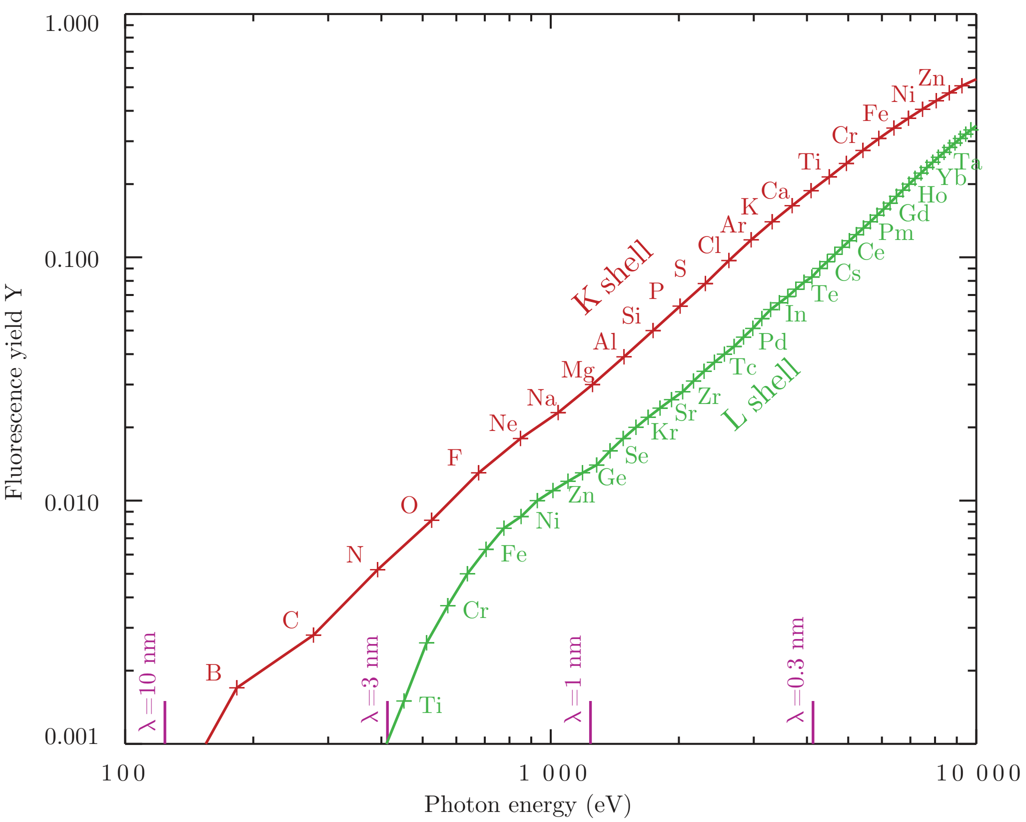

Figure 1.6: Fluorescence yields of K and L shells as a function of photon energy; indicated are the respective elemental photo-ionization energies.

barrier beyond its diffraction limit. Electron microscopy achieves superior resolution down to 50 pm but requires thin samples due to the small penetration depth of electrons and commonly requires staining or labeling methods for biological structure visualization. In comparison, x-ray microscopy can image thick specimens (*e. g.* whole cells) in states much closer to their natural environment. Furthermore, x-ray fluorescence without staining or labeling and the ease of energy tunability for spectroscopic imaging give x-ray microscopy a unique role compared to other microscopy techniques.

The field of x-ray microscopy using synchrotron radiation and zone plate optics was established in the 1970s and 80s. At Göttingen University the group of Günther Schmahl pioneered the full-field x-ray microscope [17], while at Stony Brook University the group of Janos Kirz developed the scanning x-ray microscope [18, 19]. Today many synchrotrons operate x-ray microscopes from the soft to the hard x-ray range, with many applications in the biological, medical, environmental and materials sciences (see Howells *et al.* [20] for a recent overview).

1.3.1 Radiation Sources

A large number of dedicated x-ray facility storage rings operate around the world[1] and more are being built. While synchrotrons continue to thrive, developments of laboratory based sources and techniques have emerged that have the potential to complement the heavily over-subscribed synchrotron facilities. In fact, parts of the data presented in this work have been obtained via a commercially available laboratory x-ray full-field microscope [21]. All other experimental data for this work has been collected at the Advanced Photon Source at Argonne National Laboratory.

At synchrotron facilities x-ray microscopes either utilize radiation produced by bending magnet sources (high flux of photons per second, per bandwidth, per solid angle), or undulator sources (high brightness, which is flux per source area; hence improved coherence properties of the radiation). The book of Attwood [9] gives a description of the sources characteristics for soft X-rays and Mills [22] for hard X-rays.

1.3.2 X-ray Microscopes

Two types of transmission x-ray microscopes are routinely used today:

1. the full-field transmission x-ray microscope (TXM)

---

[1] see `www.lightsources.org`

2. the scanning transmission x-ray microscope (STXM) .

In Fig. 1.7 in illustration of the basic imaging principle is shown. In TXM the sample is illuminated by a condenser lens and a magnified image is formed by an objective lens on a two-dimensional pixellated x-ray detector. TXMs work well with incoherent illumination and therefore can operate at bending magnet source beamlines. They are ideally suited for fast acquisition of images with exposure times in the range of seconds, which makes them also well suited for tomographic imaging applications. However, the field-of-view is limited and the radiation dose delivered to the sample is high for good quality images due to the inefficient objective lens collecting the sample information. Depending on the resolution of the zone plate and the energy used, typical efficiency values for zone plates range from 0.6% to 30%. In STXM the x-rays are focussed by

TXM: transmission x-ray microscope

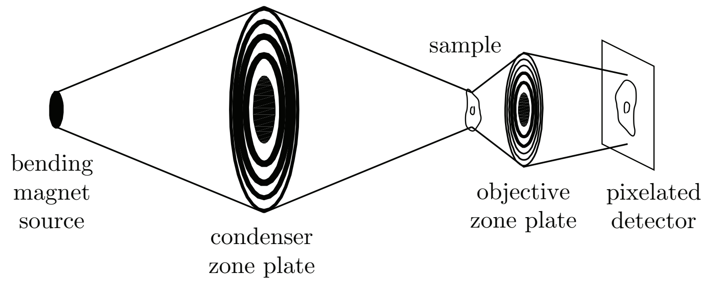

STXM: scanning transmission x-ray microscope

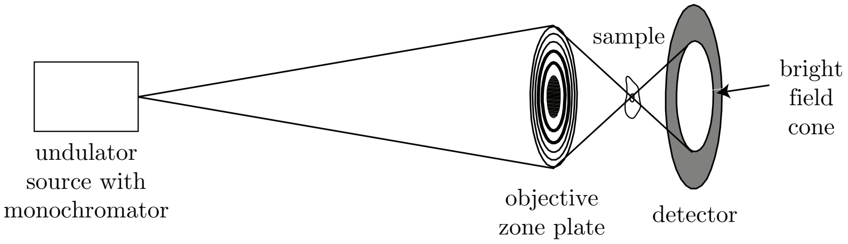

Figure 1.7: Schematic of basic imaging principals for TXM and STXM microscopes.

an objective lens to a small spot, through which the sample is raster scanned. The transmission signal is collected for each scan point and forms the image.

In order for the zone plate to create a small spot and therefore deliver good spatial resolution, it needs to be illuminated coherently, which is why STXM are commonly operated at undulator beamlines. Image acquisition is slower in STXM due to the raster scan approach; however, the field-of-view is easily variable and the delivered dose to the sample is significantly reduced as the majority of the radiation interacting with the sample is collected in the process, merely limited by the detector size. An extension of STXM is the scanning x-ray fluorescence microscope (SXFM), where off the optical axis the emitted x-ray fluorescence spectrum is collected for each raster scan point, which enables the elemental mapping of the specimen. The STXM and the SXFM can be well combined into one instrument and can deliver complementary information about the specimen.

1.3.3 X-ray Focussing Optics - Fresnel Zone Plates

Both the TXM and the STXM rely on the use of x-ray lenses. Common x-ray focussing and lens optics are reflective, refractive and diffractive optics; for an overview see Howells *et al.* [20]. Not all of them are image forming lenses as required for the described microscopes and they come with various sets of issues. All experiments described in this work use diffractive Fresnel zone plate optics, of which in the following we will summarize their properties.

A Fresnel zone plate is a circular diffraction grating as depicted in Fig. 1.8. In order to achieve constructive interference at the lens focus, the path difference to the focus from radiation passing through adjacent open zones has to be λ times the diffraction order. Although higher diffractive orders can be used in practice most common is the first order $m = 1$. The properties of a zone plate are fully specified by three parameters[2]: diameter D, outermost zone width $\mathrm{d}r_\mathrm{N}$ and the wavelength λ. Other quantities of interest can then be derived based on these parameters and are given in the following: the number of zones N

$$N = \frac{D}{4\,\mathrm{d}r_\mathrm{N}}\,, \tag{1.14}$$

the focal length f

$$f = \frac{D\,\mathrm{d}r_\mathrm{N}}{\lambda}\,, \tag{1.15}$$

and the numerical aperture

$$\mathrm{NA} = \alpha_\mathrm{NA} = \frac{\lambda}{2\,\mathrm{d}r_\mathrm{N}}\,. \tag{1.16}$$

---

[2] Not considering spherical aberration corrections, which depend on object position.

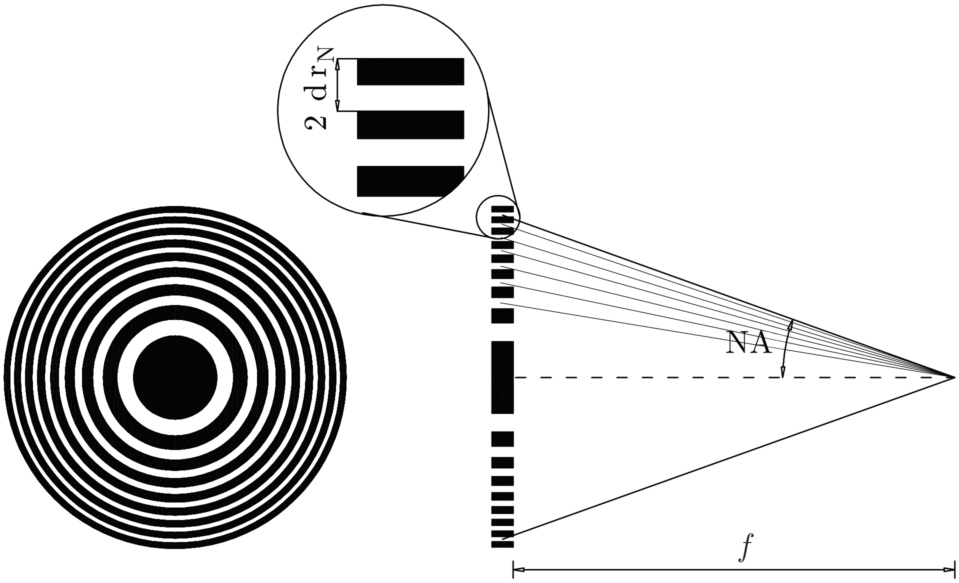

front view

cross section of side view

Figure 1.8: Schematic of a Fresnel zone plate in front and cross section view. Alternating transparent and opaque zones are arranged such that the path difference between adjacent rings lead to constructive interference at the focal spot.

It can be shown that the transverse resolution for a diffraction limited focal spot is

$$\delta_\mathrm{t} = 1.22\ \mathrm{d}r_\mathrm{N}\,, \tag{1.17}$$

which requires a uniform plane wave illumination of the zone plate. Note that the outermost zone width alone specifies the diffraction-limited transverse resolution, independent of the wavelength as long as $\mathrm{d}r_\mathrm{N} >> \lambda$. The intensity distribution in the focal plane is referred to a point spread function. In fact, the wave field in the focal plane in case of a plane wave illumination os given by the Fourier transform of the lenses aperture (see [23]). The longitudinal resolution along the optical axis is given by

$$\delta_\mathrm{l} = \pm\frac{\lambda}{2\,(\mathrm{NA})^2} = \pm\frac{2\,(\mathrm{d}r_\mathrm{N})^2}{\lambda}\,. \tag{1.18}$$

Zone plates are chromatic optics (the focal length is inversely proportional to the wavelength) and therefore require monochromatic illumination. Specifically, the monochromaticity must be higher than the number of zones to avoid chromatic blurring:

$$\frac{\lambda}{\Delta\lambda} > N\,. \tag{1.19}$$

Since the zone plate is a diffractive optic, the largest part of the illumination passes through undiffracted. In order to isolate the first order diffracted focus and arrangement of central stop and order-sorting-aperture (OSA) has to be used (see Fig. 1.9.)

1.3.4 Image Contrast Mechanism with X-rays

In order to visualize the structure and features of a specimen we rely on different methods of image contrast. In the following we briefly detail the different contrast mechanism for microscopy with X-rays.

Absorption Contrast

From Eq. 1.11 we know that the intensity of X-rays after propagating through a material with thickness t and index of refraction n (Eq. 1.2) is given by the modulus squared of the wave amplitude

$$I(t) = |\psi(t)|^2 = I_0\,\exp(-2\beta k t)\,. \tag{1.20}$$

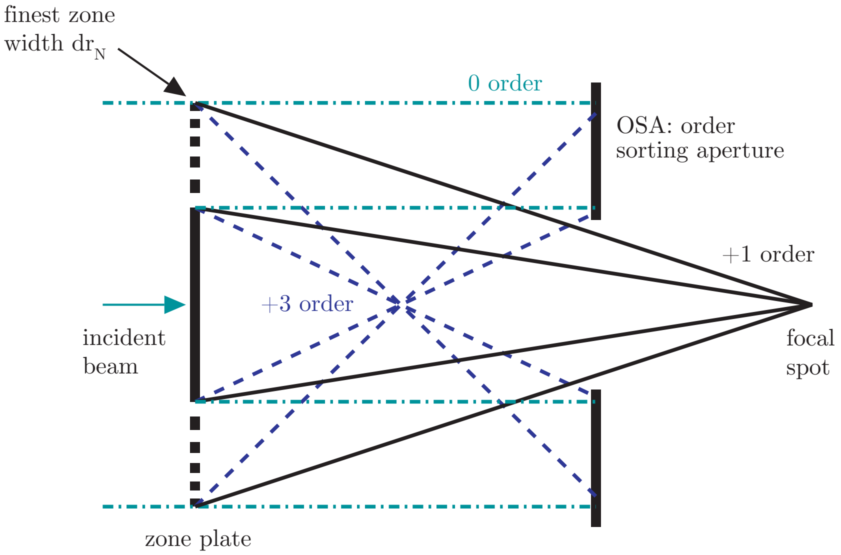

Figure 1.9: Isolation of first order focus through an arrangement of central stop (here incorporated in the zone plate) and an order-sorting-aperture (OSA). The required distance from the focus to the OSA determines the minimum OSA diameter, and successively the diameter of the central stop. The central stop should not cover more than half of the zone plates diameter in order to not degrade to focal spot quality negatively.

For practical purposes we define the attenuation coefficient μ

$$\mu \equiv 2\beta k = \frac{4\pi\beta}{\lambda}\,. \tag{1.21}$$

The inverse attenuation coefficient is referred to as the $1/e$ penetration depth of wavelength λ with optical constant β. When measuring the absorption in transmission imaging, the specimen thickness is not known in most cases. Instead the optical density is measured and is defined as

$$\mathrm{OD} = -\ln\left(\frac{I}{I_0}\right), \tag{1.22}$$

where I_0 is the intensity incident on the specimen and I is the intensity afterwards. Comparison of the previous equations yields for the optical density $\mathrm{OD} = \mu\, t$.

A collected absorption image reflects the specimen's absorption at each point by

$$\mathrm{OD}(\boldsymbol{r}) = -\ln\left(\frac{I(\boldsymbol{r})}{I_0}\right) = \mu(\boldsymbol{r})\, t(\boldsymbol{r})\,; \tag{1.23}$$

the contrast is therefore due to thickness variations and variations in the attenuation coefficient. For thick specimens, where different materials lie on top of each other, the transmission contrast will yield a projection through the specimen. If z is the direction of the optical axis, one will measure

$$\mathrm{OD}(\boldsymbol{r}) = \int_0^t \mathrm{d}z\, \mu(\boldsymbol{r}, z)\,. \tag{1.24}$$

Phase Contrast

Instead of mapping the absorption of the specimen, one can also measure its phase shift

$$\Delta\phi = \delta(\boldsymbol{r}) \cdot k \cdot t(\boldsymbol{r}) \tag{1.25}$$

which is imposed onto the incident x-ray wave field through the specimen as a function of specimen position $\boldsymbol{r}$. For thick specimens, one measures

$$\Delta\phi = \int_0^t \mathrm{d}z\, \delta(\boldsymbol{r}, z)\, k \tag{1.26}$$

in analogy to projected absorption. As x-ray detectors are sensitive only to the intensity of the wave, and not to its phase, one must use indirect methods that turn phase differences into an intensity variatons. Phase contrast is the key topic of this work and we will show different methods for imaging in phase for full-field and scanning microscopes in the following chapters.

Fluorescence

The emission of fluorescence photons and their detection can be used to obtain element specific images or maps of the specimen. The contrast in this case comes from the identification of the elemental content of the specimen through the collected fluorescence spectra. Note that in order to get a two dimensional image of the element content the fluorescence needs to be collected in a raster scanning way in order to attribute spatial location to the measured fluorescence photons.

Dark Field

Instead of collecting the transmitted intensity through the specimen, in dark field imaging only the total scattering signal is collected. Small structures will scatter the incident radiation at large angles outside of the directly transmitted beam mainly contributing to the dark-field signal. Sensitivity is therefore given to structures that are small in size and edge features of specimen.

Other Modes of Contrast

A large set of other contrast modes is available for the visualization of specimen features and characteristics, such as spectroscopy, labeling, etc., but these are beyond the scope of this work.

1.4 Phase Contrast with X-rays and its Applications

1.4.1 Phase Versus Absorption Contrast

As we have seen in the previous section, transmission x-ray microscopes generally image the spatial distribution of the refractive index of the specimen; that is, either its imaginary part in absorption contrast, or its real part in phase contrast. Absorption contrast is generally straightforward to measure due to the intensity sensitivity of available detectors. By comparison, phase contrast requires indirect methods, which turn phase differences somehow into detectable intensity differences. Why is it then still useful to measure phase given the additional hurdles?

As we have seen in Sec. 1.2.2 and Fig. 1.2 the real part of the atomic scattering factor (connected with phase contrast) remains approximately constant over a wide range of photon energies, while the imaginary part responsible for absorption contrast falls off with the square of the wavelength. Hence phase is the dominating contrast mechanism for transmission imaging at hard x-ray energies. Figure 1.10 compares the number of photons required to visualize a 50 nm protein structure in absorption and differential phase contrast (see Sec. 3.1.2) at a signal-to-noise ratio of 5 (Rose criterion [24]), with far fewer photons and therefore dose delivered to the sample for phase contrast. One can estimate in a simplified model that the number of photons to resolve a structure at the same signal-to-noise ratio in absorption N_{Abs} versus phase contrast N_{PC} scales as [25]

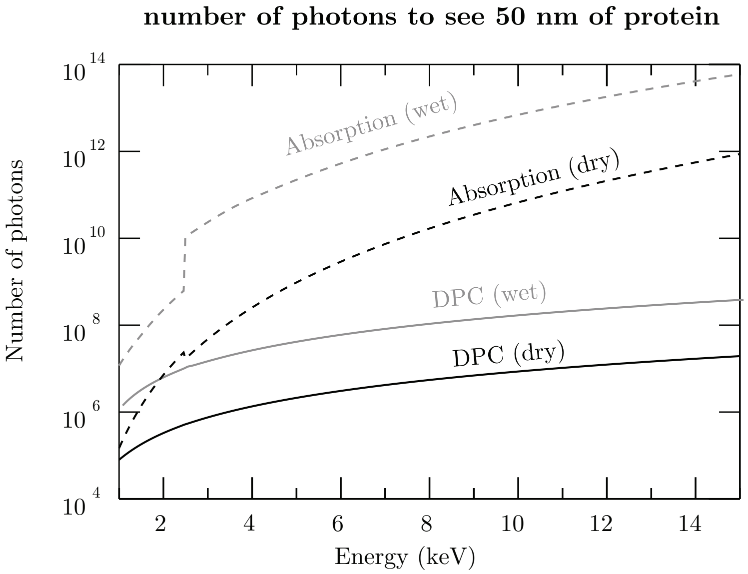

Figure 1.10: Number of photons to visualize a 50 nm protein structure in either air of water as a function of photon energy in respective contrast modes of absorption and phase. Figure reproduced from [25].

$$\frac{N_{\mathrm{PC}}}{N_{\mathrm{Abs}}} = \frac{\beta^2}{\delta^2}\,, \tag{1.27}$$

where in the hard x-ray regime for typical specimens this ratio ranges from 10^{-2} to 10^{-6}; giving phase contrast a clear advantage.

1.4.2 Methods of Phase Contrast

The first phase contrast measurements in lens-based x-ray microscopes were done by Schmahl *et al.* [26], using the Zernike technique [27] in a full-field microscope. More methods, including the Nomarski, interferometric, holographic and propagation-based methods, are described in a recent review by Momose [28]. In scanning systems, there have been demonstrations with configured detectors as described above [29, 30], a wavefront profiler in combination with a slit detector [31–33], aperture alignment [34], and the use of offset zone plate doublets [35].

The presented work will consider phase contrast methods in scanning microscopy based on segmented detectors and Zernike phase contrast for full-field and a newly developed scanning method [7].

1.4.3 Stony Brook Segmented Detector for Phase Contrast

It turns out that a low level of spatial sensitivity to the transmitted intensity in a scanning microscope is enough to obtain phase contrast images. Such a detector system for soft and hard X-rays has been developed at Stony Brook University in the past [11, 36]. Figure 1.11 shows a photograph of the complete detector system, which since has found applications across the synchrotron community at several facilities including the Australian Synchrotron (Melbourne, Australia), NSLS (Brookhaven, USA), APS (Agonne, IL) and SOLEIL (Paris, France).

The segmented structure of the detector builds the basis for the qualitative and quantitative phase contrast approaches discussed in Ch. 3. Figure 1.12 shows three of the segmentation geometries available for this detector system.

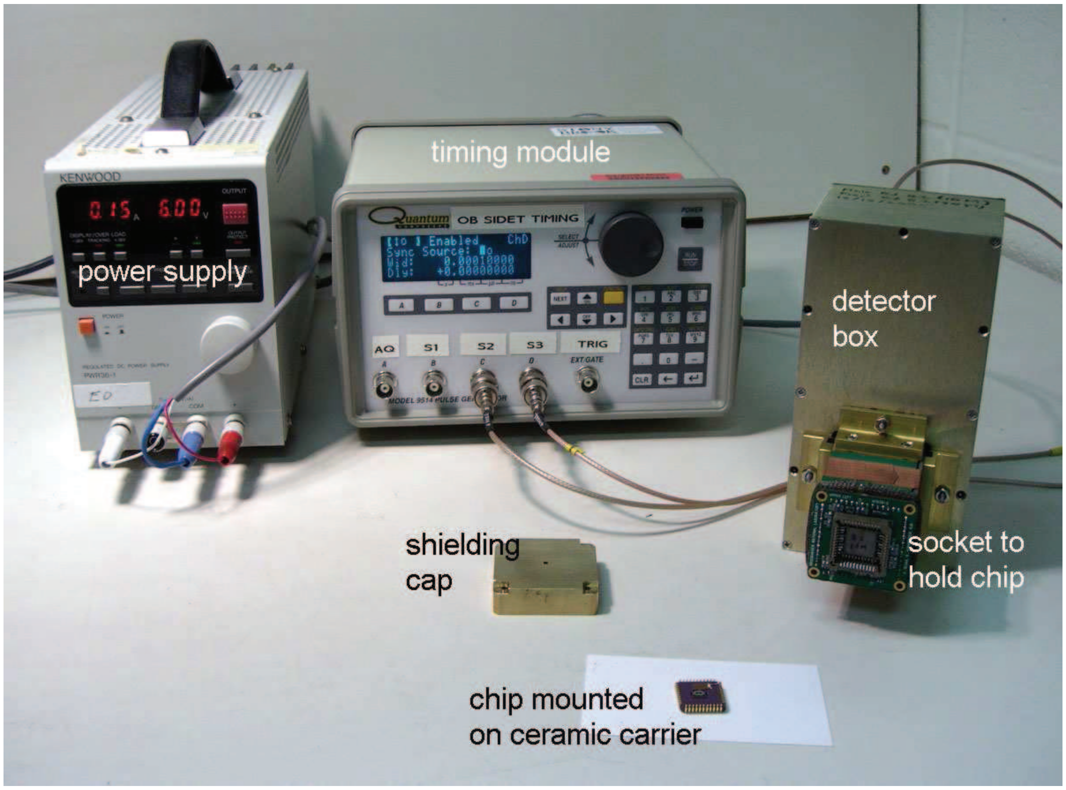

Figure 1.11: Stony Brook segmented detector system.

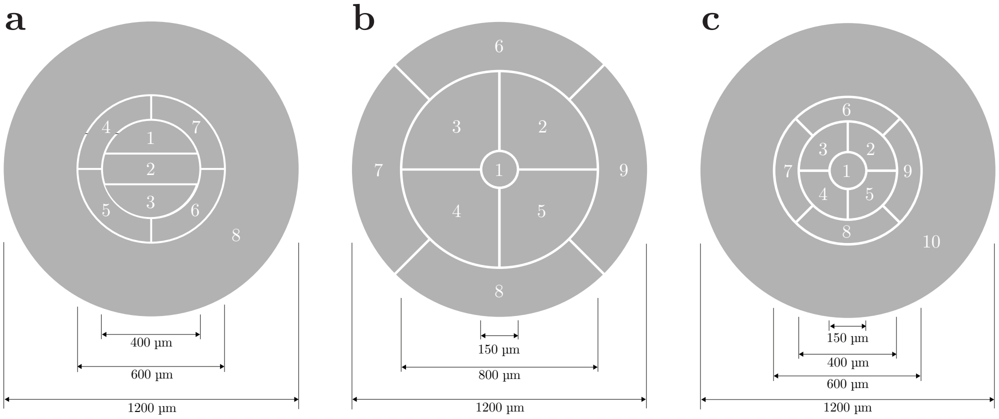

Figure 1.12: Segmented detector geometries; (**a**) 8, (**b**) 9 and (**c**) 10 segment structure.

Chapter 2

Image Formation and Reciprocity

This chapter deals with the treatment of image formation in the two major direct imaging systems: scanning and full-field microscopes. First, the wave field propagation employed in the successive treatment is discussed, resulting in the main propagation expressions for wave fields between two planes (Eq. 2.5). A detailed description of the image formation process in the scanning and full-field imaging systems is then laid out. We conclude the chapter by highlighting the equivalence of both imaging systems, which will be of further importance for the latter part of this work.

2.1 Wave Field Propagation

To propagate wave fields from one plane to another we use the Fresnel-Kirchhoff diffraction integral [23, 37]. Figure 2.1 illustrates the coordinate space for the propagation from the plane with coordinates $\boldsymbol{r}_1$ to a parallel plane $\boldsymbol{r}_2$ a distance z away. We consider the diffraction of monochromatic light by a finite aperture Σ in an infinite opaque screen. The wave field ψ_2 in the plane specified by $\boldsymbol{r}_2$ due to a wave field ψ_1 and the aperture Σ is given by the

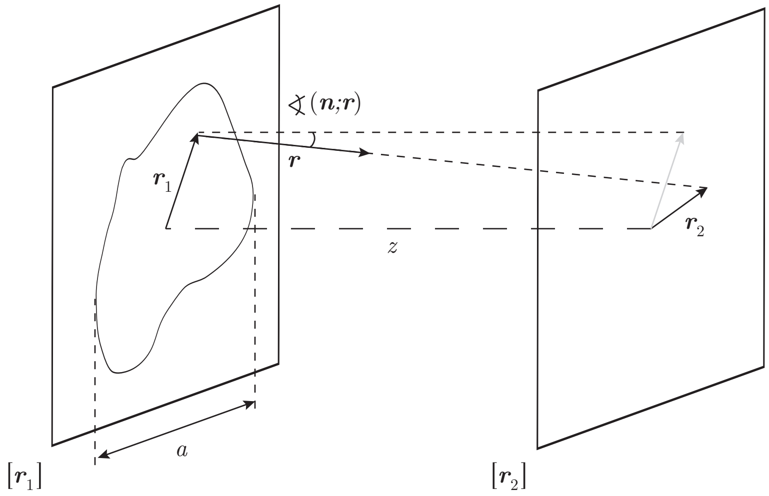

Figure 2.1: Wave field propagation between two planes.

Fresnel-Kirchhoff / Rayleigh-Sommerfeld diffraction formula

$$\psi_2(\boldsymbol{r}_2) = \int_\Sigma \mathrm{d}^2\boldsymbol{r}_1 \, \frac{\mathrm{e}^{-\mathrm{i}kr}}{\mathrm{i}\lambda r} \, \cos(\boldsymbol{n}, \boldsymbol{r}) \, \psi_1(\boldsymbol{r}_1)\,, \tag{2.1}$$

where $r = \sqrt{z^2 + (\boldsymbol{r}_2 - \boldsymbol{r}_1)^2}$ is the distance between a point in the aperture and the observation plane and $(\boldsymbol{n}, \boldsymbol{r})$ is the angle between the normal to the surface Σ and the distance vector $\boldsymbol{r}$. Note, that the choice of sign in the exponential term is a matter of convention with respect to the traveling direction one chooses for the propagating fields. Furthermore, it is common to consider an integral with infinite limits, where it is understood that ψ_1 is identical to zero outside of the aperture. The maximum linear extend of the aperture is denoted by a.

Initial approximations

Some initial approximations to the above diffraction integral can be made if we assume that the distance z between aperture and observation plane is much greater than the maximal linear extend a of the aperture. Furthermore, we will assume that in the observation plane only a finite region about the optical axis is of interest, and that z is also much greater than the maximal linear dimension of this region. With these assumptions the vectors $\boldsymbol{n}$ and $\boldsymbol{r}$ will be nearly parallel and we can readily conclude $\cos(\boldsymbol{n}, \boldsymbol{r}) \approx 1$.

Similarly, these conditions can be applied to the distance r in the denominator, which will not differ much from z, so that we can simplify the weighting function of Eq. 2.1 to be

$$\frac{\mathrm{e}^{-\mathrm{i}kr}}{\mathrm{i}\lambda r} \, \cos(\boldsymbol{n}, \boldsymbol{r}) \approx \frac{\mathrm{e}^{-\mathrm{i}kr}}{\mathrm{i}\lambda z}\,. \tag{2.2}$$

Note, that the distance r in the exponent cannot be simply replaced by z, as it is multiplied with a large number k, and consequently would lead to rapidly varying phase errors exceeding 2π rad.

Fresnel approximation

Continuing simplifications can be obtained by considering specific approximations to the quantity r in the exponent, which is given by

$$r = \sqrt{z^2 + (\boldsymbol{r}_2 - \boldsymbol{r}_1)^2} = z\sqrt{1 + \left(\frac{\boldsymbol{r}_2 - \boldsymbol{r}_1}{z}\right)^2}\,. \tag{2.3}$$

Performing a binomial expansion of the square root[1] and assuming that an adequate representation is given through the first two terms we can write

$$z\sqrt{1+\left(\frac{\boldsymbol{r}_2-\boldsymbol{r}_1}{z}\right)^2} \approx z\left[1+\frac{1}{2}\left(\frac{\boldsymbol{r}_2-\boldsymbol{r}_1}{z}\right)^2\right] \tag{2.4}$$

which is commonly referred to as the *Fresnel approximation*. If the conditions are fulfilled for this approximation to be valid, one is said to be in the *Fresnel regime* of diffraction.

The resulting expression of wave propagation in the Fresnel regime is

$$\psi_2(\boldsymbol{r}_2) = \frac{\mathrm{e}^{-\mathrm{i}kz}}{\mathrm{i}\lambda z} \int \mathrm{d}^2\boldsymbol{r}_1\, \psi_1(\boldsymbol{r}_1)\, \exp\left(\frac{-\mathrm{i}k}{2z}\,(\boldsymbol{r}_2-\boldsymbol{r}_1)^2\right). \tag{2.5}$$

The critical part of this approximation is that we replace spherical wavelets with quadratic surfaces. For this to be valid, certain margins have to be imposed on the sizes of the aperture, propagation distance and observation region. A sufficient condition is

$$z^3 >> \frac{\pi}{4\lambda}\,\mathrm{Max}[(\boldsymbol{r}_2-\boldsymbol{r}_1)^2]^2\,, \tag{2.6}$$

which implies that the contribution to the next higher order term in the expansion is much less than 1 rad; for a more detailed discussion see Born and Wolf [37] or Goodman [23]. As a general, statement one can say that the considered field-of-view needs to be small for the Fresnel approximation to be applicable.

Through writing Eq. 2.5 in a more explicit way we can identify a few more characteristics of the expression

$$\psi_2(\boldsymbol{r}_2) = \frac{\mathrm{e}^{-\mathrm{i}kz}}{\mathrm{i}\lambda z} \exp\left(\frac{-\mathrm{i}k}{2z}\,\boldsymbol{r}_2^2\right) \int \mathrm{d}^2\boldsymbol{r}_1\, \psi_1(\boldsymbol{r}_1)\, \exp\left(\frac{-\mathrm{i}k}{2z}\,\boldsymbol{r}_1^2\right)\, \exp\left(\frac{\mathrm{i}k}{z}\,\boldsymbol{r}_2\boldsymbol{r}_1\right), \tag{2.7}$$

where we can see that aside from pre-factors, ψ_2 corresponds to a Fourier transform of the function $\psi_1(\boldsymbol{r}_1)\,\exp\left(-\mathrm{i}k\boldsymbol{r}_1^2/(2z)\right)$ with frequency coordinates $\boldsymbol{f}_2 = \boldsymbol{r}_2/(\lambda z)$. Frequency coordinates such as $\boldsymbol{f}_2$ in essence represent a wavelength normalized diffraction angle and are usually referred to as *spatial frequencies*; these quantities are often used in two-dimensional image analysis, as they provide a description of the diffraction that is independent of the observation plane. However, note that the limiting conditions for the Fresnel and other approximations need to be fulfilled; one cannot just simply consider any

---

[1] Expansion: $\sqrt{1+x} = 1 + \frac{1}{2}x - \frac{1}{8}x^2 + ... \qquad |x| < 1$

specific plane.

Fraunhofer approximation

From Eq. 2.7 we can see that further simplifications can be applied when considering more rigorous restrictions than those of the Fresnel approximation. If the stronger *Fraunhofer* assumption is satisfied

$$z >> \frac{k\,\mathrm{Max}[\boldsymbol{r}_1^2]}{2}\,, \tag{2.8}$$

the quadratic phase factor of the integrand in Eq. 2.7 can be neglected to yield the *Fraunhofer approximation* of the diffraction integral

$$\psi_2(\boldsymbol{r}_2) = \frac{\mathrm{e}^{-\mathrm{i}kz}}{\mathrm{i}\lambda z} \exp\left(\frac{-\mathrm{i}k}{2z}\,\boldsymbol{r}_2^2\right) \int \mathrm{d}^2\boldsymbol{r}_1\, \psi_1(\boldsymbol{r}_1) \exp\left(\frac{\mathrm{i}k}{z}\,\boldsymbol{r}_2\boldsymbol{r}_1\right). \tag{2.9}$$

Besides pre-factors the resulting wave field ψ_2 is the direct Fourier transform of the wave field within the aperture ψ_1 with spatial frequencies $\boldsymbol{f}_2 = \boldsymbol{r}_2/(\lambda z)$. The region where this expression describes the diffraction appropriately is called the *Fraunhofer* or *far-field* regime.

Note, that the conditions required for Eq. 2.8 to be fulfilled can be quite severe; however, Fraunhofer diffraction can be observed at distances closer than implied by Eq. 2.8 if the wave field illuminating the aperture is spherically convergent. An example of this will be seen in Sec. 2.2 when considering the image formation in a scanning microscope.

Fresnel number

The Fresnel number F provides a measure to identify the regime of the observed diffraction; it is given by

$$F = \frac{a^2}{\lambda z}\,, \tag{2.10}$$

where a is the maximal linear extend of the considered aperture. The classification is done as follows [37]:

$$\begin{aligned} F &\gtrsim 1 &\longrightarrow\quad &\text{Fresnel / near-field regime}\\ F &<< 1 &\longrightarrow\quad &\text{Fraunhofer / far-field regime}\end{aligned}$$

2.2 Scanning Image Formation

We now turn our attention to the image formation process in a scanning transmission x-ray microscope (STXM). Figure 2.2 shows a schematic of the optical arrangement in the microscope. A point-like source illuminates the zone plate.

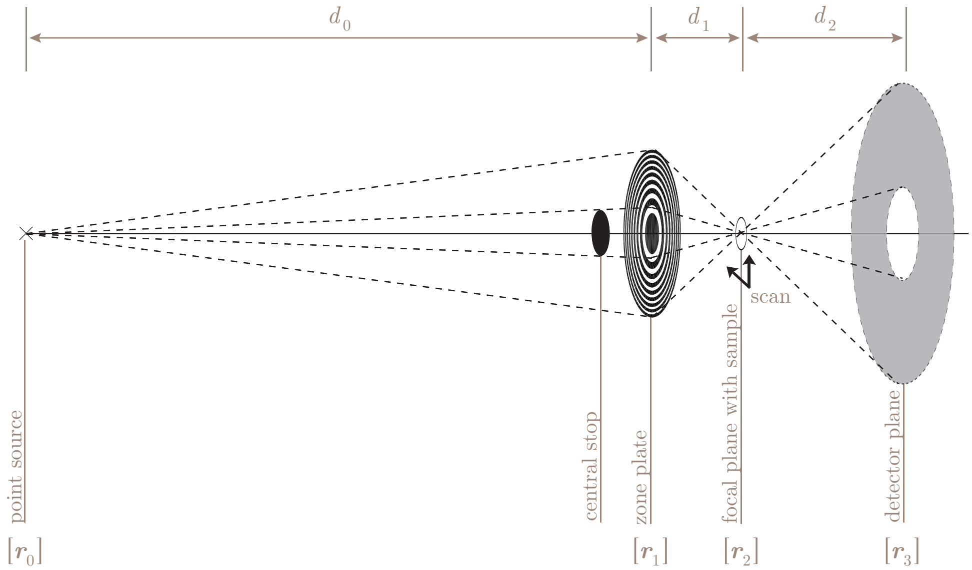

Figure 2.2: Schematic of scanning transmission x-ray microscope. Distances between the respective planes, as well as the according coordinates, are indicated.

In order to obtain a diffraction limited spot size and therefore resolution of the microscope, the source must be sufficiently small and far away from the objective zone plate, so that the lens is illuminated with a high degree of spatial coherence [38]. The objective lens then focuses the radiation to a small spot through which the sample is raster scanned. The transmitted intensity for each scan displacement ($\boldsymbol{r}_s$) is recorded in a far-field plane from the focus with a detector having a response R. The central stop in front of the objective can be considered part of the lens.

The objective lens is a zone plate with diameter D_o and outermost zone width $\mathrm{d}r_\mathrm{N}$ and hence a spatial cut-off frequency $f_\mathrm{o}^\mathrm{cut-off} = 1/(2\,\mathrm{d}r_\mathrm{N})$. To isolate the first order focus (see Sec. 1.3.3) a central stop has to be used, which has a diameter D_stop; its corresponding cut-off in spatial frequency space will then be $f_\mathrm{stop}^\mathrm{cut-off} = (D_\mathrm{stop}/D_\mathrm{o})\, f_\mathrm{o}^\mathrm{cut-off}$. The objective aperture is described by having a real pupil function

$$P_\mathrm{o}(\boldsymbol{f}) = \begin{cases} 0 & : \quad |\boldsymbol{f}| < f_\mathrm{stop}^\mathrm{cut-off} \\ 1 & : \quad f_\mathrm{stop}^\mathrm{cut-off} \leq |\boldsymbol{f}| \leq f_\mathrm{o}^\mathrm{cut-off} \\ 0 & : \quad |\boldsymbol{f}| > f_\mathrm{o}^\mathrm{cut-off} \end{cases} . \tag{2.11}$$

The zone plate is assumed to be operated in its first diffraction order, where its focal length is given by f_o. If the zone plate consists of enough zones its influence on the wave field can be considered to that of a thin lens and therefore is described by a quadratic phase factor (see [9]), so that the total transmission function of the zone plate is given by

$$t(\boldsymbol{r}_1) = P_\mathrm{o}(\boldsymbol{r}_1)\, \exp\left(\frac{\mathrm{i}k}{2f_\mathrm{o}}\,\boldsymbol{r}_1^2\right) . \tag{2.12}$$

Wave propagation to detector plane

In order to propagate wave fields between planes in the following, we will use the Fresnel approximation of the diffraction integral of Eq. 2.5; note that constant phase factors preceding the integrals will be left out as they will not contribute to the final image.

We will assume the point source to be monochromatic and of amplitude ψ_0 at a point on the optical axis a distance d_0 away from the zone plate; its spatial distribution is described by a Delta-function $\Delta(\boldsymbol{r}_0)$. Propagation of this wave field to the objective lens and multiplication with the zone plate's transmission function (Eq. 2.12) gives for the wave field ψ_1' exiting the zone plate

$$\psi_1'(\boldsymbol{r}_1) = \frac{1}{\mathrm{i}\lambda d_0} \int \mathrm{d}^2\boldsymbol{r}_0\, \psi_0 \Delta(\boldsymbol{r}_0)\, \exp\left(\frac{-\mathrm{i}k}{2d_0}\,(\boldsymbol{r}_1 - \boldsymbol{r}_0)^2\right) P_\mathrm{o}(\boldsymbol{r}_1)\, \exp\left(\frac{\mathrm{i}k}{2f_\mathrm{o}}\,\boldsymbol{r}_1^2\right) . \tag{2.13}$$

The wavefield ψ_2 in the focal plane a distance d_1 away is then given by

$$\begin{aligned} \psi_2(\boldsymbol{r}_2) = \frac{-1}{\lambda^2 d_0 d_1} \int \mathrm{d}^2\boldsymbol{r}_1 \int \mathrm{d}^2\boldsymbol{r}_0\, \psi_0 \Delta(\boldsymbol{r}_0)\, \exp\left(\frac{-\mathrm{i}k}{2d_0}\,(\boldsymbol{r}_1 - \boldsymbol{r}_0)^2\right) \\ P_\mathrm{o}(\boldsymbol{r}_1)\, \exp\left(\frac{\mathrm{i}k}{2f_\mathrm{o}}\,\boldsymbol{r}_1^2\right)\, \exp\left(\frac{-\mathrm{i}k}{2d_1}\,(\boldsymbol{r}_2 - \boldsymbol{r}_1)^2\right) . \end{aligned} \tag{2.14}$$

Satisfying the lens law

$$\frac{1}{d_0} + \frac{1}{d_1} = \frac{1}{f_\mathrm{o}} \tag{2.15}$$

will cancel the quadratic phase factors in $\boldsymbol{r}_1$ and yield

$$\begin{aligned}\psi_2(\boldsymbol{r}_2) = \frac{-1}{\lambda^2 d_0 d_1} \exp\left(\frac{-\mathrm{i}k}{2d_1}\boldsymbol{r}_2^2\right) \int \mathrm{d}^2\boldsymbol{r}_1 \int \mathrm{d}^2\boldsymbol{r}_0\, \psi_0 \Delta(\boldsymbol{r}_0)\, P_\mathrm{o}(\boldsymbol{r}_1) \\ \exp\left(\frac{-\mathrm{i}k}{2d_0}\boldsymbol{r}_0^2\right) \exp\left(\mathrm{i}k\left(\frac{\boldsymbol{r}_2}{d_1} + \frac{\boldsymbol{r}_0}{d_0}\right)\boldsymbol{r}_1\right) .\end{aligned} \tag{2.16}$$

Now we perform the integral over $\boldsymbol{r}_0$ via the Delta-function and get

$$\psi_2(\boldsymbol{r}_2) = \frac{-1}{\lambda^2 d_0 d_1}\, \psi_0 \exp\left(\frac{-\mathrm{i}k}{2d_1}\boldsymbol{r}_2^2\right) \int \mathrm{d}^2\boldsymbol{r}_1\, P_\mathrm{o}(\boldsymbol{r}_1) \exp\left(\frac{\mathrm{i}k}{d_1}\boldsymbol{r}_1\boldsymbol{r}_2\right) , \tag{2.17}$$

which is the wave field in the focal plane.

The phase term quadratic in $\boldsymbol{r}_2$ can be left out given the following consideration. With a zone plate of outermost zone width $\mathrm{d}r_\mathrm{N}$ and consequently a Rayleigh resolution of $1.22\,\mathrm{d}r_\mathrm{N}$, there will be no noticeable optical amplitude at distances exceeding approximately five Rayleigh resolution lengths. Therefore, one can limit the consideration within the $[\boldsymbol{r}_2]$ plane to distances $|\boldsymbol{r}_2| < 5 \times 1.22\,\mathrm{d}r_\mathrm{N}$ and the absolute value of the phase term then becomes

$$\phi = 25\,(1.22)^2\,\mathrm{d}r_\mathrm{N}^2 \frac{\pi}{\lambda d_1} . \tag{2.18}$$

If we take typical experimental values for hard X-rays: $\mathrm{d}r_\mathrm{N} = 100\,\mathrm{nm}$ at a wavelength of $\lambda = 0.121\,\mathrm{nm}$ (10 keV), then d_1 is approximately 130 mm; the resulting value is $\phi \approx 2 \times 10^{-3} << 1$. Hence, we can neglect the quadratic phase factor preceding the integral.

The wave field in the focal plane of the microscope is therefore

$$p_\mathrm{o}(\boldsymbol{r}_2) \equiv \psi_2(\boldsymbol{r}_2) = \frac{-1}{\lambda^2 d_0 d_1}\, \psi_0 \int \mathrm{d}^2\boldsymbol{r}_1\, P_\mathrm{o}(\boldsymbol{r}_1) \exp\left(\frac{\mathrm{i}k}{d_1}\boldsymbol{r}_1\boldsymbol{r}_2\right) , \tag{2.19}$$

which is often referred to as *probe function* p_o. Notice that the probe function in essence is the Fourier transform of the objective pupil function

$$p_\mathrm{o}(\boldsymbol{r}_2) = \mathcal{C}\, \mathcal{F}^{-1}_{\boldsymbol{r}_2}\{P_\mathrm{o}(\boldsymbol{f}_1)\} , \tag{2.20}$$

with spatial frequency $\boldsymbol{f}_1 = \boldsymbol{r}_1/(\lambda d_1)$ and $\mathcal{C}$ some constant. In the focal plane the probe function interacts with the specimen function h and the wave field exiting the specimen is thus given by (see Sec. 1.12)

$$\psi_2'(\boldsymbol{r}_2) = h(\boldsymbol{r}_2)\, p_o(\boldsymbol{r}_2 - \boldsymbol{r}_\mathrm{s}) , \tag{2.21}$$

where $\boldsymbol{r}_\mathrm{s}$ is the scan displacement of the probe with respect to specimen. For a detailed discussion of this expression to be valid we refer to the supplementary material of Thibault *et al.* [39]. The wave field is then propagated a distance d_2 to the detector plane:

$$\begin{aligned}\psi_3(\boldsymbol{r}_3;\boldsymbol{r}_\mathrm{s}) = \frac{\mathrm{i}}{\lambda^3 d_0 d_1 d_2}\,\psi_0\,\exp\left(\frac{-\mathrm{i}k}{2d_2}\,\boldsymbol{r}_3^2\right)\\ \int \mathrm{d}^2\boldsymbol{r}_2\, h(\boldsymbol{r}_2)\, p_\mathrm{o}(\boldsymbol{r}_2-\boldsymbol{r}_\mathrm{s})\,\exp\left(\frac{-\mathrm{i}k}{2d_2}\,\boldsymbol{r}_2^2\right)\,\exp\left(\frac{\mathrm{i}k}{d_2}\,\boldsymbol{r}_2\boldsymbol{r}_3\right);\end{aligned} \tag{2.22}$$

similarly to Eq. 2.17 we can argue to neglect the quadratic phase factor in $\boldsymbol{r}_2$ (the distance d_2 is usually a multiple of d_1, making the value of Eq.2.18) even smaller). The quadratic phase factor in $\boldsymbol{r}_3$ preceding the integral can be disregarded, as in the end we are only interested in the intensity of the wave field in the detector plane, where then this phase factor will be canceled.

We have now arrived at the answer of interest, the wave field in the microscopes detection plane

$$\psi_3(\boldsymbol{r}_3;\,\boldsymbol{r}_s) = \frac{\mathrm{i}\,\psi_0}{\lambda^3 d_0 d_1 d_2}\int \mathrm{d}^2\boldsymbol{r}_2\, h(\boldsymbol{r}_2)\, p_o(\boldsymbol{r}_2-\boldsymbol{r}_s)\,\exp\left(\frac{\mathrm{i}k}{d_2}\,\boldsymbol{r}_2\boldsymbol{r}_3\right), \tag{2.23}$$

which is essentially the Fourier transform of the wave field exiting the specimen

$$\Psi_3(\boldsymbol{f}_3;\,\boldsymbol{r}_s) = \mathcal{C}\,\mathcal{F}^{-1}_{\boldsymbol{f}_3}\{h(\boldsymbol{r}_2)\,p_o(\boldsymbol{r}_2-\boldsymbol{r}_\mathrm{s})\}\,, \tag{2.24}$$

with $\boldsymbol{f}_3 = \boldsymbol{r}_3/(\lambda d_2)$ and $\mathcal{C}$ some constant; we write Ψ_3 to indicate its formulation in terms of spatial frequency, but there is no substantial difference to ψ_3.

Intensity in detector plane

In order to consider the intensity caused by Eq. 2.23 in the detector plane we will expand its expression by inserting the probe function p_o

$$\begin{aligned}\psi_3(\boldsymbol{r}_3;\,\boldsymbol{r}_s) = \frac{\mathrm{i}\,\psi_0}{\lambda^3 d_0 d_1 d_2}\int \mathrm{d}^2\boldsymbol{r}_2\int \mathrm{d}^2\boldsymbol{r}_1\, h(\boldsymbol{r}_2)\, P_\mathrm{o}(\boldsymbol{r}_1)\,\exp\left(\frac{\mathrm{i}k}{d_2}\,\boldsymbol{r}_2\boldsymbol{r}_3\right)\\ \exp\left(\frac{\mathrm{i}k}{d_1}\,\boldsymbol{r}_1(\boldsymbol{r}_2-\boldsymbol{r}_\mathrm{s})\right),\end{aligned} \tag{2.25}$$

The intensity measured with a detector that has a response function $R(\boldsymbol{r}_3)$ is given by

$$\begin{aligned} I_3(\boldsymbol{r}_s) &= \int \mathrm{d}^2\boldsymbol{r}_3\, R(\boldsymbol{r}_3)\, |\psi_3(\boldsymbol{r}_3;\, \boldsymbol{r}_s)|^2 \\ &= \frac{|\psi_0|^2}{\lambda^6 d_0^2 d_1^2 d_2^2} \int \mathrm{d}^2\boldsymbol{r}_3\, R(\boldsymbol{r}_3) \bigg| \int \mathrm{d}^2\boldsymbol{r}_2 \int \mathrm{d}^2\boldsymbol{r}_1\, h(\boldsymbol{r}_2)\, P_\mathrm{o}(\boldsymbol{r}_1) \\ &\quad \exp\left(\frac{\mathrm{i}k}{d_1}\,\boldsymbol{r}_1(\boldsymbol{r}_2 - \boldsymbol{r}_\mathrm{s}) + \frac{\mathrm{i}k}{d_2}\,\boldsymbol{r}_2\boldsymbol{r}_3\right)\bigg|^2 , \end{aligned} \tag{2.26}$$

We can now further simplify this by expressing the specimen function in terms of its spatial frequency content

$$h(\boldsymbol{r}_2) = \int \mathrm{d}^2\boldsymbol{f}_2\, H(\boldsymbol{f}_2)\, \exp\left(2\pi\mathrm{i}\boldsymbol{f}_2\,\boldsymbol{r}_2\right). \tag{2.27}$$

Inserting this into the intensity yields

$$\begin{aligned} I_3(\boldsymbol{r}_s) = \frac{|\psi_0|^2}{\lambda^6 d_0^2 d_1^2 d_2^2} &\int \mathrm{d}^2\boldsymbol{r}_3\, R(\boldsymbol{r}_3) \bigg| \int \mathrm{d}^2\boldsymbol{r}_2 \int \mathrm{d}^2\boldsymbol{r}_1 \int \mathrm{d}^2\boldsymbol{f}_2\, H(\boldsymbol{f}_2)\, P_\mathrm{o}(\boldsymbol{r}_1) \\ &\exp\left(\mathrm{i}k\left(\frac{\boldsymbol{r}_1}{d_1} + \frac{\boldsymbol{r}_3}{d_2} + \lambda\boldsymbol{f}_2\right)\boldsymbol{r}_2\right) \exp\left(-\mathrm{i}k\,\frac{\boldsymbol{r}_1}{d_1}\,\boldsymbol{r}_\mathrm{s}\right)\bigg|^2 ; \end{aligned} \tag{2.28}$$

integration over $\boldsymbol{r}_2$ will yield a Delta-function

$$\int \mathrm{d}^2\boldsymbol{r}_2 \exp\left(\mathrm{i}k\left(\frac{\boldsymbol{r}_1}{d_1} + \frac{\boldsymbol{r}_3}{d_2} + \lambda\boldsymbol{f}_2\right)\boldsymbol{r}_2\right) = |\lambda^2 d_1^2|\, \Delta\left(\boldsymbol{r}_1 + \frac{d_1\boldsymbol{r}_3}{d_2} + \lambda d_1\boldsymbol{f}_2\right), \tag{2.29}$$

with which we can perform the integral over $\boldsymbol{r}_1$. The intensity then will be

$$\begin{aligned} I_3(\boldsymbol{r}_s) = \frac{d_1^2|\psi_0|^2}{\lambda^2 d_0^2 d_2^2} &\int \mathrm{d}^2\boldsymbol{r}_3\, R(\boldsymbol{r}_3) \bigg| \int \mathrm{d}^2\boldsymbol{f}_2\, H(\boldsymbol{f}_2)\, P_\mathrm{o}\left(d_1\left(\lambda\boldsymbol{f}_2 + \frac{\boldsymbol{r}_3}{d_2}\right)\right) \\ &\exp\left(2\pi\mathrm{i}\boldsymbol{f}_2\boldsymbol{r}_\mathrm{s}\right) \exp\left(\mathrm{i}k\,\frac{\boldsymbol{r}_3}{d_2}\,\boldsymbol{r}_\mathrm{s}\right)\bigg|^2 , \end{aligned} \tag{2.30}$$

where the last phase factor containing $\boldsymbol{r}_3$ will cancel out, as it does not depend on the integration over $\boldsymbol{f}_2$ and stands inside the absolute value. Now we expand the absolute value to yield the final result

$$\begin{aligned} I_3(\boldsymbol{r}_s) = \frac{d_1^2|\psi_0|^2}{\lambda^2 d_0^2 d_2^2} \int \mathrm{d}^2\boldsymbol{r}_3\, R(\boldsymbol{r}_3) \int \mathrm{d}^2\boldsymbol{f}_2 \int \mathrm{d}^2\boldsymbol{f}_2'\, H(\boldsymbol{f}_2)\, H^*(\boldsymbol{f}_2') \\ P_\mathrm{o}\left(-d_1\left(\lambda\boldsymbol{f}_2 + \frac{\boldsymbol{r}_3}{d_2}\right)\right) P_\mathrm{o}^*\left(-d_1\left(\lambda\boldsymbol{f}_2' + \frac{\boldsymbol{r}_3}{d_2}\right)\right) \exp\left(2\pi\mathrm{i}(\boldsymbol{f}_2 - \boldsymbol{f}_2')\,\boldsymbol{r}_\mathrm{s}\right), \end{aligned} \tag{2.31}$$

In this form we can separate regarding an expression describing the image formation in terms of scanning bilinear transfer functions ($\mathcal{B}^{\mathrm{scan}}$)

$$\begin{aligned} I_3(\boldsymbol{r}_s) = \frac{d_1^2}{\lambda^2 d_0^2 d_2^2} \int \mathrm{d}^2\boldsymbol{f}_2 \int \mathrm{d}^2\boldsymbol{f}_2'\, \mathcal{B}^{\mathrm{scan}}(\boldsymbol{f}_2;\boldsymbol{f}_2')\, H(\boldsymbol{f}_2)\, H^*(\boldsymbol{f}_2') \\ \exp\left(2\pi\mathrm{i}(\boldsymbol{f}_2 - \boldsymbol{f}_2')\,\boldsymbol{r}_\mathrm{s}\right), \end{aligned} \tag{2.32}$$

and the optical system given by the bilinear transfer functions

$$\begin{aligned} \mathcal{B}^{\mathrm{scan}}(\boldsymbol{f}_2;\boldsymbol{f}_2') = \int \mathrm{d}^2\boldsymbol{r}_3\, |\psi_0|^2\, R(\boldsymbol{r}_3)\, P_\mathrm{o}\left(-d_1\left(\lambda\boldsymbol{f}_2 + \frac{\boldsymbol{r}_3}{d_2}\right)\right) \\ P_\mathrm{o}^*\left(-d_1\left(\lambda\boldsymbol{f}_2' + \frac{\boldsymbol{r}_3}{d_2}\right)\right), \end{aligned} \tag{2.33}$$

This result will become useful when we compare the scanning and full-field image formation in Sec. 2.4.

2.3 Full-field Image Formation

This section discusses the image formation in a full-field transmission x-ray microscope (TXM). In Fig. 2.3 a schematic of the optical components and their arrangement is shown. An extended source is focussed by a condenser zone plate to illuminate the specimen in the sample plane. An objective zone plate images the sample onto a spatially resolving detector. Note that in this configuration no central stop and order sorting aperture are needed for the objective zone plate, as the 0th order light passing through the objective will reach the image plane far away from the region where the actual image is formed (see Fig. 2.3). The condenser is incoherently illuminated by the source, which is desired to achieve a large field-of-view in the sample plane; see *e. g.* Vogt [40] for a discussion of incoherence in the TXM.

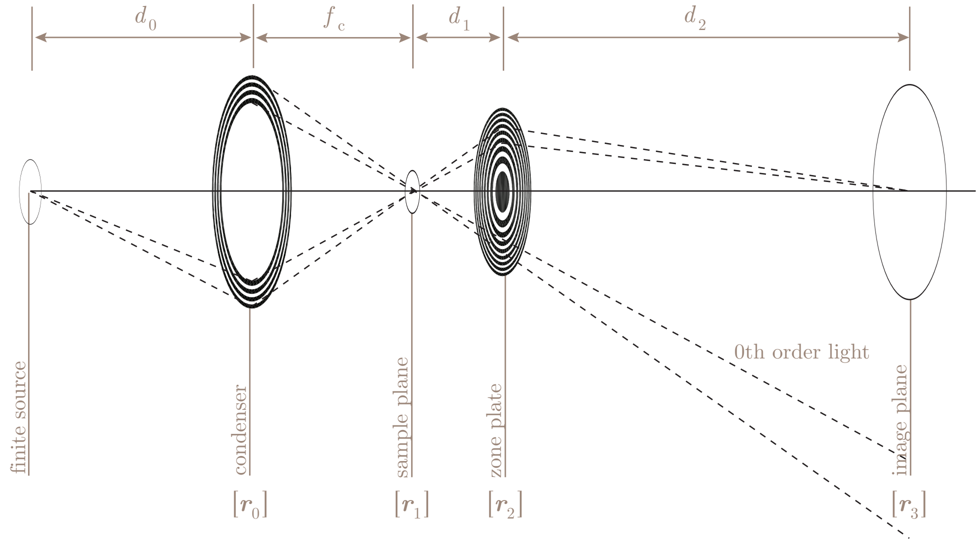

Figure 2.3: Schematic of full-field transmission x-ray microscope. Distances between the respective planes, as well as the according coordinates, are indicated.

The objective zone plate's pupil function is given by

$$P_{\mathrm{o}}(\boldsymbol{f}) = \begin{cases} 1 & : \quad |\boldsymbol{f}| \le f_{\mathrm{o}}^{\mathrm{cut-off}} \\ 0 & : \quad |\boldsymbol{f}| > f_{\mathrm{o}}^{\mathrm{cut-off}} \end{cases} , \tag{2.34}$$

and acts as a thin lens with transmission function as given by Eq. 2.12, with focal length f_{o}. The condenser zone plate with pupil function P_{c} and focal length f_{c} does have a similar transmission function.

Wave propagation to detector plane

Wave fields between image planes will be propagated by the Fresnel approximation of the diffraction integral of Eq. 2.5, omitting constant phase factors.

The extended source will cause a wave field with amplitude distribution $\psi_0(\boldsymbol{r}_0)$ in the condenser plane, the wave field exiting the condenser is given by

$$\psi_0'(\boldsymbol{r}_0) = \psi_0(\boldsymbol{r}_0)\, P_{\mathrm{c}}(\boldsymbol{r}_0)\, \exp\left(\frac{\mathrm{i}k}{2f_{\mathrm{c}}}\, \boldsymbol{r}_0^2\right) . \tag{2.35}$$

Since the condenser is incoherently illuminated, there is no phase correlation in between different points within the condenser. In order to calculate the light distribution in the image plane a single point of the wave field exiting the condenser is propagated through the imaging system, which successively leads to an intensity distribution in the image plane. The total intensity distribution due to all source points in the condenser is then obtained through integration of the individual intensity distributions.

The wave field illuminating the sample is obtained by propagating Eq. 2.35 via the Fresnel propagator a distance f_c

$$\begin{aligned}\psi_1(\boldsymbol{r}_1;\boldsymbol{r}_0) &= \frac{1}{\mathrm{i}\lambda f_\mathrm{c}}\,\psi_0'(\boldsymbol{r}_0)\,\exp\left(\frac{-\mathrm{i}k}{2f_\mathrm{c}}\,(\boldsymbol{r}_1-\boldsymbol{r}_0)^2\right)\\ &= \frac{1}{\mathrm{i}\lambda f_\mathrm{c}}\,\psi_0(\boldsymbol{r}_0)\,P_\mathrm{c}(\boldsymbol{r}_0)\,\exp\left(\frac{-\mathrm{i}k}{2f_\mathrm{c}}\,\boldsymbol{r}_1^2\right)\,\exp\left(\frac{\mathrm{i}k}{f_\mathrm{c}}\,\boldsymbol{r}_0\boldsymbol{r}_1\right),\end{aligned} \tag{2.36}$$

where we do not perform an integration over $\boldsymbol{r}_0$ in the propagator since we are only considering one point in the incoherently illuminated condenser lens. Note, that the actual plane the condenser focusses to is a distance d_c away, obtained by the lens law $1/d_0 + 1/d_c = 1/f_\mathrm{c}$; however, the source distance d_0 is typically three orders of magnitude larger than the lens' focal length, making the above assumption valid to a very good degree. This way, the quadratic terms in $\boldsymbol{r}_0$ between the propagator and the phase curvature of the lens transmittance function cancel out.

Successively, this wave field is multiplied by the specimen function h to yield the exit wave behind the sample, which is then propagated to the objective lens plane a distance d_1 away, where it is multiplied by the objective lens transmission function to yield to wave field exiting the objective

$$\begin{aligned}\psi_2'(\boldsymbol{r}_2;\boldsymbol{r}_0) = \frac{1}{\mathrm{i}\lambda d_1}\int \mathrm{d}^2\boldsymbol{r}_1\,\psi_1(\boldsymbol{r}_1;\boldsymbol{r}_0)\,h(\boldsymbol{r}_1)\,\exp\left(\frac{-\mathrm{i}k}{2d_1}\,(\boldsymbol{r}_2-\boldsymbol{r}_1)^2\right)\\ P_\mathrm{o}(\boldsymbol{r}_2)\,\exp\left(\frac{\mathrm{i}k}{2f_\mathrm{o}}\,\boldsymbol{r}_2^2\right).\end{aligned} \tag{2.37}$$

From here, we propagate the wave field into the image plane a distance d_2 away

$$\begin{aligned}\psi_3(\boldsymbol{r}_3;\boldsymbol{r}_0) = \frac{-1}{\lambda^2 d_1 d_2}\int \mathrm{d}^2\boldsymbol{r}_2\int \mathrm{d}^2\boldsymbol{r}_1\,\psi_1(\boldsymbol{r}_1;\boldsymbol{r}_0)\,h(\boldsymbol{r}_1)\,\exp\left(\frac{-\mathrm{i}k}{2d_1}\,(\boldsymbol{r}_2-\boldsymbol{r}_1)^2\right)\\ P_\mathrm{o}(\boldsymbol{r}_2)\,\exp\left(\frac{\mathrm{i}k}{2f_\mathrm{o}}\,\boldsymbol{r}_2^2\right)\,\exp\left(\frac{-\mathrm{i}k}{2d_2}\,(\boldsymbol{r}_3-\boldsymbol{r}_2)^2\right).\end{aligned} \tag{2.38}$$

The objective lens is placed in the optical setup such that the lens equation

$1/d_1 + 1/d_2 = 1/f_\mathrm{o}$ is fulfilled, which will cancel the phase factors quadratic in $\boldsymbol{r}_2$ in Eq. 2.38 and give

$$\begin{aligned}\psi_3(\boldsymbol{r}_3;\boldsymbol{r}_0) = \frac{-1}{\lambda^2 d_1 d_2} \exp\left(\frac{-\mathrm{i}k}{2d_2}\,\boldsymbol{r}_3^2\right) \int \mathrm{d}^2\boldsymbol{r}_2 \int \mathrm{d}^2\boldsymbol{r}_1\, \psi_1(\boldsymbol{r}_1;\boldsymbol{r}_0)\, h(\boldsymbol{r}_1)\, P_\mathrm{o}(\boldsymbol{r}_2)\\ \exp\left(\frac{-\mathrm{i}k}{2d_1}\,\boldsymbol{r}_1^2\right) \exp\left(\mathrm{i}k\left(\frac{\boldsymbol{r}_3}{d_2}+\frac{\boldsymbol{r}_1}{d_1}\right)\boldsymbol{r}_2\right),\end{aligned} \tag{2.39}$$

which is the answer of interest. Compared to the expression for the scanning case (Eq. 2.23) there is no intuitive relation in terms of a Fourier transform given.

Intensity in detector plane

However, through a few more considerations it will be possible to make Eq. 2.39 nicer to look at. We so far have only considered the wave field due to one point of the condenser. The total intensity recored in the detector plane is given through integration over all condenser points $\boldsymbol{r}_0$:

$$\begin{aligned}I_3(\boldsymbol{r}_3) &= \int \mathrm{d}^2\boldsymbol{r}_0\, |\psi_3(\boldsymbol{r}_3;\boldsymbol{r}_0)|^2\\ &= \frac{1}{\lambda^6 f_\mathrm{c}^2 d_1^2 d_2^2} \int \mathrm{d}^2\boldsymbol{r}_0 \Bigg| \psi_0(\boldsymbol{r}_0)\, P_\mathrm{c}(\boldsymbol{r}_0) \int \mathrm{d}^2\boldsymbol{r}_2 \int \mathrm{d}^2\boldsymbol{r}_1\, h(\boldsymbol{r}_1)\, P_\mathrm{o}(\boldsymbol{r}_2)\\ &\quad \exp\left(\frac{-\mathrm{i}k}{2}\left(\frac{1}{f_\mathrm{c}}+\frac{1}{d_1}\right)\boldsymbol{r}_1^2\right) \exp\left(\frac{\mathrm{i}k}{f_\mathrm{c}}\,\boldsymbol{r}_0\boldsymbol{r}_1\right) \exp\left(\mathrm{i}k\left(\frac{\boldsymbol{r}_3}{d_2}+\frac{\boldsymbol{r}_1}{d_1}\right)\boldsymbol{r}_2\right)\Bigg|^2.\end{aligned} \tag{2.40}$$

Let us consider the phase factor quadratic in $\boldsymbol{r}_1$. If the objective lens used in the microscope has a sufficiently large numerical aperture, only a small region around a point imaged from the sample plane will contribute to the formed image of that point in the detector plane. This is the case because a large numerical aperture lens will have a narrow point spread function and give images of high resolution, as desired from an imaging system. Considering a specific point $\boldsymbol{r}_1^\mathrm{s}$ in the sample plane, the geometrical relation

$$\frac{\boldsymbol{r}_1^\mathrm{s}}{d_1} = -\frac{\boldsymbol{r}_3^\mathrm{s}}{d_2} \tag{2.41}$$

relates it to its image point $\boldsymbol{r}_3^\mathrm{s}$. Now, points farther than 5 Rayleigh resolution distances away from $\boldsymbol{r}_1^\mathrm{s}$ in the sample plane will not significantly contribute to the image; an argument similar to that of Eq. 2.18 can be made. Hence, factors of $\boldsymbol{r}_1^2$ can be neglected from the expression of Eq. 2.40 leaving us with

$$I_3(\boldsymbol{r}_3) = \frac{1}{\lambda^6 f_\mathrm{c}^2 d_1^2 d_2^2} \int \mathrm{d}^2\boldsymbol{r}_0 \left| \psi_0(\boldsymbol{r}_0)\, P_\mathrm{c}(\boldsymbol{r}_0) \int \mathrm{d}^2\boldsymbol{r}_2 \int \mathrm{d}^2\boldsymbol{r}_1\, h(\boldsymbol{r}_1)\, P_\mathrm{o}(\boldsymbol{r}_2) \right. \\ \left. \exp\left(\frac{\mathrm{i}k}{f_\mathrm{c}}\,\boldsymbol{r}_0\boldsymbol{r}_1\right) \exp\left(\mathrm{i}k\left(\frac{\boldsymbol{r}_3}{d_2} + \frac{\boldsymbol{r}_1}{d_1}\right)\boldsymbol{r}_2\right)\right|^2, \tag{2.42}$$

Similar to the case of scanning image formation, considering the specimen in term of its Fourier spectrum will enable us to do some more simplifications

$$h(\boldsymbol{r}_1) = \int \mathrm{d}^2\boldsymbol{f}_1\, H(\boldsymbol{f}_1)\, \exp\left(2\pi\mathrm{i}\boldsymbol{f}_1\boldsymbol{r}_1\right). \tag{2.43}$$

With this expression for the specimen function we obtain for the intensity

$$I_3(\boldsymbol{r}_3) = \frac{1}{\lambda^6 f_\mathrm{c}^2 d_1^2 d_2^2} \int \mathrm{d}^2\boldsymbol{r}_0 \left| \psi_0(\boldsymbol{r}_0)\, P_\mathrm{c}(\boldsymbol{r}_0) \int \mathrm{d}^2\boldsymbol{r}_2 \int \mathrm{d}^2\boldsymbol{r}_1 \int \mathrm{d}^2\boldsymbol{f}_1\, H(\boldsymbol{f}_1)\, P_\mathrm{o}(\boldsymbol{r}_2) \right. \\ \left. \exp\left(\mathrm{i}k\left(\frac{\boldsymbol{r}_0}{f_\mathrm{c}} + \frac{\boldsymbol{r}_2}{d_1} + \lambda\boldsymbol{f}_1\right)\boldsymbol{r}_1\right) \exp\left(\mathrm{i}k\,\frac{\boldsymbol{r}_3}{d_2}\,\boldsymbol{r}_2\right)\right|^2, \tag{2.44}$$

where a Delta-function can be identified

$$\int \mathrm{d}^2\boldsymbol{r}_1 \exp\left(\mathrm{i}k\left(\frac{\boldsymbol{r}_0}{f_\mathrm{c}} + \frac{\boldsymbol{r}_2}{d_1} + \lambda\boldsymbol{f}_1\right)\boldsymbol{r}_1\right) = |\lambda^2 d_1^2|\,\Delta\left(\boldsymbol{r}_2 + \frac{d_1\boldsymbol{r}_0}{f_\mathrm{c}} + \lambda d_1\boldsymbol{f}_1\right). \tag{2.45}$$

Therefore,

$$I_3(\boldsymbol{r}_3) = \frac{d_1^2}{\lambda^2 f_\mathrm{c}^2 d_2^2} \int \mathrm{d}^2\boldsymbol{r}_0 \left| \psi_0(\boldsymbol{r}_0)\, P_\mathrm{c}(\boldsymbol{r}_0) \int \mathrm{d}^2\boldsymbol{f}_1\, H(\boldsymbol{f}_1) \right. \\ \left. P_\mathrm{o}\left(-d_1\left(\lambda\boldsymbol{f}_1 + \frac{\boldsymbol{r}_0}{f_\mathrm{c}}\right)\right) \exp\left(-\mathrm{i}k\frac{d_1}{d_2}\lambda\boldsymbol{f}_1\boldsymbol{r}_3\right) \exp\left(-\mathrm{i}k\,\frac{d_1}{d_2}\,\frac{\boldsymbol{r}_0}{f_\mathrm{c}}\,\boldsymbol{r}_3\right)\right|^2, \tag{2.46}$$

where the phase factor containing $\boldsymbol{r}_0$ will cancel when expanding the absolute value. Hence we get

$$\begin{aligned} I_3(\boldsymbol{r}_3) = \frac{d_1^2}{\lambda^2 f_\mathrm{c}^2 d_2^2} & \int \mathrm{d}^2\boldsymbol{r}_0 \, |\psi_0(\boldsymbol{r}_0)\, P_\mathrm{c}(\boldsymbol{r}_0)|^2 \int \mathrm{d}^2\boldsymbol{f}_1 \int \mathrm{d}^2\boldsymbol{f}_1' \, H(\boldsymbol{f}_1)\, H^*(\boldsymbol{f}_1') \\ & P_\mathrm{o}\left(-d_1\left(\lambda\boldsymbol{f}_1 + \frac{\boldsymbol{r}_0}{f_\mathrm{c}}\right)\right) P_\mathrm{o}^*\left(-d_1\left(\lambda\boldsymbol{f}_1' + \frac{\boldsymbol{r}_0}{f_\mathrm{c}}\right)\right) \\ & \exp\left(-2\pi\mathrm{i}\, \frac{d_1}{d_2}\, (\boldsymbol{f}_1 - \boldsymbol{f}_1')\, \boldsymbol{r}_3\right), \end{aligned} \tag{2.47}$$

Again we can perform a separation of the image formation and the optical system

$$\begin{aligned} I_3(\boldsymbol{r}_3) = \frac{d_1^2}{\lambda^2 f_\mathrm{c}^2 d_2^2} & \int \mathrm{d}^2\boldsymbol{f}_1 \int \mathrm{d}^2\boldsymbol{f}_1' \, \mathcal{B}^\mathrm{ff}(\boldsymbol{f}_1;\boldsymbol{f}_1')\, H(\boldsymbol{f}_1)\, H^*(\boldsymbol{f}_1') \\ & \exp\left(-2\pi\mathrm{i}\, \frac{d_1}{d_2}\, (\boldsymbol{f}_1 - \boldsymbol{f}_1')\, \boldsymbol{r}_3\right), \end{aligned} \tag{2.48}$$

and

$$\begin{aligned} \mathcal{B}^\mathrm{ff}(\boldsymbol{f}_1;\boldsymbol{f}_1') = \int \mathrm{d}^2\boldsymbol{r}_0 \, |\psi_0(\boldsymbol{r}_0)|^2 \, |P_\mathrm{c}(\boldsymbol{r}_0)|^2 \, & P_\mathrm{o}\left(-d_1\left(\lambda\boldsymbol{f}_1 + \frac{\boldsymbol{r}_0}{f_\mathrm{c}}\right)\right) \\ & P_\mathrm{o}^*\left(-d_1\left(\lambda\boldsymbol{f}_1' + \frac{\boldsymbol{r}_0}{f_\mathrm{c}}\right)\right). \end{aligned} \tag{2.49}$$

2.4 Principle of Reciprocity

The principle of reciprocity was first introduced by Helmholtz [41]. It states that if a wave is emitted from a source at point $\boldsymbol{r}_1$ and detected at point $\boldsymbol{r}_2$, then the same signal in amplitude and phase would be detected at $\boldsymbol{r}_1$ if the source be placed at $\boldsymbol{r}_2$. Helmholtz initially proved this for the scalar wave equation, which includes electromagnetic waves in the paraxial approximation; it has be shown that it also holds in the vector case [42] considering the relevant polarisations.

In imaging theory the principle of reciprocity is reflected in the symmetry of spatial variables in the Fresnel diffraction integral (Eq. 2.5). A direct consequence of this principle is the equivalence of the scanning and full-field image formation, as we will show in the following.

Let us repeat the expression for the intensities we have found for the scanning and full-field image formation

$$I_3^{\mathrm{scan}}(\boldsymbol{r}_s) = \frac{d_1^2}{\lambda^2 d_0^2 d_2^2} \int \mathrm{d}^2 \boldsymbol{f}_2 \int \mathrm{d}^2 \boldsymbol{f}_2' \, \mathcal{B}^{\mathrm{scan}}(\boldsymbol{f}_2; \boldsymbol{f}_2') \, H(\boldsymbol{f}_2) \, H^*(\boldsymbol{f}_2') \\ \exp\Big(2\pi\mathrm{i}(\boldsymbol{f}_2 - \boldsymbol{f}_2') \, \boldsymbol{r}_{\mathrm{s}}\Big) \tag{2.50}$$

$$I_3^{\mathrm{ff}}(\boldsymbol{r}_3) = \frac{d_1^2}{\lambda^2 f_{\mathrm{c}}^2 d_2^2} \int \mathrm{d}^2 \boldsymbol{f}_1 \int \mathrm{d}^2 \boldsymbol{f}_1' \, \mathcal{B}^{\mathrm{ff}}(\boldsymbol{f}_1; \boldsymbol{f}_1') \, H(\boldsymbol{f}_1) \, H^*(\boldsymbol{f}_1') \\ \exp\left(-2\pi\mathrm{i} \, \frac{d_1}{d_2} \, (\boldsymbol{f}_1 - \boldsymbol{f}_1') \, \boldsymbol{r}_3\right) , \tag{2.51}$$

with the corresponding bilinear transfer functions

$$\mathcal{B}^{\mathrm{scan}}(\boldsymbol{f}_2; \boldsymbol{f}_2') = \int \mathrm{d}^2 \boldsymbol{r}_3 \, |\psi_0|^2 \, R(\boldsymbol{r}_3) \, P_{\mathrm{o}}\left(-d_1\left(\lambda \boldsymbol{f}_2 + \frac{\boldsymbol{r}_3}{d_2}\right)\right) \\ P_{\mathrm{o}}^*\left(-d_1\left(\lambda \boldsymbol{f}_2' + \frac{\boldsymbol{r}_3}{d_2}\right)\right) \tag{2.52}$$

$$\mathcal{B}^{\mathrm{ff}}(\boldsymbol{f}_1; \boldsymbol{f}_1') = \int \mathrm{d}^2 \boldsymbol{r}_0 \, |\psi_0(\boldsymbol{r}_0)|^2 \, |P_{\mathrm{c}}(\boldsymbol{r}_0)|^2 \, P_{\mathrm{o}}\left(-d_1\left(\lambda \boldsymbol{f}_1 + \frac{\boldsymbol{r}_0}{f_{\mathrm{c}}}\right)\right) \\ P_{\mathrm{o}}^*\left(-d_1\left(\lambda \boldsymbol{f}_1' + \frac{\boldsymbol{r}_0}{f_{\mathrm{c}}}\right)\right) . \tag{2.53}$$

From this direct comparison of expressions we can identify the equivalence of the scanning and full-field image formation processes, which is also illustrated by Fig. 2.4. Note that the orientation of the full-field setup in the schematic has been flipped in the horizontal as to make the identification of the equivalence more eye-catching. Table 2.1 details the respectively equivalent quantities. However, there are a few particularities which need further explanation. In the scanning case the image is formed by raster scanning the probing wave field with respect to the sample; the scan displacement $\boldsymbol{r}_{\mathrm{s}}$ denotes the position of the probe on the sample and represents the actual image coordinate. In the full-field case the image coordinate is the position in the respective detector plane $\boldsymbol{r}_3$ and not directly a position on the sample. Yet, through the geometric magnification $\boldsymbol{r}_1/d_1 = -\boldsymbol{r}_3/d_2$ the detector plane coordinate is directly related to the sample plane coordinate $\boldsymbol{r}_1$. Therefore,

$$-\frac{d_1}{d_2} \boldsymbol{r}_3 = \boldsymbol{r}_1 , \tag{2.54}$$

which we can insert in the phase factor of the full-field image intensity Eq. 2.51.

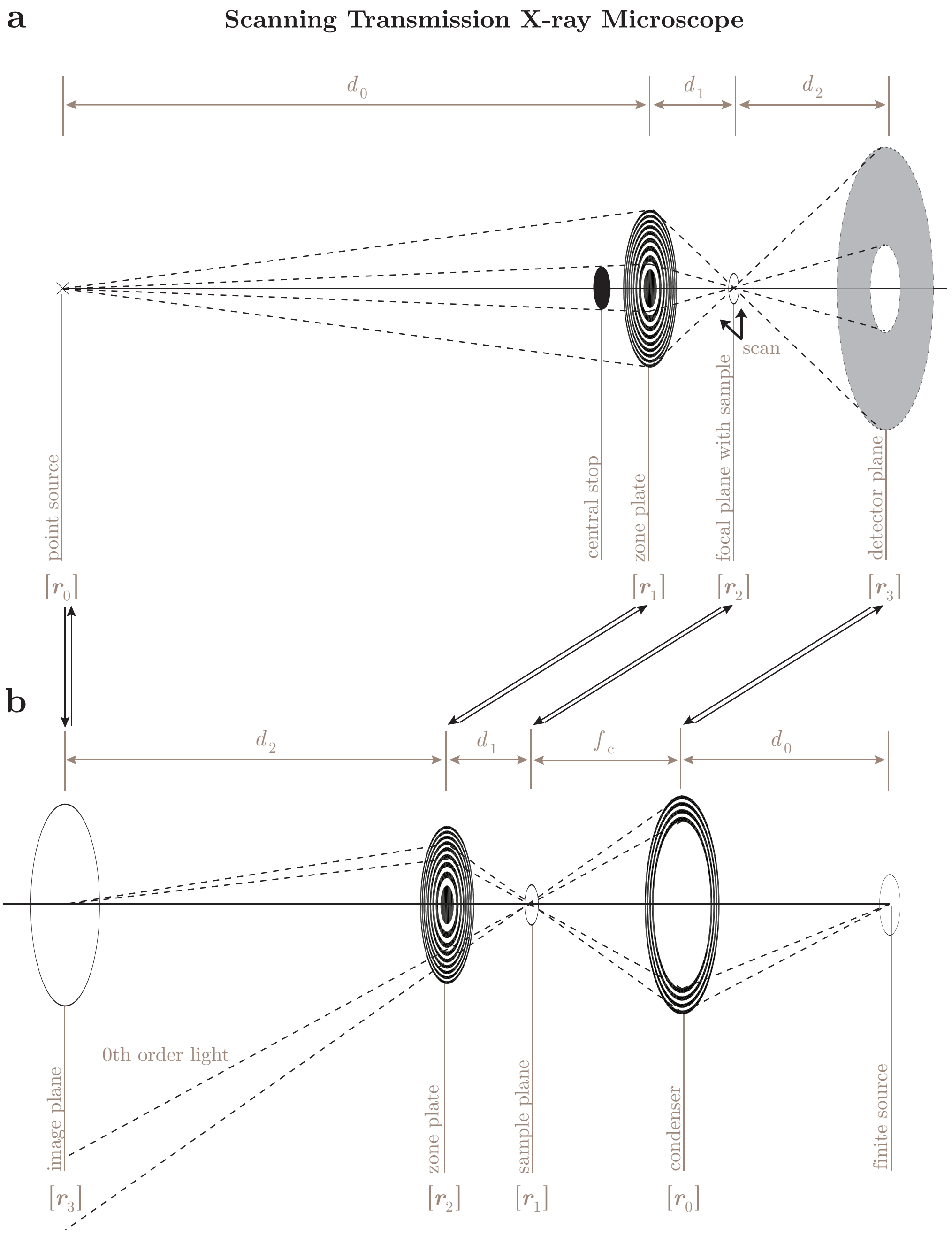

Figure 2.4: Schematic of (**a**) scanning and (**b**) full-field transmission x-ray microscope. The equivalence between planes in the imaging systems are indicated.

Equivalence	**Scanning**	**Full-field**
detector - condenser	$R(\boldsymbol{r}_3)$	$\|P_\mathrm{c}(\boldsymbol{r}_0)\|^2$
distance sample to	detector d_2	condenser f_c
sample plane	$\boldsymbol{r}_2$	$\boldsymbol{r}_1$
distance sample to objetive	d_1	d_1
objective plane	$\boldsymbol{r}_1$	$\boldsymbol{r}_2$
objective pupil coordinates	$-d_1\left(\lambda\boldsymbol{f}_2+\frac{\boldsymbol{r}_3}{d_2}\right)$	$-d_1\left(\lambda\boldsymbol{f}_1+\frac{\boldsymbol{r}_0}{f_\mathrm{c}}\right)$
distance objective to	source d_0	image d_2
source - image	$\boldsymbol{r}_0$	$\boldsymbol{r}_3$

Table 2.1: Equivalence of quantities between scanning and full-field image formation

Henceforth, the phase factors of Eq. 2.50 and Eq. 2.51 will be identical, with both containing the sample position coordinate

$$\exp\left(2\pi\mathrm{i}(\boldsymbol{f}_2-\boldsymbol{f}_2')\,\boldsymbol{r}_\mathrm{s}\right)\longleftrightarrow\exp\left(2\pi\mathrm{i}\left(\boldsymbol{f}_1-\boldsymbol{f}_1'\right)\underbrace{\left(-\frac{d_1}{d_2}\boldsymbol{r}_3\right)}_{=\boldsymbol{r}_1}\right). \qquad (2.55)$$

In the scanning case a central stop within the objective pupil is required to isolate the first or focus; this addition to the objective pupil function will result in a modification of the lens' modulation transfer function (*e. g.* as shown in Fig. 4.11). This difference in frequency response needs to be kept in mind when comparing the exact imaging behavior of the two microscopes [20], but does not lead to substantially different images.

Furthermore, note that both microscopes are mathematically completely equivalent for on-axis image points, where this equivalence is also given to a very good approximation for image points near the optical axis for the full-field case. Significant deviations will occur for image points that are far away from the optical axis. For a detailed discussion of the equivalence between the two microscopes including many particularities, we refer to work by Zeitler and Thomson [43] and Sheppard and Wilson [44] and references therein; a more detailed discussion is beyond the scope if this work.

By establishing the equality of the scanning and full-field microscope, we have laid the foundation for the work discussed in Ch. 4 and Ch. 5.

Chapter 3

Quantitative Reconstruction of Scanning Differential Phase Contrast

In Sec. 2.2 a detailed treatment of the general image formation process in a scanning x-ray microscope has been laid out. In the present chapter we will extend on these results with particular emphasize towards phase contrast imaging. The expression for the wave field in the detection plane (Eq. 2.23) will serve as a starting point for our considerations. We will introduce the concept of differential phase contrast (DPC) based on a refraction model. While being a useful and important tool, DPC has some drawbacks due to the nature of the contrast mechanism.

Two methods for the quantitative reconstruction of the specimen from such DPC images are presented. The first is the integration method, which applies a Fourier derivative technique to integrate directional phase gradients, independent of optical imaging properties and image noise levels. The second procedure, the filtering method is a deconvolution and Wiener filtering type approach in the limit of a weak specimen. It takes into account the imaging properties of the microscope and considers the inherent noise in the data. We compare both methods in their performance of quantitative reconstruction of scanning hard x-ray phase contrast data. It will be shown that both methods are very similar and can be reconciled in a unified formalism. Subtle differences due to different assumptions and approximations employed in both approaches are discussed.

3.1 Intensity in the Detector Plane

Let us start by repeating a result we found while describing the image formation process in a scanning system (see Fig. 3.1). The wave field in the detection plane ($[\boldsymbol{r}_3]$) of the microscope was found to be (Eq. 2.23)

$$\Psi_3(\boldsymbol{f}_3;\, \boldsymbol{r}_\mathrm{s}) = \mathcal{C} \int \mathrm{d}^2\boldsymbol{r}_2\, h(\boldsymbol{r}_2)\, p_\mathrm{o}(\boldsymbol{r}_2 - \boldsymbol{r}_\mathrm{s})\, \exp\left(\mathrm{i}2\pi \boldsymbol{r}_2 \boldsymbol{f}_3\right) . \tag{3.1}$$

Remember for this to be valid that the detector needs to be placed in the far-field with respect to the sample plane. The sample of interest is described by the specimen function h; p_o is the wave field in the sample plane, *i. e.* the *probe*, $\boldsymbol{r}_\mathrm{s}$ describes the scan displacement of the probe with respect to the sample and $\boldsymbol{f}_3 \equiv \boldsymbol{r}_3/(\lambda\, d_2)$ is the spatial frequency for the detector plane. What we actually measure is the intensity in the detection plane, which is simply given by

$$I_3(\boldsymbol{f}_3;\, \boldsymbol{r}_\mathrm{s}) = |\Psi_3(\boldsymbol{f}_3;\, \boldsymbol{r}_\mathrm{s})|^2 . \tag{3.2}$$

In the absence of a specimen, which means $h(\boldsymbol{r}_2) = 1$, and furthermore inserting the defining relation of the probe function p_o (Eq. 2.24) the expression

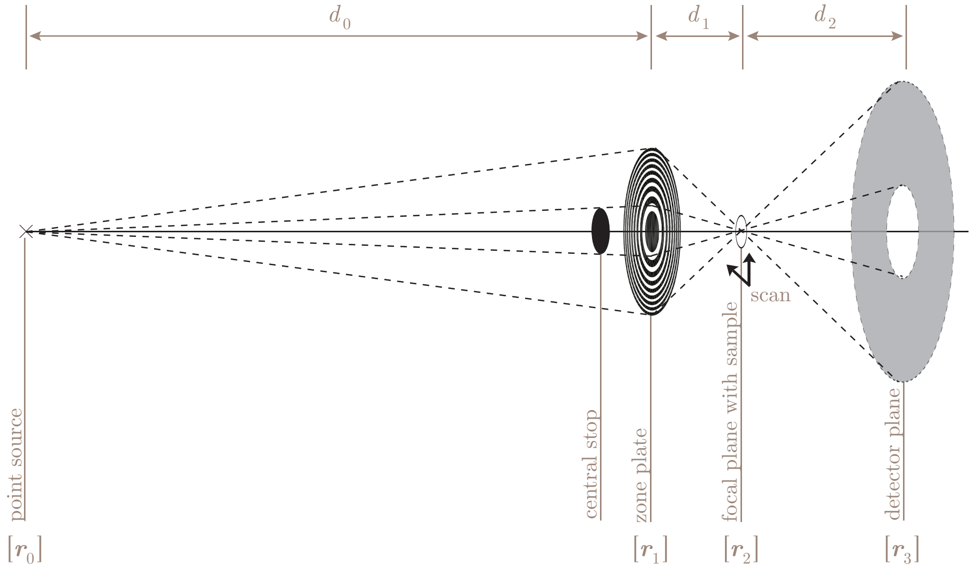

Figure 3.1: Schematic of scanning transmission x-ray microscope.

for the intensity takes an intuitive form (at this point we can drop the scan displacement coordinate, since no specimen is present)

$$I_3(\boldsymbol{f}_3) = \left| \mathcal{C}' \int \mathrm{d}^2\boldsymbol{r}_2 \int \mathrm{d}^2\boldsymbol{f}_1 \, P_\mathrm{o}(\boldsymbol{f}_1) \, \exp\left(\mathrm{i}2\pi\boldsymbol{f}_1\boldsymbol{r}_2\right) \, \exp\left(\mathrm{i}2\pi\boldsymbol{r}_2\boldsymbol{f}_3\right) \right|^2 . \tag{3.3}$$

This is a double inverse Fourier transform of the pupil function $P_\mathrm{o}(\boldsymbol{f}_1)$ of the objective lens. Performing two Fourier transforms in a row brings back the original function up to a global phase factor and furthermore point mirrored with respect to the origin of the coordinate system (for a derivation of this property see Sec. A.2.1).

$$I_3(\boldsymbol{f}_3) = \left| \mathcal{F}^{-1}\{\mathcal{F}^{-1}\{P_\mathrm{o}(\boldsymbol{f}_1)\}\} \right|^2 = \left| P_\mathrm{o}(-\boldsymbol{f}_3) \right|^2 \tag{3.4}$$

The fact that the far-field image of the pupil is mirrored should come at no surprise, since it is exactly what one expects from the imaging properties of a converging lens, here derived in a Fourier optical treatment.

An example intensity distribution typical for a scanning x-ray microscope is given in Fig. 3.2.

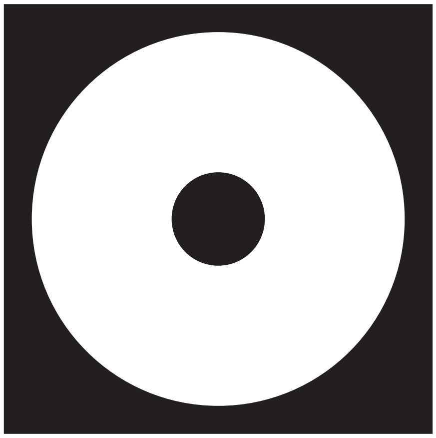

Figure 3.2: Example far-field intensity distribution in a scanning microscope, showing the typical annular structure which is due to the requirement of a central stop for isolating the first order focus of the zone plate.

3.1.1 Refractive Model

Now we want to consider what happens if we introduce a specimen in the sample plane; *i. e.* $h(\boldsymbol{r}) \neq 1$. For simplicity, we will assume here that the sample is a pure phase object, with no absorption towards the transmitted intensity. This approximation agrees well with the experimental case of imaging biological samples with hard X-rays. The specimen function then reads

$$h(\boldsymbol{r}) = \exp\Big(\mathrm{i}\delta(\boldsymbol{r})kt(\boldsymbol{r})\Big) \equiv \exp\Big(\mathrm{i}\phi(\boldsymbol{r})\Big)\,. \tag{3.5}$$

In a refractive model analogous to fundamental optics, a phase object will reflect the incoming light by an angle that is proportional to the phase gradient of the object at the point of illumination [37].

$$\boldsymbol{\alpha}_{\mathrm{ref}} = \frac{1}{k}\boldsymbol{\nabla}\phi\,, \tag{3.6}$$

and the direction of reflection follows the direction of the gradient. The situation is depicted by Fig. 3.3 for the one dimensional case of a pure phase object. A transparent prism (*i. e.* phase wedge in the y-direction) will reflect the intensity in the y-direction. Note that the situation shown in the figure is only valid for X-rays; the beam gets shifted away from the thicker part of

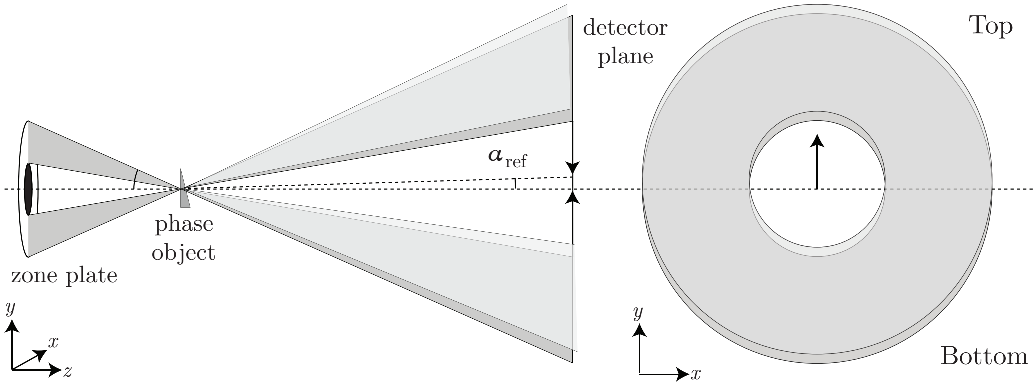

Figure 3.3: Beam deflection in a scanning microscope with a wedge phase object at the focus. In the absence of a phase gradient, the illumination after the sample (dark grey) is not influences and; therefore, stays centered in the detector plane. Introducing a sample with a phase gradient (here along the y-direction) the illumination (light grey) behind the sample gets deflected in the y-direction towards the top half of the detector.

the prism due to the fact that the object introduces a phase advance (see Sec. 1.2), rather than a phase delay as would be the case for visible light, where the reflection would be in the opposite direction.

Let us briefly consider the scale of the quantities involved in this angular deflection, to get a feel for the effect. The numerical aperture of the objective lens is usually on the order of mrad, the specimen phase shift (wedge angle) is on the order of rad and the resulting deflection is typically on the order of μrad.

3.1.2 Differential Phase Contrast

The inconspicuous circumstance that the intensity distribution gets shifted by a phase gradient is an important fact, since now we are in position to measure the phase structure of the specimen of interest and take advantage of the superior signal-to-noise of phase compared to absorption contrast (see Sec. 1.4.1).

All that is needed now is some spatial sensitivity to the intensity movement in the detection plane. For the case given in Fig. 3.3, a detector with a response function that is split along the horizontal direction in a top (T) and bottom (B) half plane would be sufficient. With no specimen present, the intensity in both half planes would be equal ($I_{\mathrm{T}} = I_{\mathrm{B}}$). Putting the linear phase wedge in the focal plane as indicated in Fig. 3.3 will reflect the intensity towards the top half plane, leading to an increased intensity on the top versus the bottom ($I_{\mathrm{T}} > I_{\mathrm{B}}$); where the resulting intensity shift is proportional to the phase gradient. This lets us define a *differential phase contrast* (DPC) signal for the vertical (y-direction)

$$\mathrm{DPC}_y = I_{\mathrm{T}} - I_{\mathrm{B}} \, (\propto \nabla_y \, \phi) \, . \tag{3.7}$$

For the very special case of a phase wedge, this signal would be constant, since the sample has a constant phase gradient. Furthermore, note that with a detector split in an upper and lower half plane we are only sensitive to gradients along this particular direction, or to be more precise, to the projected phase gradients along this direction.

In order to quantify arbitrary deflections of the intensity distribution, a quadrant detector is the simplest choice. In the absence of a specimen, the detector needs to be aligned symmetrically with respect to the illumination annulus. As can be seen in Fig. 3.4 an arbitrary deflection ($\boldsymbol{D}$) can be decomposed into two orthogonal components D_x and D_y, to which we will be sensitive to through the detector combinations ($I_{\mathrm{L}} - I_{\mathrm{R}}$) and ($I_{\mathrm{T}} - I_{\mathrm{B}}$), respectively. Hence, a complete definition of differential phase contrast signals for

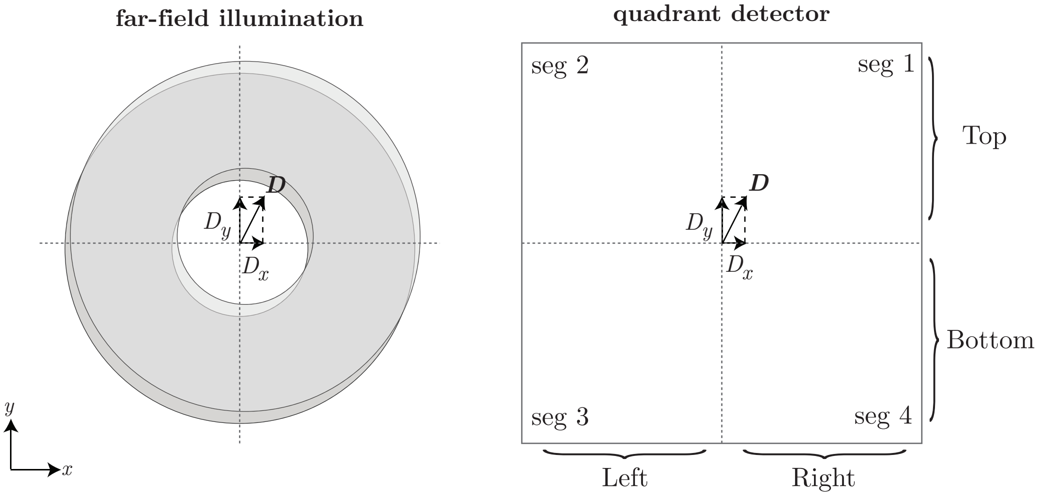

Figure 3.4: Arbitrary shift and quadrant detector.

each scan point can be given as follows:

$$\begin{aligned} \mathrm{DPC}_x &= \frac{I_{\mathrm{L}} - I_{\mathrm{R}}}{I_{\mathrm{total}}} = \frac{(I_2 + I_3) - (I_1 + I_4)}{(I_1 + I_2 + I_3 + I_4)} \propto \nabla_x \, \phi \\ \mathrm{DPC}_y &= \frac{I_{\mathrm{T}} - I_{\mathrm{B}}}{I_{\mathrm{total}}} = \frac{(I_1 + I_2) - (I_3 + I_4)}{(I_1 + I_2 + I_3 + I_4)} \propto \nabla_y \, \phi \, . \end{aligned} \tag{3.8}$$

Note that we divide the difference signals by the total detected intensity I_{total}. Normalizing the signal to the total intensity removes the effect caused by source intensity variations and accounts for the local specimen absorption. Even though we so far have treated phase-only specimens, which is a good approximation for a large class of samples when imaging with hard X-rays, absorption effects can still play a rold (albeit a small one). Through dividing each scan point by the total intensity we effectively normalize the DPC signal by the absorption image.

Other DPC signals are of course possible. With the quadrant detector, we can be sensitive to diagonal gradients by looking at the signal differences of segments 2 and 4 or segments 1 and 3. These additional signals can be helpful for sample visualizations; however, mathematically no additional information is gained.

We want to conclude this section by pointing out the implicit assumptions and implications that have been made in the treatment of DPC so far. The most important assumption for imaging DPC with a quadrant detector is that the intensity in the detector plane is centro-symmetric, for obvious reasons; but bear in mind that it not necessarily has to be even (see Sec. 3.1.4). Furthermore, the sample is assumed to be completely contained within the depth of focus, so that no differential absorption effects come into play. Also, the observed quantities of absorption (βkt) and phase ($\phi = \delta kt$) are assumed to not vary across the focal spot size (see further discussions in Sec. 3.1.4). Of course, DPC only works as long as there is a phase gradient present. Putting a uniformly thick slap of transparent material at the focus will not have any effect, since we are not able to measure absolute phase.

Bear in mind that for practical purposes the z-position of the quadrant detector is not critical, as long as the illumination is fully contained within the quadrants.

3.1.3 Fourier Optical Treatment of Intensity Shift

Lets have a more rigorous look at the behavior of the far-field intensity in the presence of a specimen through a Fourier optics treatment. Our starting point, will again be the intensity formed by the wave field (Eq. 2.23 or Eq. 3.1) in the detection plane of a scanning microscope .

$$I_3(\boldsymbol{r}_3;\, \boldsymbol{r}_{\text{s}}) = |\Psi_3(\boldsymbol{r}_3;\, \boldsymbol{r}_{\text{s}})|^2 = \left| \mathcal{C} \int \mathrm{d}^2\boldsymbol{r}_2\, h(\boldsymbol{r}_2)\, p_o(\boldsymbol{r}_2 - \boldsymbol{r}_s)\, \exp\left(\frac{\mathrm{i}k}{d_2} \boldsymbol{r}_2 \boldsymbol{r}_3\right) \right|^2 . \tag{3.9}$$

This time we have omitted the use of spatial frequency coordinates by replacing $\boldsymbol{f}_3 \equiv \boldsymbol{r}_3/(\lambda\, d_2)$. The detector is supposed to be in the far-field, the specimen is described by h, the probe by p_o and the scan displacement vector by $\boldsymbol{r}_\mathrm{s}$. Without loss of generality we can choose $\boldsymbol{r}_\mathrm{s}=\boldsymbol{0}$.

The specimen function is given by (see Sec. 1.2)

$$h(\boldsymbol{r}_2) = \exp\Big(-\beta(\boldsymbol{r}_2)kt(\boldsymbol{r}_2) + \mathrm{i}\delta(\boldsymbol{r}_2)kt(\boldsymbol{r}_2)\Big) \equiv \exp\Big(\varepsilon(\boldsymbol{r}_2)\Big)\,, \tag{3.10}$$

Expanding the terms in the exponential in a Taylor series[1] around the point illuminated by the probe (without loss of generality chosen to be 0) gives

$$\begin{aligned}\varepsilon(\boldsymbol{r}_2) &= \varepsilon\Big|_0 + \varepsilon^{(1)}\Big|_0 \boldsymbol{r}_2 + \mathcal{O}(\boldsymbol{r}_2^2)\\ &= -\big(\beta kt\big)\Big|_0 + \mathrm{i}\big(\delta kt\big)\Big|_0 - \boldsymbol{\nabla}\big(\beta kt\big)\Big|_0 \boldsymbol{r}_2 + \mathrm{i}\boldsymbol{\nabla}\big(\delta kt\big)\Big|_0 \boldsymbol{r}_2 + \mathcal{O}(\boldsymbol{r}_2^2)\,.\end{aligned} \tag{3.11}$$

Inserting Eq. 3.11 into Eq. 3.9 and ignoring the second order terms for now we get

$$\begin{aligned}I_3(\boldsymbol{r}_3) = \exp\Big(-2(\beta kt)_0\Big)\Big|\mathcal{C}\int \mathrm{d}^2\boldsymbol{r}_2\, p_\mathrm{o}(\boldsymbol{r}_2)\\ \exp\Big(-\underbrace{\boldsymbol{\nabla}(\beta kt)_0}_{\rightarrow\mathrm{DAC}}\boldsymbol{r}_2 + \mathrm{i}\,\underbrace{\boldsymbol{\nabla}(\delta kt)_0}_{\rightarrow\mathrm{DPC}}\boldsymbol{r}_2\Big)\ \exp\Big(\frac{\mathrm{i}k}{d_2}\boldsymbol{r}_2\boldsymbol{r}_3\Big)\Big|^2\,.\end{aligned} \tag{3.12}$$

The factor preceding the absolute value denotes the usual absorption contrast. The gradient terms within the integral represent *differential absorption contrast* (DAC) and *differential phase contrast* (DPC) respectively. The role of DAC will be discussed at a later point in Sec. 3.1.4. For now we can be content with knowing that DAC is negligible as long as the ratio δ/β is large and the probe small. Note that for hard X-rays δ/β is in the range of 10 to 1000 and larger; in particular for biological specimens 1000 is common. When neglecting DAC we can write for the intensity

$$I_3(\boldsymbol{r}_3) = \exp\Big(-2(\beta kt)_0\Big)\Big|\mathcal{C}\int \mathrm{d}^2\boldsymbol{r}_2\, p_o(\boldsymbol{r}_2)\, \exp\Big(\frac{\mathrm{i}k}{d_2}\boldsymbol{r}_2\big(\boldsymbol{r}_3 + \frac{d_2}{k}\,\boldsymbol{\nabla}(\delta kt)_0\big)\Big)\Big|^2\,. \tag{3.13}$$

Aside from the leading absorption contrast factor, note that Eq. 3.13 is identical to the intensity of Eq. 3.9 in the absence of a specimen ($h=1$) and with a shift in the coordinate $\boldsymbol{r}_3 \rightarrow \big(\boldsymbol{r}_3 + \frac{d_2}{k}\,\boldsymbol{\nabla}(\delta kt)_0\big)$. Hence, we can identify the

---

[1] Taylor expansion: $g(x) = \sum_n^\infty g^{(\mathrm{n})}(x)|_{x=x_0}(x-x_0)^n$.

resulting function as the non-specimen intensity shifted by an amount proportional to the phase gradient (and attenuated through the specimen absorption)

$$I_3(\boldsymbol{r}_3) = \exp\Big(-2(\beta k t)_0\Big)\, I_3^{h=1}\Big(\boldsymbol{r}_3 + \frac{d_2}{k}\,\boldsymbol{\nabla}(\delta k t)_0\Big). \tag{3.14}$$

With this we have derived the predictions of the previously used simple refractive model of Sec. 3.1.1 in a wave field treatment! Note that the resulting angular deflection through the shift is in perfect agreement with the angle given by Eq. 3.6, keeping in mind that the propagation distance from the focal to the detector plane is d_2.

To illustrate our findings, Fig. 3.5 shows three simulated intensity distributions from different scan positions on a 5 μm polystyrene sphere at 2.5 keV x-ray energy. For all three distributions their respective center-of-mass positions are indicated by a small cross-hair. The strongest effect can be observed in Fig. 3.5(c), where the intensity is shifted noticeably towards the bottom left. The scan position is close the sphere's edge for which the phase gradient is rather large at this point compared to Fig. 3.5(d) with a dwell position closer to the sphere center. Take notice of the fact that even for a scan position outside the sphere Fig. 3.5(b), there is some effect on the intensity due to the side lobes of the PSF; however, the effect is small and also does not shift the COM of the distribution. We also want to point out that besides a shift, the intensity gets redistributed within the annulus, this will be discussed in the following.

3.1.4 Higher Order Terms and DAC

We will have a closer look at approximations that have been made in the derivation of the previous section. The higher order terms that have been left out in subsequent expressions following the Taylor expansion of Eq. 3.11 can be divided into the categories of even and odd powers of the focal plane coordinate $\boldsymbol{r}_2$. Including all orders of the differential phase terms, Eq. 3.12

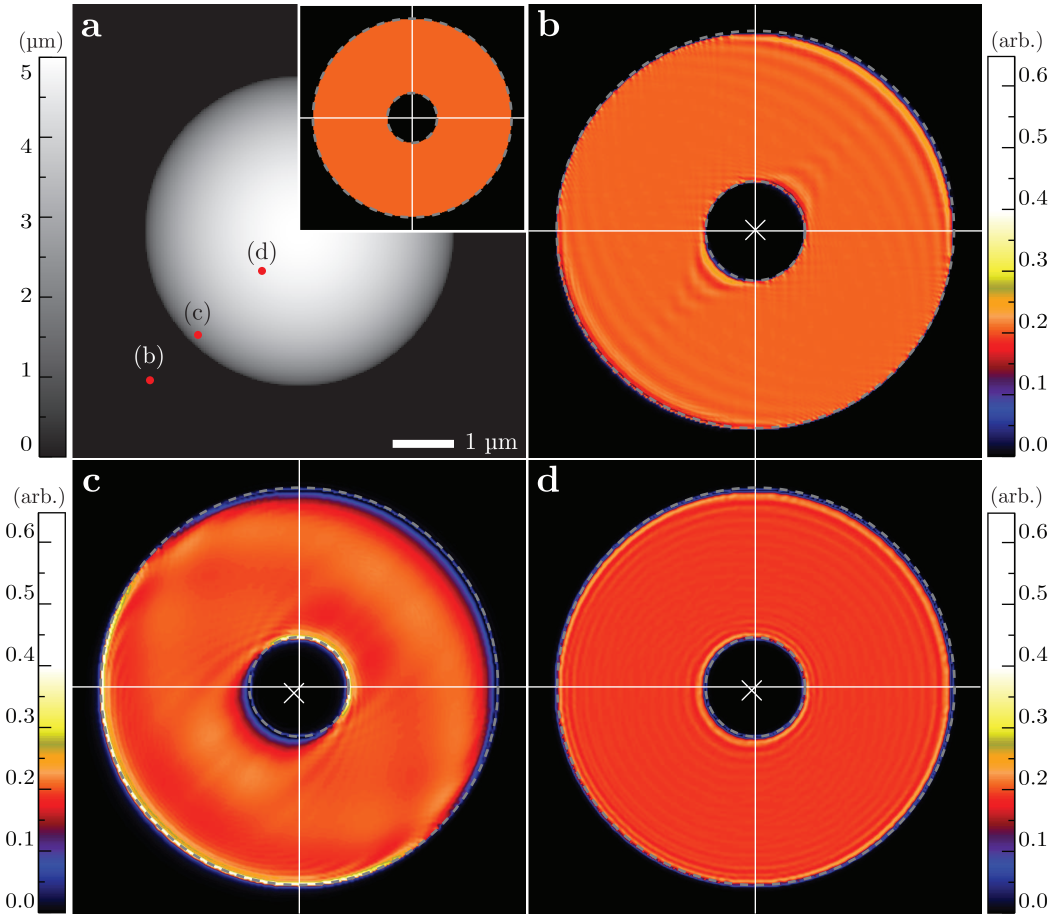

Figure 3.5: Simulated intensity from different dwell positions on a 5 μm polystyrene sphere at 2.5 keV with a zone plate of 50 nm outermost zone width. **(a)** Thickness profile of the sphere with dwell positions of subsequent subpanels indicated; an inlay shows the far-field intensity in the absence of a specimen. (b)-(d) Intensity in detector plane, all scaled to the same range; the large cross-hairs indicate the spatial frequency origins. The small cross-hairs are highlighting the center of mass for each intensity distribution. Dashed gray circles indicate the outline of the intensity with no specimen present. The spatial frequency at the pupil cut-off is $10(\mu\mathrm{m})^{-1}$.

becomes

$$\begin{aligned} I_3(\boldsymbol{f}_3) = \Bigg| \int \mathrm{d}^2\boldsymbol{r}_2 \; & \underbrace{p_o(\boldsymbol{r}_2) \, \exp\left(\mathrm{i} \sum_n \boldsymbol{\nabla}^{2n} (\delta k t)_0 \boldsymbol{r}_2^{2n} \right)}_{\equiv \mathrm{G}(\boldsymbol{r}_2)} \\ & \underbrace{\exp\left(\mathrm{i} \sum_n \boldsymbol{\nabla}^{2n+1} (\delta k t)_0 \boldsymbol{r}_2^{2n+1} \right)}_{\equiv \mathrm{U}(\boldsymbol{r}_2)} \, \exp\Big(\mathrm{i}2\pi \boldsymbol{r}_2 \boldsymbol{f}_3 \Big) \Bigg|^2 \\ = & \left| \mathcal{F}^{-1}_{\boldsymbol{f}_3} \Big\{ G(\boldsymbol{r}_2) \, U(\boldsymbol{r}_2) \Big\} \right|^2 , \end{aligned} \tag{3.15}$$

where for the ease of discussion pre-factors have been left out and spatial frequency coordinates $\boldsymbol{f}_3 \equiv \boldsymbol{r}_3/(\lambda \, d_2)$ are introduced again. Furthermore, we will still omit the DAC terms for now. Remember that in the absence of a specimen $I_3(\boldsymbol{f}_3)$ is an even, centro-symmetric function with respect to the origin ($\boldsymbol{f}_3 = \mathbf{0}$) because $p_o(\boldsymbol{r}_2)$ is supposed to be even and centro-symmetric. Note that we refer to "even" here only in a strict mathematical sense concerning symmetry and not in a topological way. We have seen that through keeping the first order term in the Taylor expansion the intensity gets shifted (see Eq. 3.14) and hence is not a centro-symmetric function with respect to the origin anymore; *i. e.* its center of mass and center of symmetry are shifted, which was the motivating factor in Sec. 3.1.2 to define differential phase contrast.

What are the effects of the other order terms of Eq. 3.15 that have been neglected so far, on this center of mass shift? The quantity G identified in the expression is an even function, while U is odd. Through the help of the convolution theorem we can write for Eq. 3.15

$$I_3(\boldsymbol{f}_3) = \left| \mathcal{F}^{-1}_{\boldsymbol{f}_3} \Big\{ G(\boldsymbol{r}_2) \, U(\boldsymbol{r}_2) \Big\} \right|^2 = g(\boldsymbol{f}_3) \otimes u(\boldsymbol{f}_3) \, , \tag{3.16}$$

where the respective Fourier transforms g and u inherit the respective symmetry properties: g is even and u is odd (see Table A.2). The convolution of $g \otimes u$ will also be odd. Since g is an even function, it does not contribute to any changes on the position of the center of mass or symmetry; it merely redistributes intensity symmetrically around the shifted center. Hence g does not contribute to any location changes on the center of mass and has successively no influence on the differential phase contrast signal. Therefore, we can neglect all even orders in the Taylor series expansion of the phase terms and write $G(\boldsymbol{r}_2) = p_o(\boldsymbol{r}_2)$.

The odd function U is the sole source for the center of mass changes of the intensity. Its first term ($n = 0$) resulted in the notion of the intensity shift of Eq. 3.14. The higher order terms of U further contribute to center of mass changes. However, their effect can be argued as negligible due to the use of a focussed probe, which restricts the contribution of these terms due to the small values of $\boldsymbol{r}_2$.

The wave field simulations of Fig. 3.5 further illustrate the interaction of the specimen with the beam, which results in an intensity shift but also gives rise to intensity fringes. These fringes are the result of the higher order terms of the preceding discussion and their effect on the center of mass location are minimal.

We still need to consider the DAC terms of Eq. 3.12. As it has been briefly argued before, the contribution from DAC to the integral governing the intensity in the far-field plane is negligible if the ratio δ/β is large and the probe small, making the DAC contribution much smaller than DPC. Particularly, the DAC terms can be neglected if it does not vary appreciably across the probe size. As 94% of the total intensity is located within the first four maxima of the focal spot [37], the condition of an insignificant variation across the probe size becomes [2]

$$\exp\left(\frac{B_4 \, \mathrm{d}r_N |\boldsymbol{\nabla}(\beta k t)_0|}{\pi}\right) - \exp\left(\frac{-B_4 \, \mathrm{d}r_N |\boldsymbol{\nabla}(\beta k t)_0|}{\pi}\right) << 1 \, , \qquad (3.17)$$

where $B_4 \approx 13.324$ is the fourth zero of the Bessel function and $\mathrm{d}r_N$ is the outermost zone width of the zone plate (indicative of the numerical aperture). As an example we can consider the situation of polystyrene at 2.5 keV x-ray energy: presuming a constant β and examining the condition in terms of a thickness variation, the requirement of Eq. 3.17 translates in a thickness gradient limit of $\boldsymbol{\nabla}(t)_0 << 144$, which is most likely only violated at the sphere edges. Similarly, for gold at 2.5 keV we get $\boldsymbol{\nabla}(t)_0 << 1$ and at 10 keV it is $\boldsymbol{\nabla}(t)_0 << 20$; hence DAC contributions can become significant. Recent work by Thibault *et al.* [45] considers DAC contributions on an analytical basis, where they arrive at conclusions supporting our findings. However, they also find that if one takes effects of defocus into account, DAC contributions can become significant enough to explore them as a dedicated mechanism of imaging contrast.

3.2 Integration Method

As we have seen in a simple refractive model in Sec. 3.1.1, the intensity in the far-field gets shifted in the presence of a phase gradient in the sample plane, which let to the definition of differential phase contrast (DPC) (Eq. 3.8). The value of DPC for specimen visualization in particular for hard X-rays is extremely high, since absorption contrast is usually negligibly low at these x-ray energies as seen in Sec. 1.4. However, DPC images can be difficult to interpret due to their differential nature. The images are only qualitative and in addition have a directional dependence, which makes DPC not very useful for quantitative interpretations.

In the following we will consider one way of reconstructing quantitative images from differential phase contrast data. But before getting into the reconstruction scheme we will first need to establish a quantitative relation between the intensity shift and the specimen phase gradient.

3.2.1 Phase Gradient Quantitation

Through Eq. 3.6 it was shown that the reflection angle is related to a phase gradient, which was further validated by Eq. 3.14. We will restrict ourselves now to a one-dimensional case of this fact:

$$\alpha_{\mathrm{ref}} = \frac{1}{k}\frac{\mathrm{d}\phi}{\mathrm{d}y}\,, \tag{3.18}$$

where ϕ is the total phase advance. As usual for scanning x-ray microscopes we consider an optic with a central stop. A sample with a phase gradient will refract the beam, leading to a shift of the beam footprint on the detector, shown in Fig. 3.6. We know that such a shift is small. Since we only consider a one-dimensional case, a split detector with a top (T) and bottom (B) half is sufficient.

If a total intensity of I_{total} is incident and uniformly distributed over the pupil, then the intensity in each half plane will be $I_T = I_B = I_{\mathrm{total}}/2$ in the case of no phase gradient present. If the beam is refracted by an angle α_{ref}, it will be shifted on the detector by an amount of $D_y = \alpha_{\mathrm{ref}} \cdot d$ as illustrated by the red area in Fig. 3.6; where d is the distance between sample and detector plane. Given that f_{stop} is the diameter of the central stop relative to the total pupil diameter, outer and inner radius of the beam footprint on the detector are $\alpha_{\mathrm{NA}} \cdot d$ and $\alpha_{\mathrm{NA}} \cdot d \cdot f_{\mathrm{stop}}$, respectively. The numerical aperture (see Sec. 1.3.3) is the half opening angle of the zone plate

$$\mathrm{NA} = \alpha_{\mathrm{NA}} = \frac{\lambda}{2\,\mathrm{d}r_{\mathrm{N}}}\,. \tag{3.19}$$

Now, the intensity that is shifted from the bottom to the top half plane is

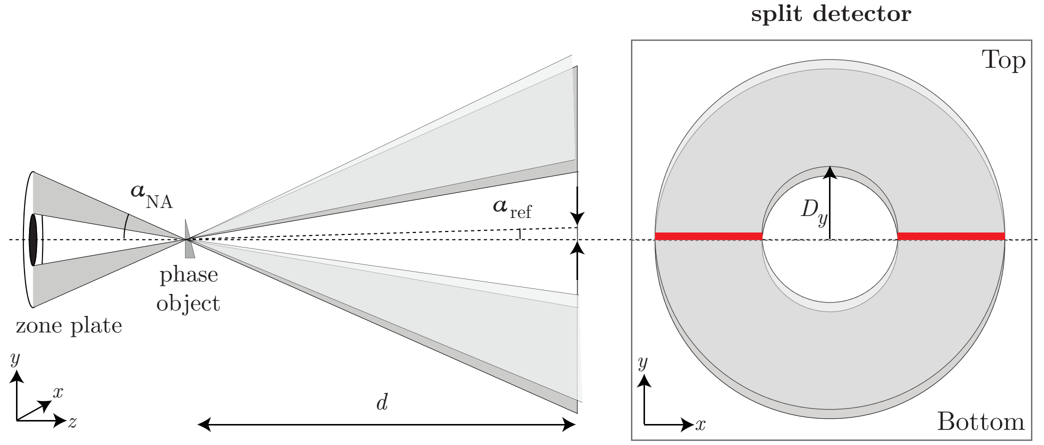

Figure 3.6: Refractive model. The red area denotes the changes of intensity in the top half of the detector.

given by the ratio of the red marked area to the total area, or

$$\begin{aligned} I_{\mathrm{shift}} &= I_{\mathrm{total}} \frac{2\,D_y\,(1-f_{\mathrm{stop}})\,d\,\alpha_{\mathrm{NA}}}{\pi (d\,\alpha_{\mathrm{NA}})^2 (1-f_{\mathrm{stop}}^2)} \\ &= I_{\mathrm{total}} \frac{2\,\alpha_{\mathrm{ref}}}{\pi\,\alpha_{\mathrm{NA}}\,(1+f_{\mathrm{stop}})}\,. \end{aligned} \tag{3.20}$$

Following this, we get for the intensity in each of the two half planes

$$I_{T,B} = I_{\mathrm{total}} \left(\frac{1}{2} \pm \frac{2\,\alpha_{\mathrm{ref}}}{\pi\,\alpha_{\mathrm{NA}}\,(1+f_{\mathrm{stop}})} \right). \tag{3.21}$$

The difference between the top and bottom, which is indicative for differential phase contrast as given by Eq. 3.8, then becomes

$$\mathrm{DPC}_y = \frac{I_{\mathrm{T}} - I_{\mathrm{B}}}{I_{\mathrm{total}}} = \frac{4\,\alpha_{\mathrm{ref}}}{\pi\,\alpha_{\mathrm{NA}}\,(1+f_{\mathrm{stop}})}\,. \tag{3.22}$$

Now we can connect the differential phase contrast signal with the phase gradient by solving above relation for $\mathrm{d}\phi/\mathrm{d}y$ with the help of Eq. 3.18 and Eq. 3.19:

$$\frac{\mathrm{d}\phi}{\mathrm{d}y} = \frac{\pi^2}{4} \frac{(1+f_{\mathrm{stop}})}{\mathrm{d}r_N}\,\mathrm{DPC}_y\,, \tag{3.23}$$

which is the quantitative relation we have been looking for. The relation for $\mathrm{d}\phi/\mathrm{d}x$ is analogous.

Note that an equivalent relation to Eq. 3.23, as it is used in [2], is given by

$$\frac{\mathrm{d}\phi}{\mathrm{d}y} = \frac{\pi\, k\, (R_{\mathrm{ZP}} + R_{\mathrm{CS}})}{4 f_{\mathrm{o}}}\, \mathrm{DPC}_y\,, \tag{3.24}$$

where R_{ZP} and R_{CS} are the radii of the zone plate and central stop and f_{o} is its focal length.

An example of a phase gradient quantitation is given in Fig. 3.7, which shows a cluster of $5\,\mu$m diameter polystyrene spheres at 2.5 keV x-ray energy. The imaging was done with a detector and illumination alignment shown in Fig. 3.8, resembling an effective quadrant detector arrangement; hence making above quantitation possible. Note that the far-field illumination is completely contained within the inner quadrant structure of the detector.

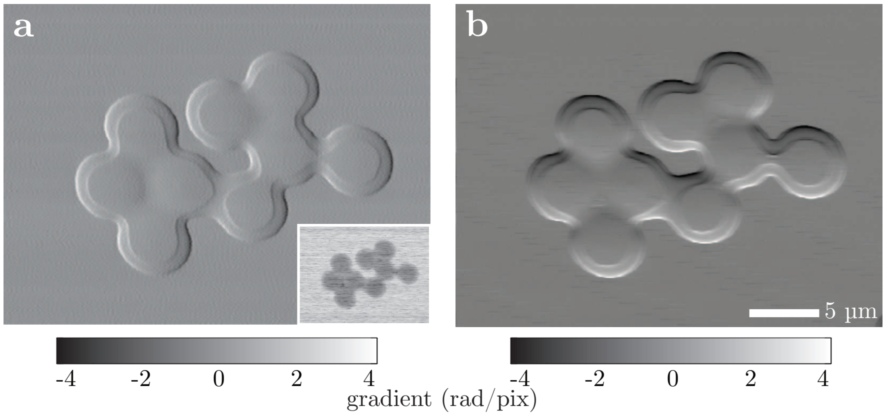

Figure 3.7: Quantified phase gradient images of polystyrene sphere cluster in (**a**) x- and (**b**) y- direction; an inlay shows the corresponding absorption image. Experimental details: 2.5 keV, steps 75 nm, ZP $160\,\mu$m, $\mathrm{d}r_N$ 50 nm, stop $40\,\mu$m, quadrant detector arrangement as shown in Fig. 3.8.

3.2.2 One-dimensional Integration

With the quantitative relations of Sec. 3.2.1 we are now in the position to quantitatively reconstruct the specimen phase shift. Of course, we could have done a reconstruction much earlier, when we had realized that a phase gradient causes a proportional shift to the intensity; however, this would have been a qualitative reconstruction only, since we lacked a quantitative relation between shift and phase gradient.

Naturally, the total phase shift can be obtained by a one-dimensional integration of Eq. 3.23 or Eq. 3.24:

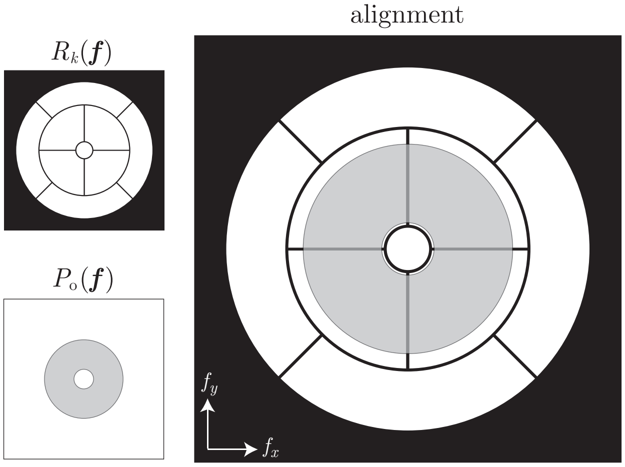
$R_k(\boldsymbol{f})$

$P_\mathrm{o}(\boldsymbol{f})$

alignment

Figure 3.8: Detector configuration, far-field illumination and their respective alignment. The arrangement corresponds to an effective quadrant detection.

$$\delta k t = \phi = \int \mathrm{d}j \, \frac{\mathrm{d}\phi}{\mathrm{d}j} \,, \tag{3.25}$$

with j substituting the direction of the phase gradient and respective integration direction.

Lets put this to use by applying it to measured differential phase contrast data of the cluster of $5\,\mu$m diameter polystyrene spheres, which is shown in Fig. 3.7 and has been quantified via Eq. 3.23. Both images show a gradient distribution that is symmetric around the origin reaching from approximately -4 to $+4\,$rad/pix. Note, that besides quantitation these images have been normalized in a way following [2] in order to correct for detector misalignment and beam drift. We imposed the condition that each row of Fig. 3.7(a) and each column of Fig. 3.7(b) sums to zero (see Sec. 3.2.6).

Applying a one-dimensional integration to the phase gradient images yields the results shown in Fig. 3.9. The one-dimensional integration of these images is performed on a row-by-row basis for the x-gradient image $\partial_x \phi$ and a column-by-column basis for the y-gradient image $\partial_y \phi$. Theoretically, it is expected that both images of Fig. 3.9 are equal, because they represent the same quantity. However, differences are apparent. The streaks in both images are a result of noise that is present in the data. The directional integration accumulates noise along the respective direction of integration, which naturally differs between neighboring rows or columns. The sources of this noise are various: photon shot noise, beam fluctuations, sample or detector vibrations,

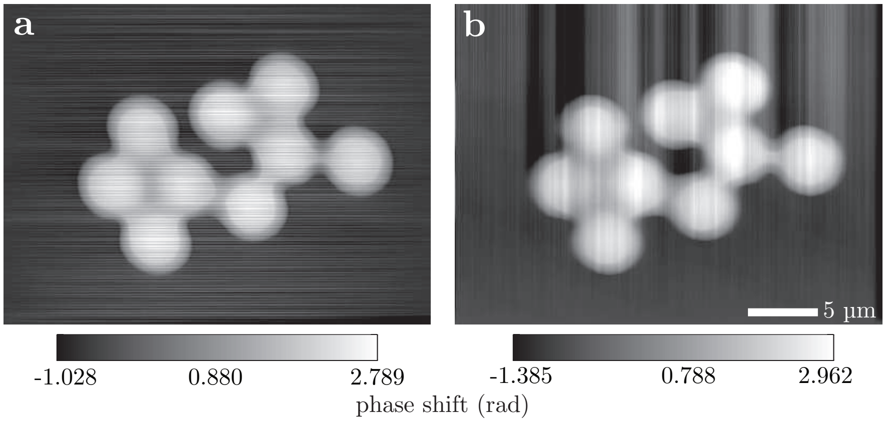

Figure 3.9: One-dimensional integration reconstruction of sphere cluster from Fig. 3.7 with (**a**) the integrated phase of $\partial_x \phi$ and (**b**) the integrated phase of $\partial_y \phi$. Noticeable in both images are streaks that follow the integration direction and are a result of noise in the data.

misalignment, etc. and are difficult to quantify. The normalization treatment as mentioned above for Fig. 3.7 reduces these noise effects partially, but cannot completely eliminate them. Besides in appearance, the integrated images also show quantitative differences with respect to the reconstructed phase shift values. A pursuing discussion involving one-dimensional integration of DPC images can be found in [11].

While images reconstructed in this way can be potentially useful, the results are rather unsatisfactory. The higher the signal-to-noise ratio of the acquired images, the better the results will be. However, note that the images of Fig. 3.7 are already of good SNR; similarly to Talbot-interferometrically obtained DPC images [46], which also show this streaking effect when only integrated in one dimension. There are, however, instances where 1d integrations yield good results, when applied in connection with tomographic imaging as in the work by Pfeiffer *et al.* [47] - the necessary redundancy in the information comes then from the different projections.

3.2.3 Orthogonal Integration

Besides the simple approach of one-dimensional integration, more advanced treatments exist. The reconstruction of gradient maps is a general physical problem. A very common technique in observational astronomy and adaptive optics is the Hartmann sensor, where reconstructions have used physical constraints to optimize orthonormal basis sets with least-square fitting methods [48]. Alternative matrix techniques are computationally intensive [49, 50]. Instead we will follow a simple and elegant integration technique outlined below.

The following method was first introduced by Arnison *et al.* [51] and utilizes the Fourier-derivative theorem (see Appendix A.2.2); we demonstrated its applicability for scanning transmission x-ray microscopy [2]. By realizing that we are dealing with two orthogonal gradient maps $\partial_x\phi$ and $\partial_y\phi$ of the specimen phase shift ϕ that hold redundant information, we can use this to our advantage by combining them in one complex function and write the derivatives in terms of Fourier transforms by using Eq. A.9:

$$\partial_x\phi(x,y) + \mathrm{i}\partial_y\phi(x,y) = \int \mathrm{d}f_x \int \mathrm{d}f_y \, 2\pi\mathrm{i}(f_x + \mathrm{i}f_y)\,\Phi(f_x,f_y)\,\mathrm{e}^{2\pi\mathrm{i}(f_x x + f_y y)}\,. \tag{3.26}$$

Taking the Fourier transform of both sides of the equation, we get

$$\mathcal{F}\{\partial_x\phi(x,y) + \mathrm{i}\partial_y\phi(x,y)\} = 2\pi\mathrm{i}(f_x + \mathrm{i}f_y)\,\Phi(f_x,f_y) \tag{3.27}$$

which we can solve for Φ and use an inverse Fourier transformation to obtain the final result

$$\phi(x,y) = \mathcal{F}^{-1}_{x,y}\left\{\frac{\mathcal{F}_{f_x,f_y}\{\partial_x\phi(x,y) + \mathrm{i}\partial_y\phi(x,y)\}}{2\pi\mathrm{i}(f_x + \mathrm{i}f_y)}\right\}. \tag{3.28}$$

This relation represents a simultaneous integration of two orthogonal gradient maps and is often referred to as *Fourier Integration Method*. We will refer to this technique for the remainder of this work simply as *integration method*.

3.2.4 Reconstruction Example for Integration Method

The integration method exploits the redundant information given through the two orthogonal gradients and; therefore, has some inherent resistance to imaging noise. Application of the integration method through Eq. 3.28 to the two gradient maps of Fig. 3.7 leads to a reconstructed phase shift map shown in Fig. 3.10. The result is a significant improvement to the previously obtained one-dimensional integration attempts of Fig. 3.9.

In terms of quantitation we need to have a closer look. Figure 3.10 has two color bars: the one on the left side in the image corresponds to the "raw" reconstruction by just applying the integration method formula (Eq. 3.28) to the gradient maps. The image scale on the right corresponds to a background corrected image, where we have subtracted the mean image value of a background region (triangular area) from the total image. We apply this background subtraction in order to give a reference region for the total image. Within the background region the reconstructed phase shift is expected to

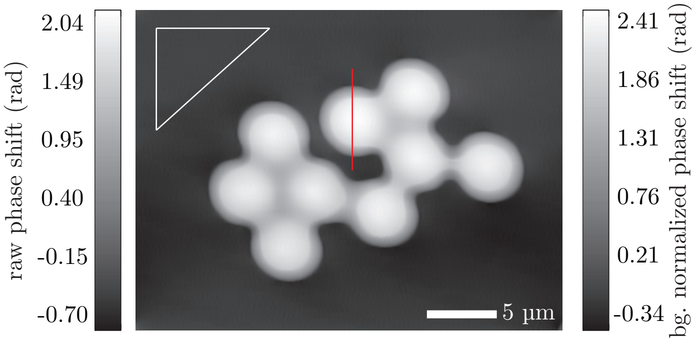

Figure 3.10: Raw and background corrected integration reconstruction of sphere cluster. Displayed is the real part of the integrated phase from Eq. 3.28. The left color scale shows the image values for the raw integration reconstruction; the right color bar refers to the image obtained by subtraction of the mean background value within the indicated triangular area from the total image. The red line indicates the position of the sphere profile for Fig. 3.11. The step appearance present in all spheres is likely due to residual solution and further discussed by Fig. 3.11.

be zero. However, due to imperfections in the imaging process mostly in the form of noise and a not completely even illumination, the non-specimen region reconstructs in a non-ideal way.

In the case of background subtraction the resulting values are very close to the theoretically expected phase shift of 5 μm polystyrene spheres, which is 2.41 rad at the sphere center and an imaging energy of 2.5 keV. A profile through one of the spheres in Fig. 3.10 is shown in Fig. 3.11. First of all we note that the diameter of the sphere is reconstructed properly as 5 μm, which can be seen from the horizontal axis showing the scan position. At the sphere center the reconstruction value of the phase shift agrees perfectly with the theoretically expected. We already noted before that the spheres have a step-like appearance inside. With the help of the profile we can understand this better. Besides the reconstructed data values in Fig. 3.11, different sphere scenarios and their respective projection profiles are shown. A simple sphere lying on a surface is shown in black; the corresponding projection profile matches already well with the measured data towards the outer part of the spheres at a radial distance between 1.9 μm and 2.5 μm from the center. After that the reconstructed sphere profile has a kink, which is likely due to residual solution that dried underneath the sphere. Such a scenarios is shown in red; for the theoretical phase shift projection profile it was assumed that the material, which

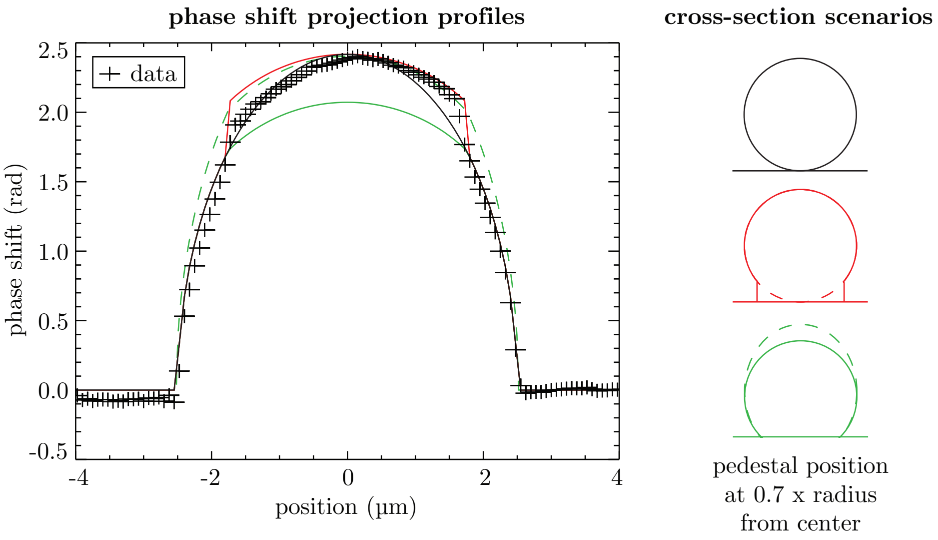

Figure 3.11: Phase shift profile through sphere of Fig. 3.10 on background normalized scale including theoretical projection profiles through spheres with different cross-section scenarios. Respective cross-section scenarios are shown on right: normal sphere (black), sphere with pedestal (red), sphere with extended contact surface (green) and same sphere scaled to thickness maximum of previous spheres (dashed-green). The position of the various sphere modifications appear at a distance corresponding to 70% of the sphere radius from the center.

makes up this pedestal, is of comparable optical density. The profile of the reconstructed data values follows this scenario nicely, in particular on the right hand side. Other scenarios are shown in green, but their projection profiles do not agree well with the reconstruction. While the pedestal scenario in red describes the data the best, it is probably not the complete reality, which is likely to be a more complex situation.

At this point we have obtained a good, quantitative reconstruction of the phase shift δkt induced by the sphere cluster. Since we know that the sample is made out of polystyrene (PS) and can determine its theoretical index of refraction real part δ_{PS} from Henke *et al.* [14] to be 3.81×10^{-5}. Together with the x-ray energy we can determine a thickness map from the phase shift:

$$t\,[\,\mu\mathrm{m}] = \frac{\delta kt}{\delta_{\mathrm{PS}} k}\,, \tag{3.29}$$

which is shown in Fig. 3.12. Looking at the individual spheres in the figure

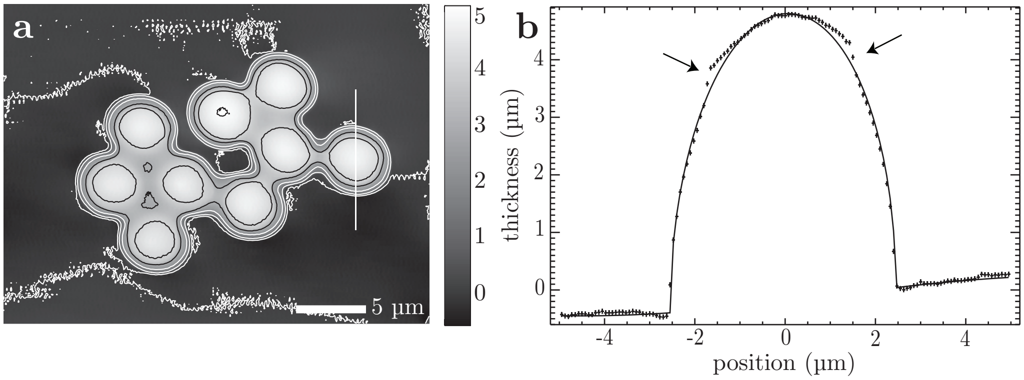

Figure 3.12: (**a**) Thickness map from integration reconstruction of sphere cluster including contour lines. (**b**) Line profile through sphere indicated in (a); arrows indicate similar pedestals as described by Fig. 3.11.

we note that all compare well with each other; in particular in terms of their quantitative thickness. The line profile of Fig. 3.12(b) also shows the pedestal behavior that we have identified previously.

In the following we will discuss a few particularities and advanced topics of the integration reconstruction process.

3.2.5 The Imaginary Part - Reconstruction Errors

The reconstructed phase shift $\phi = \delta kt$ is given by the real part of Eq. 3.28. Non-zero elements in the imaginary part of Eq. 3.28, as shown by Fig. 3.13

for the above sphere clutser reconstruction, reflect errors in the reconstruction and can provide feedback for accuracy of the integrated phase. Leakage of power from the real to the imaginary part can arise from contradictions in the two orthogonal gradient maps. In the present example the imaginary part is approx. 12% of the real part and the contradictions occur mostly at the edges of the spheres and pedestals underneath the spheres. At these positions higher order terms and contributions from DAC (see Sec. 3.1.3) will become noticeable. In particular for edge features in samples the theoretically expected derivatives are infinite. The choice of smaller step sizes will mitigate the effects of local contradictions and lessen the leakage into the imaginary part.

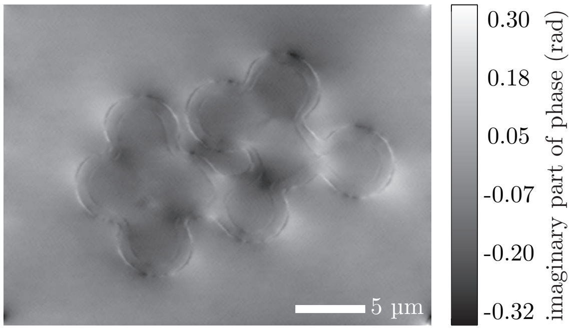

Figure 3.13: Imaginary part from the integration reconstruction of the sphere from Sec. 3.2.4.

3.2.6 Gradient Normalization

In Sec. 3.2.2 the gradient images leading to Fig. 3.7 were normalized following a procedure, which we mention in [2]. Here we want to briefly discuss the motivation for such normalizations and the cases of isolated and non-isolated specimens.

A detector misalignment will lead to a constant gradient offset that will reflect itself in a global DC-offset of the resulting reconstruction for the phase shift. Beam drift (motion of the beam on the time scale of the total image acquisition) during the scan will change the alignment of the illumination with respect to the detector that leads to a similar effect as the detector misalignment, but on a subregion within the scan that will cause a local DC-offset of the reconstruction. In order to reduce the effects of these experimental conditions on the reconstruction process one needs to apply corrections to the gradient images.

For isolated specimens a convenient method is to require that each row of a horizontal and each column of a vertical gradient image sum to zero. This follows the notion of ”what goes up most come down” for a derivative of an isolated object. We have observed that application of this normalization greatly improves image reconstruction quality as can be monitored through the imaginary part (see Sec. 3.2.5).

For non-isolated samples, *i. e.* either partially or completely filling the field of view, the previous method is not applicable for obvious reasons. In such a case a method following an approach by Menzel *et al.* [52], which they employ to create von-Neumann boundary conditions can potentially prove useful. The procedure requires to mirror each gradient image first in the horizontal, and then the two resulting image together in the vertical. This way we duplicate the image information four times and create an image of each gradient map that is point symmetric with respect to its center. For these images we then perform the above gradient normalization for isolated objects and then perform the integration reconstruction for the two gradient maps as usual. From the reconstructed image we can choose one of the four copies as our final result (they are all identical). We have not tested this method extensively; however, initial results look encouraging on partially isolated objects. Further and more rigorous investigations are necessary.

3.2.7 Background Subtraction

The background normalization of Fig. 3.12 differs from Fig. 3.10, where we subtracted a mean value of an isolated background region from the total image. In Fig. 3.12 we chose to set the average of the perimetric values to zero. The result of both normalization methods is comparable and equally justified.

Often observed in experimental cases were sinusoidal backgrounds along the slow scanning direction as shown in Fig. 3.14(a). These are likely due to drifts of the beam and / or the motors of the setup, changing the illumination condition during the scan which results in an uneven reconstructed background. Note that in this case a mere background subtraction as done in a previous example would make the final result strongly dependent on the chosen area. Certainly, a perimeter normalization is also not a good choice. Since the background is to a good approximation constant along the x-direction, it is suggestive to approximate its sinusoidal form along the y-direction. We can do this by averaging its form in the direction within the dashed area, and then use this average to reproduce a background image (see Fig. 3.14(b)). Successive subtraction from the image then yields a well-background corrected image in Fig. 3.14(c).

Depending on the situation other methods can be suitable. In the case

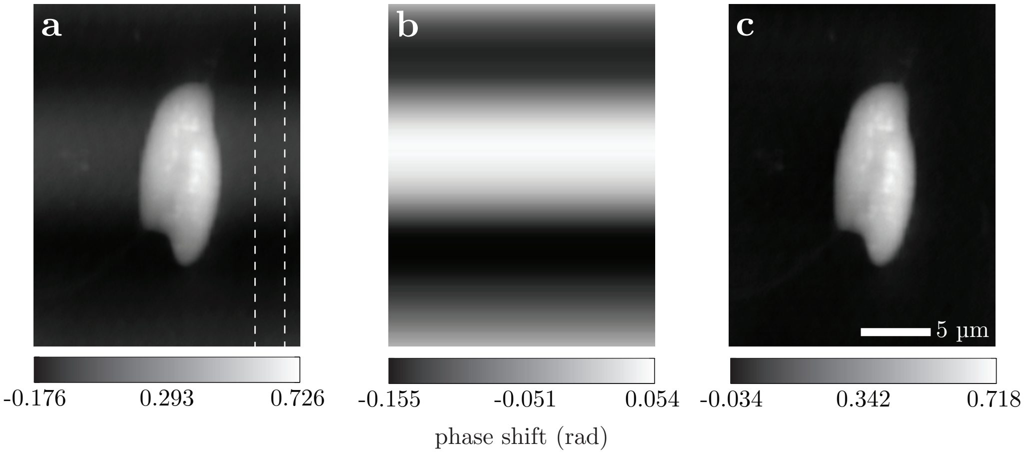

Figure 3.14: (**a**)Reconstructed phase shift of the freshwater flagellate *Cryptomonas* without background correction. (**b**) Sinusoidal background images produced by averaging the data in between the two dashed lines in (a) and reproducing it to a complete image. (**c**) Background corrected image by subtracting (b) from (a). Experimental details: 10.2 keV, steps 50 nm, ZP 160 μm, dr_N 100 nm, stop 40 μm, quadrant detector arrangement.

of scans where the sample completely covers the field of view, the presented approaches are of course not valid. A possible way out in such cases can be the absorption image or the monitored incident illumination upstream of the sample through an ion-chamber (to register the total intensity) and beam position monitors. The analysis in these cases is more involved and beyond the scope of our treatment here.

3.2.8 The Phase Part - Sample Identification

Besides the real part ($\mathcal{R}(\delta kt)$) of the integration reconstruction, which represents the integrated phase, and the imaginary part ($\mathcal{I}(\delta kt)$) indicative for errors and contradictions in the reconstruction, we can also make use of the phase (ω) of the reconstructed phase shift image;

$$(\delta kt) = \mathcal{R}(\delta kt) + \mathrm{i}\,\mathcal{I}(\delta kt) = |(\delta kt)|\, \mathrm{e}^{\mathrm{i}\omega}\,. \tag{3.30}$$

Figure 3.15 shows the phase ω of the sphere cluster reconstruction from Sec. 3.2.4. We note that in the region of the image where no sample is present, the phase ω jumps between ±π; only within the sample area the behavior of ω is uniform. This should not come as a large surprise, because only where a sample is present the resulting phase shift (δkt) is well defined and with a phase ω of approx. 0.

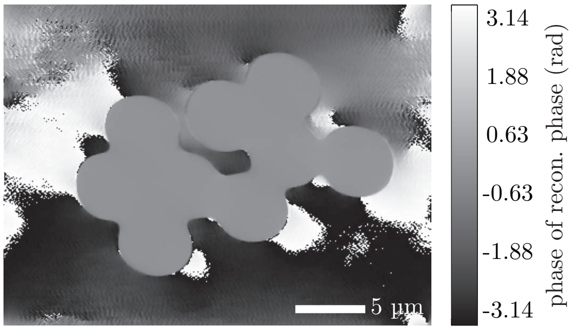

Figure 3.15: Phase of integration reconstruction from sphere cluster in Sec. 3.2.4.

This fact can potentially be used experimentally in order to automatically identify sample and no-sample regions.

3.3 Fourier Filtering Method

Now we will turn our attention to a different method of reconstruction for phase contrast images. The following *Fourier Filtering Method* was initially developed for scanning transmission electron microscopy [53–56] to retrieve quantitative absorption and phase contrast images of the specimen with the help of a segmented detector. This work has since been transfered and applied to scanning x-ray microscopy [57], where it turns out to be very useful.

We will describe the essential parts of this method and its derivation in the present section. A detailed mathematical derivation that includes all intermediate steps can be found in the Appendix C; for a complementary discussion we refer to Hornberger [11].

3.3.1 Image Formation through Transfer Functions

Our starting point will again be, the wave field in the detector plane of a scanning microscope

$$\Psi_3(\boldsymbol{f};\, \boldsymbol{r}_\mathrm{s}) = \int \mathrm{d}^2\boldsymbol{r}\, h(\boldsymbol{r})\, p_\mathrm{o}(\boldsymbol{r}-\boldsymbol{r}_\mathrm{s})\, \exp\left(\mathrm{i}2\pi\boldsymbol{r}\boldsymbol{f}\right), \tag{3.31}$$

which we have seen on multiple occasions in the present chapter. Note, that this time we have omitted indices of specific imaging planes and left out constant pre-factors in order to simplify the notation for the successive treatment. Generally we can do this since each particular quantity is intrinsically connected with a certain plane in the imaging system. Furthermore, for a correct mathematical treatment and computational implementation all quantities have to be setup on the same coordinate spaces.

By employing properties of Fourier transforms and the defining relation of the probe function p_o (Eq. 2.19) above Eq. 3.31 can equivalently be written as a convolution (see Eq. C.2)

$$\psi_3(\boldsymbol{f};\, \boldsymbol{r}_\mathrm{s}) = \left[P_\mathrm{o}(-\boldsymbol{f})\, \exp\left(\mathrm{i}2\pi\boldsymbol{r}_\mathrm{s}\boldsymbol{f}\right)\right] \otimes_{\boldsymbol{f}} H(-\boldsymbol{f})\,. \tag{3.32}$$

To measure the intensity distribution caused by this wave field we use a detector with separate segments (indexed by k) and respective response functions $R_k(\boldsymbol{f})$. The signal recorded by any specific segment k is given by

$$s_k(\boldsymbol{r}_\mathrm{s}) = \int \mathrm{d}^2\boldsymbol{f}\, R_k(\boldsymbol{f})\, |\psi_3(\boldsymbol{f};\, \boldsymbol{r}_\mathrm{s})|^2\,. \tag{3.33}$$

The segmentation of the detector can be arbitrary. The quadrant detector used in Sec. 3.1.2 is one possible realization. Albeit, there is no restriction on the way of the spatial segmentation of the detector (one can either use a specially designated segmented detector, or just a pixellated detector such as a PAD or CCD), it can be useful for analysis purposes that each segment has a corresponding opposite. We will keep the segmentation general for the following derivation, as it will not have any advantage to restrict ourselves to one particular configuration and; furthermore, we will see that configurations other than a quadrant can lead to superior results.

We can expand $|\psi_3|^2$ into $\psi_3\psi_3^*$ and use Eq. 3.32 to arrive at the Fourier transform of the recorded detector signals $s_k(\boldsymbol{r}_\mathrm{s})$ in terms of the probe displacement $\boldsymbol{r}_\mathrm{s}$

$$S_k(\boldsymbol{f}_\mathrm{s}) = \int \mathrm{d}^2\boldsymbol{f}\, R_k(\boldsymbol{f}) \Big[P_\mathrm{o}(-\boldsymbol{f})\, P_\mathrm{o}^*(-\boldsymbol{f}-\boldsymbol{f}_\mathrm{s}) \otimes_{\boldsymbol{f}} H(-\boldsymbol{f})\, H^*(-\boldsymbol{f}-\boldsymbol{f}_\mathrm{s}) \Big]\,, \quad (3.34)$$

see Appendix C.1 and Eq. C.11 for a derivation of this expression.

Our attention focusses now on the product HH^* in Eq. 3.34. The specimen function can without loss of generality always be written as

$$h(\boldsymbol{r}) = 1 + h_r(\boldsymbol{r}) + \mathrm{i}\, h_i(\boldsymbol{r})\,, \quad (3.35)$$

where $h_{r,i}$ are real functions. The specific form of h is of no further importance at this point, as long as it is possible to write it in the previous form in terms of h_r and h_i. The corresponding Fourier spectrum of Eq. 3.35 is then

$$H(\boldsymbol{f}) = \Delta(\boldsymbol{f}) + H_r(\boldsymbol{f}) + \mathrm{i}\, H_i(\boldsymbol{f})\,. \quad (3.36)$$

Be aware that even though $h_{r,i}$ are real functions and can be viewed as the real and imaginary parts of h (aside from the leading 1), their respective Fourier transforms $H_{r,i}$ are not the real and imaginary parts of H, but complex functions by themselves.

By employing the expression of Eq. 3.36 for the specimen in Eq. 3.34 and neglecting terms of order $\mathcal{O}({H_{r,i}}^2)$ (see Eq. C.14) we can arrive at

$$\begin{aligned} S_k(\boldsymbol{f}_\mathrm{s}) \;&=\; \Delta(\boldsymbol{f}_\mathrm{s})\, C_k(0,0,\boldsymbol{f}_\mathrm{s}) + \\ &\quad + H_r(\boldsymbol{f}_\mathrm{s})\, \left[C_k(-1,0,\boldsymbol{f}_\mathrm{s}) + C_k(0,1,\boldsymbol{f}_\mathrm{s})\right] + \\ &\quad + \mathrm{i}\, H_i(\boldsymbol{f}_\mathrm{s})\, \left[C_k(-1,0,\boldsymbol{f}_\mathrm{s}) - C_k(0,1,\boldsymbol{f}_\mathrm{s})\right]\,, \end{aligned} \quad (3.37)$$

where

$$C_k(m, n, \boldsymbol{f}_{\mathrm{s}}) = \int \mathrm{d}^2\boldsymbol{f}\, R_k(\boldsymbol{f})\, P_{\mathrm{o}}(m\boldsymbol{f}_{\mathrm{s}} - \boldsymbol{f})\, P^*_{\mathrm{o}}(n\boldsymbol{f}_{\mathrm{s}} - \boldsymbol{f}) \tag{3.38}$$

are bilinear transfer functions [58] that represent the optical setup.

We can identify contrast transfers functions for the respective parts of the specimen function $H_{r,i}$ as follows

$$\begin{aligned} T_r^{(k)}(\boldsymbol{f}_{\mathrm{s}}) &= C_k(-1, 0, \boldsymbol{f}_{\mathrm{s}}) + C_k(0, 1, \boldsymbol{f}_{\mathrm{s}}) \\ T_i^{(k)}(\boldsymbol{f}_{\mathrm{s}}) &= C_k(-1, 0, \boldsymbol{f}_{\mathrm{s}}) - C_k(0, 1, \boldsymbol{f}_{\mathrm{s}})\,, \end{aligned} \tag{3.39}$$

so that the final result for the Fourier spectrum of the signal collected by the individual segments k of the detector reads

$$S_k(\boldsymbol{f}_{\mathrm{s}}) = \Delta(\boldsymbol{f}_{\mathrm{s}})\, C_k(0, 0, \boldsymbol{f}_{\mathrm{s}}) + H_r(\boldsymbol{f}_{\mathrm{s}})\, T_r^{(k)}(\boldsymbol{f}_{\mathrm{s}}) + \mathrm{i}\, H_i(\boldsymbol{f}_{\mathrm{s}})\, T_i^{(k)}(\boldsymbol{f}_{\mathrm{s}})\,. \tag{3.40}$$

We now have arrived at an expression for the image formation in terms of transfer functions. This represents an important result since we have achieved two important facts with Eq. 3.40: a *linearization* and *separation* of the formed images with respect to the specimen contributions H_r and H_i (compare to Eq. 3.34). Each of the two functions contributes to the final image through their respective transfer function. This result serves as the basis for the filtering reconstruction method.

3.3.2 Transfer Function Properties

Transfer functions, such as the ones identified in the previous section, are a common tool in image formation theory and can prove particularly useful when investigating certain behaviors and properties of imaging systems. An inherent and central property of describing an image formation process in terms of transfer functions is the separation of the imaging system (*i. e.* the optical setup) from the object that is imaged (as seen in Eq. 3.40). The transfer functions, which are completely independent from the object and describe the imaging system, allow the characterization of the imaging behavior. The literature on transfer functions is vast and contrast transfer functions for detector configurations important for the presented work have been published before [11, 36, 59–61]. Here we want to discuss some of the properties and characteristics of the bilinear (Eq. C.18) and contrast transfer functions (CTF) (Eq. 3.39) of the previous section, and give some examples.

Absence of specimen

The bilinear transfer function $C_k(0, 0, \boldsymbol{f}_{\mathrm{s}})$ is constant for all $\boldsymbol{f}_{\mathrm{s}}$ and represents the measured intensity by segment k in the absence of a specimen.

Total spectral transfer and MTF

A convenient way to describe the total spectral transfer of the optical system for the real and imaginary parts $(h_{r,i})$ of the sample is given through

$$T_{r,i}^{\mathrm{tot}}(\boldsymbol{f}_{\mathrm{s}}) = \sum_k \left| T_{r,i}^{(k)}(\boldsymbol{f}_{\mathrm{s}}) \right| . \tag{3.41}$$

The $T_{r,i}^{\mathrm{tot}}(\boldsymbol{f}_{\mathrm{s}})$ do not allow the interpretation of specific images, but pose a measure to describe and compare different optical systems in terms of their total spectral coverage and transfer.

The real part total transfer function T_r^{tot} is in its essence the same as the modulation transfer function (MTF) of the imaging system.

Symmetry properties

A detailed derivation of the CTF symmetry properties can be found in Sec. C.2 of the Appendix. Assuming a real and symmetric pupil function P_{o} the CTF properties are as follows

- real part CTF (T_r):
  - positive
  - symmetric with respect to $\boldsymbol{f} = \mathbf{0}$
  - identical for opposite segments
- imaginary part CTF (T_i):
  - antisymmetry with respect to $\boldsymbol{f} = \mathbf{0}$
  - opposite sign for opposite segments
  - vanish for individual, symmetric segments

For a more detailed list of properties in particular with less restraints in the pupil function we refer the reader to the Appendix (Sec. C.2).

Imaging interpretations through symmetry properties

A few consequences from these symmetry properties and the respective imaging interpretations can be made as follows. For the case of incoherent bright field imaging (absorption imaging) all the segments of a detector are summed up. From above symmetry properties we can see that all the contributions from the imaginary part CTFs will cancel out. We will be left only with the contributions from the real part CTFs summing up to T_r^{tot}, which in turn represents the MTF of a large-area detector configuration.

It has been stated in the past [11, 36] that displaying difference signals of opposing segments, for which due to the symmetry only the imaginary part CTFs and hence only h_i will contribute information, allows to obtain phase contrast information (as for example already seen before in Sec. 3.1.2). We generally agree with this observation, but would like to point out possible misconceptions of this interpretation. The notion that only the differencing of segment signals allows observation of phase information assumes that all of the specimens phase information is contained within h_i, intrinsically implying the weak specimen approximation

$$h = \mathrm{e}^{-\beta kt + \mathrm{i}\delta kt} \approx 1 - \beta kt + \mathrm{i}\,\delta kt \equiv 1 + h_r^{\mathrm{w}} + \mathrm{i}\, h_i^{\mathrm{w}}\,, \tag{3.42}$$

This is a very limiting assumption which is not generally true compared to

$$h = \mathrm{e}^{-\beta kt + \mathrm{i}\delta kt} = \mathrm{e}^{-\beta kt}\cos(\delta kt) + \mathrm{i}\,\mathrm{e}^{-\beta kt}\sin(\delta kt) \equiv 1 + h_r + \mathrm{i}\, h_i\,, \tag{3.43}$$

where the specimen absorption and phase contributions are contained in both functions h_r and h_i. Therefore, we generally also have phase contrast information in h_r. But why, from the transfer function point of view, is displaying difference signals advantageous to obtain phase contrast information? We believe it inherently lies within the asymmetry of the imaginary part CTF response for one segment, which gets further amplified through subtracting the in-sign opposite CTF response from the opposing segment. This intensified asymmetric response is key to obtain the specimen phase information because as we have seen in Sec. 3.1.3, the influence of the specimen phase term redistributes intensity asymmetrically around the zero spatial frequency center. In most cases the intensity redistribution is subtle and will only be observable through the imaginary part CTFs and hence differencing of segments. It has been observed that in stronger phase shifting specimens already signals from individual segments show phase contrast information. For very extremely phase specimens we would expect that even the summation of opposing segments (only real part CTF contributions) can give rise to phase contrast.

Example transfer functions

Let us give an example of contrast transfer functions. In Fig. 3.16 we show the real and imaginary part CTFs for the imaging situation given through Fig. 3.8 of the polystyrene sphere cluster discussed in Sec. 3.2. The illumination in this case only covered the inner quadrant structure of the segmented detector chip, which means that only the transfer functions from these segments will contribute to the image formation process in this case. All segments that are not illuminated have vanishing transfer functions (compare Eq. 3.39). Note the symmetry of the CTFs for the individual segments as identified early in the present section. The images are displayed in normalized spatial frequency coordinate space; a spatial frequency of 1 corresponds to the pupil function cut-off frequency (numerical aperture.) The transfer functions extend to a normalized spatial frequency of 2 as expected for an incoherent imaging system. The corresponding total real and imaginary transfer functions are shown in Fig. 3.17. Note a particular attribute of the total imaginary part CTF at and around the zero spatial frequency: the CTF values in this region are zero, corresponding to no information transfer. Of course, we cannot measure absolute phase shifts, which why it should come at no surprise that the CTF at $\boldsymbol{f}=\mathbf{0}$ vanishes. However, the region in the vicinity of $\boldsymbol{f}=\mathbf{0}$ also shows little to no transfer, which is a consequence of the quadrant detection scheme of this setup. Note that the regions of low transfer within the CTF region resemble a symmetry ("X" shape) in the directions of the four quadrant segments. In the light of these observations we will in the following investigate different detection schemes with a particular focus on their respective imaginary part transfer behavior.

Different detector geometries

As established before, the total contrast transfer $T_{r,i}^{\mathrm{tot}}$ can be used to describe and classify different imaging systems regarding their transfer of information from the real and imaginary parts of the specimen. At this point we would like to consider a few detector scenarios. Note that the real part transfer functions T_r are all positive and of even symmetry; hence, the total real transfer T_r^{tot} will be the same for all detector geometries as long as the detector segments taken together cover the complete far-field illumination cone. The absorption imaging properties therefore do not depend on the detector configuration.

In case of the imaginary part CTFs the total imaginary transfer, and therefore the phase contrast sensitivity, strongly depends on the detector layout. In Fig. 3.18(a, c, e, g, i) we show five different detector scenarios, all of which consider the same pupil function. Their respective total imaginary transfer

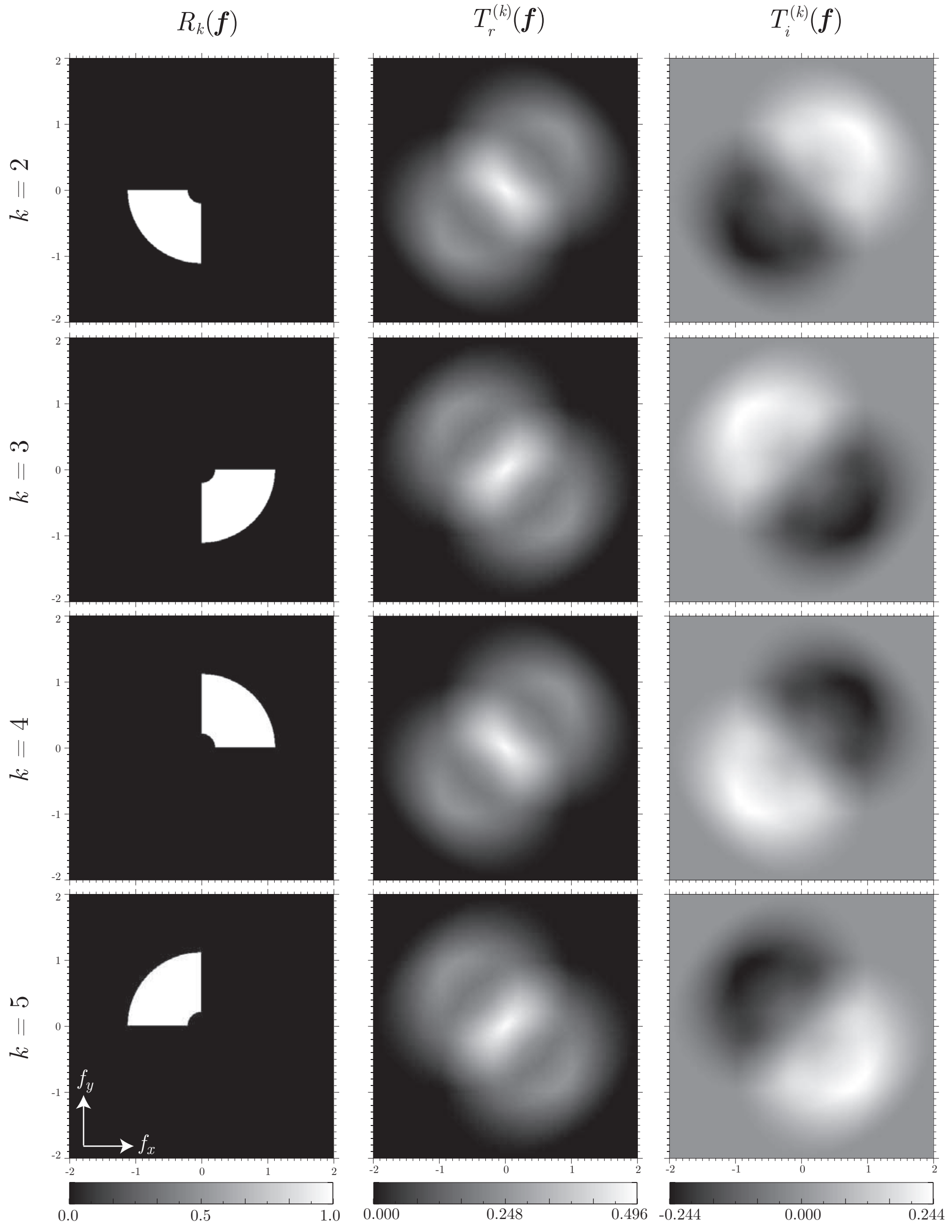

Figure 3.16: Contrast transfer functions for the illumination of the polystyrene sphere cluster of Fig. 3.8. Only segments that are illuminated have non-zero transfer functions. Note the even and odd symmetry for the real and imaginary part CTFs.

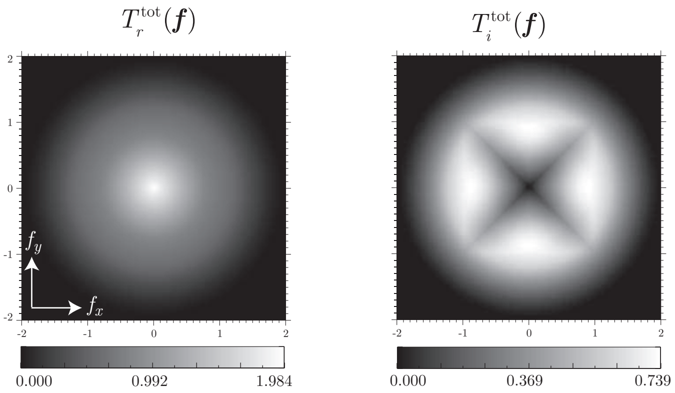

Figure 3.17: Total contrast transfer functions for the illumination of the polystyrene sphere cluster of Fig. 3.8

functions are depicted in Fig. 3.18(b, d, f, g, i). Images (a) and (b) represent a simple quadrant geometry as seen before; (c) and (d) is a similar quadrant geometry that in addition has a division in the radial direction. The added finer segmentation in the radial direction manifests itself in an improved coverage of the frequency space through the transfer function in the radial direction (compare (b) and (d)). Yet, regions of lower transfer along the diagonal direction remain. Images (e) and (f) show an octant geometry, where the finer segmentation in the azimuthal direction leas to a correspondingly more isotropic response in the azimuthal direction in frequency space (compare (a) and (f)). Combining the benefits of cases (c) and (e) leads to the a configuration of a double quadrant structure of images (g) and (h), where the outer quadrant has been rotated azimuthally by 45° with respect to the inner quadrant. This results in a more even coverage of frequency space than all previous cases. In comparison, an extreme case of segmentation in the form of a 256 element pixelated detector is shown in (i) and (j). The spectral coverage of the rotated double quadrant of case (g) and the pixelated detector of (i) are not drastically different, yielding a comparable frequency response.

Of course, one can raise objection and demand to use the pixelated detector since it gives superior information; however, practical experimental aspects should also be taken into account. A largely pixelated detector system, with fast read-out as desired for scanning type operation, is a complex and expensive apparatus which in addition requires substantial data storage capacity. On the other hand, a 8-segment detector is much easier to realize and is by far easier to operate, significantly less expensive and requires drastically less data storage space.

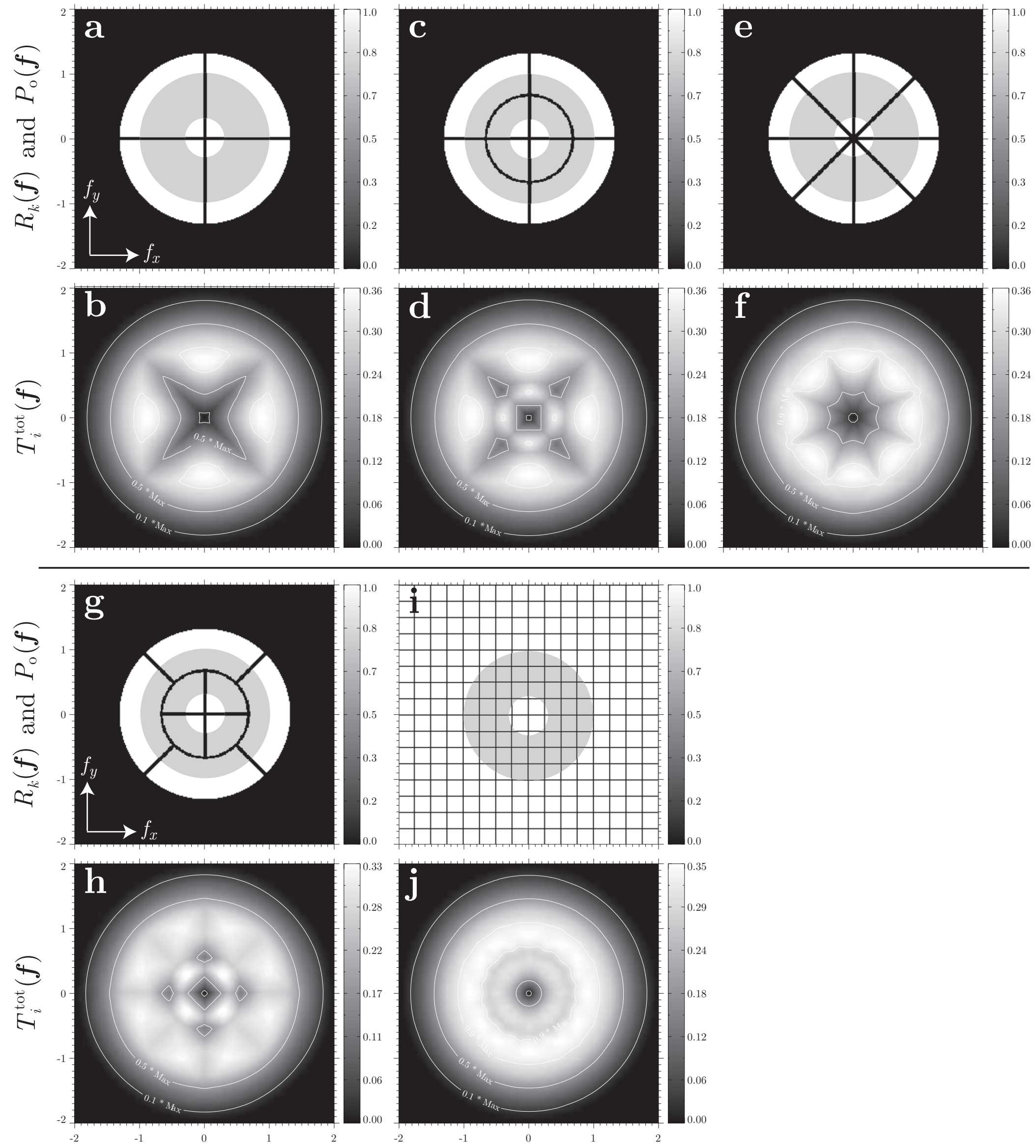

Figure 3.18: Comparison of five different detector geometries and their respective total imaginary part transfer functions. The first and third row (**a, c, e, g, i**) show the different detector response layouts including the pupil function as a gray overlay. The pupil function is the same in all cases. The second and fourth row (**b, d, f, g, i**) shows the T_i^{tot} for each of the five detector cases. Lines show the iso-contours of 10%, 50% and 90% of the maximum transfer for the respective T_i^{tot}.

A common objection for using a low segments number compared to a pixelated detector geometry or CCD has been the fact that through the pixelation one can determine the true center-of-mass shift of the illumination and with it the true specimen phase gradient. However, the Fourier filtering reconstruction methods does not require or infer any phase gradient information from the intensity shift in the far-field as necessary for the integration method. Instead, as we will see, the signal of all segments is used in an independent way to reconstruct the specimen phase information. Therefore, we think the comparison of cases (g) and (i) of Fig. 3.18 and the conclusion that both give a comparable and similar result is completely valid.

Different illumination alignment

With the rotated double quadrant structure we have identified a detector geometry that has a low number of segments and at the same time good contrast transfer. An additional free parameter regarding the imaging properties is the alignment of the detector with respect to the far-field illumination. When we examined different detector geometries in Fig. 3.18 above the illumination was the same in all cases. Let us now consider the situation of different illumination conditions.

In Fig. 3.19 we show two different alignments of the rotated double quadrant. In alignment scheme 1 the beam illuminates all 8 segments, while in alignment scheme 2 only the inner quadrant is illuminated, which effectively corresponds to the quadrant detection of Fig. 3.16 and 3.17. Note, that the different alignments are realized by scaling the pupil and leaving the detector fixed in spatial frequency space. One might think that alignment 2 has a poorer areal spatial frequency coverage; *i. e.* it does not extend as far out as alignment 1. However, this is not true, both cases cover the same spatial frequency extend with respect to the pupil cut-off frequency (edge of pupil function), which in essence determines the imaging properties of the system. For the ease of comparison between both alignments we have chosen to affix the spatial frequency coordinate system to the detector response.

Having clarified this alleged difference between alignment 1 and 2 we can draw our attention to the qualitative differences of both. In the case alignment 1, where a radially divided segmentation is used to detect the illumination we have already seen before that this reduces the areas of low transfer in the imaginary part CTF. In the quadrant detection of alignment 2 we have larger areas of little to no transfer. While this seemingly gives the advantage to alignment 1, we will discuss a few points in the following, which makes the choice less clear than it seems.

For a quadrant detection the actual size of the illumination on the detector is not important for the CTfs, as long as the illumination is fully contained within the quadrant structure. However, in this case of double quadrant structure of alignment 1 the precise knowledge of the actual size of the beam on the detector is more critical, as the transfer function will strongly depend on it. Furthermore, this case will be strongly sensitive to a radial unevenness of the pupil[2], because the transfer functions assume an even radial illumination which results in an equal weighting of information on the segments. On the other hand, as we can already guess without having actually done a reconstruction with segmented detector data, the alignment case 1 has the potential to yield superior reconstruction results due to the improved frequency coverage[3]. In the end it will be a compromise between how good the illumination conditions are and what quality of reconstruction one hopes to obtain. A future development of the technique can potentially be to incorporate measured illumination profiles into the transfer functions.

As an example of the criticality to know the correct illumination on the detector the imaginary part CTF of a particular segments of alignment scheme 1 in Fig. 3.19 highlights a specific detail. Around the zero spatial frequency area we can observe a reversal on contrast transfer. If the correct illumination size would be unknown and we were to reconstruct data obtained in alignment scheme 1 with contrast transfer functions calculated for scheme 2, severe images distortions would be the consequence, as the calculated transfer functions for scheme 2 do not correct for the contrast reversal in the low to intermediate frequency region.

3.3.3 Fourier Filtering Reconstruction Derivation

Having described the image formation process in terms of transfer functions and understanding their properties poses the basis for the subsequent analysis. The following methods represents an inversion of the image formation process, where all signals from individual segments are combined in an ideal way, to determine the complex specimen function. Originally this approach was developed for scanning electron microscopy [53–56], but has since been applied to scanned x-ray imaging [57], where the main focus lies on the true quantitative reconstruction and the inherent measurement noise treatment. The approach is similar to a Wiener filter (see Appendix B) which is commonly used in transfer function deconvolution in signal and imaging theory, and from there also gets its name *Fourier Filtering Method*.

---

[2] As it often can be the case in experimental situations through lower efficiency of zone plates to the outside, or unevenly illuminated zone plate

[3] One can consider it in a pictorial way: the more segments and therefore boundary crossings the illumination covers the more redundancy the collected information contains.

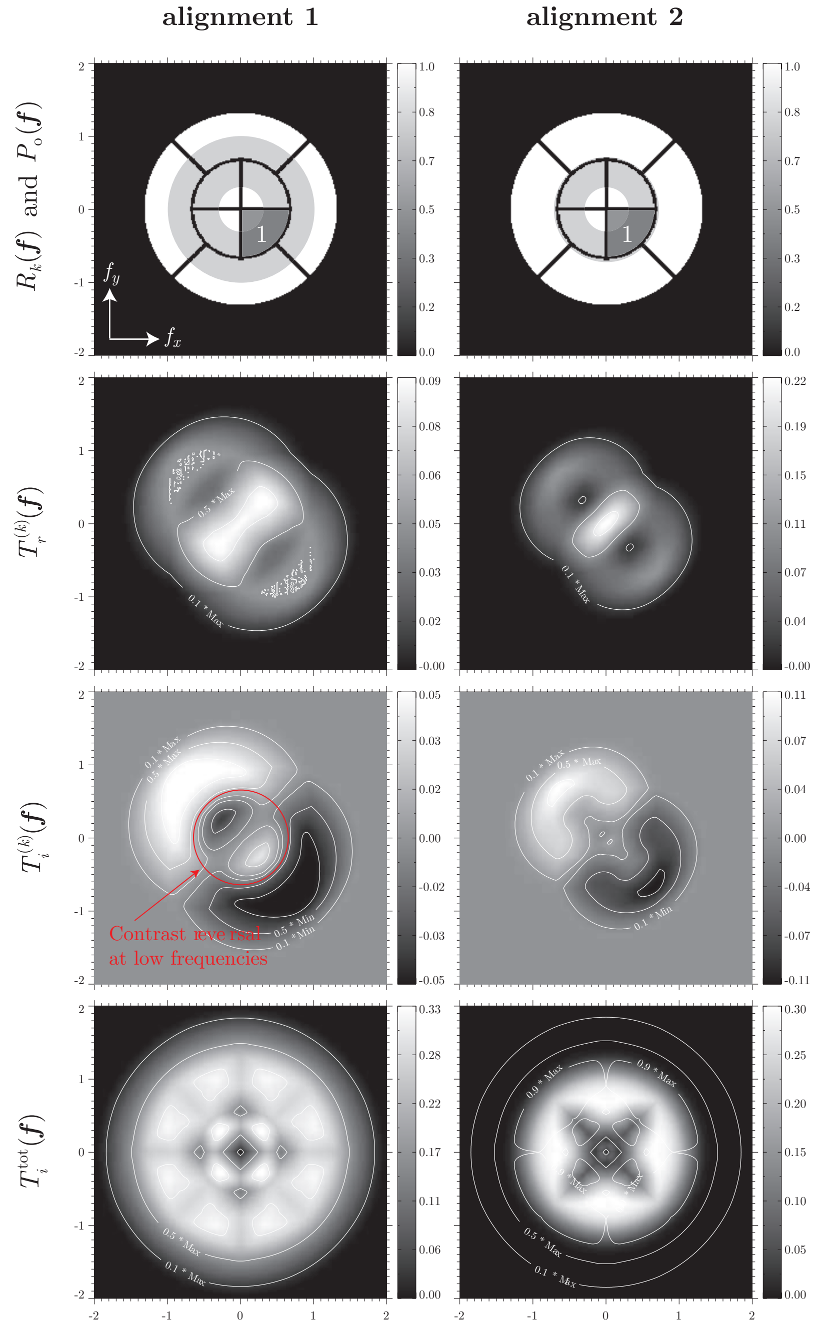

Figure 3.19: Comparison of different detectors alignment schemes for the rotated quadrant detector. In alignment 1 all segments are covered by the illumination, while in alignment 2 only the inner quadrant gets illuminated, corresponding effectively to a simple quadrant detection.

We will start by pretending that we have a reconstructed specimen function in terms of a best guess for the specimen Fourier transform $\widehat{H}(\boldsymbol{f})$. We will assume that this guess $\widehat{H}(\boldsymbol{f})$ is formed in terms of the recorded images of the individual segments $S_k(\boldsymbol{f})$ and individual weighting functions $W_k(\boldsymbol{f})$

$$\widehat{H}(\boldsymbol{f}) = \sum_k W_k(\boldsymbol{f})\, S_k(\boldsymbol{f})\,. \tag{3.44}$$

It is these weighting functions we aim to derive, which will serve as a link between the measured data and the specimen we hope to gain information about. In order to simplify the notation for the remainder of this chapter we will omit to include the subscript $_\mathrm{s}$ for the scan displacement coordinate; all quantities have to be defined on the same frequency space in any regard.

The error metric by which we measure the quality of the best guess $\widehat{H}(\boldsymbol{f})$ compared to the real specimen is given by the root means square error (RMS)

$$\epsilon = \int \mathrm{d}\boldsymbol{f}\, \left\langle \left| \widehat{H}(\boldsymbol{f}) - H(\boldsymbol{f}) \right|^2 \right\rangle\,, \tag{3.45}$$

where we average over many measurements through an expectation value ($\langle\rangle$). This error has to be minimized for an optimal reconstruction. The minimization of ϵ can be performed independently for all frequency values $\boldsymbol{f}$ due to the fact that the integrand of Eq. 3.45 is real and positive for all spatial frequencies. We perform the minimization through setting the integrands partial derivatives with respect to the weighting functions to zero (see Appendix Eqs. C.38 and) and henceforth obtain the condition

$$\left\langle S_k^* \left(\sum_l W_l\, S_l - H \right) \right\rangle = 0\,, \tag{3.46}$$

which has to be fulfilled for all segments k. The set of linear equations of Eq. 3.46 for the filter functions $W_k(\boldsymbol{f})$ can be solved analytically by substituting the Fourier spectrum of the individual segments in the weak specimen approximation from Eq. 3.40

$$S_k(\boldsymbol{f}) = H_r(\boldsymbol{f})\, T_r^{(k)}(\boldsymbol{f}) + \mathrm{i}\, H_i(\boldsymbol{f})\, T_i^{(k)}(\boldsymbol{f}) + N_k(\boldsymbol{f}) \qquad \text{for } \boldsymbol{f} \neq 0 \text{ and all } k\,, \tag{3.47}$$

where a spectral noise ($N_k(\boldsymbol{f})$) term for each segment has been added. The zero spatial frequency contribution from the Δ-term of Eq. 3.40 will be handled separately later. In order to arrive at a solution it is assumed that the noise between different detector segments is uncorrelated, and that the real and imaginary parts of the specimen are uncorrelated as well, which constitutes an additional part of the weak specimen approximation. The general solution is given in the Appendix by Eq. C.52. These expressions can be further simplified if the pupil function $P_\mathrm{o}(\boldsymbol{f})$ is real and centro-symmetric and each detector segment k has an opposing segment $\bar{k}$ such that $R_k(\boldsymbol{f}) = R_{\bar{k}}(-\boldsymbol{f})$. Then the filter functions take the form

$$W_k(\boldsymbol{f}) = \frac{T_r^{(k)*}(\boldsymbol{f})}{\sum_l \left|T_r^{(l)}(\boldsymbol{f})\right|^2 + \beta_r(\boldsymbol{f})} + \frac{T_i^{(k)*}(\boldsymbol{f})}{\sum_l \left|T_i^{(l)}(\boldsymbol{f})\right|^2 + \beta_i(\boldsymbol{f})} \qquad \text{for } \boldsymbol{f} \neq 0 \text{ and all } k\,, \tag{3.48}$$

where the noise terms are given by

$$\beta_{r,i}^{(k)}(\boldsymbol{f}) = \frac{\left\langle |N_k(\boldsymbol{f})|^2 \right\rangle}{|H_{r,i}(\boldsymbol{f})|^2} \tag{3.49}$$

and are assumed to be of equal power for all segments $\beta_{r,i}^{(k)} = \beta_{r,i}$ and the spectral noise $N_k(\boldsymbol{f})$ to be the same for the real and imaginary parts.

Let us now consider the zero spatial frequency term that has been left out following Eq. 3.46. The noise contribution for this term can assumed to be zero, as it is the definition of noise to have an average of zero. Furthermore, we will take the real part of the specimen function $H_r(\boldsymbol{f} = \boldsymbol{0})$ to be small compared to the Δ-term of Eq. 3.47. The specimen imaginary part spectrum $H_i(\boldsymbol{f} = \boldsymbol{0})$ does not need to be considered as its transfer function vanishes for $\boldsymbol{f} = \boldsymbol{0}$ (see Eq. C.58). The resulting reconstruction filter will then be (see Appendix C.3.4)

$$W_k(0) = \frac{2\, T_r^{(k)*}(0)}{\sum_l \left|T_r^{(l)}(0)\right|^2 + \beta_r(0)}\,. \tag{3.50}$$

We have now obtained expressions for the sought after weighting or filter functions $W_k(\boldsymbol{f})$ and; therefore can now reconstruct the specimen function by a simple inverse Fourier transform of Eq. 3.44 to arrive at the real space specimen function $h(\boldsymbol{r})$

$$h(\boldsymbol{r}) = \mathcal{F}^{-1}\{\widehat{H}(\boldsymbol{f})\} = \mathcal{F}^{-1}\left\{\sum_k W_k(\boldsymbol{f})\, S_k(\boldsymbol{f})\right\}. \tag{3.51}$$

Normalization to background

From the beginning we set out to obtain a quantitative reconstruction of the sample. In order to achieve this goal through Eq. 3.51 we have to pay specific attention to the scaling of quantities within the reconstruction process; in particular to the values of the pupil function which mainly contributes to the CTFs $T_{r,i}^{(k)}(\boldsymbol{f})$ contained within the filter functions $W_k(\boldsymbol{f})$. The integral of the absolute values squared of the experimental pupil function in the absence of a specimen represents the total number of incident photons, which in turn can only be estimated from the final imaging process. Furthermore, one needs to pay close attention in each step of the derivation that the total number of photons is conserved. For reasons of practicality it is significantly easier to use an arbitrarily scaled pupil for the calculation of the transfer and filtering functions, and then go through the described reconstruction process. After having obtained the final reconstruction for the specimen (Eq.3.51) the image has to be normalized by the complex mean of a background region. In case of non-isolated specimens that do not have a background region within the field of view, one can choose a region within the sample for normalization purposes; but one has to keep in mind that in this case the quantitation of this reconstruction is then relative to this "background" region.

Generic noise terms and filtering

A central part of the reconstructions filters of Eq. 3.48 are the noise parameters $\beta_{r,i}^{(k)}$, which depend on the ratio of noise to specimen power. This ratio varies for each experiment and sample imaged. Hence it is not possible to generate a generally applicable reconstruction filter that can be used for all measurements. One option is to choose a constant noise parameter value

$$\beta_{r,i}^{(k)}(\boldsymbol{f}) = \text{const.} \qquad \text{for all } \boldsymbol{f} \text{ and all } k\,, \tag{3.52}$$

and tune this generic noise parameter to obtain the visually best reconstruction. This procedure is common in Wiener filtering approaches. Alternatively, one can estimate the required quantities of noise and specimen power from the data to generate an optimal and frequency dependent noise parameter $\beta_{r,i}^{(k)}(\boldsymbol{f})$; a recipe for this will be shown in the following.

Computation of reconstruction filters - frequency dependent noise

In order to obtain the optimal filter functions for the reconstruction process we need to determine the real and imaginary noise terms

$$\beta_{r,i}(\boldsymbol{f}) = \frac{\left\langle |N(\boldsymbol{f})|^2 \right\rangle}{|H_{r,i}(\boldsymbol{f})|^2}\,. \tag{3.53}$$

The noise power N can be assessed as follows. If the signal is sufficiently strong compared to detection dark noise and no other systematic sources of noise (*e. g.* drifts and instabilities of the setup or beam) are present, photon statistics is the dominating source of noise. Then there is no correlation of the noise between scan displacement positions and we are dealing with a white-noise power spectrum that is flat and isotropic. The magnitude of the noise power can then be estimated via the radial power spectrum density (RPSD) of the recorded image data, which is defined as

$$\mathrm{RPSD}\big\{S_k\big\}(f) = \frac{1}{2\pi f}\int_0^{2\pi} \mathrm{d}\phi_{\boldsymbol{f}}\ |S_k(\boldsymbol{f})|^2\ , \tag{3.54}$$

where the integral is taken over the azimuthal angular range in spatial frequency space and the resulting RPSD is a function of frequency magnitude f. In Fiq.3.20 we show an example RPSD from experimental data. The data itself will be discussed in the section following the current (see Sec. 3.3.4). A decay to a flat line of the RPSD can be observed for spatial frequencies exceeding the transfer of the microscope or alternatively where the specimen does not have higher frequency content, whichever comes first. This flat line represents the noise power of the data. For a conservative estimate to be used in the reconstruction filters for $\big\langle|N(\boldsymbol{f})|^2\big\rangle$ we choose the largest noise power determined from RPSDs of all detector segments. Another possibility is to choose the noise power individually for all segments and then use the general filter function terms for the reconstruction; this has not been attempted as of yet.

Since the specimen function $H_{r,i}$ is not known, we also do not know its power to form the noise parameter for Eq. 3.53. However, it is fair to assume that the contrast is isotropically distributed over all spatial directions, then the power $|H_{r,i}(\boldsymbol{f})|^2$ can be well enough approximated by a RPSD. From Eq. 3.47 we can see that for frequencies where the signals dominate the noise

$$\tilde{S}_k(\boldsymbol{f}) \approx H_r(\boldsymbol{f})\,T_r^{(k)}(\boldsymbol{f}) + \mathrm{i}\,H_i(\boldsymbol{f})\,T_i^{(k)}(\boldsymbol{f}) \qquad \text{for } \boldsymbol{f} \neq 0 \text{ and all } k\,. \tag{3.55}$$

In this form we can utilize the symmetry properties of the transfer functions $T_{r,i}$ to gain access to either the real H_r or imaginary part H_i of the specimen in order to achieve the necessary RPSD power estimate for $|H_{r,i}(\boldsymbol{f})|^2$. Therefore,

$$\mathrm{RPSD}\big\{H_r\big\}(f) \approx \frac{\mathrm{RPSD}\big\{\tilde{S}_{\kappa_r}\big\}(f)}{\mathrm{RPSD}\big\{\tilde{T}_r^{\kappa_r}\big\}(f)} \tag{3.56}$$

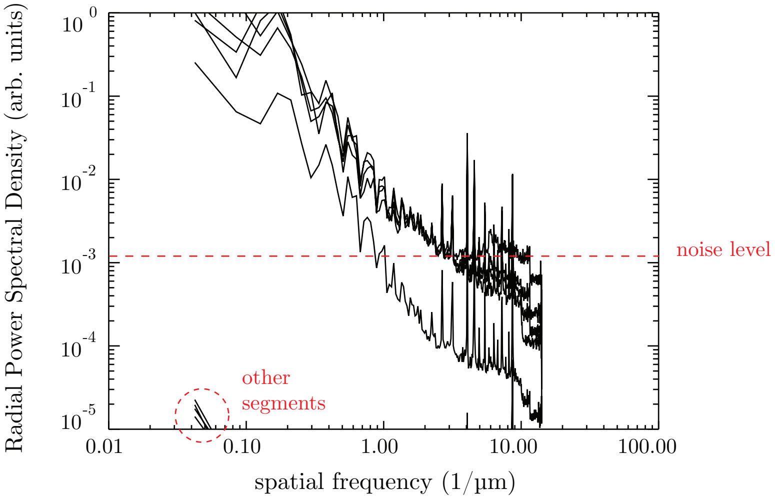

Figure 3.20: RPSD example from experimental data. The illumination condition is shown in Fig. 3.23. The RPSDs of the five segments covered by the far-field intensity are shown in the plot. Of the segments not illuminated by the direct beam only the tail end is visible (pointed out by dashed circle), as their power is orders of magnitude lower. The magnitude of the noise power chosen is shown by the horizontal line. The maximal frequency transfer for the data is $10\,(\mu\text{m})^{-1}$ corresponding to 50 nm in real space.

and

$$\mathrm{RPSD}\big\{H_i\big\}(f) \approx \frac{\mathrm{RPSD}\big\{\tilde{S}_{\kappa_i}\big\}(f)}{\mathrm{RPSD}\big\{\tilde{T}_i^{\kappa_i}\big\}(f)}\,, \tag{3.57}$$

where $\kappa_{r,i}$ resembles a specific combination of detector segment signals which either only exhibit real or imaginary contrast transfer.

In order to realize Eq. 3.56 we remember from Sec. 3.3.2 the even symmetry property of T_r, from which follows that a summation of all detector signals will only have a real part transfer and so

$$\tilde{S}_{\kappa_r}(\boldsymbol{f}) = \mathcal{F}\left\{\sum_k s_k(\boldsymbol{r})\right\}. \tag{3.58}$$

Similarly we can isolate a purely imaginary contrast transfer through computing difference images of opposing segments (anti-symmetric behavior of T_i) to achieve

$$\tilde{S}_{\kappa_i}(\boldsymbol{f}) = \mathcal{F}\left\{\sum_{k,\bar{k}}[s_k(\boldsymbol{r}) - s_{\bar{k}}(\boldsymbol{r})]\right\}, \tag{3.59}$$

where the sum is formed over pairs $(k, \bar{k})$ of opposite segments. By having formed the sums of Equations 3.58 and 3.59 we have isolated real and imaginary transfer-only signals as desired; *i. e.* we gained individual access of the first and second term of Eq. 3.55 respectively. Note, that these signals still contain both information from the optics through the CTFs and the specimen. This is why in Equations 3.58 and 3.59 the contributions from the CTFs are divided out to correct for the microscope transfer. Figure 3.21 shows example RPSD plots for the previous calculations. As the specimen powers come into the region where the noise is comparable, the corrected RPSDs (red lines) will loose their meaning and diverge steeply upwards. For a large class of specimens the signal decline with frequency can be well approximated by a power law (linear fit in log-log scale). A power law fit for the real and imaginary specimen RPSDs is shown in Fig.3.21. These fits will be used as input for $|H_{r,i}(\boldsymbol{f})|^2$ to estimate the noise parameters of Eq. 3.53. In cases where the RPSDs do not show a mere linear decay, piecewise power law fits can be done instead.

The respective noise parameters $\beta_{r,i}(\boldsymbol{f})$ following the above derivation obtained for the example data are shown in Fig. 3.22. Note that through the previous derivation a radial form of $\beta_{r,i}(f)$ is derived. In order to obtain image arrays for the noise parameters, the radial forms are simply revolved azimuthally, since we assumed that the noise is distributed isotropically.

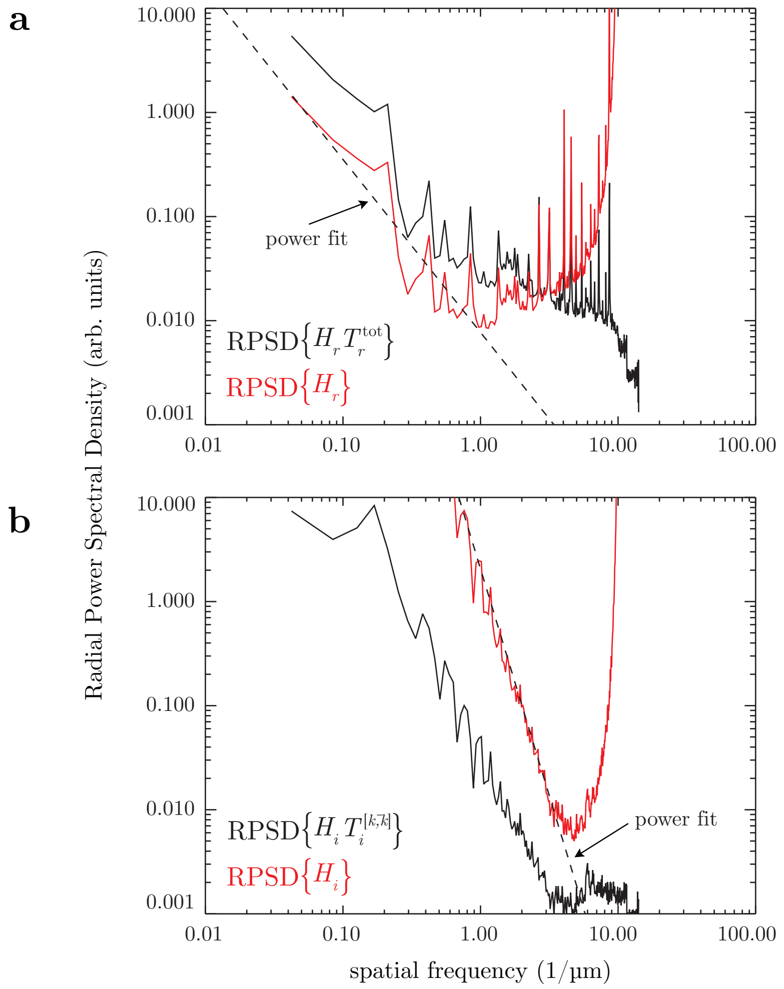

Figure 3.21: RPSD plots for estimating the real and imaginary specimen power by means of Equations 3.58 and 3.59. (**a**) Real part specimen power estimate by means of Eq. 3.58. (**b**) Imaginary part specimen power estimate by means of Eq. 3.59. Black lines resemble the signal RPSDs, while red are transfer corrected signal RPSDs, representing the respective specimen power spectra. Linear power fits to the corrected signal RPSDs shown by dashed lines.

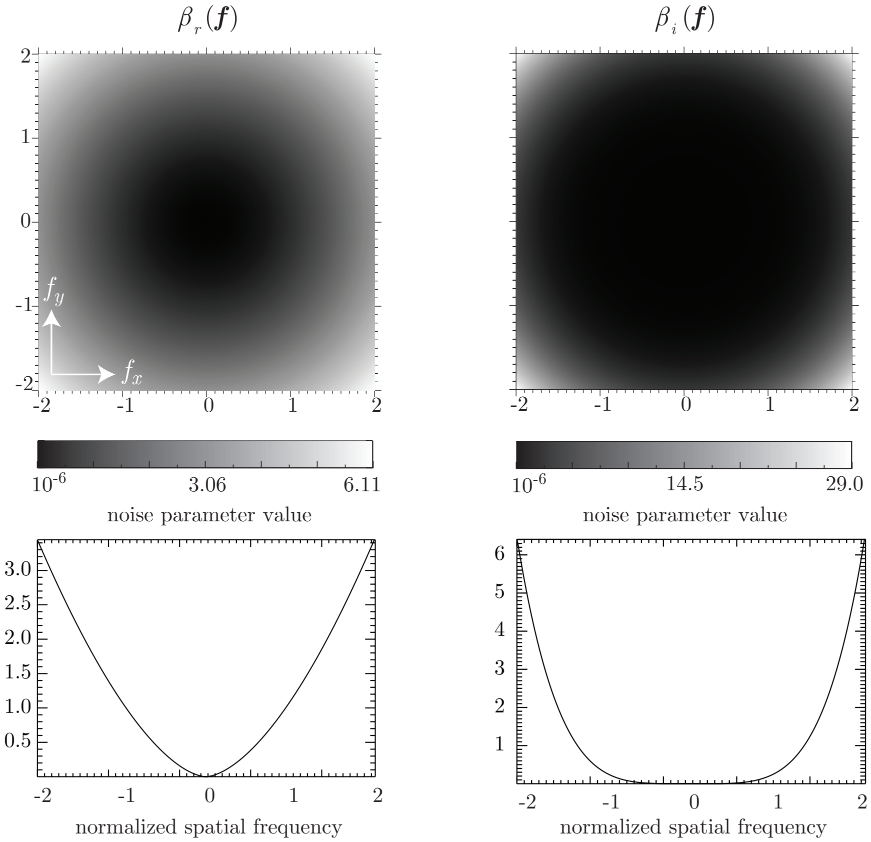

Figure 3.22: Noise parameters obtained from Eq. 3.53 through the noise power of determined in Fig. 3.20 and specimen power estimates of Fig. 3.21. The plots show horizontal profiles through each of the respective noise parameter images.

3.3.4 Reconstruction Example for Filtering Method

After having gone through the whole derivation of the filtering method including the proper determination of the noise parameters for the filter functions we now want to give an example of a filtering reconstruction from experimental data.

We will consider a cluster of 5 μm and 10 μm diameter polystyrene spheres imaged at 10 keV x-ray energy. The illumination alignment of the experiment is shown in Fig. 3.23. Note that the far-field intensity of the pupil function cover the inner quadrant of the detector, as well as part of the central segment. This alignment was chosen to take advantage of the increased frequency coverage of the transfer functions when multiple segment boundaries are crossed, as we have seen in Sec. 3.3.2. Hence this alignment does not resemble a mere quadrant detection as necessary for the integration reconstruction method of Sec. 3.2. Figure 3.24 shows differential phase contrast (DPC) images obtained by forming difference images from opposing segments of the inner quadrant structure of the detector.

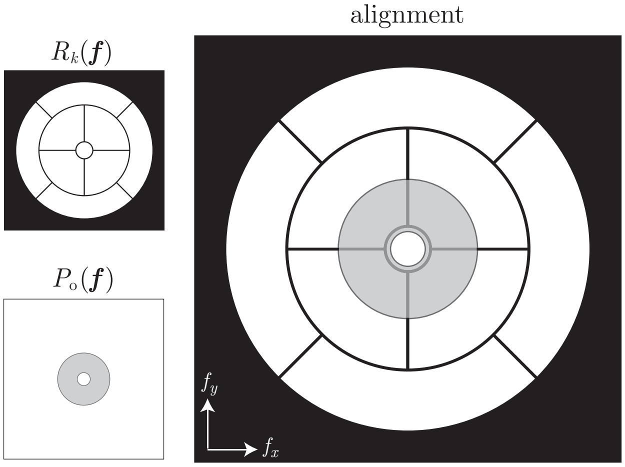

Figure 3.23: Detector configuration, far-field illumination and their respective alignment for the experiment involving the 5 μm and 10 μm diameter polystyrene sphere cluster.

It is important to note that these DPC images are only of qualitative nature and do not have a quantitative meaning like the gradient images of Fig. 3.7. Since no quadrant detection scheme was used, the gradient quantitation of Sec. 3.2.1 is not applicable.

The proper noise treatment to obtain the noise parameters for the filter functions of this data has already been done at the end of the previous

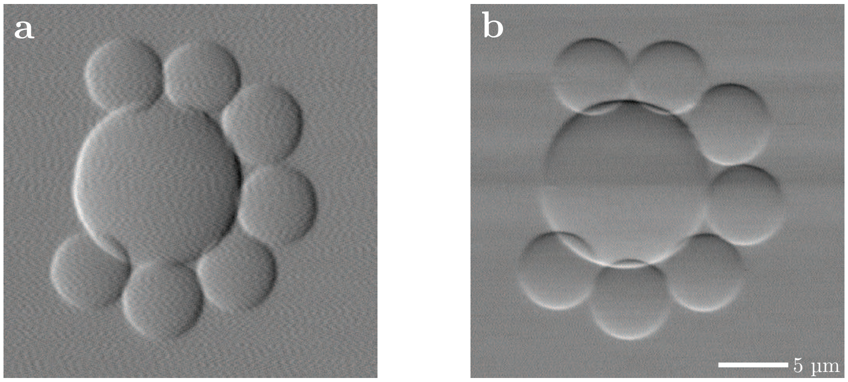

Figure 3.24: Differential phase contrast images of sphere cluster with 5 μm and 10 μm diameter polystyrene spheres in (**a**) horizontal and (**b**) vertical DPC Experimental details: 10 keV, steps 50 nm, ZP 160 μm, dr_N 100 nm, stop 40 μm, detector arrangement as shown in Fig. 3.23.

Sec. 3.3.3. In Fig. 3.25 we show the transfer functions for the central segment ($k = 1$) and one of the quadrant segments ($k = 1$) of the detector for the experimental situation. Note, that the imaginary transfer for the central segment is zero as expected for a centro-symmetric segment. Even though we are not dealing with a pure quadrant arrangement the transfer function for the quadrant segment is similar to what we have seen before in Fig. 3.16. Additionally, Fig. 3.25 shows the respective filter functions for the experimental data.

Figure 3.26 shows the filtering reconstruction of the phase shift δkt of the sphere cluster. A background subtraction as described in Sec. 3.2.6 has been applied to the final reconstruction result. The theoretically expected phase shift for 5 μm and 10 μm polystyrene spheres at 10 keV is 0.595 rad and 1.19 rad respectively (via Henke data [14]). The quantitative result for the match these theoretical values very well. The large sphere shows a reconstructed value of 1.23 rad, which is slightly above the expected phase shift. However, only a few pixel near the sphere center show this high value, which is likely a remaining artifact of the background subtraction. The subtracted background includes a horizontal line of increased phase shift going right through the sphere center, as can be seen from the small inlay. All the small spheres have reconstruction values ranging from 0.55 to 0.6 rad and with that are in excellent agreement with the expected. Since the filtering method reconstructs the complete specimen function, we can also consider the reconstructed absorption of the sphere cluster, see Fig. 3.27(a). This is remarkable since the normal

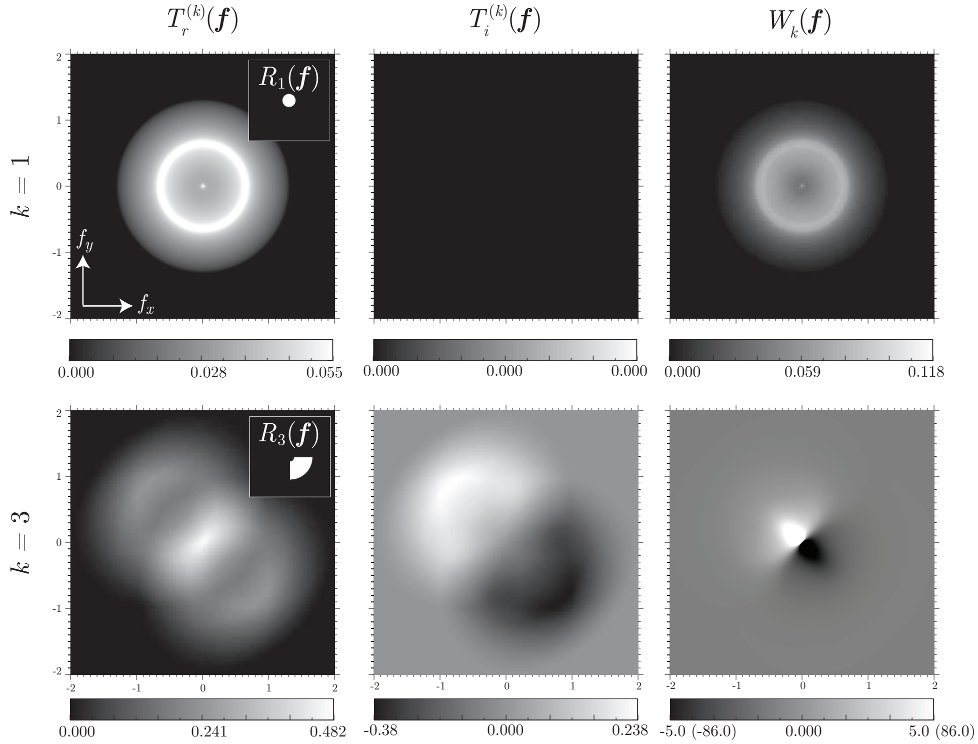

Figure 3.25: Transfer functions for the alignment shown in Fig. 3.23 (inlay shows detector response functions) and the obtained filter functions for the experimental data of the 5 μm and 10 μm sphere cluster. Filter function for segment $k = 3$ is scaled to highlight the shape of the filter; actual minimum and maximum values given in parentheses. Filter functions of other quadrant segments are equal, but rotated according to the segment orientation.

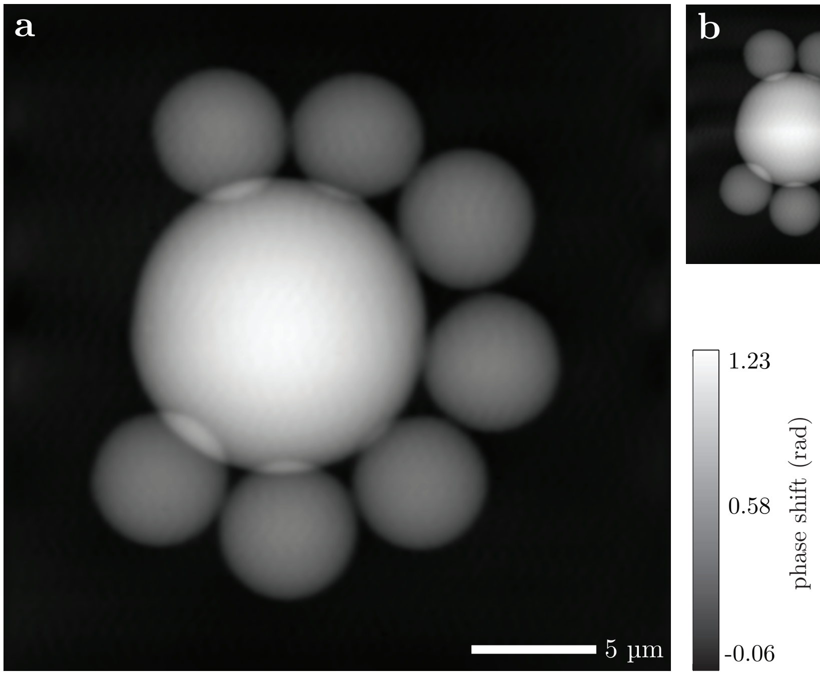

Figure 3.26: Filtering reconstruction of $5\,\mu$m and $10\,\mu$m sphere cluster. (**a**) Reconstructed phase shift after subtraction of an uneven background. (**b**) Reconstruction before background subtraction, also highlighting the area used for subtracting the uneven background similar to Sec. 3.2.7.

absorption image before the reconstruction process shows no contrast at all Fig. 3.27(b). In terms of quantitation of the absorption reconstruction we need to be careful, where the numbers most likely cannot be trusted since the values for βkt are expected to be on the order of 10^{-3} and; therefore, two orders of magnitude away from image values. The expected signal to noise ratio in the imaging process for the absorption part are approximately six orders of magnitude different from the phase shift, which is most likely the cause for the arbitrary values of the reconstruction we are seeing. But why is it then that we are getting such a good image for βkt? For the filtering reconstruction process βkt and δkt are two independent quantities (it is even explicitly assumed at specific points in the derivation). However, the true real and imaginary parts of the specimen contain information about both parts (*e. g.* see Eq. 3.43) and the reconstruction process might transfer power from one quantity to the other, but further investigations are required that are beyond the scope of this work.

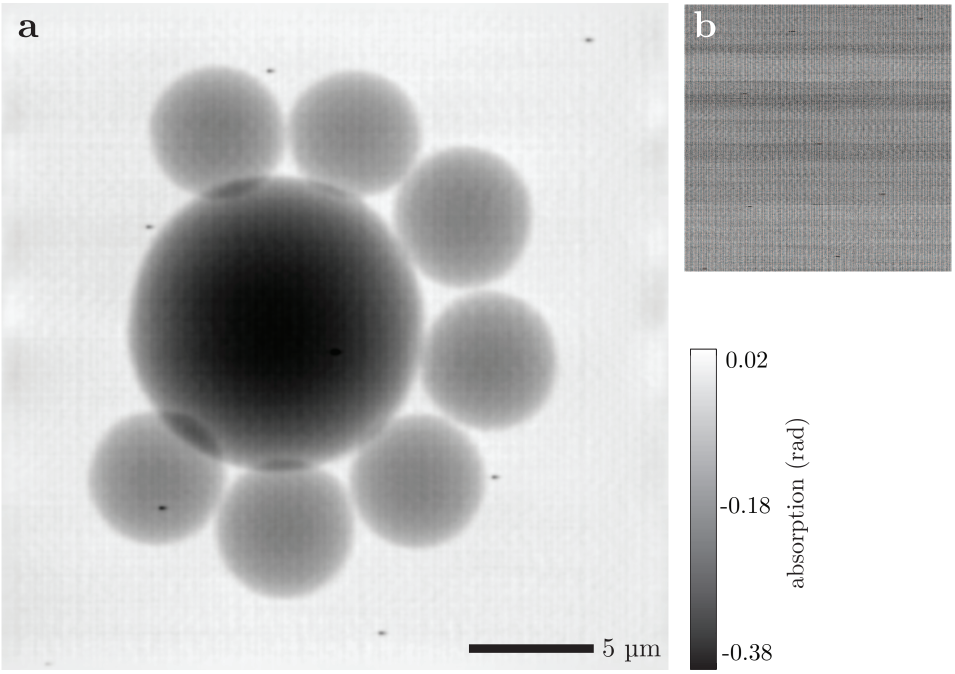

Figure 3.27: Filtering reconstruction of 5 μm and 10 μm sphere cluster. (**a**) Reconstructed absorption after subtraction of an uneven background. (**b**) Raw absorption image as sum of all detector segments; shows no visible contrast.

Interpretation of filtering reconstruction result

Through Eq. 3.51 we obtain the reconstruction result of the specimen h^{recon} for the filtering method. In order to obtain the absorption and phase shift terms βkt and δkt from h^{recon} it is suggestive to consider

$$\begin{aligned} \beta kt &= \ln\left(|h^{\text{recon}}|\right) \\ \delta kt &= \ln\left(\frac{h^{\text{recon}}}{|h^{\text{recon}}|}\right), \end{aligned} \tag{3.60}$$

as modulus and phase of the reconstruction. This is the way it has been done in the past [11]. However, our investigations show that this is likely not the correct interpretation. We propose to consider the reconstruction result as follows

$$\begin{aligned} \beta kt &\equiv \operatorname{Re}\left(h^{\text{recon}}\right) \\ \delta kt &\equiv \operatorname{Im}\left(h^{\text{recon}}\right), \end{aligned} \tag{3.61}$$

as the real and imaginary parts of the reconstruction h^{recon}. The reason for this lies in the nature of the derivation for the reconstruction method, which entails

1. a linearization and separation of h_r and h_i for the image formation process in terms of transfer functions through omission of second order terms (Sec. 3.3.1)

2. the assumption that h_r and h_i to be uncorrelated for the minimization of the RMS error metric (Sec. C.3.1) .

The reconstruction process does not put specific restraints on the form of h_r and h_i, as long as the specimen function can be written as $h = 1 + h_r + \mathrm{i}\, h_i$. Yet, the above bullet points suggest that the specimen for the filtering reconstruction process needs to be considered in the full weak specimen approximation of

$$h = \mathrm{e}^{-\beta kt + \mathrm{i}\delta kt} \approx 1 - \beta kt + \mathrm{i}\, \delta kt \equiv 1 + h_r^{\text{w}} + \mathrm{i}\, h_i^{\text{w}}, \tag{3.62}$$

which implies the interpretation of Eq. 3.61.

Confirmation of our considerations is given through Fig. 3.28, where phase shift images of the modulus and phase (Eq. 3.60) and real and imaginary part (Eq. 3.61) interpretations are shown. Most noticeable is the difference in the line profile through the large sphere in Fig. 3.28(c), where the phase shift obtained from the phase of h^{recon} does not agree well with the theoretical phase profile for the center part of the sphere. On the other hand the imaginary part

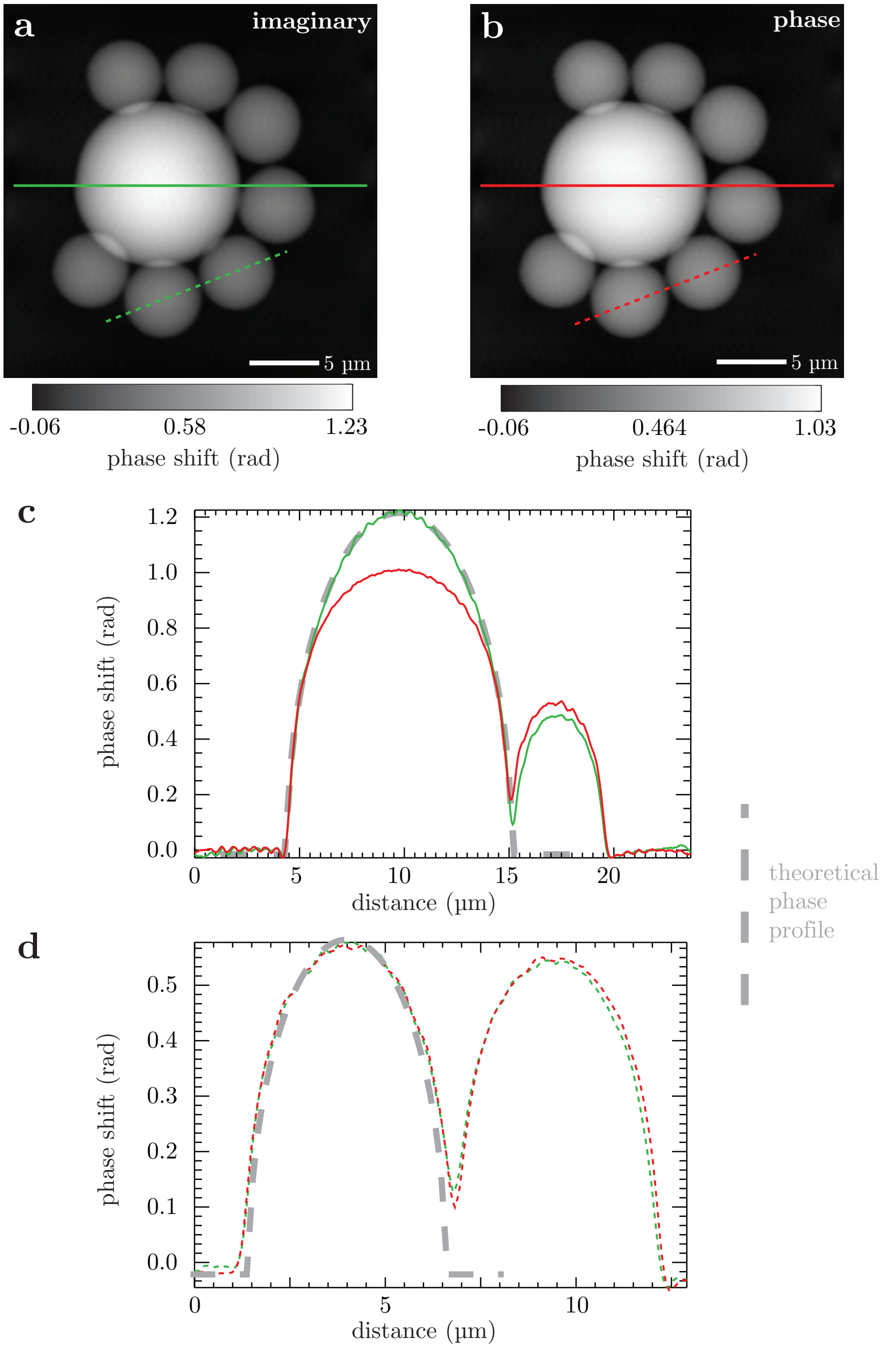

Figure 3.28: Phase shift reconstruction of sphere cluster as interpretated via (**a**) imaginary part of the reconstruction and (**b**) as the phase of the reconstruction. (**c, d**) Line profiles through the respective images as indicated by gree in (a) and red in (b). Theoretical phase shift profiles are indicated through wide dashed lines.

of h^{recon} is on good agreement with the expected phase shift profile. A line profile through two of the smaller spheres shown in Fig. 3.28(d) does not show drastic differences for both interpretations; in fact they agree with each other and the expected profile. This suggests that differences between both cases are most prominent for the very low spatial frequencies (large bulk structures), whereas for higher spatial frequencies differences will be less eminent.

Further evidence for our conclusion is given by Fig. 3.29, which shows the absorption βkt of the sphere cluster from the real and modulus interpretation.

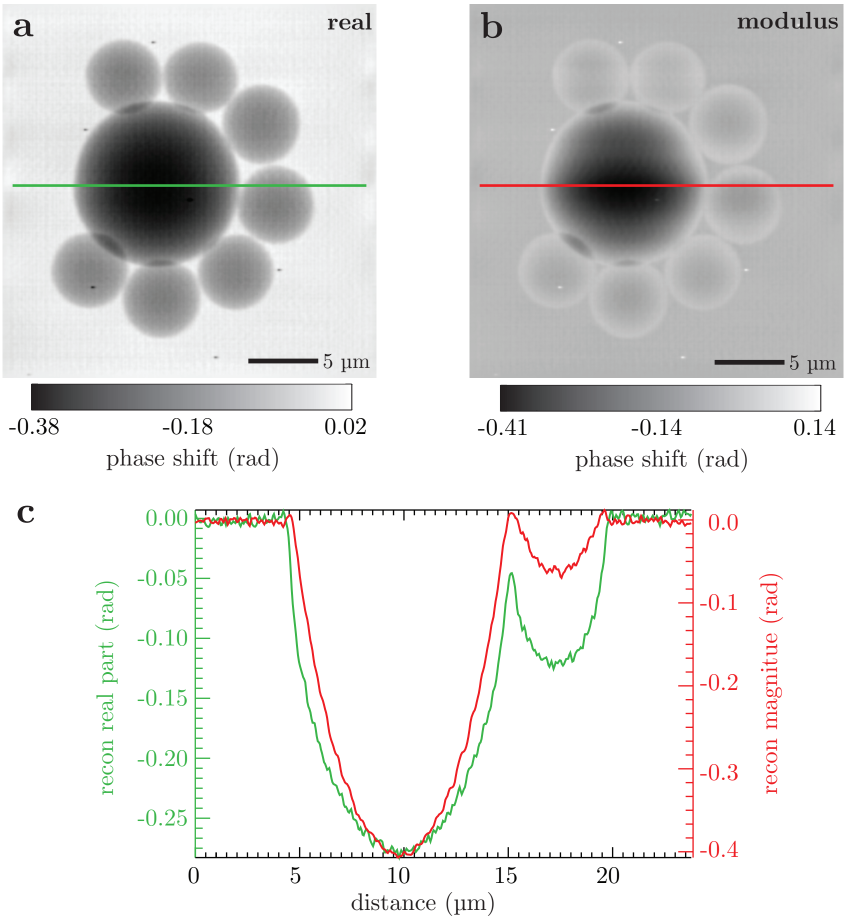

Figure 3.29: Absorption reconstruction of sphere cluster as interpretated via (**a**) real part of the reconstruction and (**b**) as the modulus of the reconstruction. (**c**) Line profiles through the respective images as indicated by green in (a) and red in (b).

It has been a common misconception so far that the filtering method does not perform well with the reconstruction of low spatial frequency objects, making it less practical for quantitative analysis. This believe was supported by observations of particularly large and thick objects not reconstructing as quantitatively as expected. However, we know now that the reason for this was an incorrect way of interpreting the reconstruction result, as demonstrated above.

3.3.5 Specimen and Weak Specimen Approximation

The objective of the filtering reconstruction has been to gain quantitative phase contrast information about the specimen. In the process of the derivation of the reconstruction method, as well as the interpretation of its results, assumptions about the specimen function were made in various ways. Here we would like to summarize these assumptions and briefly discuss their interconnection.

The specimen transmission function is defined as

$$h(\boldsymbol{r}) = \exp\left(-\beta(\boldsymbol{r})kt(\boldsymbol{r}) + \mathrm{i}\delta(\boldsymbol{r})kt(\boldsymbol{r})\right), \tag{3.63}$$

which without loss of generality can be written as

$$h(\boldsymbol{r}) = 1 + h_r(\boldsymbol{r}) + \mathrm{i}\, h_i(\boldsymbol{r})\,; \tag{3.64}$$

where in general h_r and h_i will contain information of both the specimens absorption and phase

$$\begin{aligned} h_r(\boldsymbol{r}) &= \mathrm{e}^{-\beta kt(\boldsymbol{r})}\cos(\delta kt(\boldsymbol{r})) - 1 \\ h_i(\boldsymbol{r}) &= \mathrm{e}^{-\beta kt(\boldsymbol{r})}\sin(\delta kt(\boldsymbol{r}))\,. \end{aligned} \tag{3.65}$$

Only in the form of the full weak specimen approximation the specimen information is entirely separated

$$h \approx 1 - \beta kt(\boldsymbol{r}) + \mathrm{i}\,\delta kt(\boldsymbol{r}) \equiv 1 + h_r^{\mathrm{w}}(\boldsymbol{r}) + \mathrm{i}\, h_i^{\mathrm{w}}(\boldsymbol{r})\,. \tag{3.66}$$

In the form of Eq. 3.64 the specimen is used in Sec. 3.3.1 to formulate the image formation in terms of transfer functions. During this process second order terms $\mathcal{O}({H_{r,i}}^2)$ are neglected in order to achieve the linearization and separation of H_r and H_i in the expression for the formed images of Eq. 3.40. These second order terms in essence can be viewed as the dark-field contributions of the imaging process, *i. e.* intensity that is scattered outside of the main far-field intensity annulus. Within the filtering reconstruction method, segments that are not covered by the main beam have vanishing transfer functions and successively do not contribute to the reconstruction. In the case where the specimen is strongly scattering, giving a non-negleigble signal outside the main beam (dark-field) the reconstruction method will not perform well as it does not know about this information. Hence, the dark-field signal can be used as an indicator for the validity of the filtering method. One should be aware that most biological specimen at hard x-ray energies do usually not show significant dark-field signals.

When minimizing the RMS error in Sec. C.3.1 to solve for the filter functions it is assumed that H_r and H_i are uncorrelated functions. This approximation inherently implies the weak specimen approximation of Eq. 3.66, since only in this form $h_{r,i}$ (therefore, $H_{r,i}$) are independent and uncorrelated.

When interpreting the reconstruction results from the filtering method in Sec. 3.3.4 it became evident that the real and imaginary parts of the reconstructed function h give the superior qualitative and quantitative reconstruction results. This is a result of the two assumptions about the specimen discussed in the previous two paragraphs and; furthermore, is supported by the image interpretation through transfer functions discussed in Sec. 3.3.2.

Weak specimen classification

In his work Landauer discusses a criterion for the classification of weak specimens [56, Ch. 3.2.2]. He defines a weak specimen in terms of the Fourier transform of its specimen function: a specimen is weak if

$$H(\boldsymbol{f}) = \Delta(\boldsymbol{f}) + H_{\mathrm{s}}(\boldsymbol{f}) \quad \text{where} \quad \int_{\boldsymbol{f}\neq\boldsymbol{0}} \mathrm{d}^2\boldsymbol{f}\, |H_{\mathrm{s}}(\boldsymbol{f})|^2 << 1\,. \tag{3.67}$$

This implies that the total energy that could be scattered by the specimen outside the central beam is much smaller than the central beam.

Hornberger [11, Ch. 4.1.7] disregards this criterion through the argument that Landauer's condition can always be fulfilled for any specimen by embedding it into a large transparent background and including this background in the reconstruction. His argument [62] is motivated that by embedding the specimen in a large background the "average" specimen function (in real space) becomes closer to 1, which means that its successive Fourier transform comes closer to a Delta-Function. The more transparent (data value 1) background is added in real space, the more power in Fourier space gets concentrated at $\boldsymbol{f}=\boldsymbol{0}$, hence increasing the ratio of scattered to un-scattered signal.

We tend to disagree with Hornberger's assessment that embedding a specimen into a larger background and taking it as part of the reconstruction will always fulfill Eq. 3.67. We believe the motivation for Landauer's reasoning stems from considering the total integrated specimen power

$$\begin{aligned}\int \mathrm{d}^2\boldsymbol{f}\,|H(\boldsymbol{f})|^2 &= \int_{\boldsymbol{f}=\boldsymbol{0}} \mathrm{d}^2\boldsymbol{f}\,|H(\boldsymbol{f})|^2 + \int_{\boldsymbol{f}\neq\boldsymbol{0}} \mathrm{d}^2\boldsymbol{f}\,|H(\boldsymbol{f})|^2 \\ &= \int_{\boldsymbol{f}=\boldsymbol{0}} \mathrm{d}^2\boldsymbol{f}\,|\Delta(\boldsymbol{f})|^2 + \int_{\boldsymbol{f}\neq\boldsymbol{0}} \mathrm{d}^2\boldsymbol{f}\,|H_\mathrm{s}(\boldsymbol{f})|^2 \\ &= 1 + \int_{\boldsymbol{f}\neq\boldsymbol{0}} \mathrm{d}^2\boldsymbol{f}\,|H_\mathrm{s}(\boldsymbol{f})|^2\,,\end{aligned} \tag{3.68}$$

where in the last step we used a defining relation of the Δ-function (see Appendix A.3). A transparent background will not add to the scattered signal and; therefore, also not increase the contribution to the second term in the last line of Eq. 3.68. Hence we believe Landauer's criterion for a weak specimen of Eq. 3.67 to be a valid one.

3.4 Comparison of Integration and Filtering Method

With the integration method of Sec. 3.2 and the filtering method of Sec. 3.3, we have presented two in their nature very different ways of quantitatively reconstructing the specimen phase shift from scanned imaging. We now will consider how both methods compare with one another. An obvious way of doing so will be to directly reconstruct data and do a comparison based on the reconstructed results, as will be done in Sec. 3.4.2. However, before directly contrasting both approaches, we will start by introducing a novel formulation of the integration method in terms of filter functions in Sec. 3.4.1. This will help us in the interpretation of the imaging results and gain a more fundamental understanding of both approaches. Note, that a truly quantitative comparison of both methods is only possible in the quadrant detection scheme, since only then are the differential phase contrast images quantifiable to yield phase gradient images.

3.4.1 Filter Functions for Integration Method

The reconstruction of the specimen function h by the Fourier filtering method is (see Eq. 3.51)

$$h(\boldsymbol{r}) = \mathcal{F}^{-1}\{\widehat{H}(\boldsymbol{f})\} = \mathcal{F}^{-1}\Big\{\sum_k W_k(\boldsymbol{f})\,S_k(\boldsymbol{f})\Big\}\,, \tag{3.69}$$

where the signal of all segments S_k are combined in an ideal way through weighting or filter functions W_k. The phase shift of the reconstructed specimen is best represented by the imaginary part and the absorption by the real part of the reconstructed function h (see Sec. 3.3.4).

The integration method on the other hand resembles an orthogonal integration of gradient images $\partial_{x,y}\phi$ and reconstructs the specimen phase shift ϕ by (see Eq. 3.28)

$$\phi(x,y) = \mathcal{F}^{-1}_{x,y}\left\{ \frac{\mathcal{F}_{f_x,f_y}\{\partial_x\phi(x,y) + \mathrm{i}\partial_y\phi(x,y)\}}{2\pi\mathrm{i}(f_x + \mathrm{i}f_y)} \right\}, \tag{3.70}$$

where a quadrant detection scheme is required to obtained quantitative phase gradient images (see Sec. 3.2.1) from differential phase contrast (DPC) data (see Sec. 3.1.2).

Both reconstruction approaches are very different in their nature. However, through realizing the fundamentals of the integration method it is possible to derive a filter function expression for Eq. 3.70 and, therefore, enable a comparison between both methods on an analytical basis. In order to derive the integration filter functions we will start by considering the defining relation of the gradient images $\partial_{x,y}\phi$, which are given through the DPC definition of Eq. 3.8 in connection with the quantitation of Eq. 3.23 as

$$\begin{aligned} \partial_x\phi &= \mathcal{C}\,\frac{(s_2 + s_3) - (s_1 + s_4)}{s_t} \qquad (3.71)\\ \partial_y\phi &= \mathcal{C}\,\frac{(s_1 + s_2) - (s_3 + s_4)}{s_t}, \qquad (3.72) \end{aligned}$$

where s_k is the real space signal of the segments in a quadrant arrangement, s_t is the total intensity (*i. e.* absorption) and $\mathcal{C}$ is the constant resulting from the quantitation. Through Fourier transformation of Eq. 3.70 and insertion of the expressions from Eq. 3.72 we arrive at

$$\begin{aligned} \Phi(\mathbf{f}) = {} & \frac{\mathcal{C}}{2\pi\mathrm{i}(f_x + \mathrm{i}f_y)} \times \\ & \times \left[(-1+\mathrm{i})\mathcal{F}\left\{\frac{s_1}{s_t}\right\} + (1+\mathrm{i})\mathcal{F}\left\{\frac{s_2}{s_t}\right\} + (1-\mathrm{i})\mathcal{F}\left\{\frac{s_3}{s_t}\right\} + (-1-\mathrm{i})\mathcal{F}\left\{\frac{s_4}{s_t}\right\} \right]. \end{aligned} \tag{3.73}$$

In the case of weakly absorbing samples the total intensity, which is true for a large class of specimens in the hard x-ray range, s_t will be negligible and can be left out. At this point we have arrived at a filter function formulation of the integration method. Recalling $\mathcal{F}\{s_k\} \equiv S_k$ we have arrived at a formulation of the integration method in terms of filter functions (compare Eq. 3.69):

$$\phi(\boldsymbol{r}) = \mathcal{F}^{-1}\{\Phi(\boldsymbol{f})\} = \mathcal{F}^{-1}\left\{\sum_k W_k^{\text{int}}(\boldsymbol{f})\, S_k(\boldsymbol{f})\right\}, \tag{3.74}$$

with filter functions,

$$W_1^{\text{int}}(\boldsymbol{f}) = \frac{\mathcal{C}(-1+\mathrm{i})}{2\pi\mathrm{i}(f_x+\mathrm{i}f_y)} \qquad W_2^{\text{int}}(\boldsymbol{f}) = \frac{\mathcal{C}(1+\mathrm{i})}{2\pi\mathrm{i}(f_x+\mathrm{i}f_y)} \tag{3.75}$$

$$W_3^{\text{int}}(\boldsymbol{f}) = \frac{\mathcal{C}(1-\mathrm{i})}{2\pi\mathrm{i}(f_x+\mathrm{i}f_y)} \qquad W_4^{\text{int}}(\boldsymbol{f}) = \frac{\mathcal{C}(-1-\mathrm{i})}{2\pi\mathrm{i}(f_x+\mathrm{i}f_y)}\,. \tag{3.76}$$

With this result we have brought the integration and filtering method onto equal footing. Note, that the integration filter functions are generally applicable once the optical setup is determined (*e. g.* size of illumination on detector required for quantitation of $\mathcal{C}$); as they do not contain any other experimentally varying quantities regarding noise like the Fourier filter functions do. Furthermore, the integration filters do not include any information on the imaging properties of the optical setup.

We will exemplify the integration filters in the next section by means of a specific example and directly compare and contrast them to the functions of the filtering method.

3.4.2 Comparison Through Simulated Data

In the following we will compare the integration and filtering reconstruction methods through simulated data.

Imaging simulations make it possible to explore a large variety of different imaging situations in a controlled manner, which are often difficult to achieve under experimental circumstances. The expression of wave field in the far-field detector plane for scanning microscopes of Eq. 2.23 posses the means to conveniently simulate arbitrary specimens and imaging situations. The imaging conditions for the simulation are chosen to resemble a typical scanning hard x-ray microscope setup: x-ray energy 10 keV, scanning step size 50 nm, zone plate diameter 160 μm, outermost zone width $\mathrm{d}r_N$ 100 nm, central stop 40 μm and detector arrangement as shown in Fig. 3.30. The phase shift map of the simulated specimen is shown in Fig. 3.31, where the lines in the image indicate the positions of line profiles for the subsequent analysis. The specimen phase shifts correspond the polystyrene imaged at 10 keV. The spheres shown in the images are of 10, 5, 2, 1 and 0.5 μm diameters corresponding to phase

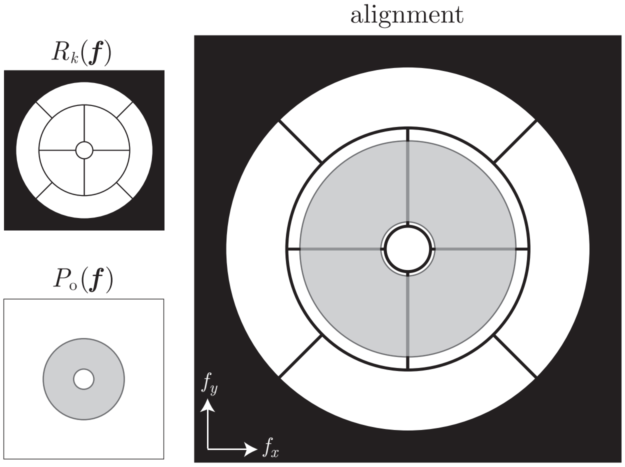

Figure 3.30: Detector configuration, far-field illumination and their respective alignment for the simulation. The diameter of the far-field illumination on the detector is 90% of the inner quadrant diameter. The alignment effectively represents a quadrant detection scheme.

shifts of 1.19, 0.595, 0.238, 0.119 and 0.06 rad respectively. The linear and radial chirped grating in the upper left corner of Fig. 3.31 are of a thickness of 5 μm or 0.595 rad. The linear chirped gratings in the upper right corner correspond to 5 μm thickness or 0.595 rad and 50%, 20%, 10% and 1% thereof. The specimen was simulated with 10^5 photons per second per scan position and Poisson statistic noise.

Reconstruction results of the integration and filtering methods are given in Fig. 3.32 and will be discussed in detail for the remainder of the present section.

Filter functions and RPSD comparison

Let us start the comparison of the two methods by considering the filter functions used to obtain the reconstructions. In Fig. 3.33 we show the filter functions for the lower right quadrant segment of the detector (see Fig. 3.30). Both filter are of similar shape and have a dipolar structure along the −45° direction. Note that the Fourier filter shows additional arch-shaped structures in the high spatial frequency range, which are not present in the integration filters. In the low spatial frequency range towards the center of the arrays both filters show similar behavior, albeit that their detailed form is not exactly the same the quantitative filter values agree match each other with slightly higher values for the integration. This observation already poses a remarkable re-

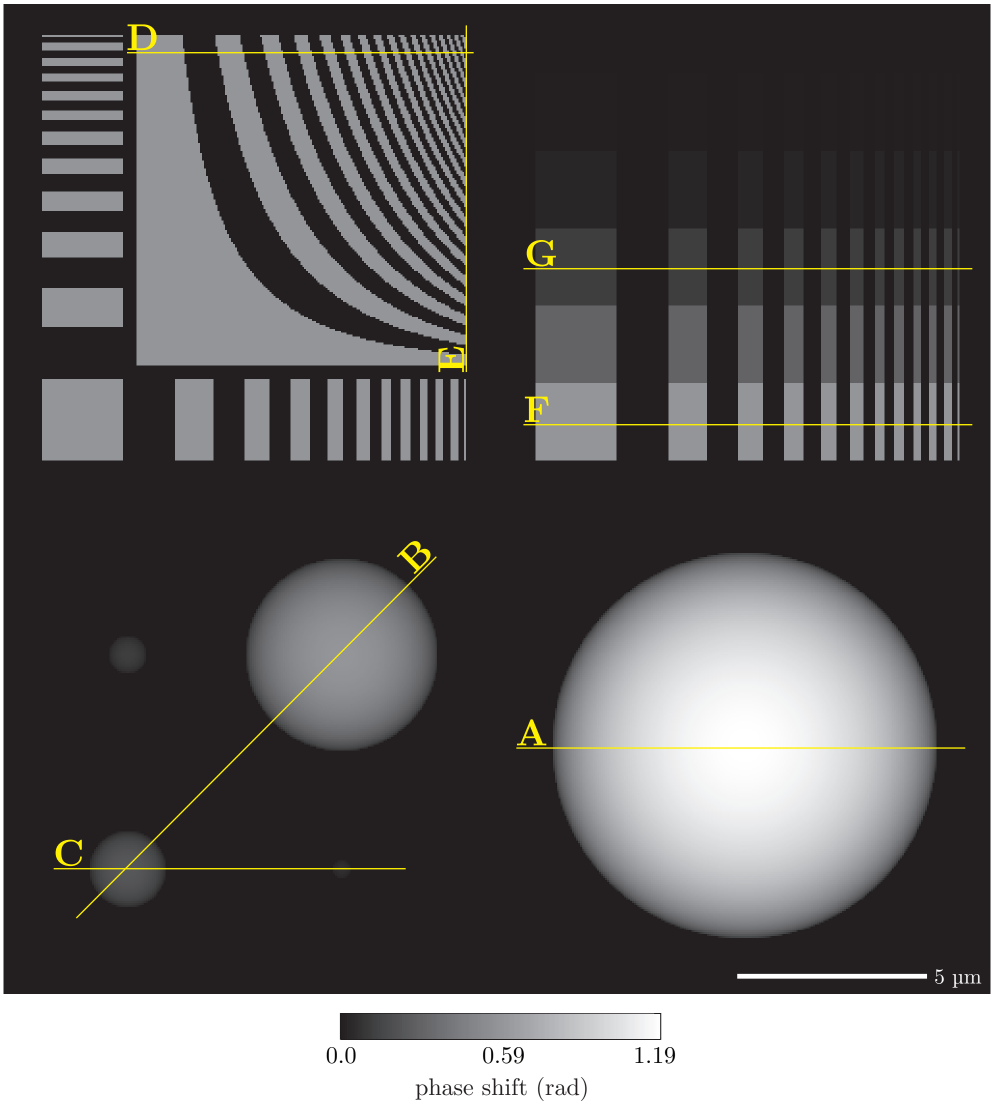

Figure 3.31: Phase map if the simulated specimen. The yellow lines indicate the positions of line profiles taken through the reconstructions for analysis purposes (see Fig. 3.32 through Fig. 3.40). Thicknesses of structures given in the following correspond to polystyrene at 10 keV x-ray energy. Structures in radians (thickness); spheres: 1.19, 0.595, 0.238, 0.119 and 0.06 rad (10, 5, 2, 1 and 0.5 μm); linear and radial chirp in upper left: 0.595 rad (5 μm); linear chirp in upper right: 0.595 rad (5 μm) and 50%, 20%, 10% and 1% thereof.

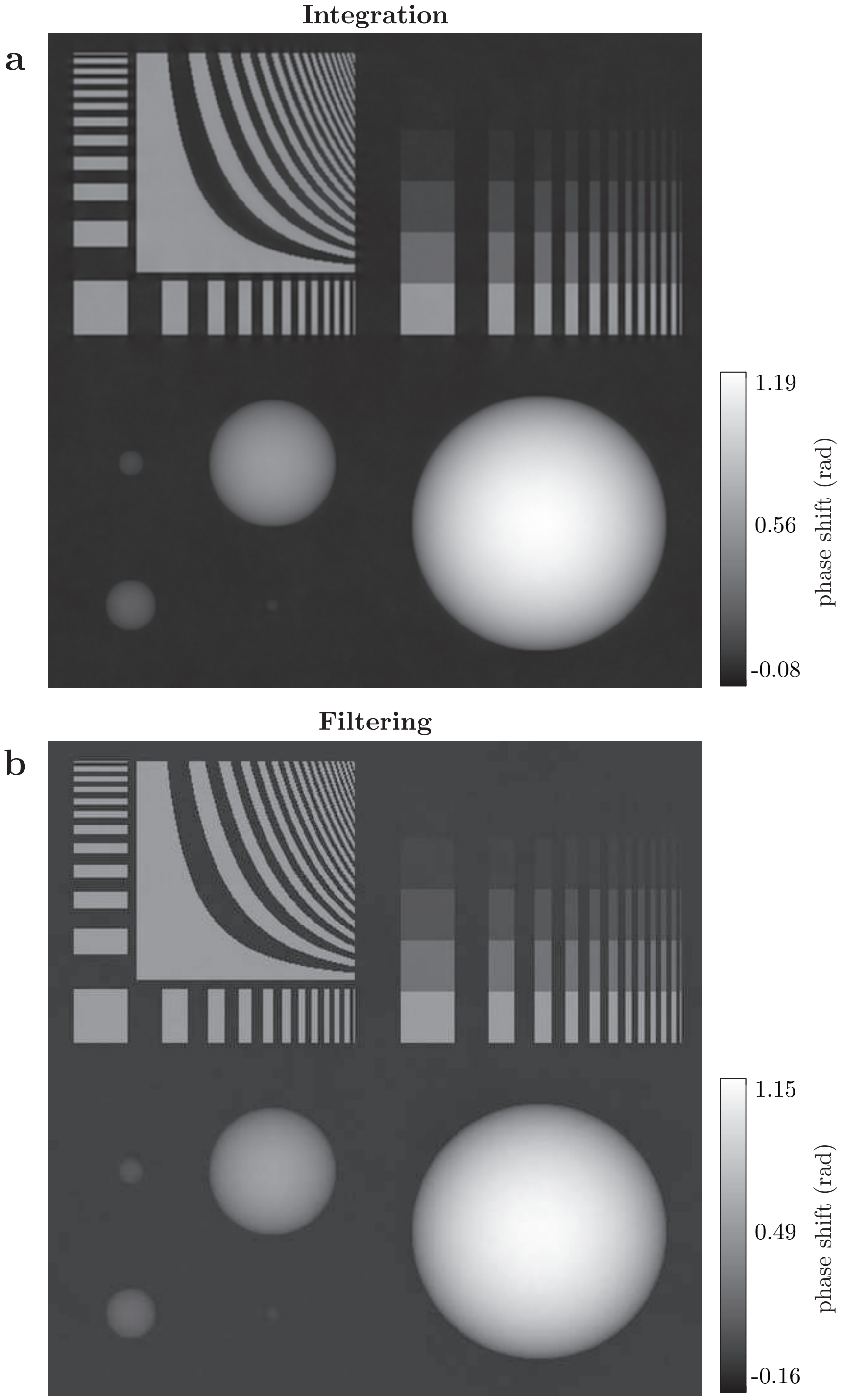

Figure 3.32: (**a**) Integration and (**b**) filtering reconstruction from simulation of the specimen given in Fig. 3.31.

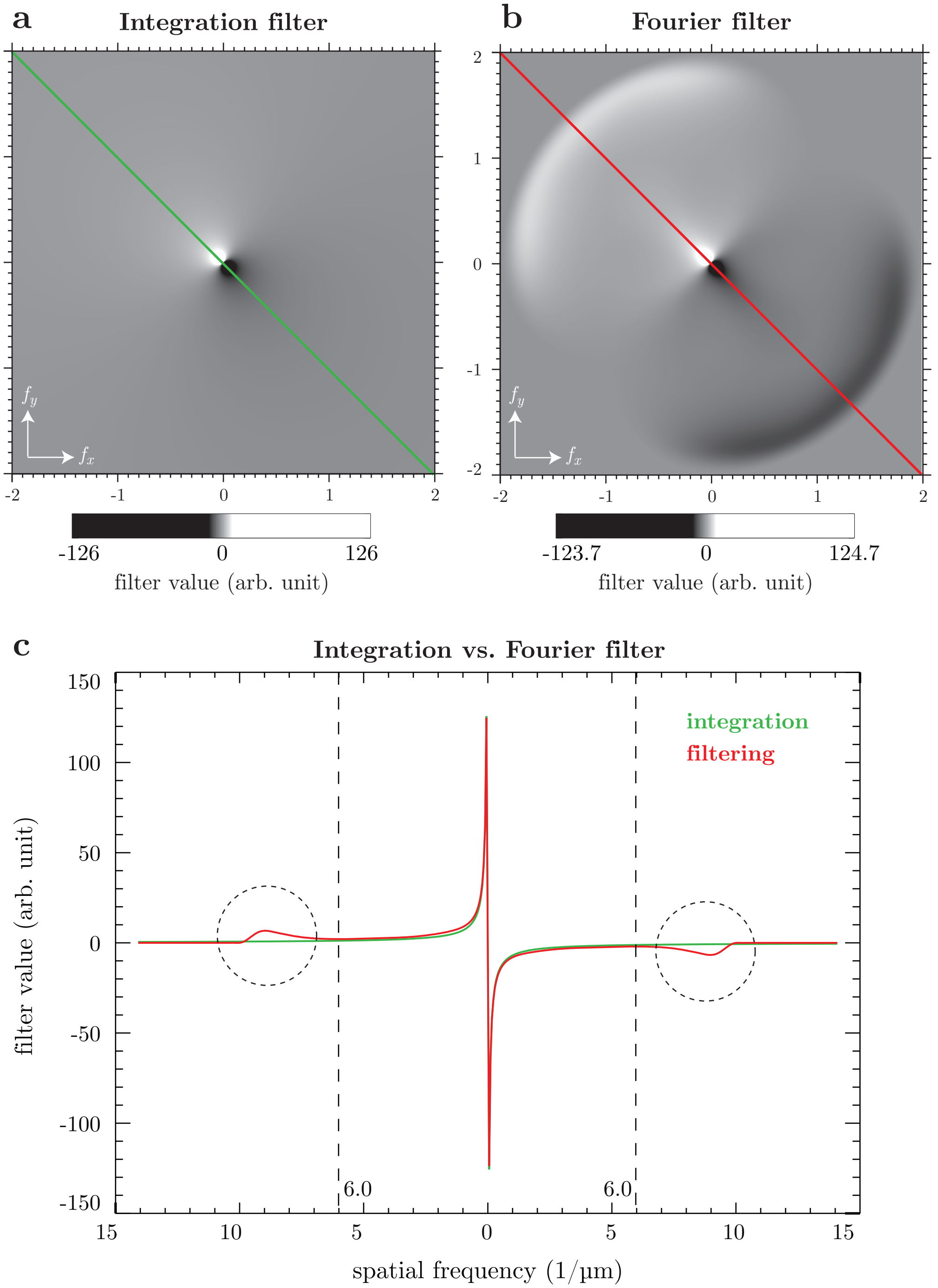

Figure 3.33: Filter functions of the reconstructions used to obtain images in Fig. 3.32 for one of the quadrant detector segments ($k = 3$). (**a**) Integration filter computed via Eq. 3.76 and (**b**) Fourier filter function; both are scaled to ±10 to highlight the shape. (**c**) Line profile through the filter functions of (a) in green and (b) in red.

sult. It so far has been believed that because of the vanishing values of the contrast transfer functions for small $\boldsymbol{f}$, the filtering method's reconstruction results should be poor for the low spatial frequencies (large and thick bulk structures); giving the integration method an advantage. At least as far as the filter functions are concerned, this is not the case. In the line profile shown in Fig. 3.33(c) we can see that both filters match up in the low frequency range.

For the high frequencies the Fourier filter has an additional "bump" (indicated by circles), which is a characteristic feature that is due to the noise treatment in the filtering method. In incoherent imaging, as it is the case here, the microscopes contrast transfer response is not uniform across the spatial frequency space, similar to what we have already seen through the transfer functions (Sec. 3.3.2). This means that the presence of noise will effect the spatial frequencies differently depending on their respective transfer strength compared to the noise level. The highest spatial frequencies are usually influenced most negatively through the noise. Since the Fourier filter is based on a Wiener filtering type approach, it corrects the noise dominated high spatial frequencies appropriately. This is a key difference to the integration method, where no noise or imaging transfer treatment is included whatsoever and the line profile of Fig. 3.33(c) supports this assessment. Therefore, it is to be expected that the filtering method will show better performance for high spatial frequency structures. Please note that by considering the shape of the filter functions we can gain insight into the behavior of the two different reconstruction methods, but we cannot understand the entire imaging process based on this.

Further understanding can be obtained by considering the radial power spectrum density (RPSD) of the input specimen and the reconstruction results as shown in Fig. 3.34. As predicted by the filter functions considerations above the integration and filtering method agree well with each other in the low spatial frequency range; and also with the specimen. At around $6\,(\mu\mathrm{m})^{-1}$ the two RPSDs start to drift apart, with the reconstructed power from the integration method strongly decreasing, while the filtering method continues to follow the expected values from the specimen up to approximately $9.5\,(\mu\mathrm{m})^{-1}$. The start of the divergence of both cases at around $6\,(\mu\mathrm{m})^{-1}$ coincides with the spatial frequency in Fig. 3.33(c) where the high frequency correction "bump" of the Fourier filter starts to pick up compared to the integration filter. An arrow points at the region of largest disagreement of integration and filtering. This substantiates the suspected behavior of the filtering method outperforming the integration for the fine features further.

Let us now have a closer look at the actual reconstructed images of Fig. 3.32 through the line profiles indicated in the simulated specimen of Fig. 3.31.

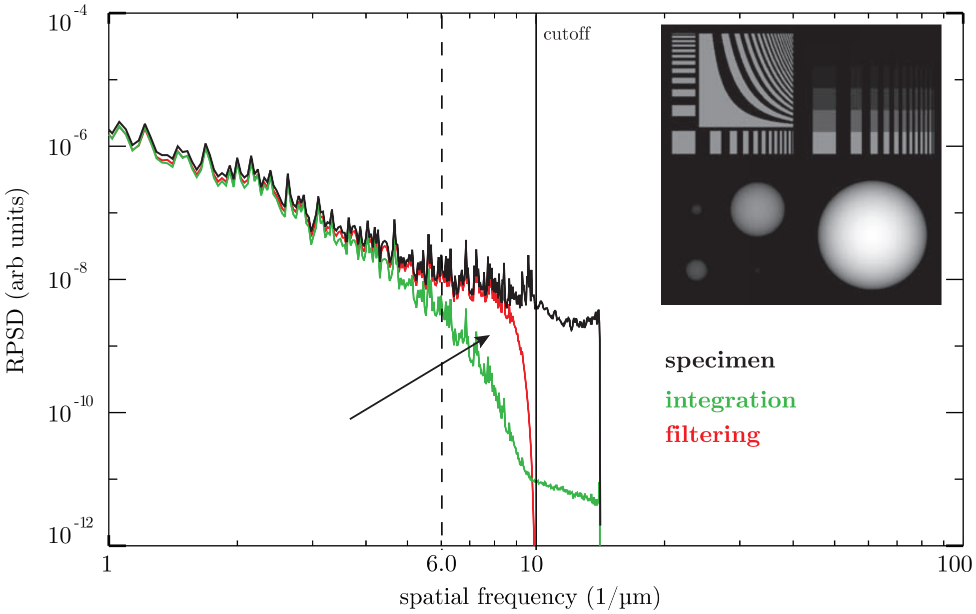

Figure 3.34: Radial power spectrum densities (RPSD) of the simulated specimen, the integration and filtering reconstruction. The spatial frequency cutoff of the imaging process is indicated at $10\,(\mu\text{m})^{-1}$. The vertical line at $6\,(\mu\text{m})^{-1}$ indicates where the integration an filtering method start to divide.

Line profiles through reconstructions

Figure 3.35 shows a profile through the large 10 μm diameter sphere. The integration reconstruction is in excellent agreement with the theoretical specimen value. The filtering method shows a lower reconstructed phase shift in the region of the thickest part of the sphere with a value of 1.15 rad where 1.19 rad would be expected, which is a 3% difference to the ideal. From the previous considerations we would have expected the two methods to agree better for such a low frequency object. What are the potential reasons for the disagreement? First, a mere consideration of an imaging process in therms of spatial frequency behavior cannot entirely describe the image results. Furthermore, one should not that the filter functions of the integration method shown in Fig. 3.33 have slightly higher maximal values than the Fourier filter. The most severe reason is the fact that we are dealing with a quadrant detection scheme (as is required for the integration method to be quantitative). We have seen in Sec. 3.17 that the total imaginary contrast transfer function exhibits a large area of low transfer in the vicinity of the zero spatial frequency. This low transfer information prevents the filtering method from properly reconstructing the lowest spatial frequencies. In the case of a more advantageous illumination alignment in terms of spectral transfer function coverage, we have seen in Sec. 3.3.4 that the filtering method retrieved the proper phase profile for a 10 μm sphere from experimental data! Furthermore, simulations show that when the illumination alignment is changed to a scheme covering more than only the quadrant segments, the retrieved phase shifts for the large sphere come closer to the theoretically expected. Simulation with an alignment equal

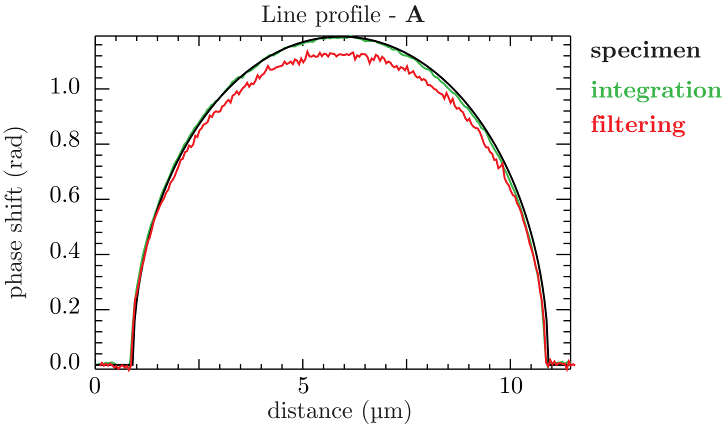

Figure 3.35: Line profile **A** through the specimen as indicated in Fig. 3.31 and the respective integration and filtering reconstruction images of Fig. 3.32.

to the case of the experimental sphere data reconstructed the phase of the sphere to 1.18 rad.

The line profile shown in Fig.3.36 is taken through the 2 μm and 5 μm spheres of the specimen. Both reconstructions are in agreement with the theoretically expected phase shift in terms of shape and quantitation. Similar observations can be made for the line profile of Fig. 3.37 through the 2 μm and 0.5 μm spheres. A general observation is that the filtering methods tends to be more noisy in the background region and also across the features, which is a hint that the performed noise analysis to obtain the Fourier filter functions is not optimal.

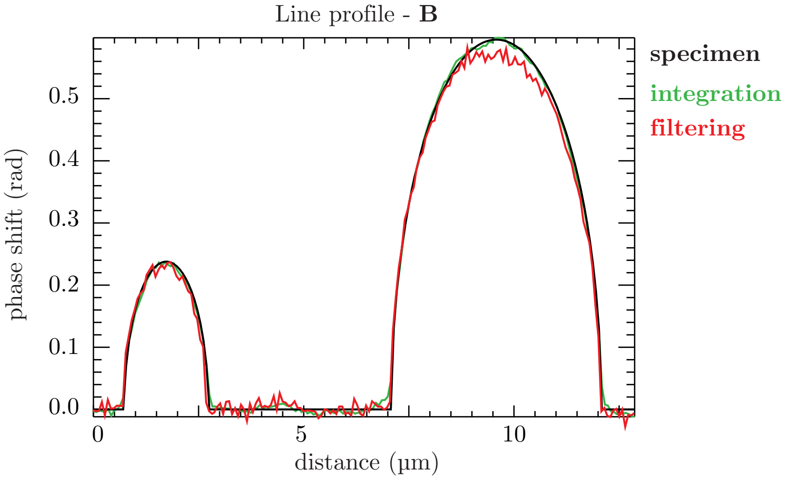

Figure 3.36: Line profile **B** through the specimen as indicated in Fig. 3.31 and the respective integration and filtering reconstruction images of Fig. 3.32.

After having considered exclusively low frequency objects we will turn our attention now to the chirped grating in the upper half of the specimen. The profile through parts of the radially chirped grating of Fig. 3.38 identify the better high frequency performance of the filtering method. The gray lines in the image represent the envelope of the fine features reconstructed by the integration method, which clearly decrease as the frequency of the grating increases, while at the same time the filtering reconstruction remains at a constant level. The lower frequency features in the profile (wide grating bars) show again the integration performing better. In the middle of the widest bar (pointed out be the arrow) we can see a fall-off of the reconstructed phase shift; as the structure of the specimen is constant in this region over an extended spatial range, no phase gradient is present, hence eliminating the phase sensitivity of the method. This effect becomes more severe the more extend a

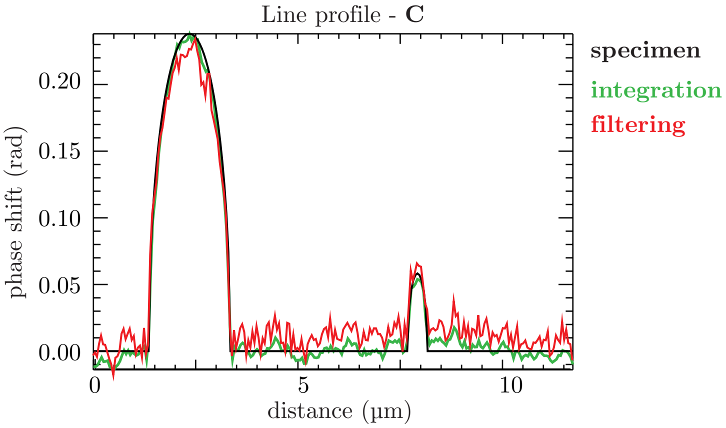

Figure 3.37: Line profile **C** through the specimen as indicated in Fig. 3.31 and the respective integration and filtering reconstruction images of Fig. 3.32.

region of constant phase shift is. In Fig. 3.39 we show the extreme case of the reconstruction of high spatial frequency content. The line profile is taken right at the edge of the radially chirped grating in the vertical direction, where the theoretical phase gradient approaches infinity, *i. e.* step function. The integration method's reconstruction result agrees with the specimen in terms of the shape of the grating; however, its quantitative values is suppressed uniformly by 20% along the line profile. The filtering method seems to have no problem retrieving the grating qualitatively and quantitatively.

We conclude this discussion by considering two of the horizontally chirped gratings of the specimen's upper right part through Fig. 3.40. Shown are the grating with 0.595 rad phase shift in (a) and 0.119 rad in (b). Both reconstruction results are in good agreement with the specimen, showing no difference in terms of total phase shift sensitivity; in fact both method are almost identical for the 0.119 rad grating including a tendency to show increased negative reconstruction values for the no-specimen region in between grating bars.

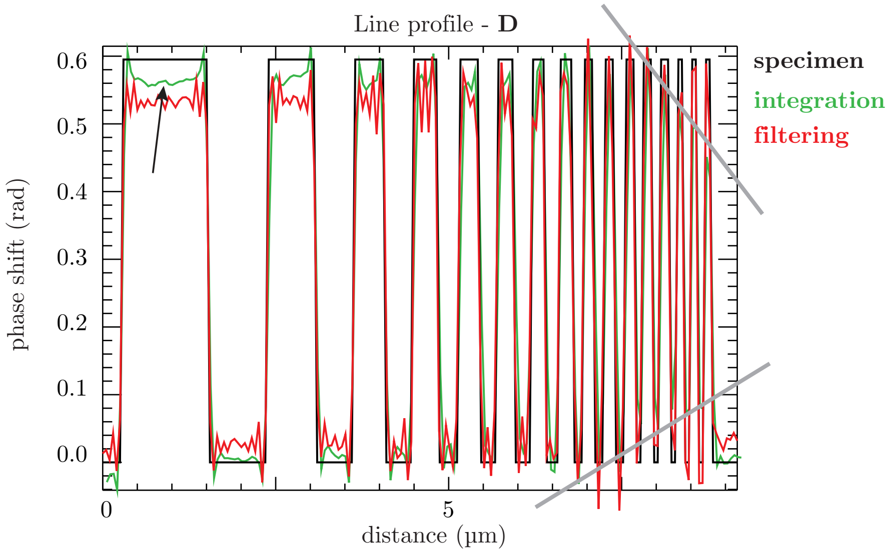

Figure 3.38: Line profile **D** through the specimen as indicated in Fig. 3.31 and the respective integration and filtering reconstruction images of Fig. 3.32. Gray lines indicate the envelope of the declining integration reconstruction values.

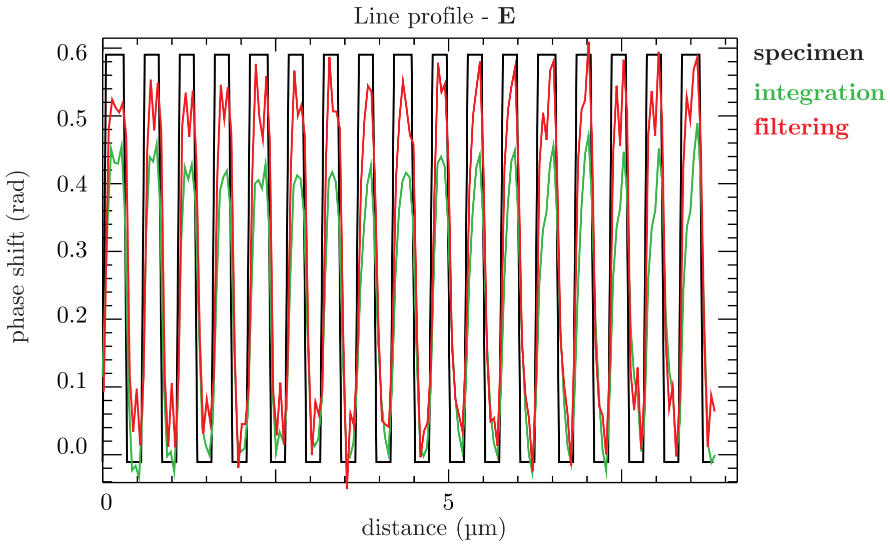

Figure 3.39: Line profile **E** through the specimen as indicated in Fig. 3.31 and the respective integration and filtering reconstruction images of Fig. 3.32.

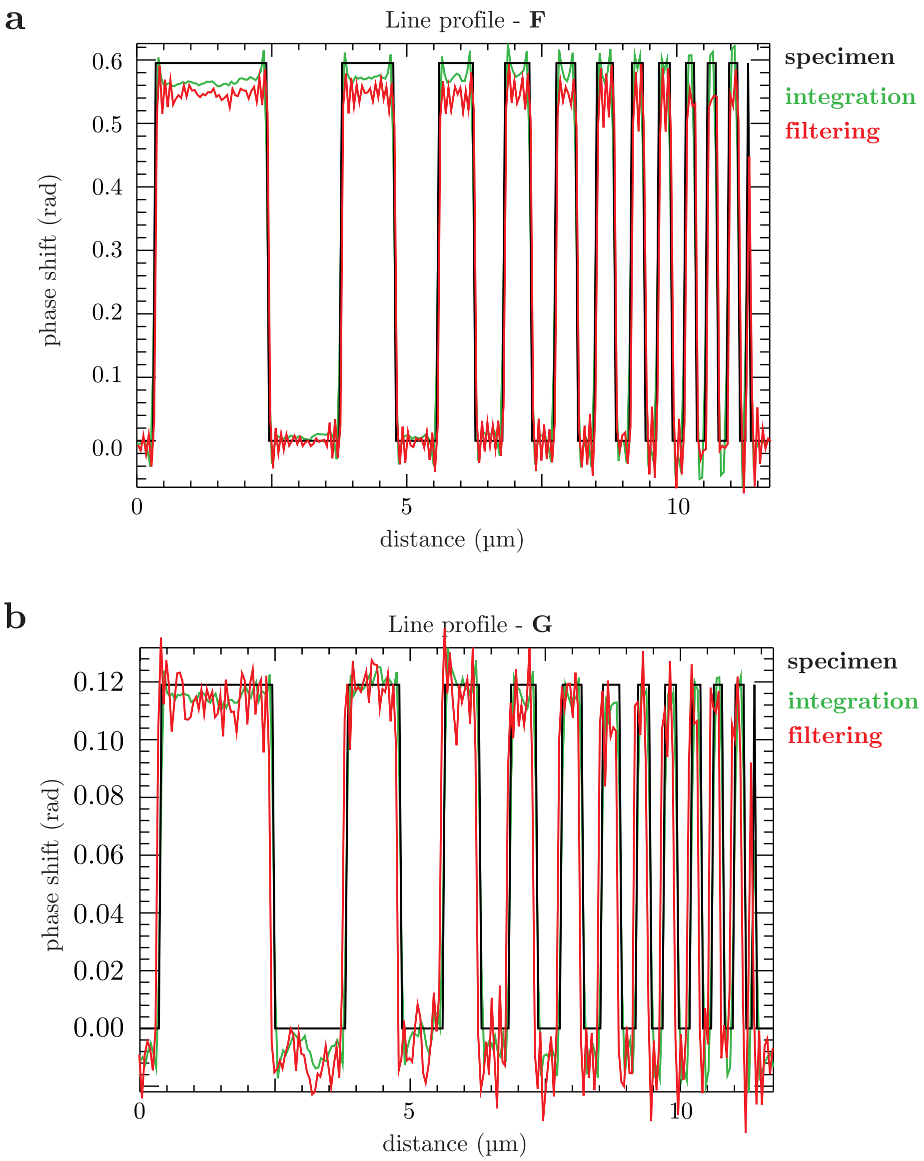

Figure 3.40: Line profile (**a**) **F** and (**b**) **G** through the specimen as indicated in Fig. 3.31 and the respective integration and filtering reconstruction images of Fig. 3.32.

3.5 Application of Quantitative Phase Contrast in X-ray Fluorescence Microscopy

The reconstruction methods described in Sec. 3.2 and Sec. 3.3 enable one to obtain truly quantitative phase contrast images, beyond the qualitative nature of differential phase contrast. In addition to this, the quantitative phase images can have an extremely useful application in scanning x-ray fluorescence (XRF) microscopy, as will be shown in the following.

3.5.1 XRF Microscopy and Its Weaknesses

The principle of x-ray fluorescence is laid out in Sec. 1.2.4 and the concept of a scanning x-ray fluorescence microscope is discussed in Sec. 1.3.2. The sample is scanned through focal spot of a focussing optic and for each scan point the emitted XRF signal is collected with an energy dispersive detector of the side from the optical axis. In order to excite a large range of elements, XRF microscopy commonly operates at hard x-ray energies. Typical for material science applications are energies up to 50, while for biological samples energies usually range from 5 to 15 keV. XRF microscopy is an excellent tool for mapping and quantification of elements down to trace amounts with sensitivity better than several thousand atoms [63] with many applications in the biological and medical sciences [64, 65].

However, there are some drawbacks of the technique. Bulk biological material that constitutes the main biological structure of the specimen almost exclusively contains light elements (H, C, N, O), which as we have seen in Sec. 1.2.4 have a low fluorescence yield and; therefore, are extremely difficult to image in fluorescence. Hence XRF microscopy does not yield images of the biological ultrastructure of specimen and, so it is not possible to contextualize the measured (trace) element content from the heavier elements with the structural information from the lighter elements. Furthermore, at the required x-ray energies to image in fluorescence the biological structure shows little to no absorption contrast. Since the transmission signal in XRF microprobes is not used it makes it an ideal candidate for combination with scanning transmission x-ray microscopy and the discussed phase contrast methods of the present chapter. We have already implemented and demonstrated the application of differential phase contrast (DPC)in XRF microscopes, where it is useful for sample localization and to put the measured elemental content into the context of the biological structure [1]; so addressing one of the drawbacks of XRF microscopy.

Through the help of standards the measured elemental signal of two dimensional XRF images can be quantified to yield maps of elemental content in terms of element mass per area. However, biological processes are driven by concentrations (mass per volume) and not absolute amounts (as mass per area). Here we propose to utilize the quantitative reconstructed phase contrast images to provide the required projected thickness information to properly normalize the element content images in order to obtain element concentration images [6]. Of course, the reconstructed phase contrast images also contribute to a better visualization of the biological structure and pose an improved way of contextualizing the elemental content compared to the qualitative and directionally dependent DPC. We the following we will briefly discuss an example of the proposed method; first in Sec. 3.5.2 the thickness images of a biological sample is derived and then applied to XRF data in Sec. 3.5.3 to retrieve elemental concentration images from two dimensional data.

3.5.2 Specimen Thickness Map

As we have seen in Sec. 3.2.4 that in principal it is possible to translate reconstructed images of the specimen phase shift into thickness images (*e. g.* see Fig. 3.12 and Eq. 3.29), given that the material and hence its δ is known.

In Fig.3.41 we shown the reconstructed phase images of a fixed and dried freshwater algae cell of the type *Cryptomonas* images at 10 keV x-ray energy and reconstructed through the filtering method, where the detector alignment was the same as shown in Fig. 3.23. In order to translate this phase shift images into a thickness map we need to know the materials real part of the index of refraction δ to properly divide it out. For this we consider the fact that biological specimen in general almost exclusively consist of protein, lipids, nucleosomes, etc., all having phase shifts similar enough at hard x-ray energies to not be distinguishable to first order at the abundance given in biological cells. Hence we can safely assume to first order that biological samples consists exclusively of protein with a given standard elemental distribution 48.6% H, 32.9% C, 8.9% N, 8.9% O and 0.6% S. at a density of $1.35\,\mathrm{g/(cm)^3}$. Together with Henke data [14] the value at 10 keV will be $\delta = 2.99\,10^{-6}$. With this we can calibrate Fig.3.41 to a thickness map of protein (see right scale bar in figure). The negative thickness values are a result of falsely reconstructed background values in the image and do not appear on the cell inside.

3.5.3 Elemental Concentration Reconstruction

We are now in the position to use the reconstructed thickness map of Fig. 3.41 for elemental concentration reconstruction, simply by dividing measured and standard calibrated XRF data and divide by the protein thickness. Figure 3.42

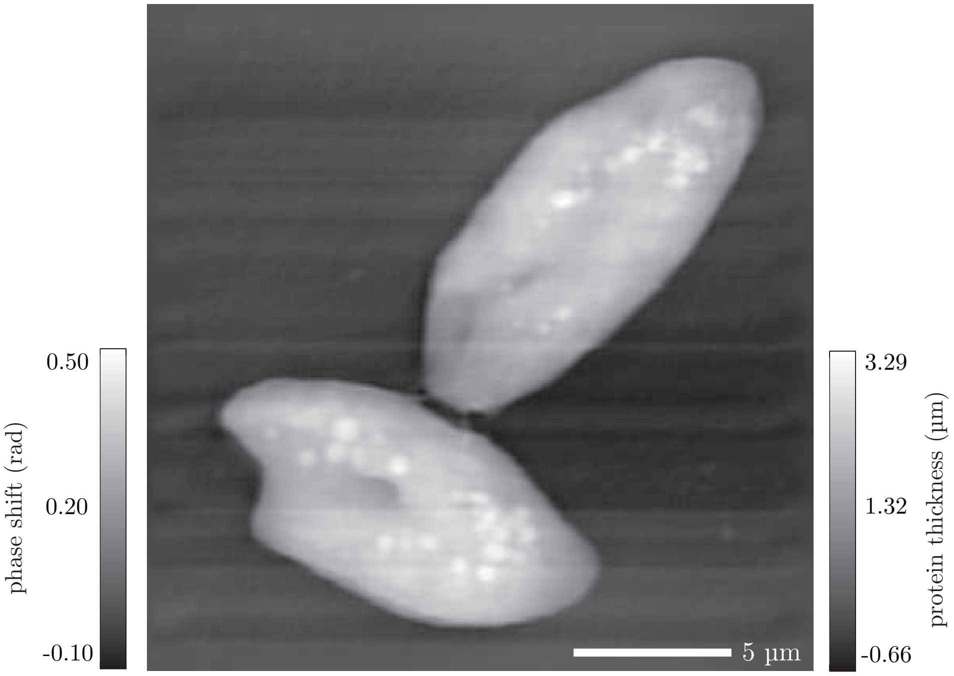

Figure 3.41: Reconstructed phase shift of a fixed and dried freshwater flagellate cell type *Cryptomonas*; calibration to thickness via the assumption that the biological material consists of protein in the decomposition 48.6% H, 32.9% C, 8.9% N, 8.9% O and 0.6% S. Experimental details: 10 keV, steps 50 nm, ZP 160 μm, dr_N 100 nm, stop 40 μm, detector arrangement as shown in Fig. 3.23.

shows elemental content and concentration images of the selected elements Cu, P and S. The left column in the figure displays the usually measured XRF images in terms of elemental content (image values correspond to μg/(cm)^2). The right column shows the respective images from the content column divided by the thickness map of Fig. 3.41. The elemental concentrations are displayed in units of (per dry weight) meaning elemental mass per dry weight of protein, instead of the protein volume; this just corresponds to a linear scaling of the protein volume by its density.

The applicational importance of these results in two-fold. First, the reconstructed concentration maps provide important clues for scientist when interpreting the elemental distribution from the two-diemnsional maps; in particular regarding questions of elemental co-localizations and potential biochemical consequences. Second, quantitative conclusions can be drawn from the data, including an independent measure of the total cell mass.

For each of the elements concentration reconstruction two global images values are given. The "integral part" represents the sum of the measured elemental content divided by the total cell mass; the "average" denotes the average reconstructed concentration on a per pixel basis. From these number we can see that the individual elemental contributions to the total cell mass (and therefore its index of refraction) are on the low percentage range, justifying the assumption that the main contributing factor to the objects index of refraction is given through the soft material with negligible contribution from the (trace) elements.

The proposed method of mass normalization of elemental content maps through quantitative phase contrast images posses a significant advancement for the data analysis from two-dimensional XRF microscopy. In case of XRF tomography, where the three dimensional structure of the specimen is imaged, the mass normalization is no longer required since the final XRF maps already represent mass per volume images. However, the quantitative phase contrast maps will still be of importance, as they depict the biological structure of the specimen and allow the measured elements to be put in their ultrastructural context.

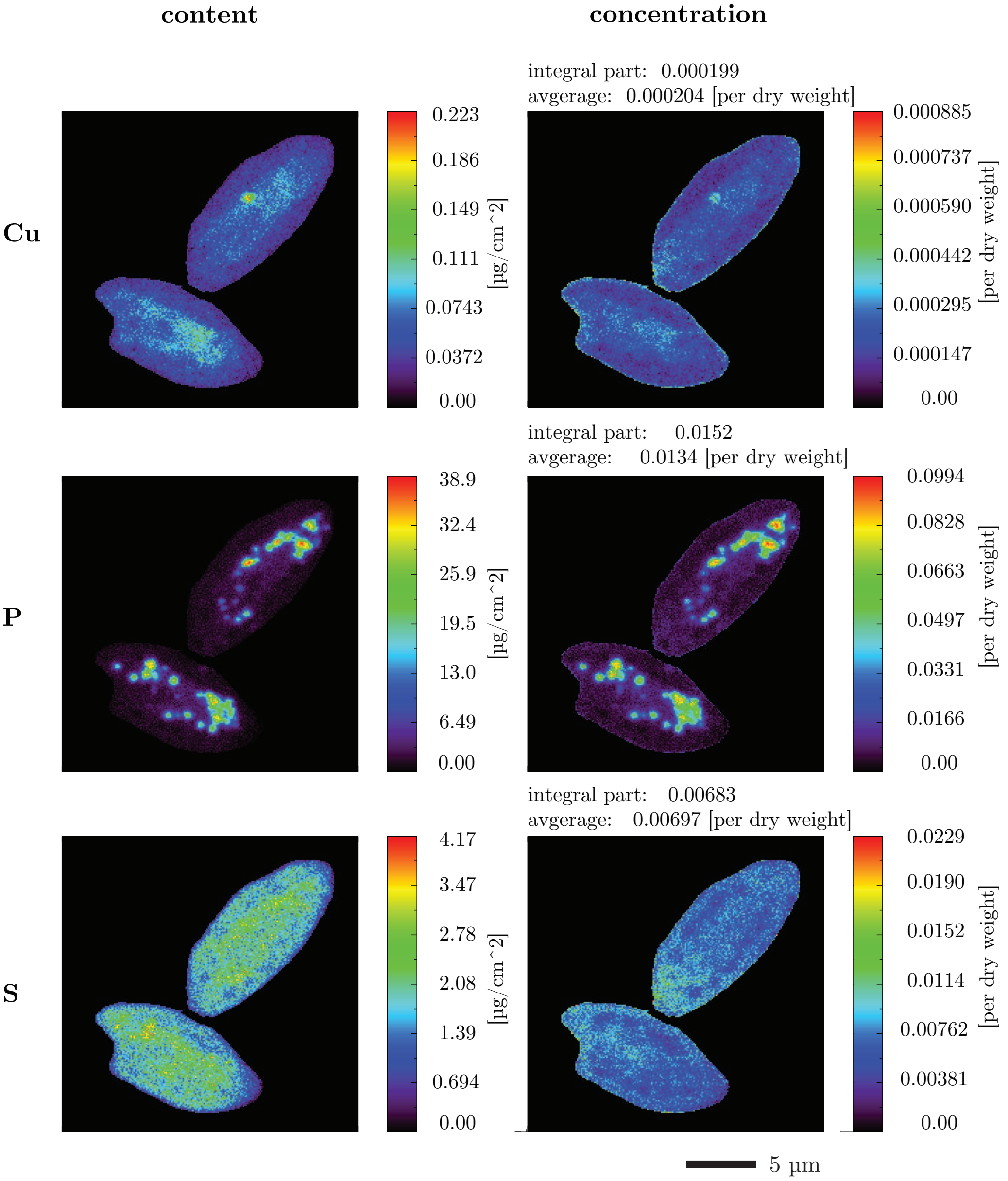

Figure 3.42: Measured and calibrated elemental content maps of Cu, p and S (left column) and their respective concentration maps (right column) by mass normalization of the content maps via Fig. 3.41.

Chapter 4

Scanning Zernike Phase Contrast Imaging

The present chapter will discuss the implementation and realization of a novel phase contrast imaging technique for scanning x-ray microscopes, which will also have general applicability to scanning microscopy with other types of radiation.

We will begin by reviewing Frits Zernike's idea of phase contrast imaging for full-field microscopy [27], which earned him the Nobel Prize in 1953. From there the principle of reciprocity is employed to arrive at Zernike phase contrast for scanning microscopy. On the example of hard x-ray scanning microcopy we will describe the experimental implementation of this new method and discuss its imaging properties. Similarly to the phase contrast methods described in Ch. 3, scanning Zernike phase contrast can be an extremely useful tool for complementary imaging in x-ray fluorescence microprobes; a few initial results and potential applications in connection with x-ray fluorescence imaging will be discussed.

4.1 Zernike Phase Contrast Principle

Zernike phase contrast (ZPC) is one of the most powerful methods of phase imaging, since it produces images which are a direct representation of to the phase changes introduced by the sample. It was first described by the Dutch physicist Frits Zernike in 1935 [27] and was awarded the 1953 Nobel Prize in physics. Zernike's method is often simply referred to as *the phase contrast method*.

Let us describe the principle of ZPC, in the style of the treatment by Born and Wolf [37]. For this purpose we consider a transparent object in the form of a one-dimensional phase grating with a specimen transmission function

$$h(x) = \mathrm{e}^{\mathrm{i}\phi(x)}\,, \tag{4.1}$$

where $\phi(x)$ is a periodic function with period d. If we assume the magnitude of ϕ to be small one can write

$$h(x) \approx 1 + \mathrm{i}\phi(x)\,. \tag{4.2}$$

Measuring the intensity of the light distribution caused by this phase grating in an image plane, we simply would get

$$I(x') = |h(x)|^2 = 1\,; \tag{4.3}$$

with $x' = xM$ and M the image magnification through the optical setup. Hence, we would not be able to visualize the grating structure of the sample.

Note, that in this treatment one is not considering potential propagation based phase effects and their successive influence on the final image intensity.

Since $h(x)$ is periodic and ϕ real and nummerically small compared to unity we can develop the specimen function into the Fourier series

$$h(x) = \sum_{j=-\infty}^{\infty} \mathcal{K}_j \exp\left(\frac{2\pi \mathrm{i} j x}{d}\right) , \tag{4.4}$$

where the coefficients are

$$\mathcal{K}_0 = 1 \tag{4.5}$$

$$\mathcal{K}_{-j} = -\mathcal{K}_j^* \qquad \text{for } j \neq 0 \, . \tag{4.6}$$

The coefficients $\mathcal{K}_j$ describe the amplitude distribution in the focal plane (Fourier plane) of the imaging objective lens[1]. Now, it was Zernike's idea to introduce a phase shifting structure in form of a thin phase plate in the back focal plane of the objective. In this arrangement the 0th or central order ($j = 0$) of the light is retarded ($-$) or advanced ($+$) with respect to the diffracted orders ($j \neq 0$) by a quarter of a wavelength (see also Fig. 4.1 below). This alters the amplitude distribution in the focal plane, which is now described by the coefficients $\widehat{\mathcal{K}}$

$$\widehat{\mathcal{K}}_0 = \mathcal{K}_0 \, \mathrm{e}^{\pm \mathrm{i}\pi/2} = \pm \mathrm{i} \, \mathcal{K}_0 \tag{4.7}$$

$$\widehat{\mathcal{K}}_j = \mathcal{K}_j \qquad \text{for } j \neq 0 \, . \tag{4.8}$$

The resulting light distribution in the image plane in this arrangement will be

$$\widehat{h}(x) = \pm \mathrm{i} + \mathrm{i}\phi(x) \, , \tag{4.9}$$

which now represents an amplitude grating compared to the previous phase grating of Eq. 4.2. The successive intensity in the image plane is then

$$\widehat{I}(x') = |\widehat{h}(x)|^2 = 1 \pm 2\phi(x) \, . \tag{4.10}$$

This results signifies the basic principle of Zernike's method of phase contrast. Phase changes that are induced by the sample are transformed into intensity changes, where the intensity at any given point in the image plane is directly proportional (aside from a global additive constant) to the phase change due to the corresponding sample structure.

---

[1] In Ch. 2 we derived the fact that the light distribution in the focal plane of a lens corresponds to a Fourier transform.

An example of this principle is depicted in Fig. 4.1. The light illuminating the object is divided into an undiffracted (0th order) and diffracted part. The diffracted part carries the information about the object structure. A spatial separation of these two components is achieved in the back-focal plane of the objective lens, where a phase shifting ring imparts the predetermined phase shift necessary for Zernike's method onto the undiffracted part. The final phase contrast image is formed by the interference of the phase shifted undiffracted component with the (undisturbed) diffracted component, translating phase modulations of the object into intensity variations in the image plane. As we have seen through Eq. 4.10, for small phase shifts, these variations are due and directly proportional to the differences in the real part (phase) of the object's index of refraction. Figure 4.2 shows example images from visible light microcopy.

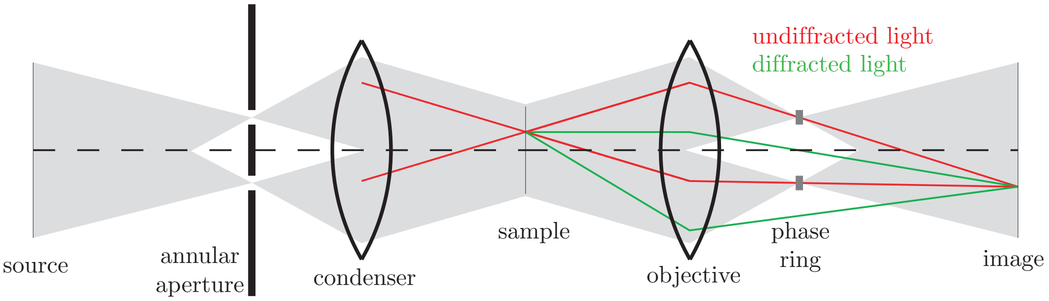

Figure 4.1: Principle of Zernike phase contrast in a full-field microscope. Interference of undiffracted light (red) that will be phase shifted by the phase ring with diffracted light (green) translates phase variations of the object into intensity modulations in the image plane.

Given the nature of X-rays, where optically thicker structures cause positive phase shifts, one distinguishes the two cases of Zernike phase contrast the following way. In case of a phase retardation ($-\pi/2$) of the 0th order through the phase plate, structures that are optically thicker will appear darker than the mean illumination, and one speaks of *negative* or *dark phase contrast*. This image representation closely matches conventional absorption contrast in its appearance. For a phase advance ($+\pi/2$) through the phase plate, structures that are optically thicker will appear brighter than the illumination mean, and one calls this case *positive* or *bright phase contrast*. Note, that in the case of visible light the above classification works vice versa.

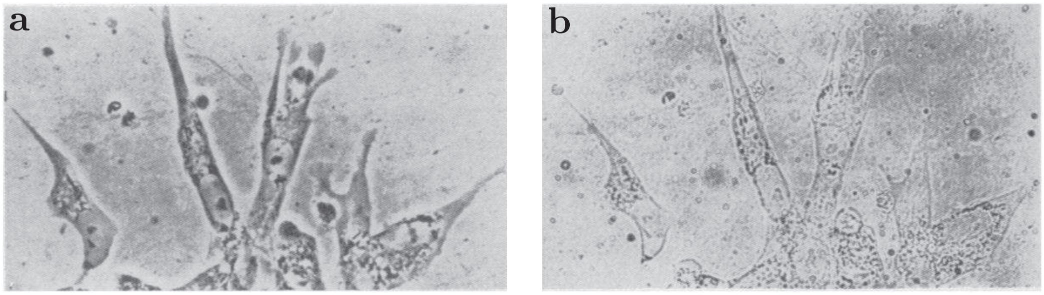

Figure 4.2: Visible light images of a living tissue culture in (**a**) Zernike phase contrast and (**b**) absorption contrast. The phase image shows a significant improved visualization of the structures. Image reproduced from F. Zernike [66]; no image scale given.

4.1.1 General Description

In the previous derivation of the Zernike phase contrast method, a rather sever assumption was that the phase object is of periodic structure. However, it can be shown that this is not a necessary requirement and the ZPC method works equally for arbitrary structures. For the detailed derivation of this case we refer to Born and Wolf [37, Ch. 8.6] and simply just state the result in the following and discuss its consequences.

A general phase object is described by the transmission function

$$h(\boldsymbol{x}) = \mathrm{e}^{\mathrm{i}\phi(\boldsymbol{x})}\,, \tag{4.11}$$

with $\phi(\boldsymbol{x})$ an arbitrary but real function. A phase shifting mask (*e. g.* phase plate or ring) is given through the transmission function

$$PR = t\,\mathrm{e}^{\pm\mathrm{i}\alpha}\,, \tag{4.12}$$

with t as the transmission and α phase shift of the mask. It can be shown (see [37, Ch. 8.6]) that this leads to an intensity in the image plane given by

$$I(\boldsymbol{x}') = \mathcal{C}\big[t^2 \pm 2\,t\,\phi(\boldsymbol{x})\,\sin\alpha\big] \tag{4.13}$$

where $\mathcal{C}$ is some constant.

Let us consider the consequences from this general result of Eq. 4.13. It becomes immediately clear that the optimal phase shift α desired by the phase shifting mask should be $\pm\pi$ as this maximizes the contribution of the term containing the sample phase ϕ to the total intensity; *i. e.* $\sin\alpha$ is maximal. In case of a non-absorbing phase plate ($t = 1$) the previous result of Eq. 4.13 is reproduced. Furthermore, if the phase mask PR is partially absorbing with a transmission coefficient $t < 1$, the ratio of the second to first term of Eq. 4.13 becomes $\pm\phi/t$, so that the contrast of the image is enhanced.

4.1.2 Improved Formula for Image Intensity in Zernike Phase Contrast

As a word of caution we would like to draw attention to the fact that the expression given in Sec. 4.1.1 for the image intensity in Zernike mode is not generally valid. It is pointed out by Beleggia [67] that the derivation is only justified in the case of a weak phase object approximation, where the majority of the light passes through the sample undisturbed (0th order is by far the largest contribution). If this is not the case the relation of Eq. 4.13 leads to image inconsistencies. Furthermore, energy conservation is violated and constant phases become can observable. A generalized expression is derived by Bellegia [67] that surpasses the limitations and results in improved image representations for the Zernike phase contrast method. However, a detailed discussion of these issues is beyond the scope of this work.

4.2 Reciprocity - Zernike Phase Contrast in Scanning X-ray Microscopy

The reciprocity theorem reflects the interchangeability of source and observation point for electromagnetic systems. As we have seen in Ch. 2, in the case of imaging theory this principle is reflected in the symmetry of the variables in the Fresnel-Kirchhoff diffraction integral for wave propagation [23, 37]. In the microscopy community is has long been recognized that this signifies the equivalence of scanning and full-field transmission microscopes, which we have mathematically proven in Sec. 2.4. Based on this realization, the concept of Zernike phase contrast in a scanning microscope was considered for visible light by Wilson and Sheppard [68] and Siegel *et al.* [69] for X-rays. However, to date, no detailed treatment or implementation has been reported, which is why we believe our work [7] poses the first demonstration of Zernike phase contrast in a scanning microscope.

Let us now consider the essence of Zernike imaging in a scanning arrangement. Figure 4.3 illustrates the equivalence of full-field and scanning Zernike imaging. In full-field imaging a condenser (commonly of annular shape) illuminates the object of interest; the transmitted light (diffracted and undiffracted)

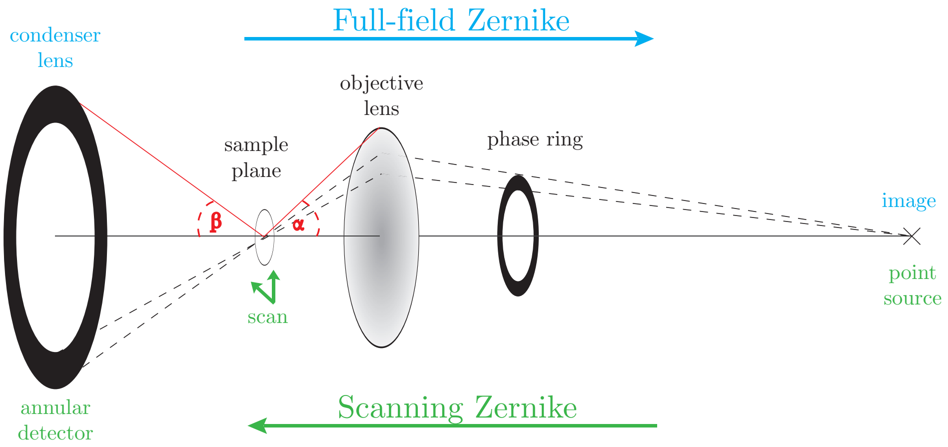

Figure 4.3: Schematic of the equivalence of full-field and scanning Zernike phase contrast imaging. Reading the image from left to right (considering the blue labels) resembles the case of a full-field setup in Zernike mode. From right to left (considering green labels) resembles the situation of a scanning microscope with Zernike phase contrast capability.

gets collected by the objective lens to form an image in the detector plane. A phase ring in the condensers conjugate plane (given through the lens law) provides the necessary phase shift for Zernike's method of phase contrast. In the scanning case the propagation direction is reversed and the image point takes the role of the source illuminating the objective lens, which then focuses the light to a spot through which the sample is raster scanned. The detected intensity for each point of the scan forms the image. To realize Zernike phase contrast in this case a phase ring is placed in front of the objective, and sensitivity to the objects phase modulation is then given by using an annular detector in the conjugate plane of the phase ring. Note, that the principle of phase advance and the subsequent sensitivity to the phase shift introduced by the specimen is the same for both cases, which are theoretically completely equivalent for on-axis image points.

4.2.1 Experimental Implementation with Hard X-rays

Following the scheme described by Fig. 4.3 we implemented the Zernike method into the scanning hard x-ray side-branch beamline 2-ID-E [70] at the Advanced Photon Source at Argonne National Laboratory.

X-rays from an undulator source are energy filtered via a Si(111) crystal monochromator. An additional beam splitting crystal is used to reflect part of the main beam into the side branch line. The existing scanning fluorescence setup was modified to accommodate the additional optical elements and realize the required detector geometry. A schematic of all the optical components used at the experimental end station for the experiment is shown inFig. 4.4. The x-ray energy chosen for the experiment was 10 keV, which is a typical value used for trace element mapping with x-ray fluorescence of life science samples. The 10 keV X-rays were focused using a 160 μm diameter Fresnel zone plate with outermost zone width of 100 nm and zone height of 1600 nm; an arrangement of 40 μm diameter central stop (approx. 80 μm thick gold) and 25 μm diameter order sorting aperture was used to isolate the first order focus of the zone plate. The phase ring for Zernike's phase contrast method was fabricated by using electron beam lithography to pattern an annulus of 75 μm inner and 85 μm outer diameter on a silicon nitride window. Gold was electroplated to a thickness of 3.52 μm.

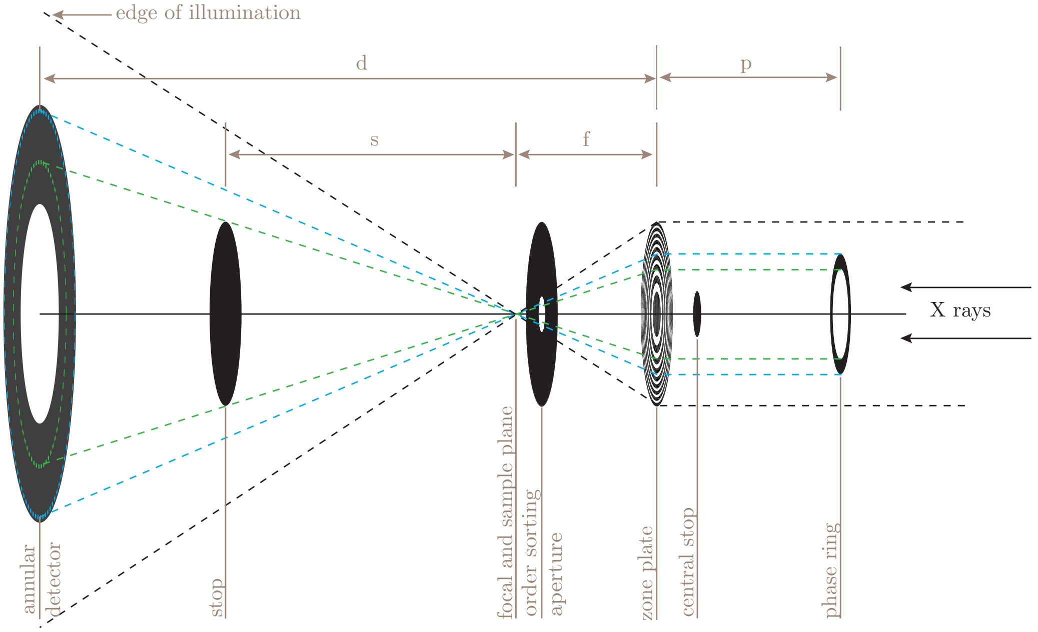

Figure 4.4: Schematic of the optical components for the scanning Zernike implementation at beamline 2-ID-E at the APS. The effective distance of the secondary source to the zone plate is larger than 15 m. In place of the annular detector and stop, a visible light coupled CCD can be brought in the setup to observe the far-field intensity distribution. Photographs of the setup are shown in Fig. 4.5 and Fig. 4.6.

Given the phase ring thickness and material, the phase of the X-rays passing through will be phase shifted by $-\pi/2$; therefore, the images will represent negative Zernike phase contrast with optically denser structures appearing darker in the final image.

The samples are placed in the focal plane of the zone plate and raster scanned through the focus spot of the lens. In order to collect the emitted fluorescence photons for each scan point, an energy dispersive detector (not shown in schematic) was placed under 90° to the optical axis to minimize the elastic scattering background and directly pointed at the focal spot of the x-rays on the sample. In order to avoid shadowing of the fluorescence through the sample holder, the sample stage is rotated by 15° around the vertical axis with respect to the optical axis.

An annular detector in the far-field was used to record the projection of the phase ring. The annular detector was realized through an existing 10-segment detector [1]; Fig. 4.7(a) shows a schematic, highlighting the four segments that were used to make up the annular detector. In Fig. 4.7(b) an image of the far-field illumination pattern recorded with a scintillator-coupled CCD in place of the segmented detector is shown. Both Suppl. Fig. 4.7(a) and 4.7(b) are of true relative scale and illustrate how the detector was aligned to the illumination pattern: the outer edge of the phase ring projection was matched with the outer edge of the annular quadrant. Since the phase rings projection was much smaller than the annular detector (see dimensions in Fig. 4.7(a), phase ring inner edge) an additional stop was put in front of the detector to mask it optimally to the projection of the phase ring and, therefore, eliminating the detection of unwanted signal. The stop with a diameter of 160 μm was put at a distance (s = 280 mm) from the sample, so as to have its diameter match the inner diameter of the phase rings projection in this plane (see Fig. 4.4).

A scanning Zernike image represents the signal of the annular detector at each raster scan point. Unless otherwise noted, images was recorded with a step size of 100 nm and a dwell time per raster point of 100 ms. Absorption images can be taken by performing a separate scan, where the phase ring and stop are removed from the setup. In this case the sum of all 10 detector segments represents the absorption image.

Given the focal length ($f = 131$ mm) of the zone plate and the necessary distance of the detector to the zone plate ($d = 1031$ mm) to align the outer edge of the phase ring with the annular detector, the position of the phase ring in front of the zone plate ($p = 151$ mm) was chosen to fulfill the lens equation $1/p + 1/d = 1/f$. Note, that the ideal detector to zone plate distance would have been $d = 1056$ mm; however, d was chosen smaller to allow some tolerance for small errors in alignment.

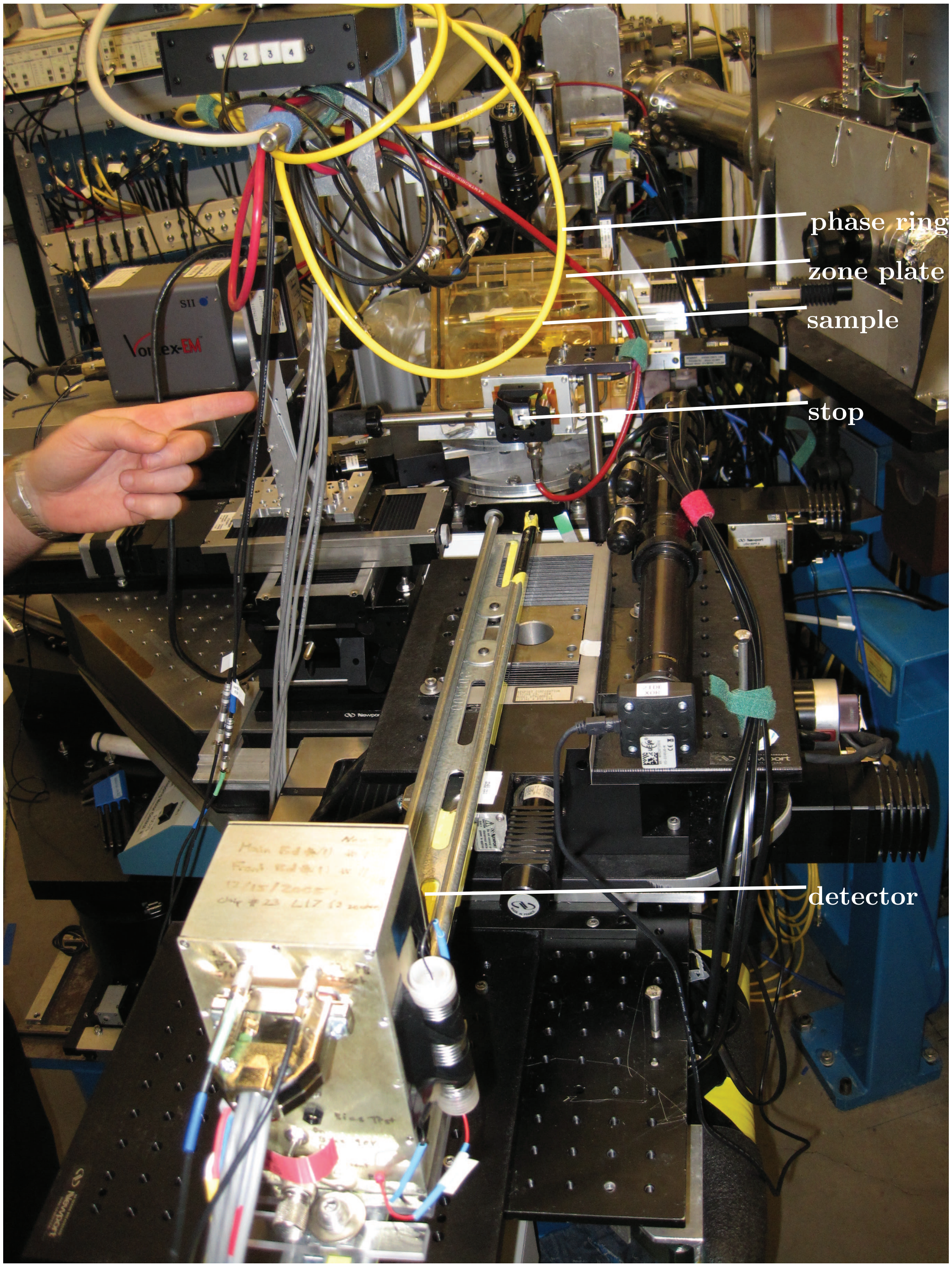

Figure 4.5: Photograph (back view) of experimental scanning Zernike setup detailed through the schematic in Fig. 4.4. Indicated are the positions of some optical components.

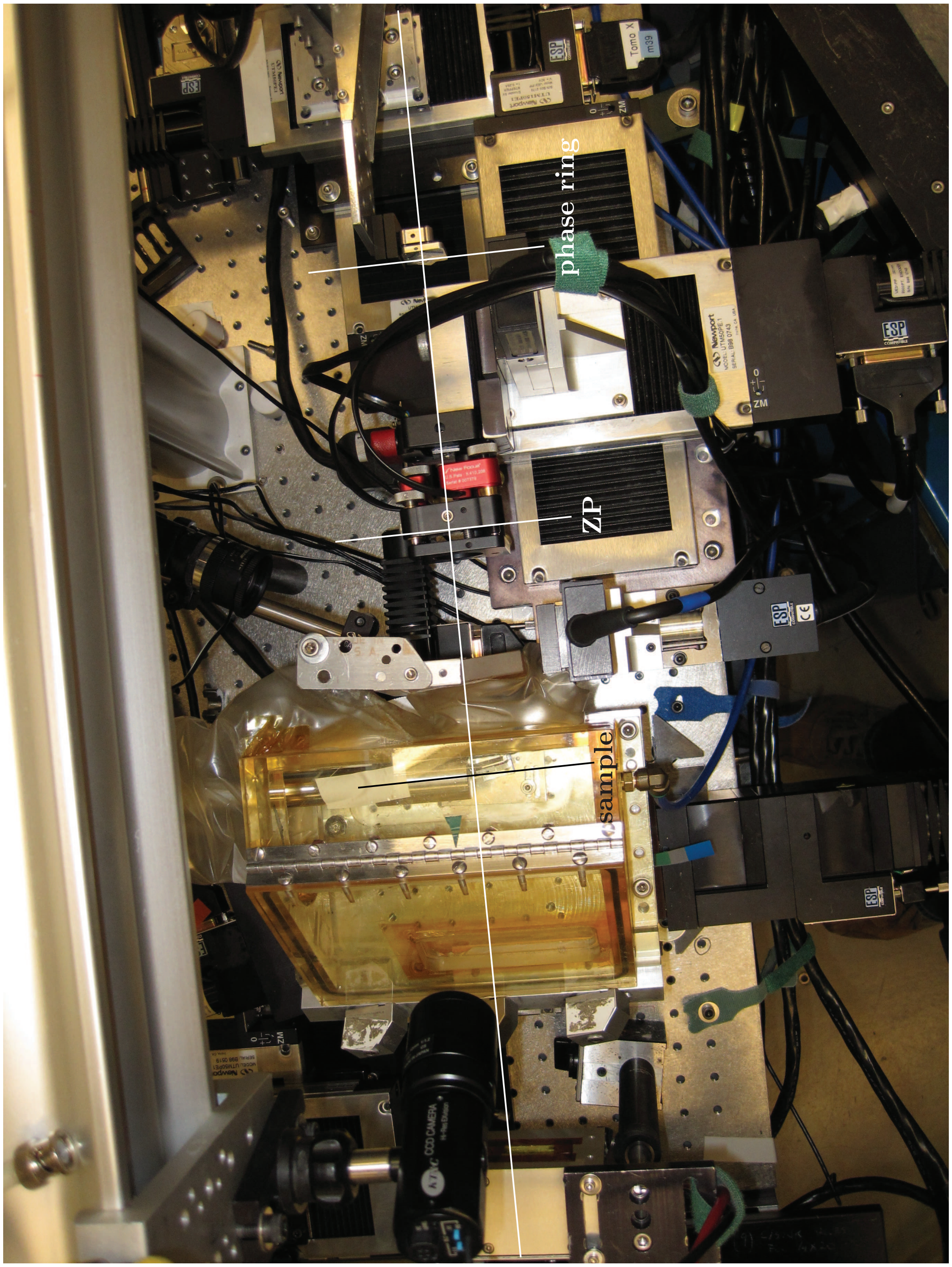

Figure 4.6: Photograph (top view) of experimental scanning Zernike setup detailed through the schematic in Fig. 4.4.Indicated are the positions of some optical components: phase ring, zone plate and sample plane.

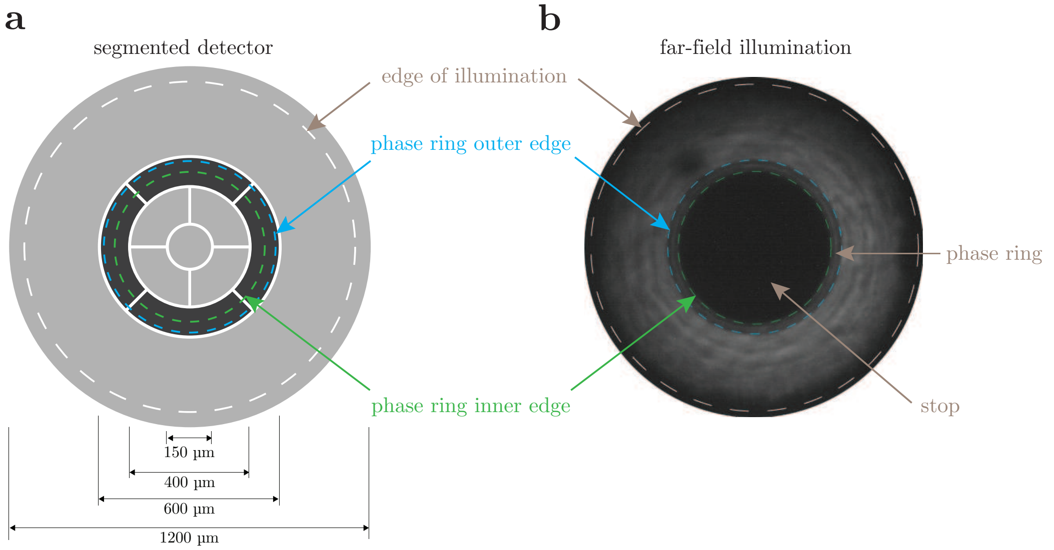

Figure 4.7: (**a**) Schematic of the 10-segment detector chip used in the experiment; the four segments that were used to realize the annular detector are highlighted in darker grey. Also shown are approximate outlines of the far-field illumination and the phase ring projection on the detector chip. (**b**) Far-field illumination recorded with a CCD in place of the segmented detector, showing the illumination region, the stop and phase ring. Both (a) and (b) are of true relative scale.

4.2.2 Experimental Results from Imaging of Test Structures

In order to evaluate the imaging properties for the proposed technique of Zernike phase contrast in a scanning microscope, we will consider some experimental results from imaging of known test structures. These test samples are a standard Siemens star test pattern made from gold, polystyrene spheres and a zone plate pattern out of plastic.

The Siemens star test pattern consists of a 700 nm thick gold structure on a Si_3N_4 membrane. In Figs. 4.8(a) and 4.8(b) we show scanning images obtained in Zernike phase contrast and absorption contrast respectively. The images were acquired with a zone plate of 100 nm outermost zone-width and thus a theoretical spoz size and Rayleigh resolution of 122 nm assuming a fully coherent illumination of the zone plate and a large area detector for incoherent detection. For a qualitative comparison, Figs. 4.8(c) and 4.8(d) show Zernike and absorption images taken with a commercially available full-field x-ray microscope at 8.04 keV [21]. Given the limitations of the laboratory instrument the imaging resolution is limited to 100 nm due to chromatic aberrations. While, of course, a direct comparison between the full-field and scanning data is difficult due to varying experimental factors we can take note of two important facts. Firstly, the scanning Zernike image is in qualitative agreement with its full-field companion in terms of feature visualization and appearance compared to the respective absorption images. Secondly, both Zernike images show a significantly improved contrast (scanning 17.3% and full-field 9.1%) compared to the absorption images (scanning 4.1% and full-field 4.9%), as one would expect from phase versus absorption imaging (see Sec. 1.4).

Before moving on to the next test structure, let us consider a few particularities of the data in Fig. 4.8. In the scanning experiment the resolution was limited by the finite and asymmetric x-ray source size, which is larger in the horizontal compared to the vertical direction (typical for third generation synchrotron sources). As mentioned in Sec. 4.2.1 the experimental apparatus is located at a side-branch line, where through a beam splitting crystal part of the intensity of the main beamline is reflected into a side-branch arm; this further worsens the beam properties in particular in terms of coherence and stability. In addition, for the fluorescence capability of the microscope, the sample is rotated by 15° around the vertical axis in order to avoid shadowing of the x-ray fluorescence detector through the holder which places the sample at the focal spot of the lens. Taking these aspects into consideration, we expect there to be a difference in image resolution between the horizontal and vertical direction, with the vertical feature resolution being superior. We can identify this expected behavior in both the scanning Zernike and absorption images of

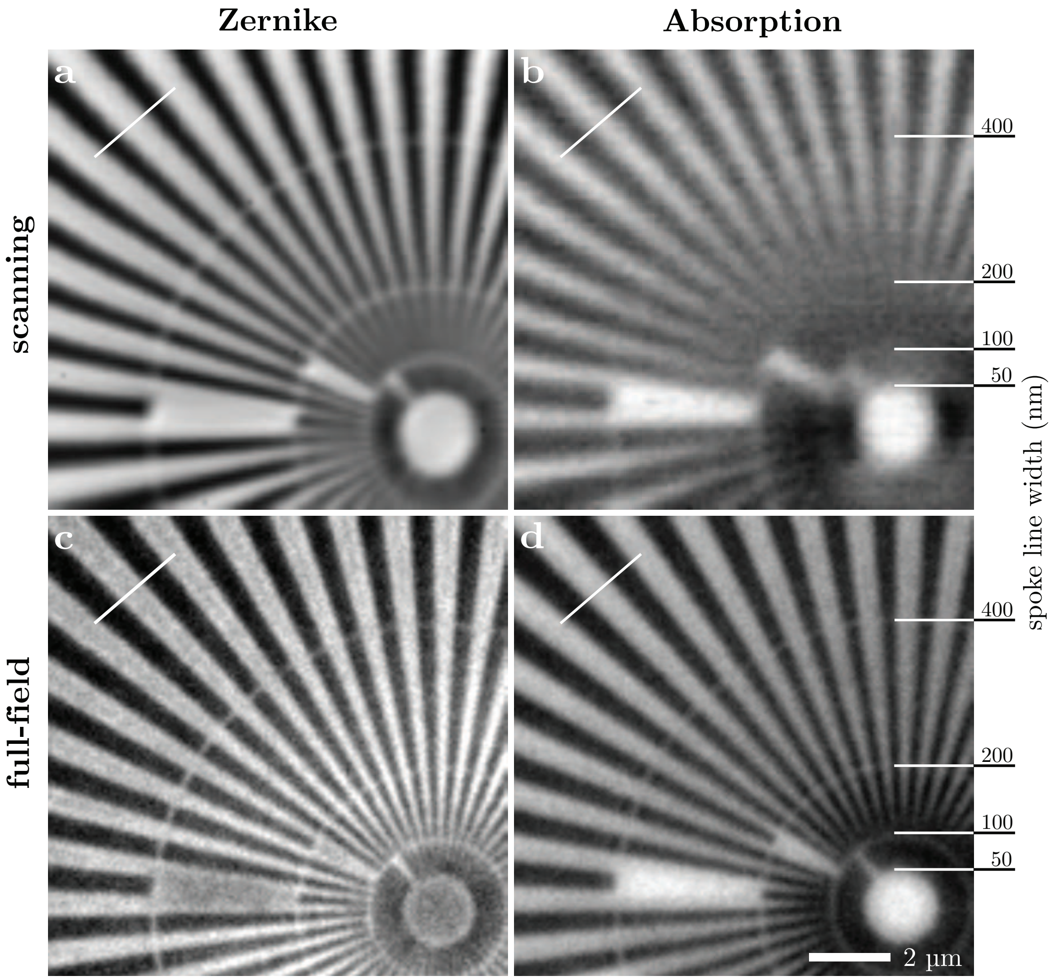

Figure 4.8: Siemens star imaged through scanning and full-field x-ray imaging. Zernike phase contrast in (**a**) scanning and (**c**) full-field microscopy; absorption contrast for the two cases respectively (**b**) and (**d**). The starting line widths of the respective spoke rings of the star pattern are indicated. The white line in each image marks the position where the contrast was determined: Zernike scanning 17.3% and full-field 9.1%; Absorption scanning 4.1% and full-field 4.9%. Experimental details for scanning data: 10 keV, steps 100 nm, ZP $160\,\mu$m, $\mathrm{d}r_N$ 50 nm, stop $40\,\mu$m, annular detector arrangement, phase ring ID $75\,\mu$m and OD $85\,\mu$m. Experimental details for full-field data: Xradia nanoXCT labtool, large FOV mode, 8.04 keV, pixel size 65 nm, ZP $320\,\mu$m, $\mathrm{d}r_N$ 30 nm.

Fig. 4.8. This can be seen particularly well in the scanning Zernike image on the second ring from the star center, where in the vertical direction one can recognize the 100 nm line widths which are not visible in the horizontal.

Furthermore, we note that the absorption image in the scanning case is of poor quality, which is likely due to a significant dark field contribution in the acquired image signal. The absorption image is taken by removing the stop and phase ring from the setup (see Fig. 4.4) and adding all detector segments to represent the final image (see Fig. 4.7). In this case the central stop of the setup will still shadow the central segment of the detector in addition to large parts of the inner quadrant structure. These partially or completely shadowed segments contribute to the absorption image, where in particular for the smaller grating structures of the Siemens star, the dark-field contribution to these segments is significant (as can be seen from considering individual signals of segments - no images shown). This dark-field contribution is "out-of-phase" with the absorption part of the image, resulting in a resolution degradation for the smaller features as can be observed in Fig. 4.8(c). The dark-field contribution from the outermost segment plays a minor role as most of this segment is covered by the far-field illumination pattern.

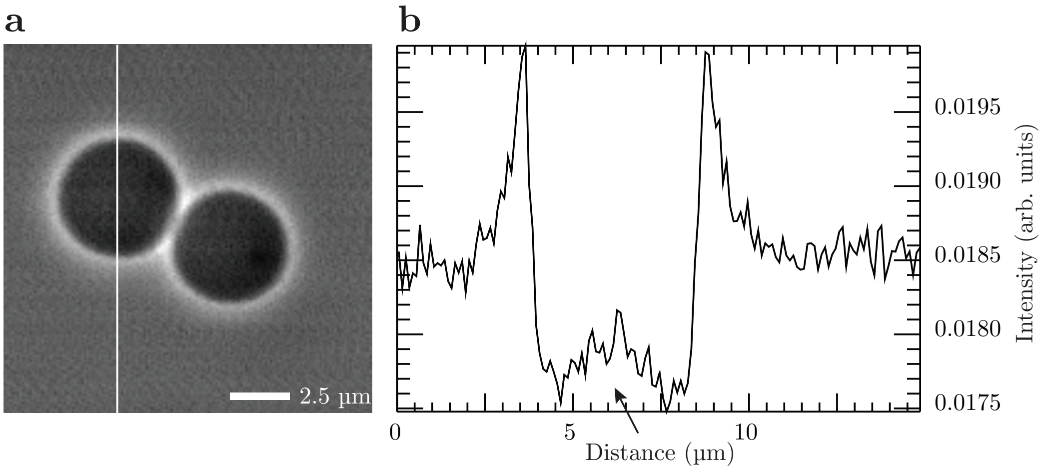

Figure 4.9: (**a**) Scanning Zernike phase contrast image of a pair polystyrene spheres with a diameter of 5 m. (**b**) Profile through the left sphere as indicated in (a) by the vertical line. The arrow points to the approximate center of the sphere. Experimental details: 10 keV, steps 100 nm, ZP 160 μm, dr_N 50 nm, stop 40 μm, annular detector arrangement, phase ring ID 75 μm and OD 85 μm.

While the previous example of the gold Siemens star already gives some impression on the imaging properties of Zernike phase contrast in scanning mode, the real advantages become apparent when imaging weakly absorbing samples. For example from Ch. 3 we already know that polystyrene spheres at hard x-ray energies show little to no contrast in absorption. In Fig. 4.9(a) we show a scanning Zernike image of a pair of 5 μm diameter polystyrene spheres imaged at 10 keV. Note, that these spheres are not visible in absorption contrast (no image shown). The spheres can be clearly identified in the Zernike image, which gives a representation of the sample density. A bright halo artifact, which is typical for Zernike phase contrast, can be seen around the edges of the two spheres. Another artifact common for this imaging method is illustrated by the line-out through the left sphere in the image (Fig. 4.9(b)). Rather than decreasing to a minimum towards the center of the sphere (indicated by the arrow), we note an increase in the image intensity (in the literature this is often referred to as shade-off effect). Both artifacts, which are due to the nature of how the contrast is formed (ring shaped phase mask and aperture), are typical for Zernike phase contrast images and are a consequence of the loss of low spatial frequencies in the image formation process. While such artifacts are not desired, here they further demonstrate the equivalence of the presented scanning Zernike phase contrast and the full-field case. (See Ch. 5 for a detailed discussion of artifacts in Zernike phase contrast and their possible removal.)

To conclude this section on imaging test structures Fig. 4.10(a) shows a scanning Zernike phase contrast image of a plastic zone plate structure, which is a ”negative” structure usually used in the metal plating production of x-ray zone plates. A corresponding absorption image (Fig. 4.10(b)) of a subregion has no noticeable contrast. In the line profile through the first column of the scanning Zernike image a decrease in contrast with feature size can be observed, confirming the imaging behavior as one would expect it from the modulation transfer function for such an incoherent imaging situation [23].

4.3 Advanced Topics of Imaging in Scanning Zernike Phase Contrast

In this section we will discuss some particularities and observations of scanning Zernike phase contrast.

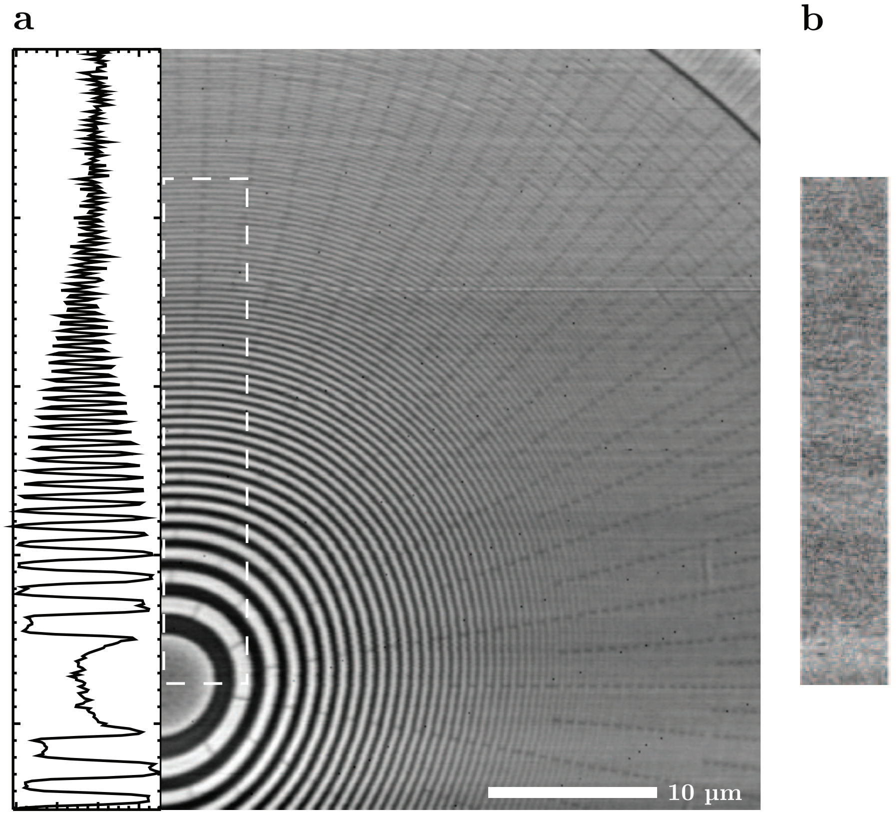

Figure 4.10: (**a**) Scanning Zernike image of a plastic zone plate test structure; also shown is a line-out through the first image column. (**b**) Absorption image of the region indicated in the Zernike image showing no noticeable contrast.Experimental details: 10 keV, steps 100 nm, ZP 160 μm, dr_N 50 nm, stop 40 μm, annular detector arrangement, phase ring ID 75 μm and OD 85 μm.

4.3.1 Equivalence of Scanning to Full-Field Zernike Phase Contrast

Theoretically and mathematically, both cases are completely equivalent for on-axis image points (see also Sec. 2.4 and works by Wilson and Sheppard [44, 68]). For X-rays a minor technical difference will be the requirement of a central stop (CS) in the objective pupil for scanning, which is not needed in the full-field case. The CS modifies the shape of the modulation transfer function (MTF) of the lens, as can be seen in Fig. 4.11. Through the central stop the MTF is suppressed in the low and medium spatial frequency range. Towards the higher frequencies one notes a small increase in the MTF value compared to the case without CS. This difference in the MTF needs to be kept in mind when directly comparing imaging results for full-field and scanning microscopy with X-rays. However, the difference has no direct disadvantageous effects on the imaging properties and is of a rather technical nature.

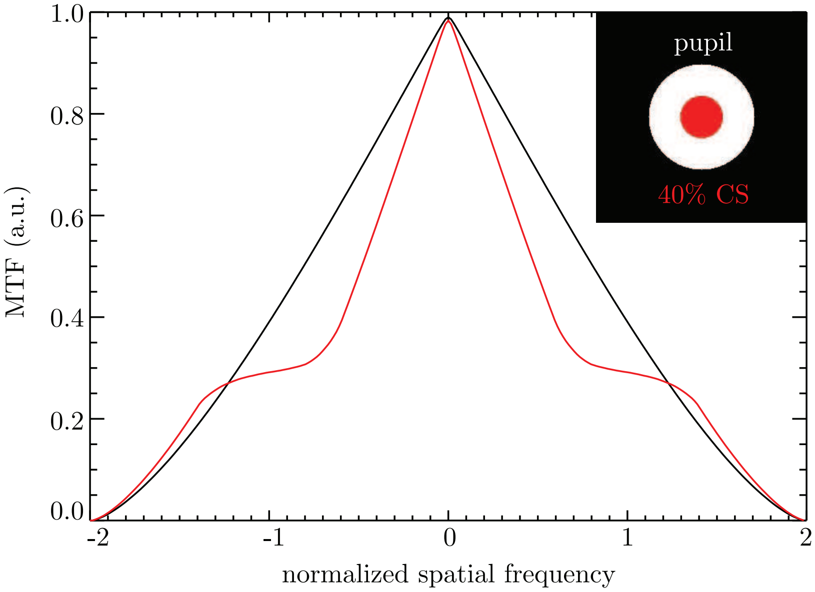

Figure 4.11: Modulation transfer function of a circular lens with (red) and without (black) a centrals stop present in the pupil (shown in inlay). Note that this computation does not include a phase ring for either case.

Note that the complete equivalence of full-field and scanning only applies to on-axis image points. Mathematical differences arise for image points that are far away from the optical axis in full-field imaging; scanned imaging is by definition always on-axis.

Furthermore, in the Zernike mode it is very likely that there will be differences for very extreme imaging cases in terms of very strong absorbing and / or phase shifting objects. Differences in the case of dark field (infinitely thick phase ring) imaging are difficult to predict due to the non-linear and higher order nature of this imaging mode. These aspects are beyond the scope of our work, but pose interesting questions for future publications.

4.3.2 Phase Ring Placement

Through the experiment described in Sec. 4.2.2 we performed tests regarding the placement of the phase ring along the optical axis. As mentioned in Sec. 4.2.1 the phase ring was placed according to the lens law, so that it got imaged onto the detector by the objective zone plate. We also considered cases where the phase ring was brought significantly closer (up to $p = 50\,\text{mm}$) or further away (up to $p = 250\,\text{mm}$) from its ideal position at $p = 151\,\text{mm}$; however, no noticeable differences in the imaging results were observed.

The relaxed positioning tolerance is associated with the fact that we are dealing with an almost planar incident wave front (rays close to parallel to the optical axis) upstream of the objective lens, attributed to a source far away ($> 15\,\text{m}$). As a consequence the rays that pass through the phase ring will hit the detector correctly regardless of the phase ring position along the optical axis.

In the full-field imaging case the phase ring position is much more restricted due to a stronger converging wave field. Its positioning becomes more relaxed when considering a smaller source size or equivalently a smaller field-of-view, which results in a lower divergence of the 0th order wave field in the back-focal region of the objective lens. It is important to note that for the on-axis image point, the phase ring placement behind the objective does not matter, since rays from the focal spot are parallel behind the lens. This condition is similar to the above behavior observed in the scanning Zernike case where the criterion for placement of the phase ring is very relaxed, due to the on-axis imaging situation.

4.3.3 Transfer Functions for Scanning Zernike Phase Contrast

Similarly to Sec. 3.3.1 the present imaging situation can be described through transfer functions in the exact same way. Hence, in the scanning Zernike case the Fourier spectrum of the signal collected by the annular detector segment is given through (compare to Eq. 3.40)

$$S(\boldsymbol{f}_\mathrm{s}) = \Delta(\boldsymbol{f}_\mathrm{s})\, C(0,0,\boldsymbol{f}_\mathrm{s}) + H_r(\boldsymbol{f}_\mathrm{s})\, T_r(\boldsymbol{f}_\mathrm{s}) + \mathrm{i}\, H_i(\boldsymbol{f}_\mathrm{s})\, T_i(\boldsymbol{f}_\mathrm{s})\,, \tag{4.14}$$

where $H_{r,i}$ are the specimen contributions and $_\mathrm{s}$ attributes the scan displacement. The pupil function $P_\mathrm{o}(\boldsymbol{f})$ and detector response $R(\boldsymbol{f})$, which contribute to the transfer functions $T_{r,i}(\boldsymbol{f})$ (definition see Eq. 3.39) and $C(0,0,\boldsymbol{f})$ (definition see Eq. C.18) are displayed in Fig. 4.12 for the scanning Zernike experiment. The pupil function is given by

$$P_\mathrm{o}(\boldsymbol{f}) = \begin{cases} 1 & \text{area of no phase ring} \\ 0.5 \times \mathrm{e}^{-\mathrm{i}\pi/2} & \text{area of phase ring} \end{cases}\,. \tag{4.15}$$

Note two important differences to the treatment in Sec. 3.3.1. First, we

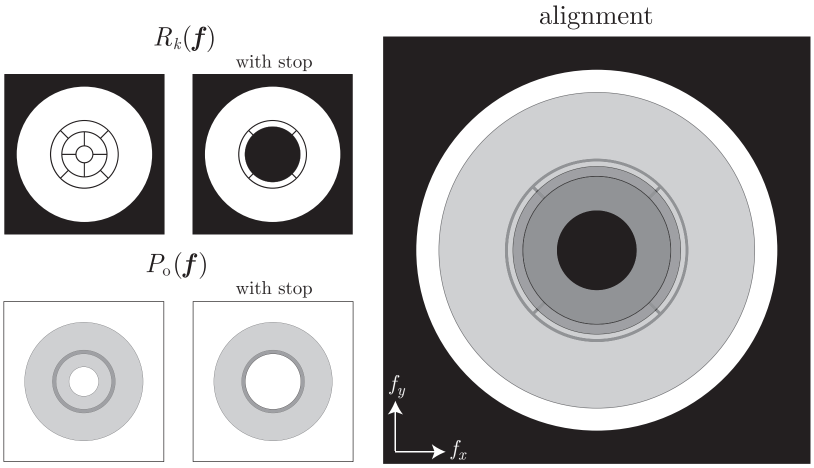

Figure 4.12: (**a**) Transmission of the pupil function, the phase ring has approximately a transmission of $t = 50\%$ at 10 keV. (**b**) Alignment of phase ring (grey) to annular detector response function; the inner diameter of the phase ring projection was well matched to the annular detector response through the help of the additional stop in the setup. As mentioned in Sec. 4.2.1 the positioning of the detector along the optical axis was chosen as to allow some tolerance for small errors in alignment. This is reflected in the fact that the outer phase ring diamter does not match the annular detector; the mismatch is estimated from calculations taking the experimental distances into account.

are dealing with a detector configuration that only has one segment - annular segment (therefore also no indices k are present). Second, through the addition of the phase ring the objective pupil function is no longer a real quantity. The latter results in the fact that the formerly real transfer functions $T_{r,i}(\boldsymbol{f})$ become generally complex. However, as it turns out for our special case of an annular detector response, the transfer functions inherit the following properties

$$\begin{aligned} T_r &= \mathcal{R}(T_r) + i\underbrace{\mathcal{I}(T_r)}_{\approx 0} = \mathcal{R}(T_r) \\ T_i &= \underbrace{\mathcal{R}(T_i)}_{\approx 0} + i\mathcal{I}(T_i) = i\mathcal{I}(T_i)\,, \end{aligned} \tag{4.16}$$

leaving the real transfer function T_r a real function and the imaginary transfer function T_i purely imaginary. Figure 4.13 shows the respective transfer functions corresponding to the experimental situation of Fig. 4.12. Note, that

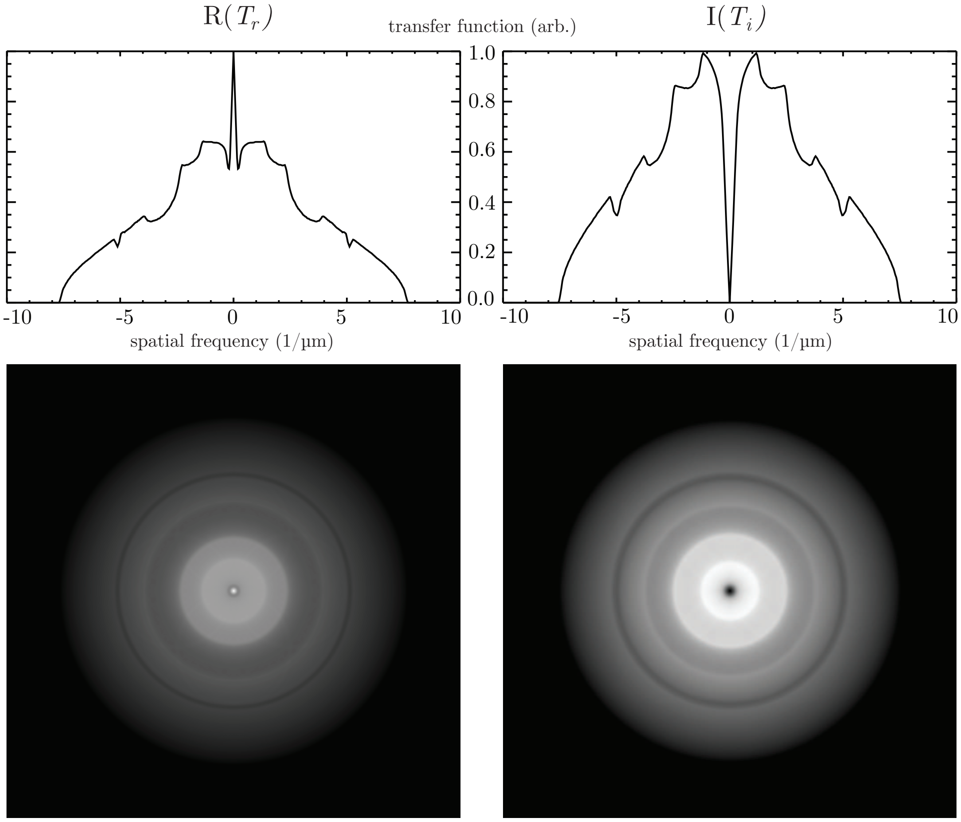

Figure 4.13: Transfer functions for the scanning Zernike experiment. The line profiles are taken through the center of each transfer function and are scaled relatively to their individual maximum.

the transfer functions do not extend to the edge of the frequency grid as they usually do in scanning or incoherent imaging system. This does not come as a surprise, since the annular detector which is supposed to match the phase ring projection has a smaller numerical aperture as the pupil function. In the usual case of conventional bright field imaging the pupil and detector functions have the same numerical aperture, hence the frequency transfer functions extend all the way to the edge (Nyquist frequency) of the frequency space.

From Sec. C.2 we know that for individual and symmetric detector segments and a symmetric pupil the imaginary transfer function T_i is zero. This means that one cannot obtain any phase contrast information from the specimen, since all its phase information is contained in H_i and the corresponding transfer of this information is absent because $T_i = 0$. The annular detector for scanning type Zernike phase contrast is such a individual and symmetric segment; however, through the addition of the phase ring to the pupil $T_i \neq 0$, and consequently we can obtain phase contrast information about the sample from this individual and symmetric segment. Removing the phase ring from the setup will henceforth result in the loss of phase contrast information. We will discuss this case in the following section.

4.3.4 Removal of Phase Ring

In order to further investigate the scanning Zernike imaging properties let us consider the situation where we still use the annular detector to record the image, but remove the phase ring from the setup (stop in front of detector remains).

Figure 4.14(a) shows the same pair of polystyrene spheres from Fig. 4.9, again in scanning Zernike phase contrast and also with the phase ring taken out (Fig. 4.14(b)). A clear difference is noticeable; only the outlines of the spheres with their edges are visible in the case without the phase ring. While the Zernike images show a representation of the sample density, there is no noticeable contrast to the sphere interior when no phase ring is present. Line profiles through both images are shown in Fig. 4.14(c) further emphasizing the absence of contrast to the sphere interior in the case without phase ring.

While by removing the phase ring almost no contrast to the latex spheres was observable, the edges of the spheres were still somewhat visible. This hints at a selective spatial frequency imaging behavior, where the imaging system is only sensitive to a certain range of spatial frequencies (*i. e.* sample features). In order to investigate this further Fig. 4.15 shows again the plastic zone plate of Fig. 4.10 in Zernike phase contrast and this time also with the phase ring removed (Fig. 4.15(b)). In addition a line profile through both images is given. While for the Zernike case the contrast is constant and then falls off as expected for an incoherent imaging system, the case without phase ring has

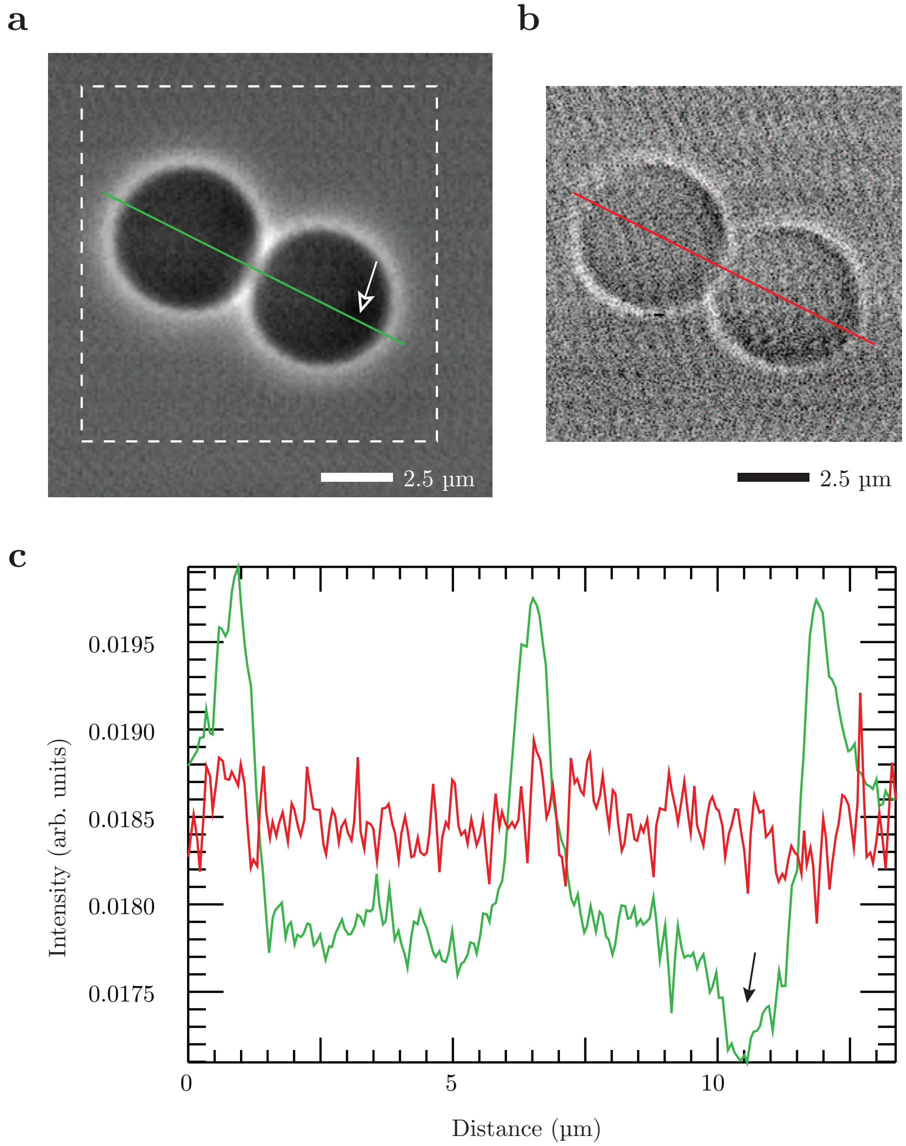

Figure 4.14: (**a**) Scanning Zernike image from a pair of polystyrene spheres (identical to Fig. 4.9a); (**b**) same pair of spheres imaged with the phase ring removed from the setup, the scan area is identified in (a) with a dashed box. (**c**) Line profiles through (a) (red) and (b) (green) as indicated in the images. The arrow in panels (a) and (c) indicates the position of radiation damage to the right sphere. (Note: (b) was imaged with a 50 nm step size, the image was linearly scaled down to match a, which had a step size of 100 nm.)

selective frequency response. The larger structures (low spatial frequencies) have significant poorer contrast. In the intermediate region up to the smaller features of the sample the contrast is comparable for both. However, despite this similarity for both cases, arrows in Fig. 4.15 point to a few selected fine features that are (among others) only resolved by the Zernike method. Also remember from Fig. 4.10(b) that conventional absorption imaging showed no noticeable contrast to the plastic zone plate features - some sort of phase contrast sensitivity is therefore indicative.

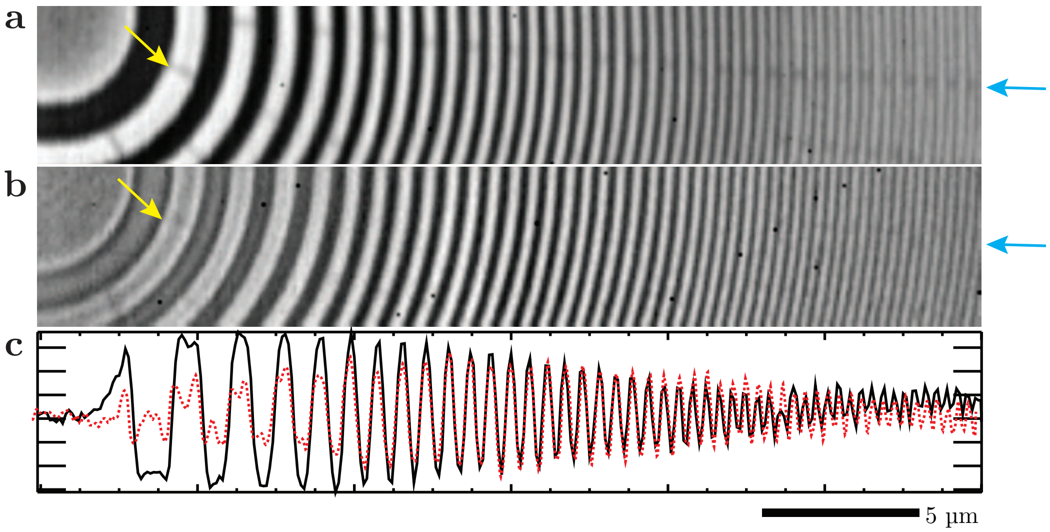

Figure 4.15: (**a**) Scanning Zernike image of a subregion of the plastic zone plate shown in Fig. 4.10 (rotated). (**b**) Same as (a) but with phase ring removed. (**c**) Line profile through first image rows of (a) (black) and (b) (red).

There are a few hypotheses that could potentially explain the observed imaging behavior. One hypothesis concerns the realization that in the case where the phase ring is not present and we use the annular detector to record the image, we have a limited conventional bright field imaging setup. Opposed to the usual case where the total transmitted intensity (bright field cone) gets collected as the image signal, we have an annular detector that only records a subregion of the bright field intensity, which might cause the selective imaging response. If we were to collect a different annular region of the bright field, the imaging response should change accordingly. Unfortunately, we do not have experimental data to support this claim as of yet. However, the detector plane intensity simulation of Fig. 3.5 can illustrate the situation. Depending which annular subregion of the far-field intensity is recorded in connection with the spatial frequency content of the respective scan point (compare different scan points in the figure) a selective feature sensitivity should be expected.

From the transfer function point of view from Sec. 4.3.3 we would not expect any phase contrast sensitivity because the corresponding imaginary part transfer function T_i is zero in the case without phase ring. However, a defocus effect could potentially explain the observed behavior, but requires further investigations and experiments which are beyond the scope of this work.

4.4 Application Scanning Zernike in X-ray Fluorescence Microscopy

Scanning Zernike phase contrast can prove particularly useful for x-ray fluorescence microscopy, similarly as the differential and quantitative phase contrast methods we discussed in Ch. 3. In the following we will consider the possible influence on the XRF images through the addition of the scanning Zernike capability in form of the phase ring. The section will conclude with a few biological imaging examples.

4.4.1 Influence on X-ray Fluorescence Imaging Properties

In the previous cases where we utilized phase contrast in combination with scanning x-ray fluorescence microprobes no alterations to the optical setup were made that could influence the XRF imaging properties. We simply utilized the transmission signal, which otherwise would have been left unused. Now the situation is different. The implementation of Zernike phase contrast into a scanning microscope requires the addition of a phase ring in front of the focussing zone plate. In which way this might alter the fluorescence imaging performance needs to be investigated.

The intensity profile in the focal plane (point spread function) of the XRF microprobe is the characteristic quantity to consider, since it defines the stimulated x-ray fluorescence emission. In Fig. 4.16(a) we show the simulated intensity point spread function (PSF) for a zone plate including a central stop without and with a Zernike phase ring in place. If we consider the fractional area of the total objective pupil which is shadowed by the partially absorbing phase ring, the total intensity that gets focused by this objective and reaches the focal plane is reduced by only 2%. We note that the intensity in the central maximum of the PSF shown in the wave field simulation of Fig. 4.16(a) is reduced by 9% compared to the case without phase ring. This is due to

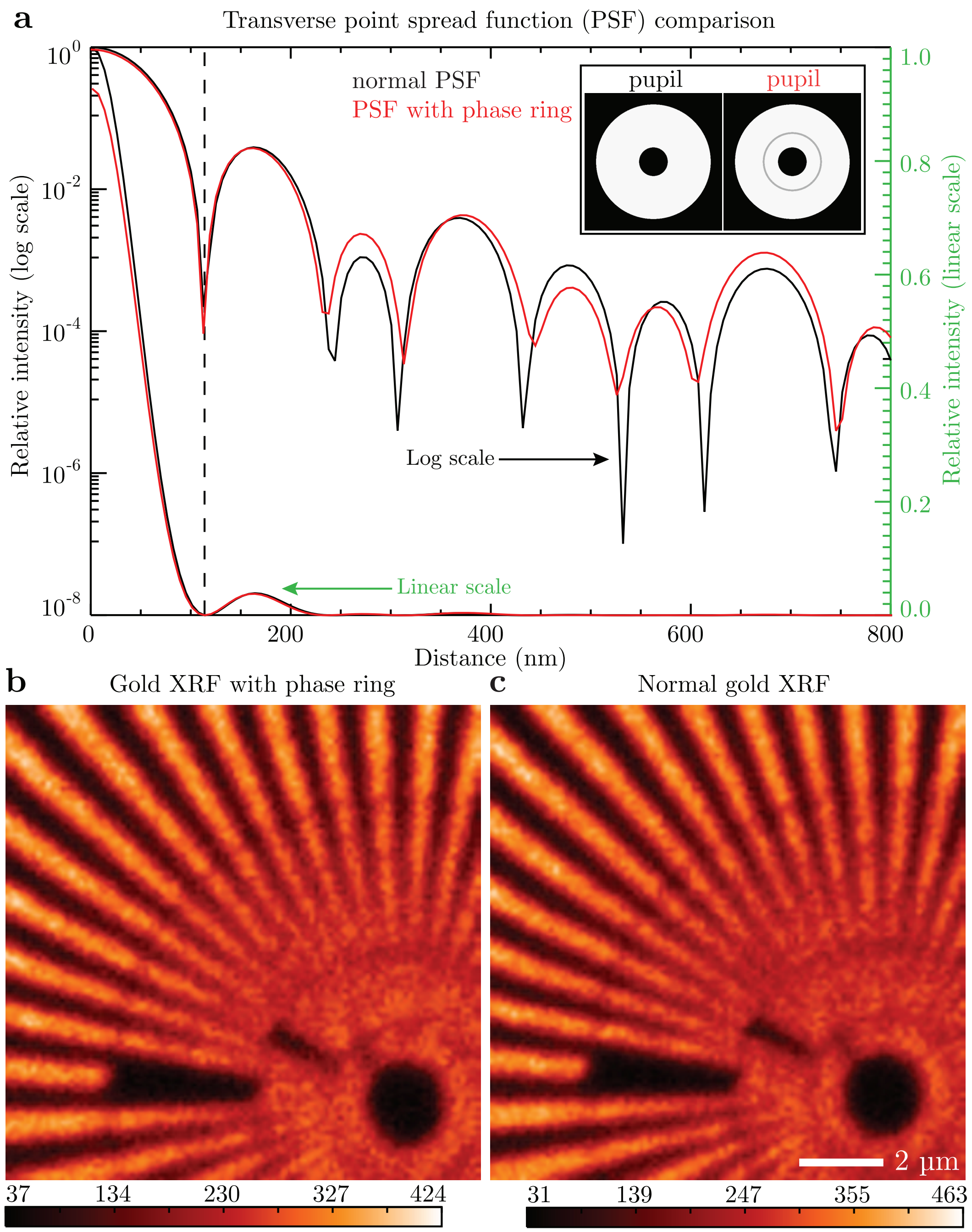

Figure 4.16: Effect of phase ring on x-ray fluorescence (XRF) imaging properties. a Computed PSF comparison with and without phase ring in linear and logarithmic scale. The inlay shows the objective transmission profile of the respective pupil functions. Experimental gold x-ray fluorescence signal of a Siemens star test pattern b with and c without phase ring present.

the redistribution of intensity into the side lobes of the PSF, giving rise to a small (7%) DC offset of the scanning signal, which is similar to the experimental background in most cases. Most importantly the shape of the central peak, in particular the position of the first minimum is unchanged, leading to no loss in imaging resolution. Figures 4.16(b) and 4.16(c) show experimental gold fluorescence images with and without the phase ring in place of the same gold star test pattern of Fig. 4.8. These fluorescence images are in very good qualitative and quantitative agreement with what we would expect from the PSF simulations. We do not see any noticeable effects in terms of image representation and resolution. Furthermore, the counts of both images differ by the predicted amount of approximately 9%.

Hence, we can conclude that the addition of the Zernike phase contrast capability leaves the PSF of the XRF microprobe largely unmodified and thus does not significantly compromise its trace element fluorescence optical response.

4.4.2 Biological Imaging Examples

To illustrate the imaging capabilities of the scanning Zernike phase contrast method for biological specimens also in connection with x-ray fluorescence Fig. 4.17, 4.18, 4.19, 4.20, 4.21 and 4.22 show various examples.

Mouse Fibroblast

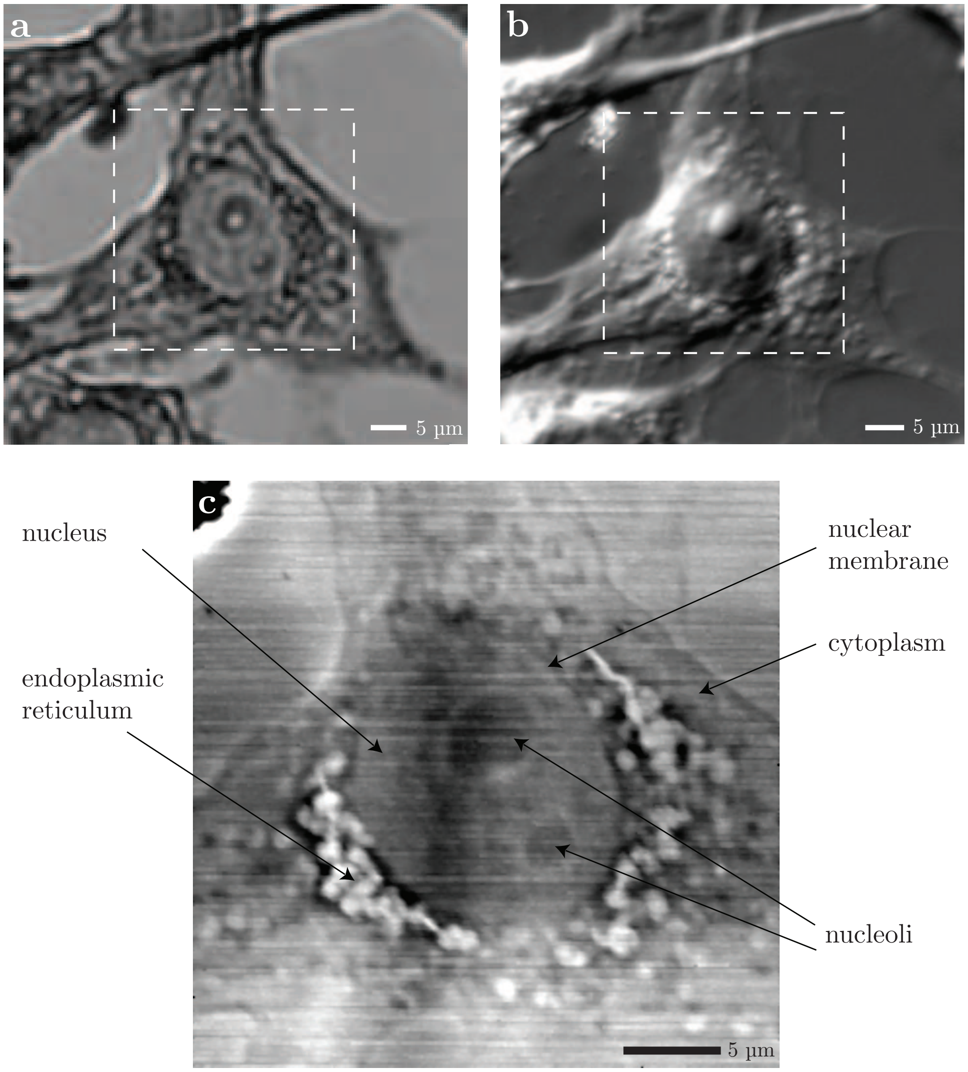

Figure 4.17: NIH 3T3 mouse fibroblast cell in (**a**) bright field and (**b**) differential interference contrast microscopy with visible light; the outlined area is the respective region of the (**c**) scanning Zernike image. Experimental details for scanning data: 10 keV, steps 100 nm, ZP 160 μm, dr_N 50 nm, stop 40 μm, annular detector arrangement, phase ring ID 75 μm and OD 85 μm. Experimental details for visible light data: 40X Leica objective.

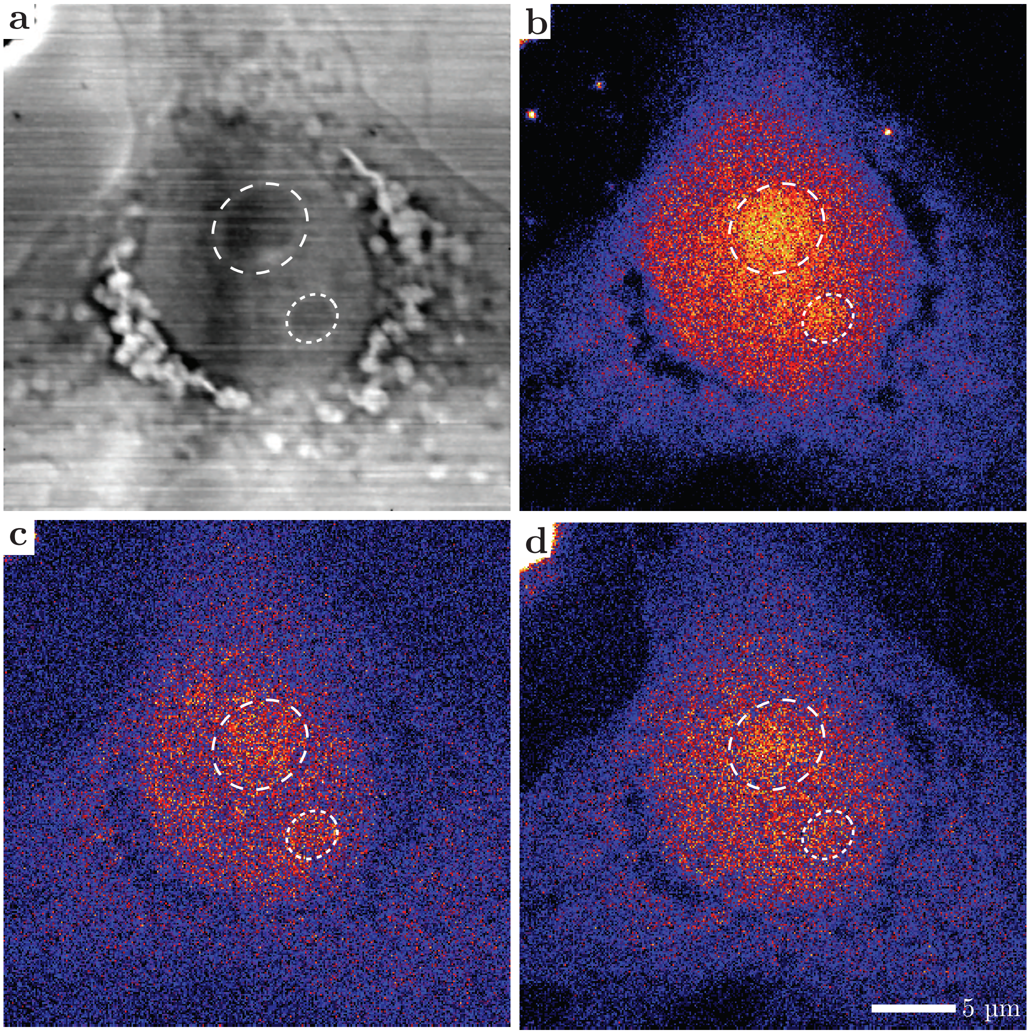

Figure 4.18: NIH 3T3 mouse fibroblast in (**a**) scanning Zernike and XRF of (**b**) Cl, (**c**) P and (**d**) Zn. Experimental details for scanning data: 10 keV, steps 100 nm, ZP 160 μm, dr_N 50 nm, stop 40 μm, annular detector arrangement, phase ring ID 75 μm and OD 85 μm.

Cardiac Mycocyte

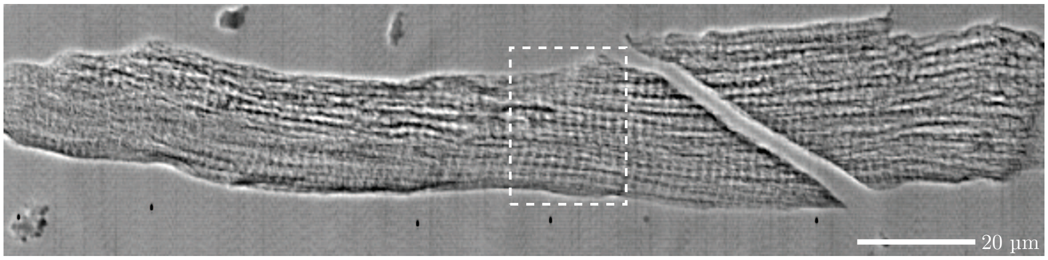

Figure 4.19: Scanning Zernike phase contrast image of a whole mouse cardiac myocyte; the dashed region indicates the area of a successive scan shown in Fig. 4.20. Experimental details for scanning data: 10 keV, steps 100 nm, ZP 160 μm, dr_N 50 nm, stop 40 μm, annular detector arrangement, phase ring ID 75 μm and OD 85 μm.

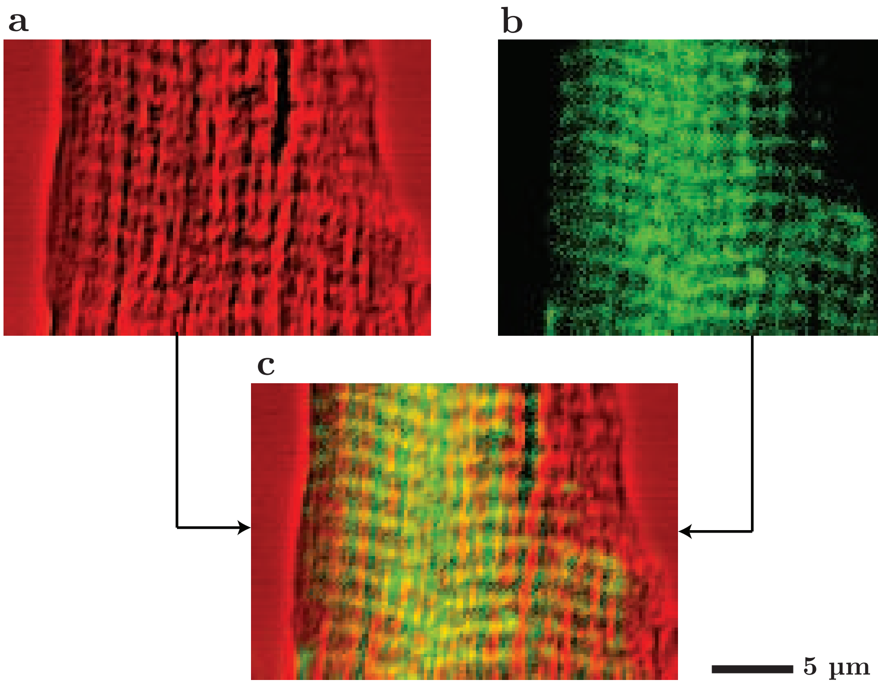

Figure 4.20: Cardiac myocyte in (**a**) Zernike and (**b**) Zn XRF of a subregion of Fig. 4.19. (**b**) Color addition image of (a) and (b); a yellow color indicates the colocation of high (red) image values from (a) with high (green) images values from (b). Experimental details for scanning data: 10 keV, steps 100 nm, ZP 160 μm, dr_N 50 nm, stop 40 μm, annular detector arrangement, phase ring ID 75 μm and OD 85 μm.

Flagellate

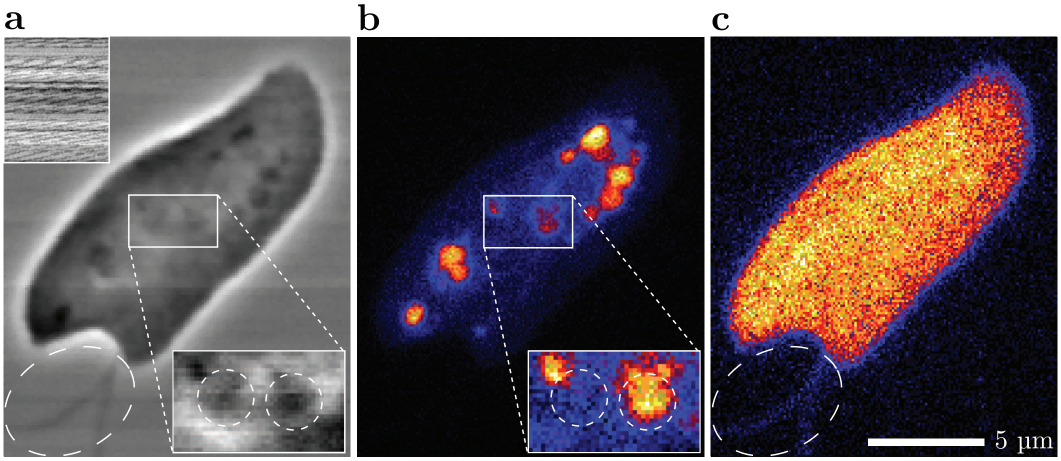

Figure 4.21: Freshwater flagellate *Cryptomonas* in (**a**) Zernike, (**b**) P and (**c**) S XRF respectively. Magnified subregions on (a) and (b) are separately scaled from the main image to highlight features. Experimental details for scanning data: 10 keV, steps 100 nm, ZP 160 μm, dr_N 50 nm, stop 40 μm, annular detector arrangement, phase ring ID 75 μm and OD 85 μm.

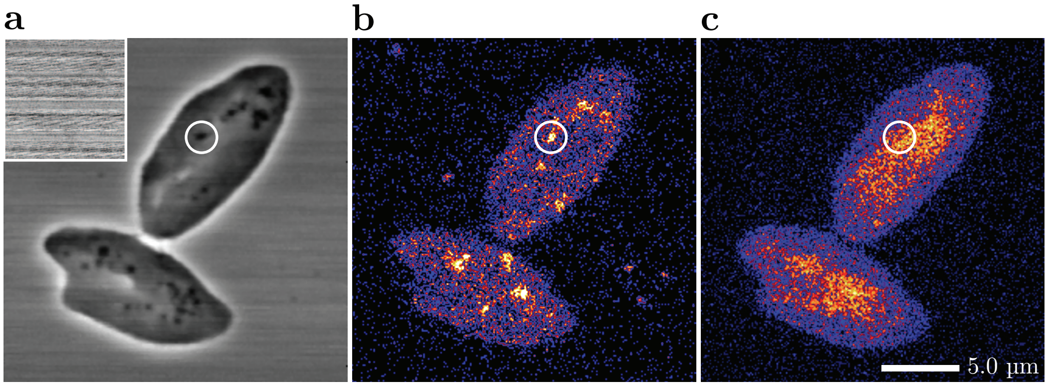

Figure 4.22: Freshwater flagellate *Cryptomonas* in (**a**) Zernike, (**b**) Mn and (**c**) Zn XRF respectively. Experimental details for scanning data: 10 keV, steps 100 nm, ZP 160 μm, dr_N 50 nm, stop 40 μm, annular detector arrangement, phase ring ID 75 μm and OD 85 μm.

Chapter 5

Reconstruction of Full-field and Scanning Zernike Phase Contrast

Zernike phase contrast images suffer from artifacts due to the nature of how the contrast is formed, which is typically through a phase shifting ring and a corresponding annular illumination for full-field or detection for scanning. A halo appearance around feature edges and a shade-off effect across extended uniform regions are common in Zernike images. These artifacts can make quantitative interpretations hard and lead to a shell-like and flat impression of tomographic reconstructions from Zernike phase contrast data, making image segmentation difficult.

By combining concepts from Ch. 3 and Ch. 4 we present a method to remove Zernike artifacts through a reconstruction technique, resulting in images better suitable for quantitation and tomography. A brief explanation of the origin of the Zernike phase contrast artifacts is followed by a discussion of the reconstruction method; we conclude the chapter with initial reconstruction results from full-field and scanning Zernike phase contrast data.

5.1 Artifacts of Zernike Phase Contrast

Zernike phase contrast is inherently associated with image artifacts; an example of such is given by Fig. 4.9. The halo appearance around feature edges and a shade-off across more uniform regions is a consequence of the finite width and shape of the phase mask, which causes a loss of low spatial frequencies and an over-emphasis of high spatial frequencies. Figure 5.1 identifies the location where this loss of low spatial frequency information is best illustrated for both the full-field and scanning Zernike phase contrast case.

In the full-field Zernike mode the back-focal plane of the objective lens contains the phase shifting ring. Here, undiffracted light coming from the specimen is phase shifted by the ring as illustrated by Fig. 5.2(a); light that is diffracted by small features in the specimen (high spatial frequencies) does not get phase shifted. For sample features with a low spatial frequency content the light is not diffracted enough and at least partially overlaps with the phase shifting mask (*i. e.* ring) and, therefore, gets erroneously phase shifted.

For scanning Zernike phase contrast we consider the detector plane of the setup shown in Fig. 5.2(b), which displays the far-field illumination annulus including the phase ring projection (also compare to Fig. 4.7). The phase contrast information in this case comes from the overlap of phase shifted light of the 0th order pupil with non-phase shifted light from higher diffracted orders. Remember from Ch. 4 that the recored signal in the far-field for scanning Zernike corresponds to the area covered by the phase ring projection in the 0th order pupil. High spatial frequencies diffract the pupil, resulting in the required interference of phase shifted light (from the diffracted pupil) and non-

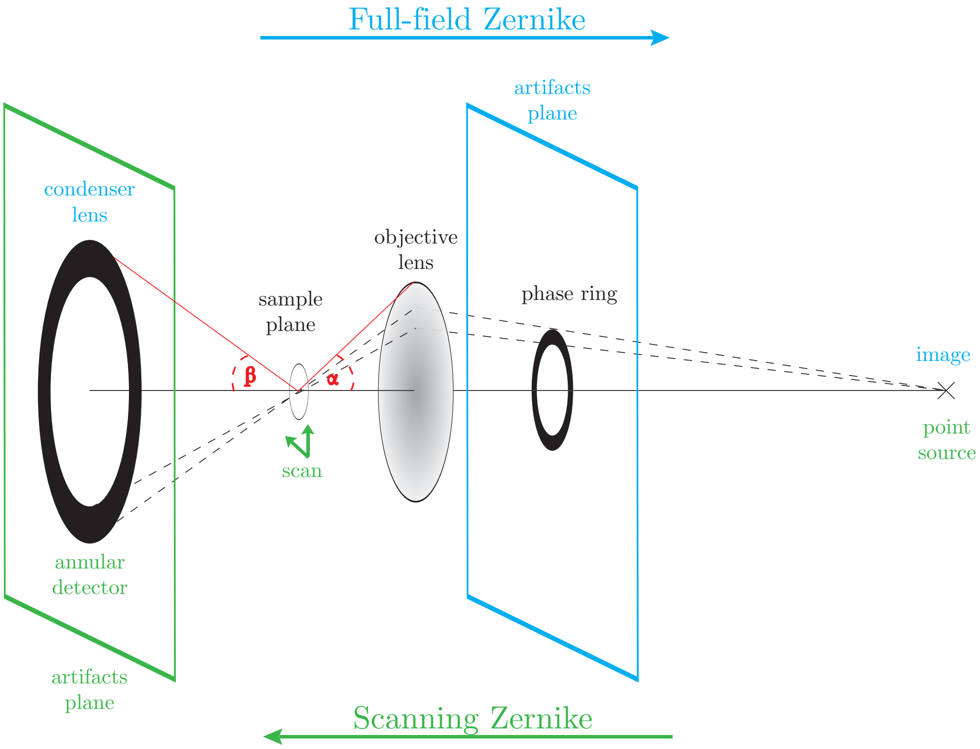

Figure 5.1: Identification of locations for the artifact interpretation in the full-field (blue) and scanning (green) Zernike phase contrast modes.

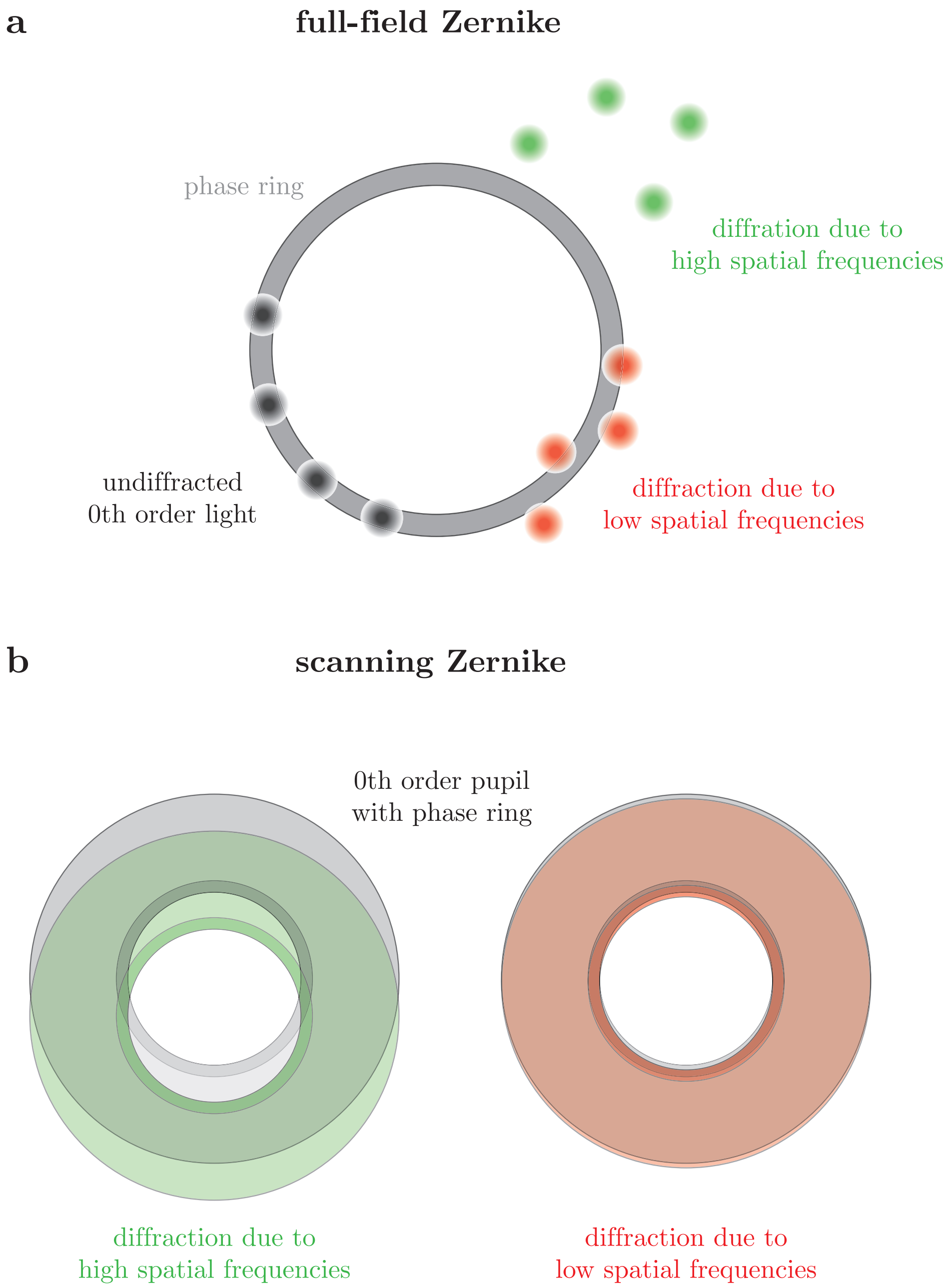

Figure 5.2: Artifacts.

phase shifted light (from the 0th order). On the other hand, the low spatial frequency information is reflected by a hardly diffracted pupil. So most of the light collected by the annular detector is interference of phase shifted light from the 0th order with phase shifted light from the diffracted order, causing no significant image contrast.

The loss of low spatial frequencies is inherent to the Zernike phase contrast method and in an optimal situation would not be present in the case of a infinitely thin width phase mask, which for practical reasons cannot be realized[1]. It is common to realize Zernike phase contrast with a ring shaped phase mask; however, differently shaped phase shifting structure, *e. g.* an array of dots as done by Stampanoni *et al.* [71], has the advantage to reduce the Zernike artifacts by a good amount.

5.2 Adaption of Fourier Filter Reconstruction for Zernike Artifact Removal

By playing the reciprocity approach of Ch. 4 in the opposite way we can utilize techniques from scanning for full-field imaging. The Fourier Filtering method for reconstruction of differential phase contrast data of Sec. 3.3 in its essence is an artifact removal process. Differential phase contrast images are a representation of the sample where low spatial frequencies are suppressed, resulting in an over-emphasis of high spatial frequencies, *i. e.* edge enhancement, which in addition also has a directional dependence.

By realizing this, we can apply the filtering method to Zernike phase contrast images in order to remove the inherent artifacts. To do so, one needs to pay attention to the respective roles of the optical components and their equivalence in the two respective cases. In Ch. 2 the image formation of both types of microscopes is discussed in detail and can be used as a roadmap for translating the filtering method. The key points to realize are that the role of the objective lens is the same in both cases, and so is the phase ring. The condenser in the full-field mode becomes the detector in the scanning case. By keeping these things in mind, one can directly apply the filtering method to full-field imaging.

In order to simplify the implementation, one can combine the phase ring with the objective pupil to one optical element for analysis purposes.

A further modification to the scanning filtering method will be the amount of information at hand to do the reconstruction process. In our initial ap-

---

[1] An infinitely thin width phase mask will also require an infinitely thin width illumination, resulting in no photons actually illuminating the sample.

proach of Sec. 3.3 we had information from multiple segments (*e. g.* 8 to 10, or more), which are combined in the reconstruction process to yield the absorption and phase shift of the specimen. This situation corresponds to a sufficiently determined problem; the amount of information through the collected data is enough to extract the two unknown quantities. In the Zernike case we only have one image (representative of one detector signal) and, therefore are facing an under-determined problem. An initial approach to address this issue is a *phase-only* approximation. We will assume that the sample is a pure phase structure, which successively reduced the number or unknowns to one (phase) instead of two (phase and absorption). The image formation in terms of transfer functions analogous to Eq. 3.40 then becomes:

$$S_k(\boldsymbol{f}_\mathrm{s}) = \Delta(\boldsymbol{f}_\mathrm{s})\, C_k(0,0,\boldsymbol{f}_\mathrm{s}) + \mathrm{i}\, H_i(\boldsymbol{f}_\mathrm{s})\, T_i^{(k)}(\boldsymbol{f}_\mathrm{s})\,, \tag{5.1}$$

which is obtained by setting the real part specimen contribution H_r to zero. This inherently also assumes the rigorous weak specimen approximation (see Sec. 3.3.5). The filter function for the phase-only approximation then is given by

$$W^{\mathrm{phase}} = \frac{T_i^*}{|T_i|^2 + \beta_i} \qquad \text{for } \boldsymbol{f} \neq 0 \text{ and all } k; \tag{5.2}$$

for a detailed derivation see Appendix C.3.5. Note that there is only one such filter function, as we also only have one image or detector signal.

The noise parameter for the Zernike filtering method in the initial application is simply chosen to yield the best visible result; future improvements of the technique will include a way to determine a specimen and spatial frequency dependent noise parameter as used in the scanning filtering method.

5.3 Reconstruction Examples

In Figs. 5.3, 5.4 and 5.5 we show some initial reconstructions of Zernike phase contrast data. While the results include some encouraging aspect of removing the Zernike artifacts and re-establishing the low spatial frequency information many aspects remain that need to be addressed, including phase ramps probably due to misalignment (Fig. 5.4(d)) and proper noise treatment. In the filtered scanning Zernike image of Fig. 5.5(c,d) we note that the low spatial frequencies have been corrected in the center of the sphere; however, the halo at the edges is not completely corrected, but washed out.

Filtered full-field Zernike

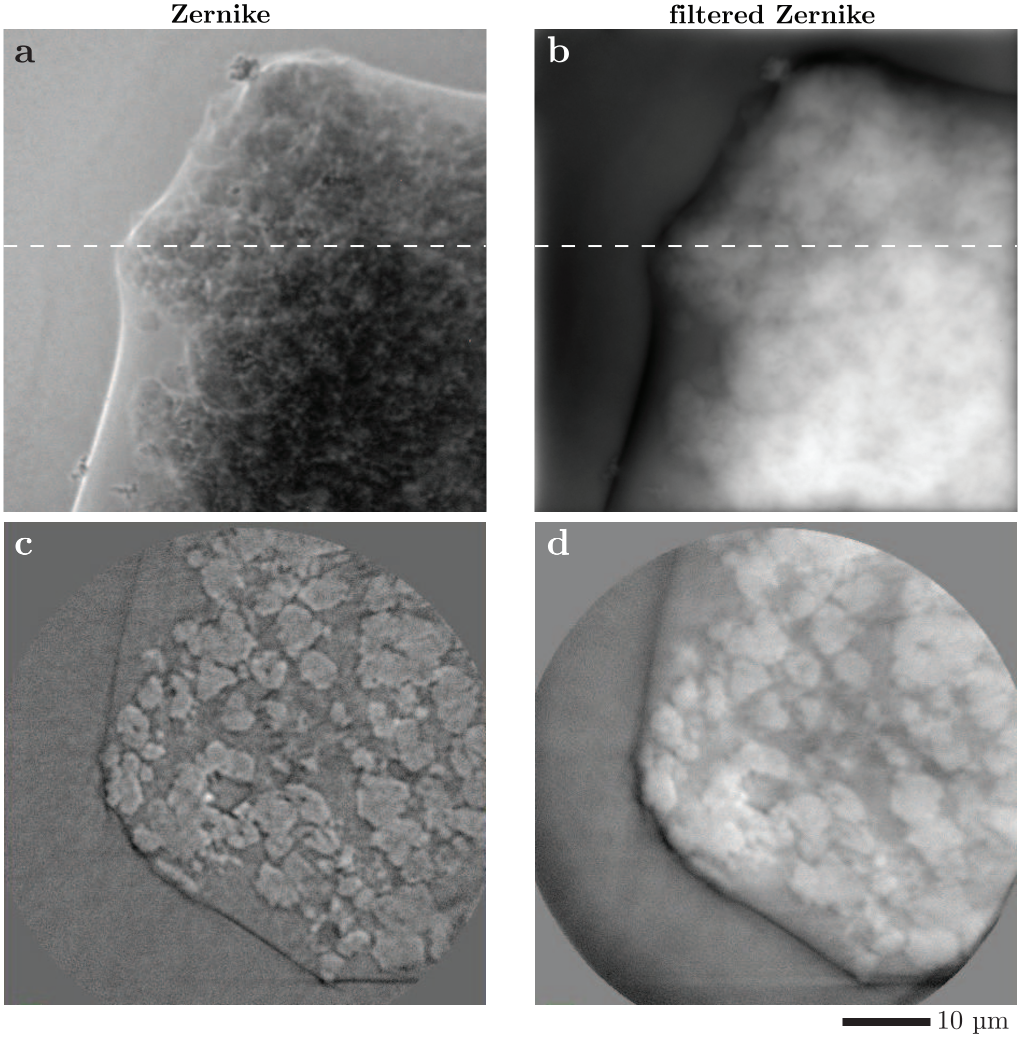

Figure 5.3: Oil shale embedded in epoxy. (**a**) Zernike phase contrast projection and (**c**) slice through tomographic reconstruction. (**b**) Filtered Zernike and (**d**) slice through tomographic reconstruction. Experimental details for full-field data: Xradia nanoXCT labtool, large FOV mode, 8.04 keV, pixel size 65 nm, ZP 320 μm, dr_N 30 nm.

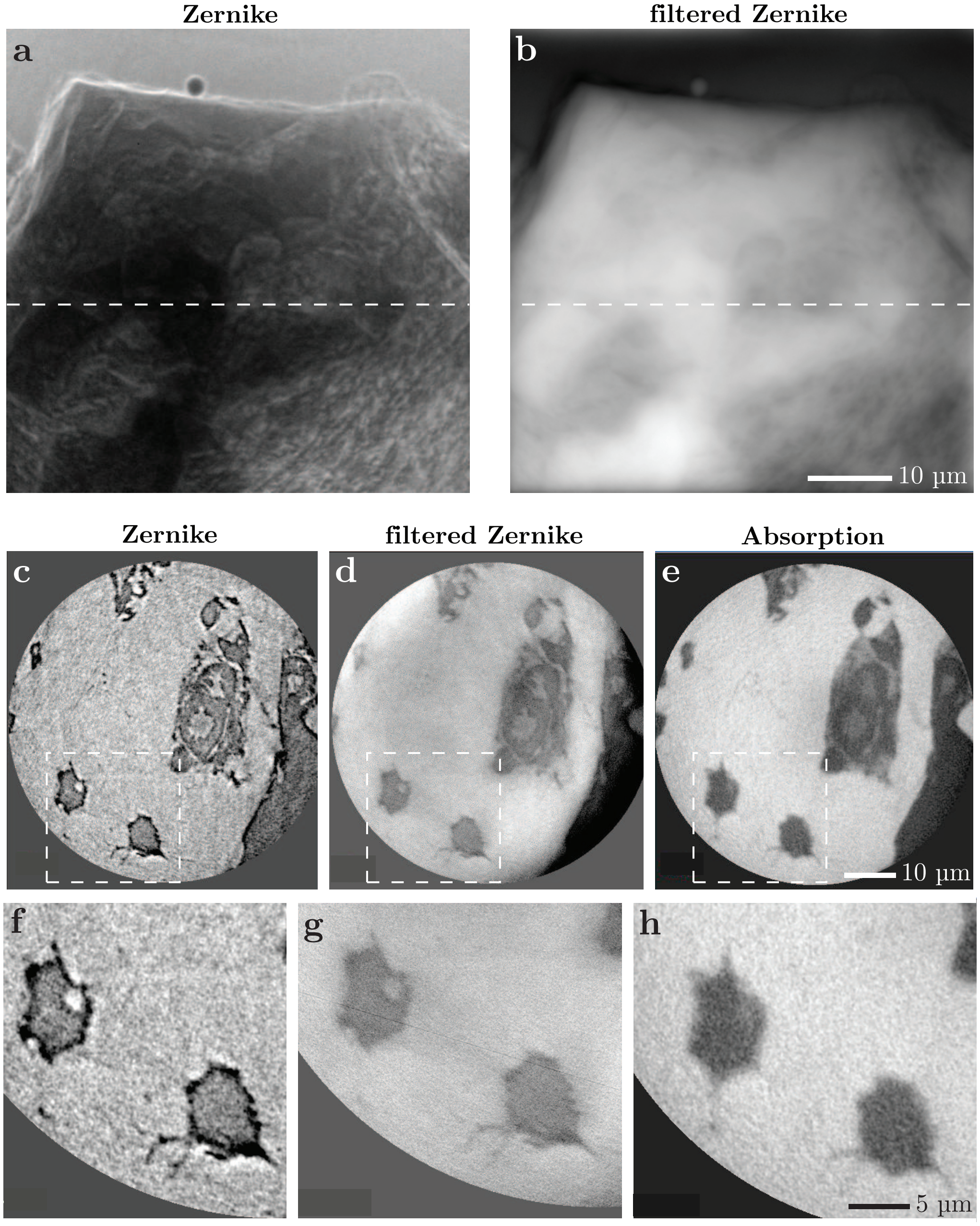

Figure 5.4: Bone stained with Os. (**a**) Zernike phase contrast projection and (**c, f**) slice through tomographic reconstruction. (**b**) Filtered Zernike and (**d, g**) slice through tomographic reconstruction; (**e, h**) slices through tomographic reconstruction of absorption contrast data. Experimental details for full-field data: Xradia nanoXCT labtool, large FOV mode, 8.04 keV, pixel size 65 nm, ZP 320 μm, dr_N 30 nm.

Filtered scanning Zernike

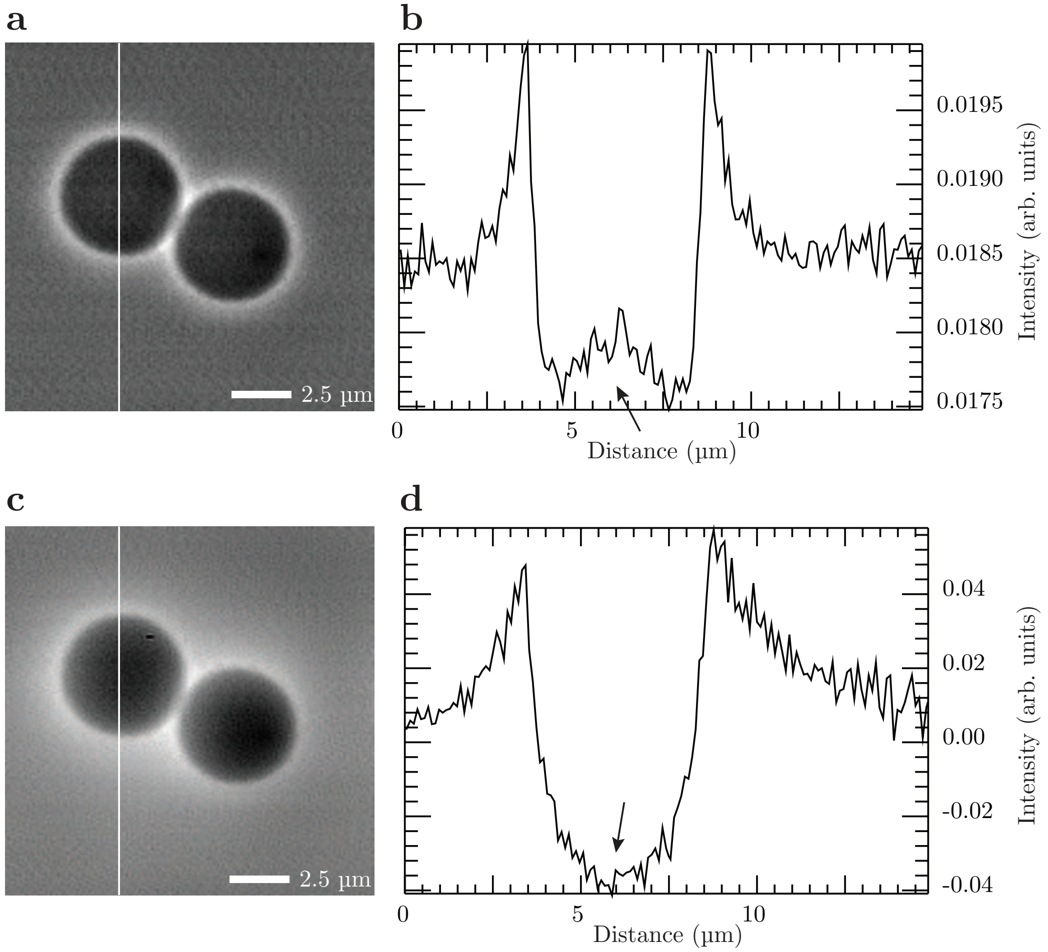

Figure 5.5: Polystyrene spheres in scanning and filtered Zernike phase contrast. (**a**) Scanning Zernike with (**b**) respective line profile. (**c**) Filtered scanning Zernike with (**d**) rspective line profile. Experimental details for scanning data: 10 keV, steps 100 nm, ZP 160 μm, dr_N 50 nm, stop 40 μm, annular detector arrangement, phase ring ID 75 μm and OD 85 μm.

Bibliography

[1] B. Hornberger, M. D. de Jonge, M. Feser, P. Holl, C. Holzner, C. Jacobsen, D. Legnini, D. Paterson, P. Rehak, L. Strüder, and S. Vogt. Differential phase contrast with a segmented detector in a scanning x-ray microprobe. *Journal of Synchrotron Radiation*, 15(4):355–362, Jul 2008.

[2] M. D. de Jonge, B. Hornberger, C. Holzner, D. Legnini, D. Paterson, I. McNulty, C. Jacobsen, and S. Vogt. Quantitative phase imaging with a scanning transmission x-ray microscope. *Physical Review Letters*, 100: 163902, 2008. doi: 10.1103/PhysRevLett.100.163902.

[3] M. D. de Jonge, S. Vogt, D. Legnini, I. McNulty, C. Rau, D. Paterson, B. Hornberger, C. Holzner, and C. Jacobsen. A method for phase reconstruction from measurements obtained using a configured detector with a scanning transmission x-ray microscope. *Nuclear Instruments and Methods in Physics Research A*, 582:218–220, 2007.

[4] M.D. de Jonge, B. Hornberger, C. Holzner, B. Twining, D. Paterson, I. McNulty, C. Jacobsen, and S. Vogt. Quantitative scanning differential phase contrast microscopy. *Journal of Physics: Conference Series*, 186: 012006, 2009. doi: 10.1088/1742-6596/186/1/012006.

[5] C. Holzner, M. Feser, M.D. de Jonge, B. Hornberger, S. Vogt, and C. Jacobsen. Comparison and unification of quantitative scanning phase contrast reconstruction methods. *in preparation*, 2010.

[6] C. Holzner, M.D. de Jonge, B. Hornberger, S. B. Baines, B.S. Twining, C. Jacobsen, and S. Vogt. Anatomy or pathology? concentration quantification in x-ray fluorescence microscopy through quantitative phase contrast. *in preparation*, 2010.

[7] C. Holzner, M. Feser, S. Vogt, B. Hornberger, S. B. Baines, and C. Jacobsen. Zernike phase contrast in scanning microscopy with x-rays. *in review at Nature Physics*, 2010.

[8] C. Holzner, B. Hornbeger, J. Gelb, and M. Feser. Artifact removal in zernike phase contrast through image reconstruction. *in preparation*, 2010.

[9] D. Attwood. *Soft X-rays and Extreme Ultraviolet Radiation*. Cambridge University Press, 1999.

[10] J. Kirz, C. Jacobsen, and M. Howells. Soft x-ray microscopes and their biological applications. *Quarterly Reviews of Biophysics*, 28(1):33–130, 1995. Also available as Lawrence Berkeley Laboratory report LBL-36371.

[11] B. Hornberger. *Phase contrast microscopy with soft and hard x-rays using a segmented detector*. PhD thesis, Department of Physics and Astronomy, Stony Brook University, 2007.

[12] A. H. Compton. A quantum theory of the scattering of x-rays by light elements. *Physical Review*, 21(5):483–502, 1923.

[13] B. L. Henke. Low energy x-ray interactions: photoionization, scattering, specular and Bragg reflection. In D. T. Attwood and B. L. Henke, editors, *Low Energy X-ray Diagnostics*, volume 75, pages 146–155, New York, 1981. American Institute of Physics. Monterey, 1981.

[14] B. L. Henke, E. M. Gullikson, and J. C. Davis. X-ray interactions: Photoabsorption, scattering, transmission, and reflection at E=50–30,000 eV, Z=1–92. *Atomic Data and Nuclear Data Tables*, 54:181–342, 1993.

[15] A. Thompson et al. X-ray data booklet. Lawrence Berkeley National Laboratory, University of California, Berkeley, CA 94720, January 2001. Online at `http://xdb.lbl.gov/`.

[16] S.W. Hell. Far-field optical nanoscopy. *Science*, 316:1153–1158, 2007.

[17] B. Niemann, D. Rudolph, and G. Schmahl. X-ray microscopy with synchrotron radiation. *Applied Optics*, 15:1883–1884, 1976.

[18] H. Rarback, J. Kenney, J. Kirz, and X. S. Xie. Scanning x-ray microscopy—first tests with synchrotron radiation˙ In E. A. Ash, editor, *Scanned Image Microscopy*, pages 449–456, London, 1980. Academic Press.

[19] H. Rarback, J. M. Kenney, J. Kirz, M. R. Howells, P. Chang, P. J. Coane, R. Feder, P. J. Houzego, D. P. Kern, and D. Sayre. Recent results from the Stony Brook scanning microscope. In G. Schmahl and D. Rudolph, editors, *X-ray Microscopy*, volume 43 of *Springer Series in Optical Sciences*, pages 203–215, Berlin, 1984. Springer-Verlag.

[20] M. Howells, C. Jacobsen, and T. Warwick. Principles and applications of zone plate x-ray microscopes. In P. W. Hawkes and J. C. H. Spence, editors, *Science of Microscopy*, chapter 13. Springer, first edition, 2006.

[21] A. Tkachuk, F. Duewer, H. Cui, M. Feser, S. Wang, and W. Yun. X-ray computed tomography in zernike phase contrast mode at 8 kev with 50-nm resolution using cu rotating anode x-ray source. *Nanocrystallography*, 222:650–655, 2007.

[22] D. M. Mills, editor. *Third-Generation Hard X-ray Synchrotron Radiation Sources*. Wiley-Interscience, 2002.

[23] J. W. Goodman. *Introduction to Fourier Optics*. McGraw-Hill, San Francisco, 1968.

[24] R. C. Gonzalez and R. E. Woods. *Digital Image Processing*. Prentice-Hall, 2nd edition, 2002.

[25] B. Hornberger, M. Feser, C. Jacobsen, S. Vogt, D. Legnini, D. Paterson, P. Rehak, G. De Geronimo, and B. M. Palmer. Combined fluorescence and phase contrast imaging at the Advanced Photon Source. In S. Aoki, Y. Kagoshima, and Y. Suzuki, editors, *X-ray Microscopy: Proceedings of the 8th International Conference*, IPAP Conference Series 7, pages 396–398, Tokyo, Japan, 2006. The Institute of Pure and Applied Physics (IPAP).

[26] G. Schmahl and D. Rudolph. Proposal for a phase contrast x-ray microscope. In P. C. Cheng and G. J. Jan, editors, *X-ray Microscopy: Instrumentation and Biological Applications*, pages 231–238, Berlin, 1987. Springer-Verlag.

[27] F. Zernike. Das Phasenkontrastverfahren bei der mikroskopischen Beobachtung. *Physikalische Zeitschrift*, 36:848–851, 1935.

[28] A. Momose. Recent advances in X-ray phase imaging. *Japanese Journal of Applied Physics*, 44(9A):6355–6367, 2005.

[29] G. R. Morrison. Some aspects of quantitative x-ray microscopy. In Rene Benattar, editor, *X-ray Instrumentation in Medicine and Biology, Plasma Physics, Astrophysics, and Synchrotron Radiation*, volume 1140, pages 41–49, Bellingham, Washington, 1989. Society of Photo-Optical Instrumentation Engineers (SPIE).

[30] G. R. Morrison. Phase contrast and darkfield imaging in x-ray microscopy. In C. Jacobsen and J. Trebes, editors, *Soft X-ray Microscopy*, volume 1741, pages 186–193, Bellingham, Washington, 1992. Society of Photo-Optical Instrumentation Engineers (SPIE).

[31] F. Polack and D. Joyeux. Soft x-ray interferential scanning microscopy: a feasibility assessment. In V. V. Aristov and A. I. Erko, editors, *X-ray Microscopy IV*, Proceedings of the 4th International Conference, Chernogolovka, Russia, September 20–24, 1993, pages 432–437, Chernogolovka, Russia, 1994. Bogorodskii Pechatnik. ISBN 5-900846-01-6.

[32] F. Polack, D. Joyeux, and D. Phalippou. Phase contrast experiments on the NSLS-X1A scanning microscope. In Thieme et al. [78], pages I–105–109.

[33] D. Joyeux and F. Polack. A wavefront profiler as an insertion device for scanning phase contrast microscopy. In Thieme et al. [78], pages II–201–205.

[34] B. Kaulich, F. Polack, U. Neuhäusler, J. Susini, Enzo di Fabrizio, and T. Wilhein. Diffracting aperture based differential phase contrast for scanning x-ray microscopy. *Opt Express*, 10(20):1112–1117, October 2002.

[35] B. Kaulich, T. Wilhein, E. Di Fabrizio, F. Romanato, M. Altissimo, S. Cabrini, B. Fayard, and J. Susini. Differential interference contrast x-ray microscopy with twin zone plates. *J. Opt. Soc. Am. A*, 19(4):797–806, 2002.

[36] M. Feser. *Scanning transmission x-ray microscopy with a segmented detector*. PhD thesis, Department of Physics and Astronomy, Stony Brook University, 2002.

[37] M. Born and E. Wolf. *Principles of Optics*. Cambridge University Press, Cambridge, seventh edition, 2006.

[38] C. Jacobsen, J. Kirz, and S. Williams. Resolution in soft x-ray microscopes. *Ultramicroscopy*, 47:55–79, 1992.

[39] P. Thibault, M. Dierolf, A. Menzel, O. Bunk, C. David, and F. Pfeiffer. High-resolution scanning x-ray diffraction microscopy. *Science*, 321:379–382, 2008.

[40] S. Vogt. *Investigations of Immunolabelled Structures in the Cell Nucleus by X-Ray and Light Microscopy.* PhD thesis, Mathematisch-Naturwissenschaftliche Fakultät, Georg-August-Universität zu Göttingen, 2001.

[41] H. von Helmholtz. *Crelle Journal*, 57, 1866.

[42] Lord Rayleigh. *Phil. Mag.*, 49:324, 1900.

[43] E. Zeitler and M. G. R. Thomson. Scanning transmission electron microscopy. *Optik*, 31:258–280, 359–366, 1970.

[44] C. J. R. Sheppard and T. Wilson. On the equivalence of scanning and conventional microscopes. *Optik*, 73:39–43, 1986.

[45] P. Thibault, M. Dierolf, C. M. Kewish, A. Menzel, O. Bunk, and F. Pfeiffer. Contrast mechanisms in scanning transmission x-ray microscopy. *Physical Review A*, 80:043813, 2009.

[46] C. Kottler, C. David, F. Pfeiffer, and O. Bunk. A two-directional approach for grating based differential phase contrast imaging using hard x-rays. *Optics Express*, 15(3):1175–1181, 2007.

[47] F. Pfeiffer, C. Kottler, O. Bunk, and C. David. Hard x-ray phase tomography with low-brilliance sources. *Physical Review Letters*, 98(10), 2007. doi: 10.1103/PhysRevLett.98.108105.

[48] M. P. Rimmer. Method for evaluating lateral shearing interferograms. *Applied Optics*, 13:623, 1974.

[49] J. Hermann. Least-squares wave front errors of minimum norm. *Journal of the Optical Society of America*, 70:28, 1980.

[50] W. H. Southwell. Wave-front estimation from wave-front slope measurements. *Journal of the Optical Society of America*, 70:998, 1980.

[51] M. R. Arnison, K. G. Larkin, C. J. R. Sheppard, N. I. Smith, and C. J. Cogswell. Linear phase imaging using differential interference contrast microscopy. *Journal of Microscopy*, 214:7–12, 2004.

[52] A. Menzel, C.M. Kewish, P. Kraft, B. Henrich, K. Jefimovs, J. Vila-Comamala, C. David, M. Dierolf, P. Thibault, F. Pfeiffer, and O. Bunk. Scanning transmission x-ray microscopy with a fast framing pixel detector. *Ultramicroscopy*, 110:1143–1147, 2010.

[53] M. N. Landauer, B. C. McCallum, and J. M. Rodenburg. Double resolution imaging of weak phase specimens with quadrant detectors in the STEM. *Optik*, 100(1):37–46, 1995.

[54] B. C. McCallum, M. N. Landauer, and J. M. Rodenburg. Complex image reconstruction of weak specimens from a three-sector detector in the STEM. *Optik*, 101(2):53–62, 1995.

[55] B. C. McCallum, M. N. Landauer, and J. M. Rodenburg. Complex image reconstruction of weak specimens from a 3-sector detector: correction. *Optik*, 103:131–132, 1996.

[56] M. N. Landauer. *Indirect modes of coherent imaging in high-resolution transmission electron microscopy*. PhD thesis, Clare College, Cambridge, UK, 1996.

[57] B. Hornberger, M. Feser, and C. Jacobsen. Quantitative amplitude and phase contrast imaging in a scanning transmission X-ray microscope. *Ultramicroscopy*, 107:644–655, 2007. doi: 10.1016/j.ultramic.2006.12.006.

[58] B. E. A. Saleh. Optical bilinear transformations: general properties. *Optica Acta*, 26(6):777–799, 1979.

[59] G. R. Morrison and J. N. Chapman. A comparison of three differential phase contrast systems suitable for use in STEM. *Optik*, 64(1):1–12, 1983.

[60] J. R. Palmer and G. R. Morrison. Differential phase contrast imaging in the scanning transmission x-ray microscope. In P. H. Bucksbaum and N. M. Ceglio, editors, *OSA Proceedings on Short Wavelength Coherent Radiation: Generation and Applications*, volume 11, pages 141–145, Washington, D. C., 1991. Optical Society of America.

[61] J. R. Palmer and G. R. Morrison. Differential phase contrast imaging in x-ray microscopy. In A. G. Michette, G. R. Morrison, and C. J. Buckley, editors, *X-ray Microscopy III*, volume 67 of *Springer Series in Optical Sciences*, pages 278–280, Berlin, 1992. Springer-Verlag.

[62] B. Hornberger, July 2010. Personal communication.

[63] B. S. Twining, S. B. Baines, N. S. Fisher, J. Maser, S. Vogt, C. Jacobsen, A. Tovar-Sanchez, and S. A. Sañudo-Wilhelmy. Quantifying trace elements in individual aquatic protist cells with a synchrotron x-ray fluorescence microprobe. *Analytical Chemistry*, 75:3806–3816, 2003.

[64] C.J. Fahrni. Biological applications of x-ray fluorescence microscopy: exploring the subcellular topography and speciation of transition metals. *Current Opinion in Chemical Biology*, 11:121–127, 2007.

[65] T. Paunesku, S. Vogt, J. Maser, B. Lai, and G. Woloschak. X-ray fluorescence microprobe imaging in biology and medicine. *Journal of Cellular Biochemistry*, 99:1489–1502, 2006.

[66] F. Zernike. How I discovered phase contrast. *Science*, 121(3141):345–349, 1955.

[67] M. Beleggia. A formula for the image intensity of phase objects in zernike mode. *Ultramicroscopy*, 108:953–958, 2008.

[68] T. Wilson and C. Sheppard. *Theory and Practice of Scanning Optical Microscopy.* Academic Press, New York, 1984.

[69] A. Siegel, G. Schmahl, and D. Rudolph. Method and device for producing phase-contrast images. *United States Patent*, 4,953,188, 1990.

[70] J. Maser, D. Legnini, S. Vogt, Z. Cai, and B. Lai. Side-branch fluorescence microprobe. unpublished, 2001.

[71] M. Stampanoni, R. Mokso, F. Marone, J. Vila-Comamala, S. Gorelick, P. Trtik, K. Jefimovs, and C. David. Phase-contrast tomography at the nanoscale using hard x rays. *Physical Review B*, 81:140105(R), 2010.

[72] J. D. Gaskill. *Linear Systems, Fourier Tranforms, and Optics.* Wiley-Interscience, 1976.

[73] E. O. Brigham. *The Fast Fourier Transform and its Applications.* Prentice Hall, 1988.

[74] R. N. Bracewell. *The Fourier Transform and its Applications.* McGraw-Hill, New York, second revised edition, 1986.

[75] N. Levinson. *The Wiener RMS (Root Mean Square) Error Criterion in Filter Design and Prediction*, volume XXV, pages 261–278. January 1947. Reprinted as an appendix to [79].

[76] W. H. Press, B. P. Flannery, S. A. Teukolsky, and W. T. Vetterling. *Numerical Recipes in C.* Cambridge University Press, Cambridge, UK, 1988.

[77] C. Jacobsen, S. Williams, E. Anderson, M. T. Browne, C. J. Buckley, D. Kern, J. Kirz, M. Rivers, and X. Zhang. Diffraction-limited imaging in a scanning transmission x-ray microscope. *Optics Communications*, 86: 351–364, 1991.

[78] J. Thieme, G. Schmahl, E. Umbach, and D. Rudolph, editors. *X-ray Microscopy and Spectromicroscopy*, Berlin, 1998. Springer-Verlag.

[79] N. Wiener. *Extrapolation, Interpolation and Smoothing of Stationary Time Series.* John Wiley & Sons, New York, 1949.

Appendix A

Definitions and Theorems

This following chapter details the notations, definitions and theorems useful for the presented work.

A.1 Notation

Here the notations used throughout this work are summarized.

> **Vectors** are indicated through bold font, *e. g.* $\boldsymbol{r}$, $\boldsymbol{f}$, and can either refer to two or three dimensions, depending on the context. The vectors absolute value is written as the non-bold form of the corresponding letter, *e. g.* $r \equiv |\boldsymbol{r}|$.
>
> **Real space coordinates** are expressed through the usual notation $\boldsymbol{r} = (x, y, z)$.
>
> **Fourier space coordinates** are given through $\boldsymbol{f} = (f_x, f_y, f_z)$. Note that these frequency coordinates do not contain a factor of 2π, opposed to $\boldsymbol{q} = (q_x, q_y, q_z)$ where $\boldsymbol{q} \equiv 2\pi\boldsymbol{f}$.
>
> **Fourier transforms** are represented by $\mathcal{F}$ and the inverse transform by $\mathcal{F}^{-1}$.
>
> **Real-space functions** are denoted with lower-case letters (*e. g.* h), and the corresponding **Fourier-transformed function** with the corresponding upper-case letter (*e. g.* H).
>
> **Integrals** run from $-\infty$ to $+\infty$ unless otherwise indicated.

As it is common for imaging theory **all functions are assumed to be two-dimensional** in planes perpendicular to the light propagation direction, unless otherwise explicitly stated. The reduction to a one-dimensional treatment is straightforward.

A.2 Fourier Transform and Relations

The forward Fourier transform of a function $g(\boldsymbol{r})$ is given by:

$$\mathcal{F}\{g(\boldsymbol{r})\} = G(\boldsymbol{f}) = \int \mathrm{d}^2\boldsymbol{r}\, g(\boldsymbol{r})\, \mathrm{e}^{-2\pi\mathrm{i}\boldsymbol{f}\,\boldsymbol{r}}\,. \tag{A.1}$$

The corresponding inverse transformation is:

$$\mathcal{F}^{-1}\{G(\boldsymbol{f})\} = g(\boldsymbol{r}) = \int \mathrm{d}^2\boldsymbol{f}\, G(\boldsymbol{f})\, \mathrm{e}^{2\pi\mathrm{i}\boldsymbol{f}\,\boldsymbol{r}}\,. \tag{A.2}$$

A.2.1 Successive Fourier Transforms

What happens when performing successive Fourier transformations on a function in the following

$$\Gamma(\boldsymbol{f}_2) \equiv \mathcal{F}_{\boldsymbol{f}_2}\{\mathcal{F}_{\boldsymbol{f}_1}\{g(\boldsymbol{r})\}\}\,? \tag{A.3}$$

Subscripts in the Fourier transform operators indicate which frequency coordinate the resulting function has after the transformation. Inserting the definition Eq. A.1 we find

$$\begin{aligned}
\Gamma(\boldsymbol{f}_2) &= \int \mathrm{d}^2\boldsymbol{f}_1 \int \mathrm{d}^2\boldsymbol{r}\, g(\boldsymbol{r})\, \mathrm{e}^{-2\pi\mathrm{i}\boldsymbol{f}_1\,\boldsymbol{r}}\, \mathrm{e}^{-2\pi\mathrm{i}\boldsymbol{f}_2\,\boldsymbol{f}_1} \\
&= \int \mathrm{d}^2\boldsymbol{r} \int \mathrm{d}^2\boldsymbol{f}_1\, g(\boldsymbol{r})\, \mathrm{e}^{-2\pi\mathrm{i}\boldsymbol{f}_1\,(\boldsymbol{r}+\boldsymbol{f}_2)} \\
&= \int \mathrm{d}^2\boldsymbol{r}\, g(\boldsymbol{r})\, \Delta(\boldsymbol{r} - (-\boldsymbol{f}_2)) \\
&= g(-\boldsymbol{f}_2)\,.
\end{aligned} \tag{A.4}$$

Where we have used the integral definition of the Dirac delta-function. The result is again the original input function, yet mirrored in the coordinate space. So performing four successive transforms resembles a unity operation

$$g(\boldsymbol{r}) = \mathcal{F}\{\mathcal{F}\{\mathcal{F}\{\mathcal{F}\{g(\boldsymbol{r})\}\}\}\}\,. \tag{A.5}$$

This behavior is analogous for the inverse transform.

A.2.2 Fourier Derivative Theorem

Here we derive the Fourier transformations of derived functions and point out the implications the result has towards performing derivatives and integrations through Fourier transforms.

We will start with a function $g(x)$ in one dimension that can be Fourier transformed; the n-th derivative of this function can then be written as follows

$$\partial_x^{(\mathrm{n})} g(x) = \partial_x^{(\mathrm{n})} \int \mathrm{d}f\, G(f)\, \mathrm{e}^{2\pi \mathrm{i} f\, x} = \int \mathrm{d}f\, (2\pi \mathrm{i} f)^n\, G(f)\, \mathrm{e}^{2\pi \mathrm{i} f\, x}\,, \tag{A.6}$$

which is the *Fourier Derivative Theorem*

$$\mathcal{F}\{\partial_x^{(\mathrm{n})} g(x)\} = (2\pi \mathrm{i} f)^n\, G(f) = (2\pi \mathrm{i} f)^n\, \mathcal{F}\{g(x)\}\,. \tag{A.7}$$

There are two immediate implications from A.7, which have very practical applications. First, we can perform integrations via Fourier transformations by solving for the function $g(x)$

$$g(x) = \mathcal{F}_x^{-1}\left\{\frac{\mathcal{F}_f\{\partial_{x'}^{(\mathrm{n})} g(x')\}}{(2\pi \mathrm{i} f)^n}\right\}. \tag{A.8}$$

Second, we can perform derivatives via Fourier transformations as follows

$$\partial_x^{(\mathrm{n})} g(x) = \mathcal{F}_x^{-1}\left\{(2\pi \mathrm{i} f)^n\, \mathcal{F}_f\{g(x')\}\right\}. \tag{A.9}$$

The extension of this to more dimensions is straightforward, as long as one keeps track of which frequency variable corresponds to which real space variable

$$\begin{aligned} \partial_x^{(\mathrm{n})} g(x,y) &= \partial_x^{(\mathrm{n})} \int \mathrm{d}f_x \int \mathrm{d}f_y\, G(f_x, f_y)\, \mathrm{e}^{2\pi \mathrm{i}(f_x\, x + f_y\, y)} \\ &= \int \mathrm{d}f_x \int \mathrm{d}f_y\, (2\pi \mathrm{i} f_x)^n\, G(f_x, f_y)\, \mathrm{e}^{2\pi \mathrm{i}(f_x\, x + f_y\, y)}\,. \end{aligned} \tag{A.10}$$

This immediately implies,

$$\begin{aligned}\boldsymbol{\nabla} g(\boldsymbol{r}) &= \boldsymbol{\nabla} \int \mathrm{d}^2\boldsymbol{f}\, G(\boldsymbol{f})\, \mathrm{e}^{2\pi \mathrm{i} \boldsymbol{f}\,\boldsymbol{r}} \\ &= \int \mathrm{d}^2\boldsymbol{f}\, (2\pi \mathrm{i} \boldsymbol{f})\, G(\boldsymbol{f})\, \mathrm{e}^{2\pi \mathrm{i} \boldsymbol{f}\,\boldsymbol{r}}\,.\end{aligned} \tag{A.11}$$

For a more detailed treatment see Gaskill [72, Ch. 7.3].

A.2.3 Fourier Transform Properties and Symmetries

Here we summarize the basic properties of Fourier transforms in Table A.1. Symmetry properties of Fourier transforms of complex functions are listed in Table A.2.

Property	Real space	Fourier space
Linearity	$a \cdot g(\boldsymbol{r}) + b \cdot h(\boldsymbol{r})$	$a \cdot G(\boldsymbol{f}) + b \cdot H(\boldsymbol{f})$
Symmetry[a]	$G(\boldsymbol{r})$	$g(-\boldsymbol{f})$
Scaling	$g(a \cdot \boldsymbol{r})$	$1/\lvert a\rvert\, G(\boldsymbol{f}/a)$
Shift	$g(\boldsymbol{r} - \boldsymbol{r}_0)$	$\exp(-2\pi \mathrm{i} \boldsymbol{r}_0 \boldsymbol{f})\, G(\boldsymbol{f})$
Modulation	$\exp(+2\pi \mathrm{i} \boldsymbol{r} \boldsymbol{f}_0)\, g(\boldsymbol{r})$	$G(\boldsymbol{f} - \boldsymbol{f}_0)$
Derivative[b]	$\partial g(\boldsymbol{r})/\partial x$	$2\pi \mathrm{i} f_x\, G(\boldsymbol{f})$

[a] In other words, a double forward FT reproduces the original function, reflected about the origin (see Appendix A.2.1 for a derivation of this property).

[b] see Appendix A.2.2 for a derivation of this property and related consequences.

Table A.1: Fourier transform properties (after Brigham [73, Table 3.2]).

Real space $g(\boldsymbol{r})$	Fourier space $G(\boldsymbol{f})$
Real	Real part even, imaginary part odd
Imaginary	Real part odd, imaginary part even
Real even, imaginary odd	Real
Real odd, imaginary even	Imaginary
Real and even	Real and even
Real and odd	Imaginary and odd
Imaginary and even	Imaginary and even
Imaginary and odd	Real and odd
Complex and even	Complex and even
Complex and odd	Complex and odd

Table A.2: Fourier transform symmetries (after Brigham [73, Table 3.1]).

A.2.4 Parseval's Theorem and the Conservation of Energy

Parseval's theorem states

$$\int \mathrm{d}^2\boldsymbol{r}\ |g(\boldsymbol{r})|^2 = \int \mathrm{d}^2\boldsymbol{f}\ |G(\boldsymbol{f})|^2 \,. \tag{A.12}$$

When propagating wave fields through Fourier transforms, this can be understood as the conservation of energy, or equivalently intensity or number of photons.

A.2.5 Convolution and Convolution Theorem

The convolution $c(\boldsymbol{r})$ of two functions $g(\boldsymbol{r})$ and $h(\boldsymbol{r})$ with respect to the variable $\boldsymbol{r}$ is defined as

$$c(\boldsymbol{r}) = g(\boldsymbol{r}) \otimes_{\boldsymbol{r}} h(\boldsymbol{r}) = \int \mathrm{d}^2\boldsymbol{r}'\, g(\boldsymbol{r}')\, h(\boldsymbol{r}-\boldsymbol{r}') \,, \tag{A.13}$$

which can equivalently be written as

$$c(\boldsymbol{r}) = g(\boldsymbol{r}) \otimes_{\boldsymbol{r}} h(\boldsymbol{r}) = \int \mathrm{d}^2\boldsymbol{r}'\, g(\boldsymbol{r}-\boldsymbol{r}')\, h(\boldsymbol{r}') \,, \tag{A.14}$$

representing the symmetry of the convolution. It does not matter which of the two functions is shifted with respect to the other.

The *convolution theorem* states that in Fourier space the convolution turns into a simple multiplication, or

$$C(\boldsymbol{f}) = G(\boldsymbol{f}) \cdot G = H(\boldsymbol{f}) \,. \tag{A.15}$$

The convolution of two inverted functions is straightforward to obtain by substituting $\boldsymbol{a} = -\boldsymbol{r}$:

$$\begin{aligned} g(-\boldsymbol{r}) \otimes_{\boldsymbol{r}} h(-\boldsymbol{r}) &= g(\boldsymbol{a}) \otimes_{\boldsymbol{r}} h(\boldsymbol{a}) \\ &= \int \mathrm{d}^2\boldsymbol{r}'\, g(\boldsymbol{a}-\boldsymbol{r}')\, h(\boldsymbol{r}') \\ &= \int \mathrm{d}^2\boldsymbol{r}'\, g(-\boldsymbol{r}-\boldsymbol{r}')\, h(\boldsymbol{r}') \,. \end{aligned} \tag{A.16}$$

A.2.6 Correlation and Correlation Theorem

The correlation $z(\boldsymbol{r})$ of two functions $f(\boldsymbol{r})$ and $g(\boldsymbol{r})$ with respect to the variable $\boldsymbol{r}$ is defined as

$$z(\boldsymbol{r}) = g(\boldsymbol{r}) \star_{\boldsymbol{r}} h(\boldsymbol{r}) = \int \mathrm{d}^2\boldsymbol{r}'\, g(\boldsymbol{r}')\, h(\boldsymbol{r}+\boldsymbol{r}'). \tag{A.17}$$

Note that the correlation is equivalent to the convolution if either of the two functions g or h is even. In the case of scanning x-ray microscopy, this is usually true for the pupil and therefore for the probe function. The correlation theorem states that

$$Z(\boldsymbol{f}) = G(\boldsymbol{f}) \cdot H^*(\boldsymbol{f}), \tag{A.18}$$

where H^* is the complex-conjugate of H.

If g and h are the same function, z is usually called the *autocorrelation* of g. For the case of different functions g and h, the term *crosscorrelation* is used.

A.2.7 Discrete Fourier Transform

Data analysis and numerical simulations are usually carried out on a grid of discrete data points (two-dimensional in the case of imaging), which represents an approximation or sampled version of the "true" continuous quantity. We use the following definition of the discrete 2-D forward Fourier transform:

$$G(u,v) = \frac{1}{N_x N_y} \sum_{x,y} g(x,y) \exp\left[-2\pi\mathrm{i}\left(\frac{ux}{N_x} + \frac{vy}{N_y}\right)\right], \tag{A.19}$$

where x, y and u, v are the indices of the data points in the real and Fourier space arrays, respectively, and N_x, N_y are the numbers of data points in the two dimensions. The inverse transform is then given by

$$g(x,y) = \sum_{u,v} G(u,v) \exp\left[+2\pi\mathrm{i}\left(\frac{ux}{N_x} + \frac{vy}{N_y}\right)\right]. \tag{A.20}$$

Note that $G(0,0) = \sum_{x,y} g(x,y)/(N_x N_y)$ is the mean value of the real space array, also often called the DC value or offset (which stands for direct current and stems from the Fourier analysis of electrical signals).

If Δx and Δy are the real space sampling intervals, the Fourier space sampling intervals are given by

$$\Delta u = \frac{1}{N_x \Delta x}, \qquad \text{and} \tag{A.21}$$

$$\Delta v = \frac{1}{N_y \Delta y}. \tag{A.22}$$

For an even number of pixels in any dimension i, it is convenient to arrange the data points in the Fourier transform array such that the frequencies are given by

$$\frac{1}{N_i \Delta i}\left(-\tfrac{N_i}{2}, -(\tfrac{N_i}{2}-1), \ldots, -1, 0, 1, \ldots, \tfrac{N_i}{2}-1\right) \tag{A.23}$$

such that the zero frequency is at the pixel just right and above of the center (in the common convention of image processing, where zero is at the lower left of the image). For an odd number of pixels, one would use the following arrangement:

$$\frac{1}{N_i \Delta i}\left(-(\tfrac{N_i-1}{2}), \ldots, -1, 0, 1, \ldots, \tfrac{N_i-1}{2}\right) \tag{A.24}$$

such that the zero frequency is right in the center. The frequency $1/(2\Delta i)$ is called the Nyquist frequency.

The Fourier transform properties listed in Sec. A.2.3 all have an equivalent in the discrete case, as do the convolution (A.2.5) and correlation (A.2.6). Note, however, that the sampling procedure introduces some specific artifacts like a band limit and an implicit periodicity. For details, the reader is referred to the literature [73, 74].

With the definition of the discrete Fourier transform above, Parseval's theorem (see Sec. A.2.4) takes the form

$$\sum_{x,y} |g(x,y)|^2 = N_x N_y \sum_{u,v} |G(u,v)|^2 . \tag{A.25}$$

An appropriate correction has to be made if Fourier transforms are used to propagate wave fields and the total intensity (number of photons) is to be preserved.

Discrete Fourier transforms can be computed quickly using Fast Fourier Transform (FFT) algorithms (see, *e. g.*, Brigham [73]). Implementations of such algorithms are readily available for all major programming languages.

A.3 The Dirac Delta-Function

In the theory of differential equations one is often confronted with questions that require solutions which cannot be defined in the classical sense of functions. The theory of distributions poses a way out if this dilemma by introducing generalized functions called *distributions*, which have the required differentiation and other properties necessary for solving these problems. One of the most prominent distributions is the Dirac Delta-Function. It is often referred to as impulse function and also represents an important concept in Fourier analysis. The Delta-Function provides a mathematical representation of infinitely small or short quantities with finite "strength," like a point source.

Note that a general convention is to denote the Delta-Function with a lower-case δ. However, in order to avoid confusion with the real part of the refractive index ($n = \delta + \mathrm{i}\beta$) we will use a capital Δ throughout this work.

The Delta-Function is commonly defined through

$$\begin{aligned} \Delta(\boldsymbol{r} - \boldsymbol{r}_0) &= 0 \qquad \text{for} \qquad \boldsymbol{r} \neq \boldsymbol{r}_0, \qquad \text{and} \\ \int \mathrm{d}^2\boldsymbol{r}\, \Delta(\boldsymbol{r} - \boldsymbol{r}_0) &= 1. \end{aligned} \tag{A.26}$$

This means that its magnitude at $\boldsymbol{r} = \boldsymbol{r}_0$ is generally undefined; but through representations of bell-shaped curves and Lorentz-Functions its value in the infinite proximity of the origin is infinity.

Its most important characteristic is the sifting property:

$$\int \mathrm{d}^2\boldsymbol{r}\, \Delta(\boldsymbol{r} - \boldsymbol{r}_0)\, g(\boldsymbol{r}) = g(\boldsymbol{r}_0)\,. \tag{A.27}$$

By substituting $g(\boldsymbol{r}) = \exp(2\pi\mathrm{i}\boldsymbol{r}\boldsymbol{f})$ and $\boldsymbol{r}_0 = \boldsymbol{0}$ in this equation, we obtain the inverse Fourier transform of the Delta-Function or

$$\int \mathrm{d}^2\boldsymbol{r}\, \Delta(\boldsymbol{r})\, \mathrm{e}^{(2\pi\mathrm{i}\boldsymbol{r}\boldsymbol{f})} = \mathrm{e}^{(2\pi\mathrm{i}\cdot\boldsymbol{0}\cdot\boldsymbol{f})} = 1\,. \tag{A.28}$$

The corresponding forward transform is given by

$$\int \mathrm{d}^2\boldsymbol{r}\, 1 \cdot \mathrm{e}^{(-2\pi\mathrm{i}\boldsymbol{r}\boldsymbol{f})} = \int \mathrm{d}^2\boldsymbol{r}\, \mathrm{e}^{(-2\pi\mathrm{i}\boldsymbol{r}\boldsymbol{f})} = \Delta(\boldsymbol{f})\,. \tag{A.29}$$

Appendix B

Wiener Filter

The Wiener filter, which was first described by Levinson [75], is commonly used to remove artifacts of the measuring process from noisy data, and the quantitative amplitude and phase reconstruction method described in Ch. 3 and Appendix C is a simple extension of it. In the following we want to give a brief outline roughly following Landauer [56]. Further information is given, for example, by Gonzalez and Woods [24], Press *et al.* [76] or other books on signal processing.

Assume that a "true" function $h(x)$ is to be measured, but in the measuring process it gets smeared out or corrupted (mathematically: convolved) with a known instrument function $t(x)$. Moreover, statistical noise described by a function $n(x)$ is added, so that the measured function is

$$s(x) = h(x) \otimes t(x) + n(x). \tag{B.1}$$

Taking the Fourier transform and using the convolution theorem, we get

$$S(f) = H(f) \times T(f) + N(f), \tag{B.2}$$

where f is the Fourier variable and $S(f)$, $H(f)$, $T(f)$ and $N(f)$ are the Fourier transforms of $s(x)$, $h(x)$, $t(x)$ and $n(x)$, respectively. $t(x)$ is often called the *impulse response* of the instrument, or the *point spread function* in an imaging system (the image of a point, or delta function, object). Its Fourier transform $T(f)$ can be called the *frequency transfer*, or in incoherent imaging systems the *modulation transfer function* (MTF). Note that in imaging the exact nomenclature also depends on whether the quantities describe amplitude or intensity.

If there was no noise, and if the frequency response $T(f)$ did not have any zeroes, we could obtain the true signal spectrum by a simple inverse filter:

$$H(f) = \frac{S(f)}{T(f)}. \tag{B.3}$$

However, in practical applications, the frequency transfer can be quite low at certain (usually high) frequencies so that the noise dominates the signal, and the inverse filter would just amplify that noise. The Wiener filter calculates an estimate

$$\widehat{H}(f) = W(f) \times S(f) \tag{B.4}$$

such that the root mean square (rms) error

$$\epsilon = \int \mathrm{d}f \left\langle \left| \widehat{H} - H \right|^2 \right\rangle \tag{B.5}$$

is minimized. $W(f)$ is called the Wiener filter function. The brackets $\langle\rangle$

indicate an expectation value which averages over many measurements of the noisy data S. Since the integrand of Eq. B.5 is real and greater than or equal to zero for all f, we can perform the minimization for each value of f independently and omit the integral in the following. Substituting Eq. B.4 into Eq. B.5 and minimizing with respect to W, we obtain

$$\frac{\partial \epsilon}{\partial W} = \langle S^* (WS - H) \rangle = 0. \tag{B.6}$$

Now we can subsitute Eq. B.2 into Eq. B.6, and if we assume that N and H are uncorrelated, we get

$$W |H|^2 |T|^2 - |H|^2 T^* + W\eta = 0, \quad \text{where} \quad \eta = \left\langle |N|^2 \right\rangle . \tag{B.7}$$

We solve for W and substitute the result into Eq. B.4 to obtain the best estimate of $H(f)$ as

$$\widehat{H} = \frac{T^*}{|T|^2 + \beta} S, \quad \text{where} \quad \beta = \frac{\eta}{|H|^2}. \tag{B.8}$$

An alternative, but equivalent way to write this is

$$\widehat{H} = \frac{|HT|^2}{|HT|^2 + \eta} \frac{S}{T}. \tag{B.9}$$

How can we interpret this? If we look at Eq. B.9, we see on the very right that first a simple inverse filter is applied to the measured data S. Then an additional filter of the form

$$\frac{|HT|^2}{|HT|^2 + \eta} \tag{B.10}$$

is applied, which is close to one at frequencies where the power spectrum of the transferred signal $|HT|^2$ is large compared to the expectation value of the noise power spectrum η, and close to zero at frequencies where the noise dominates the transferred signal. In other words, the Wiener filter consists of an inverse filter plus an additional filter which suppresses frequencies which are dominated by noise.

To calculate the filter function W, we need to separately estimate the power spectra of the transferred signal $|HT|^2$ and the noise η. In many practical cases, this can easily be read from a plot of the power spectrum of the measured signal $|S|^2$ (see Fig. B.1). Usually one can see the power spectrum of the signal which declines down to a noise floor at higher frequencies. The noise level can then be extrapolated into the region dominated by the signal, and vice versa.

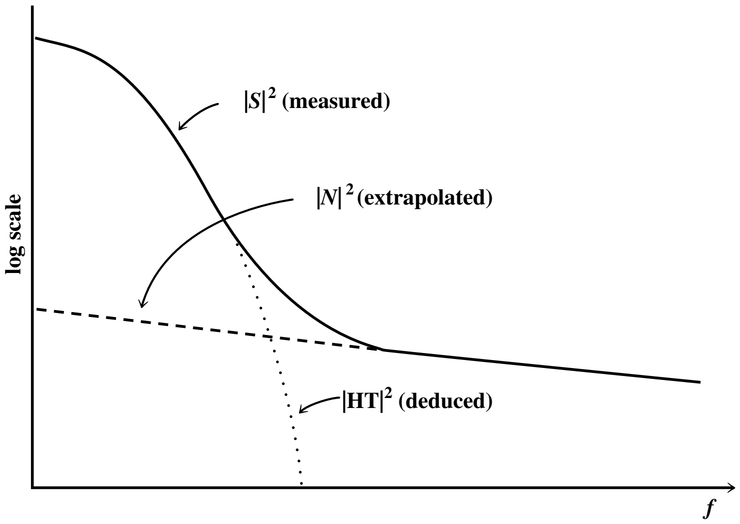

Figure B.1: Estimation of the signal and noise power spectra for the calculation of the Wiener filter; see text. Figure modified from Press *et al.* [76].

For a graphical illustration of the Wiener filter, in Fig. B.2 we plot the Modulation Transfer Function (MTF) of an apodized lens, as is often used in x-ray microscopy (see Sec. 1.3.3), as an example for a frequency transfer function T. Also shown are Wiener filter functions of the form

$$W = \frac{\mathrm{MTF}^*}{|\mathrm{MTF}|^2 + \beta} \tag{B.11}$$

(compare Eq. B.8), where we have used a constant β instead of the true frequency-dependent ratio of noise to signal spectrum. We can see that at high frequencies, where the value of the MTF is small, the inverse filter ($\beta = 0$) would boost the noise to infinity, making the result useless. As we increase β, those frequencies are suppressed more and more, until (when β becomes too large) the signal is overly suppressed. Often, instead of the more elaborate power-spectrum estimation described above, one can just use this version of the Wiener filter and adjust β interactively to yield the "visually best" results [24].

The application of the Wiener filter to remove the effects of the zone plate transfer function in a scanning transmission x-ray microscope was demonstrated by Jacobsen *et al.* [77].

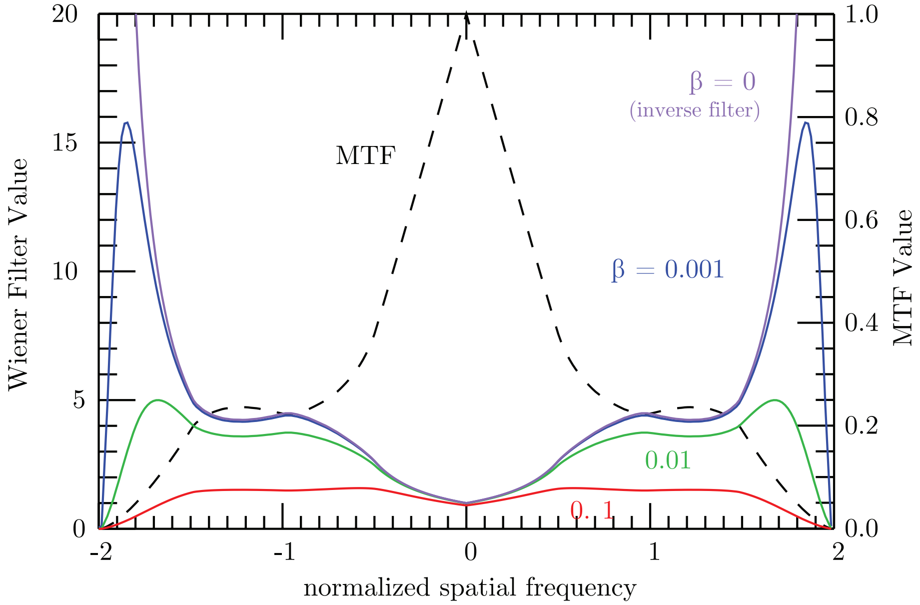

Figure B.2: Graphical illustration of the Wiener filter. The scale on the right is for the MTF (dashed curve), whereas the scale on the left is for the Wiener filter functions. Compared to the inverse filter, the Wiener filter suppresses frequencies with low transfer, which are dominated by noise. The correct value of the noise parameter β is crucial for good quantitative results.

Appendix C

Detailed Derivation of Fourier-Filter Reconstruction

The present chapter contains a detailed derivation of the Fourier filtering reconstruction method. It is meant to complement Sec. 3.3 by giving a complete treatment including all necessary intermediate steps. The derivations steps closely follow [11], but also contain new observations and interpretations.

C.1 Image Formation in Terms of Transfer Functions

Starting point is the far-field intensity distribution in the scannning microscope

$$\Psi_3(\boldsymbol{f};\, \boldsymbol{r}_\mathrm{s}) = \int \mathrm{d}^2\boldsymbol{r}\, h(\boldsymbol{r})\, p_\mathrm{o}(\boldsymbol{r}-\boldsymbol{r}_\mathrm{s})\, \exp\left(\mathrm{i}2\pi \boldsymbol{r}\boldsymbol{f}\right), \tag{C.1}$$

omitting constant pre-factors and image plane indices.

Employing the defining relation of the probe function (Eqs. 2.19) and using convolution, shift and symmetry theorems of Fourier transforms (see Appendix A.2) we can rewrite Eq. C.1 as

$$\begin{aligned}
\Psi_3(\boldsymbol{f}, \boldsymbol{r}_\mathrm{s}) &= \int \mathrm{d}^2\boldsymbol{r}\, h(\boldsymbol{r})\, p_\mathrm{o}(\boldsymbol{r}-\boldsymbol{r}_\mathrm{s})\, \exp\left(\mathrm{i}2\pi \boldsymbol{r}\boldsymbol{f}\right)\\
&= \mathcal{F}^{-1}\{p_\mathrm{o}(\boldsymbol{r}-\boldsymbol{r}_0)\, h(\boldsymbol{r})\}\\
&= \mathcal{F}^{-1}\{p_\mathrm{o}(\boldsymbol{r}-\boldsymbol{r}_0)\} \otimes_{\boldsymbol{f}} \mathcal{F}^{-1}\{h(\boldsymbol{r})\}\\
&= \big(\mathcal{F}^{-1}\{p_\mathrm{o}(\boldsymbol{r})\} \exp(2\pi\mathrm{i}\boldsymbol{r}_0\boldsymbol{f})\big) \otimes_{\boldsymbol{f}} \mathcal{F}^{-1}\{h(\boldsymbol{r})\}\\
&= \big(\mathcal{F}^{-1}\{\mathcal{F}^{-1}\{P_\mathrm{o}(\boldsymbol{f})\}\} \exp(2\pi\mathrm{i}\boldsymbol{r}_0\boldsymbol{f})\big) \otimes_{\boldsymbol{f}}\\
&\quad \big(\mathcal{F}^{-1}\{\mathcal{F}^{-1}\{H(\boldsymbol{f})\}\}\big)\\
&= \left[P_\mathrm{o}(-\boldsymbol{f}) \exp\left(2\pi\mathrm{i}\boldsymbol{r}_0\boldsymbol{f}\right)\right] \otimes_{\boldsymbol{f}} H(-\boldsymbol{f})\,,
\end{aligned} \tag{C.2}$$

which reproduces Eq. 3.32. Writing out the convolution integral for the result of Eq. C.2 we get

$$\Psi_3(\boldsymbol{f}, \boldsymbol{r}_\mathrm{s}) = \int \mathrm{d}^2\boldsymbol{f}_1\, P_\mathrm{o}(-\boldsymbol{f}-\boldsymbol{f}_1)\, \exp[2\pi\mathrm{i}\boldsymbol{r}_\mathrm{s}(\boldsymbol{f}+\boldsymbol{f}_1)]\, H(\boldsymbol{f}_1)\,, \tag{C.3}$$

where we used the result for the convolution of inverted functions of Eq. A.16.

We now measure the intensity of this wave field with a detector that has various segments k with respective response functions $R_k(\boldsymbol{f})$ (*e. g.* segmented or pixelated detector), so that the image recorded by a specific segment becomes

$$s_k(\boldsymbol{r}_\mathrm{s}) = \int \mathrm{d}^2\boldsymbol{f}\, R(\boldsymbol{f})\, |\Psi_3(\boldsymbol{f},\boldsymbol{r}_\mathrm{s})|^2 \,, \tag{C.4}$$

where the scan displacement coordinate $\boldsymbol{r}_\mathrm{s}$ simultaneously is the image coordinate. If not otherwise noted, the detector response $R_k(\boldsymbol{f})$ will be one within the sensitive area of the individual detector segment, and zero otherwise.

Now we expand $|\Psi_3(\boldsymbol{f},\boldsymbol{r}_\mathrm{s})|^2$ from Eq. C.4 into $\Psi_3\Psi_3^*$, which gives

$$\begin{aligned} |\Psi_3(\boldsymbol{f},\boldsymbol{r}_\mathrm{s})|^2 &= \int \mathrm{d}^2\boldsymbol{f}_1\, P_\mathrm{o}(-\boldsymbol{f}-\boldsymbol{f}_1)\, H(\boldsymbol{f}_1) \exp[2\pi \mathrm{i}\boldsymbol{r}_\mathrm{s}(\boldsymbol{f}+\boldsymbol{f}_1)] \times \\ &\quad \times \int \mathrm{d}^2\boldsymbol{f}_2\, P_\mathrm{o}^*(-\boldsymbol{f}-\boldsymbol{f}_2)\, H^*(\boldsymbol{f}_2) \exp[-2\pi \mathrm{i}\boldsymbol{r}_\mathrm{s}(\boldsymbol{f}+\boldsymbol{f}_2)] \\ &= \int \mathrm{d}^2\boldsymbol{f}_1 \int \mathrm{d}^2\boldsymbol{f}_2\, P_\mathrm{o}(-\boldsymbol{f}-\boldsymbol{f}_1)\, P_\mathrm{o}^*(-\boldsymbol{f}-\boldsymbol{f}_2) \times \\ &\quad \times H(\boldsymbol{f}_1)\, H^*(\boldsymbol{f}_2) \exp[2\pi \mathrm{i}\boldsymbol{r}_\mathrm{s}(\boldsymbol{f}_1-\boldsymbol{f}_2)] \,. \end{aligned} \tag{C.5}$$

We take the Fourier transform of Eq. C.4,

$$S_k(\boldsymbol{f}_\mathrm{s}) = \int \mathrm{d}^2\boldsymbol{r}_\mathrm{s}\, s_k(\boldsymbol{r}_\mathrm{s}) \exp(-2\pi \mathrm{i}\boldsymbol{r}_\mathrm{s}\boldsymbol{f}_\mathrm{s}) \,, \tag{C.6}$$

and insert from Eqs. C.4 and C.5:

$$\begin{aligned} S_k(\boldsymbol{f}_\mathrm{s}) &= \int \mathrm{d}^2\boldsymbol{r}_\mathrm{s} \int \mathrm{d}^2\boldsymbol{f}\, R_k(\boldsymbol{f}) \int \mathrm{d}^2\boldsymbol{f}_1 \int \mathrm{d}^2\boldsymbol{f}_2\, P_\mathrm{o}(-\boldsymbol{f}-\boldsymbol{f}_1)\, P_\mathrm{o}^*(-\boldsymbol{f}-\boldsymbol{f}_2) \times \\ &\quad \times H(\boldsymbol{f}_1)\, H^*(\boldsymbol{f}_2)\, \exp[-2\pi \mathrm{i}\boldsymbol{r}_\mathrm{s}(\boldsymbol{f}_2-(\boldsymbol{f}_1-\boldsymbol{f}_\mathrm{s}))] \,. \end{aligned} \tag{C.7}$$

By recalling the Fourier transform of the Delta-Function (Eq. A.29) we can replace

$$\int \mathrm{d}^2\boldsymbol{r}_\mathrm{s}\, \exp[-2\pi \mathrm{i}\boldsymbol{r}_\mathrm{s}(\boldsymbol{f}_2-(\boldsymbol{f}_1-\boldsymbol{f}_\mathrm{s}))] = \Delta(\boldsymbol{f}_2-(\boldsymbol{f}_1-\boldsymbol{f}_\mathrm{s})) \,. \tag{C.8}$$

Now we can perform the integral over $\boldsymbol{f}_2$ in Eq. C.7:

$$\int \mathrm{d}^2\boldsymbol{f}_2\, G(\boldsymbol{f}_2)\, \Delta(\boldsymbol{f}_2-(\boldsymbol{f}_1-\boldsymbol{f}_\mathrm{s})) = G(\boldsymbol{f}_1-\boldsymbol{f}_\mathrm{s}) \tag{C.9}$$

(see Eq. A.27), where $G(\boldsymbol{f}_2)$ represents all other remaining terms. Eq. C.7

then becomes

$$\begin{aligned} S_k(\boldsymbol{f}_\mathrm{s}) \;&=\; \int \mathrm{d}^2\boldsymbol{f}\, R_k(\boldsymbol{f}) \int \mathrm{d}^2\boldsymbol{f}_1\, P_\mathrm{o}(-\boldsymbol{f}-\boldsymbol{f}_1)\, P_\mathrm{o}^*(-\boldsymbol{f}-\boldsymbol{f}_1+\boldsymbol{f}_\mathrm{s}) \times \\ &\qquad\qquad \times\, H(\boldsymbol{f}_1)\, H^*(\boldsymbol{f}_1-\boldsymbol{f}_\mathrm{s})\,. \end{aligned} \tag{C.10}$$

We can identify the integral over $\boldsymbol{f}_1$ as convolution integral (see Eq. A.16); hence we can write

$$S_k(\boldsymbol{f}_\mathrm{s}) = \int \mathrm{d}^2\boldsymbol{f}\, R_k(\boldsymbol{f}) \Big[P_\mathrm{o}(-\boldsymbol{f})\, P_\mathrm{o}^*(-\boldsymbol{f}-\boldsymbol{f}_\mathrm{s}) \otimes_{\boldsymbol{f}} H(-\boldsymbol{f})\, H^*(-\boldsymbol{f}-\boldsymbol{f}_\mathrm{s}) \Big]\,, \tag{C.11}$$

which reproduces Eq. 3.34.

Without loss of generality, the specimen function can always be written as

$$h(\boldsymbol{r}) = 1 + h_r(\boldsymbol{r}) + \mathrm{i}\, h_i(\boldsymbol{r})\,, \tag{C.12}$$

where $h_{r,i}$ are real. The Fourier transform of the specimen is then

$$H(\boldsymbol{f}) = \Delta(\boldsymbol{f}) + H_r(\boldsymbol{f}) + \mathrm{i}\, H_i(\boldsymbol{f})\,; \tag{C.13}$$

where a detailed discussion on the meaning of H_r and H_i and successive consequences is given throughout Sec. 3.3 and in particular in Sec. 3.3.5. For the derivation at hand it is only necessary that one is able to write the specimen function in the foregoing way of Eq. C.13, which can be done without loss of generality. The complex product of specimen functions in Eq. C.11 can then be written as

$$\begin{aligned} H(\boldsymbol{f}_1)\cdot H^*(\boldsymbol{f}_1-\boldsymbol{f}_\mathrm{s}) \;&=\; \Delta(\boldsymbol{f}_1)\cdot\Delta(\boldsymbol{f}_1-\boldsymbol{f}_\mathrm{s}) + \\ &\quad + \Delta(\boldsymbol{f}_1)\, \left[H_r^*(\boldsymbol{f}_1-\boldsymbol{f}_\mathrm{s}) - \mathrm{i}\, H_i^*(\boldsymbol{f}_1-\boldsymbol{f}_\mathrm{s})\right] + \\ &\quad + \Delta(\boldsymbol{f}_1-\boldsymbol{f}_\mathrm{s})\, \left[H_r(\boldsymbol{f}_1) + \mathrm{i}\, H_i(\boldsymbol{f}_1)\right] + \\ &\quad \underbrace{+ H_r(\boldsymbol{f}_1)\, H_r^*(\boldsymbol{f}_1-\boldsymbol{f}_\mathrm{s}) + H_i(\boldsymbol{f}_1)\, H_i^*(\boldsymbol{f}_1-\boldsymbol{f}_\mathrm{s}) -}_{\mathcal{O}(\mathrm{H_{r,i}}^2)} \\ &\quad \underbrace{- \mathrm{i}H_r(\boldsymbol{f}_1)\, H_i^*(\boldsymbol{f}_1-\boldsymbol{f}_\mathrm{s}) + \mathrm{i}H_i(\boldsymbol{f}_1)\, H_r^*(\boldsymbol{f}_1-\boldsymbol{f}_\mathrm{s})}_{\mathcal{O}(\mathrm{H_{r,i}}^2)}\,. \end{aligned} \tag{C.14}$$

The crucial step at this point is that the terms of higher than first order ($\mathcal{O}({H_{r,i}}^2)$) will assumed to be small compared to the terms containing Delta-

Functions and; therefore, will be left out in the successive treatment. This omission of terms is part of the *weak specimen approximation*.

Within this approximation we can rewrite Eq. C.11 in the following

$$\begin{aligned} S_k(\boldsymbol{f}_\mathrm{s}) \;&=\; \int \mathrm{d}^2\boldsymbol{f}\, R_k(\boldsymbol{f}) \int \mathrm{d}^2\boldsymbol{f}_1\, P_\mathrm{o}(-\boldsymbol{f}-\boldsymbol{f}_1)\, P_\mathrm{o}^*(-\boldsymbol{f}-\boldsymbol{f}_1+\boldsymbol{f}_\mathrm{s}) \times \\ &\quad \times\; \Delta(\boldsymbol{f}_1)\, \Delta(\boldsymbol{f}_1-\boldsymbol{f}_\mathrm{s}) + \\ &\quad + \int \mathrm{d}^2\boldsymbol{f}\, R_k(\boldsymbol{f}) \int \mathrm{d}^2\boldsymbol{f}_1\, P_\mathrm{o}(-\boldsymbol{f}-\boldsymbol{f}_1)\, P_\mathrm{o}^*(-\boldsymbol{f}-\boldsymbol{f}_1+\boldsymbol{f}_\mathrm{s}) \times \\ &\quad \times\; \Delta(\boldsymbol{f}_1)\, \left[H_r^*(\boldsymbol{f}_1-\boldsymbol{f}_\mathrm{s}) - \mathrm{i}\, H_i^*(\boldsymbol{f}_1-\boldsymbol{f}_\mathrm{s})\right] + \\ &\quad + \int \mathrm{d}^2\boldsymbol{f}\, R_k(\boldsymbol{f}) \int \mathrm{d}^2\boldsymbol{f}_1\, P_\mathrm{o}(-\boldsymbol{f}-\boldsymbol{f}_1)\, P_\mathrm{o}^*(-\boldsymbol{f}-\boldsymbol{f}_1+\boldsymbol{f}_\mathrm{s}) \times \\ &\quad \times\; \Delta(\boldsymbol{f}_1-\boldsymbol{f}_\mathrm{s})\, \left[H_r(\boldsymbol{f}_1) + \mathrm{i}\, H_i(\boldsymbol{f}_1)\right]\,. \end{aligned} \tag{C.15}$$

In each of the three summands in this equation, we can perform the integral over the respective delta function, where in the first term we choose to integrate over the first one of the two delta functions (for the final result, it does not matter which one we integrate over). Now the motivation becomes clear why it was desired to neglect the $\mathcal{O}({H_{r,i}}^2)$ terms of Eq. C.14. When keeping those terms one cannot get rid of an integral since they do not carry a Delta-Function with them. After performing the integrations through the Delta-Functions we get

$$\begin{aligned} S_k(\boldsymbol{f}_\mathrm{s}) \;&=\; \int \mathrm{d}^2\boldsymbol{f}\, R_k(\boldsymbol{f})\, P_\mathrm{o}(-\boldsymbol{f})\, P_\mathrm{o}^*(-\boldsymbol{f}+\boldsymbol{f}_\mathrm{s})\, \Delta(\boldsymbol{f}_\mathrm{s}) + \\ &\quad + \int \mathrm{d}^2\boldsymbol{f}\, R_k(\boldsymbol{f})\, P_\mathrm{o}(-\boldsymbol{f})\, P_\mathrm{o}^*(-\boldsymbol{f}+\boldsymbol{f}_\mathrm{s})\, \left[H_r^*(-\boldsymbol{f}_\mathrm{s}) - \mathrm{i}\, H_i^*(-\boldsymbol{f}_\mathrm{s})\right] + \\ &\quad + \int \mathrm{d}^2\boldsymbol{f}\, R_k(\boldsymbol{f})\, P_\mathrm{o}(-\boldsymbol{f}-\boldsymbol{f}_\mathrm{s})\, P_\mathrm{o}^*(-\boldsymbol{f})\, \left[H_r(\boldsymbol{f}_\mathrm{s}) + \mathrm{i}\, H_i(\boldsymbol{f}_\mathrm{s})\right]\,, \end{aligned} \tag{C.16}$$

where in the second summand we have used the fact that the Fourier transforms of the specimen are conjugate symmetric functions, or

$$H_{r,i}(\boldsymbol{f}_\mathrm{s}) = H_{r,i}^*(-\boldsymbol{f}_\mathrm{s})\,, \tag{C.17}$$

because $h_{r,i}$ are real. (see also Table A.2). Note, that with Eq. C.16 we have achieved a linearization of all the terms with respect to the specimen contributions H_r and H_i.

Now we define the bilinear transfer functions

$$C_k(m, n, \boldsymbol{f}_\mathrm{s}) = \int \mathrm{d}^2\boldsymbol{f}\, R_k(\boldsymbol{f})\, P_\mathrm{o}(m\boldsymbol{f}_\mathrm{s} - \boldsymbol{f})\, P_\mathrm{o}^*(n\boldsymbol{f}_\mathrm{s} - \boldsymbol{f})\,, \tag{C.18}$$

so that the final result for the image recorded by detector segment k becomes

$$\begin{aligned} S_k(\boldsymbol{f}_\mathrm{s}) &= \Delta(\boldsymbol{f}_\mathrm{s})\, C_k(0, 0, \boldsymbol{f}_\mathrm{s}) + \\ &\quad + C_k(0, 1, \boldsymbol{f}_\mathrm{s})\, [H_r(\boldsymbol{f}_\mathrm{s}) - \mathrm{i}\, H_i(\boldsymbol{f}_\mathrm{s})] + \\ &\quad + C_k(-1, 0, \boldsymbol{f}_\mathrm{s})\, [H_r(\boldsymbol{f}_\mathrm{s}) + \mathrm{i}\, H_i(\boldsymbol{f}_\mathrm{s})] \\ &= \Delta(\boldsymbol{f}_\mathrm{s})\, C_k(0, 0, \boldsymbol{f}_\mathrm{s}) + \\ &\quad + H_r(\boldsymbol{f}_\mathrm{s})\, [C_k(-1, 0, \boldsymbol{f}_\mathrm{s}) + C_k(0, 1, \boldsymbol{f}_\mathrm{s})] + \\ &\quad + \mathrm{i}\, H_i(\boldsymbol{f}_\mathrm{s})\, [C_k(-1, 0, \boldsymbol{f}_\mathrm{s}) - C_k(0, 1, \boldsymbol{f}_\mathrm{s})]\ , \end{aligned} \tag{C.19}$$

whereby we have proven Eq. 3.40. For the term containing $\Delta(\boldsymbol{f}_\mathrm{s})$ in Eq. C.19 we implicitly take advantage of the fact that only the $\boldsymbol{f}_\mathrm{s} = \mathbf{0}$ component can contribute and is of interest. Because

$$C_k(m, n, \boldsymbol{f}_\mathrm{s}{=}0) = \int \mathrm{d}^2\boldsymbol{f}\, R_k(\boldsymbol{f})\, |P(-\boldsymbol{f})|^2 \tag{C.20}$$

is independent of m and n; therefore,

$$\Delta(\boldsymbol{f}_\mathrm{s}) \cdot C_k(0, 1, \boldsymbol{f}_\mathrm{s}) = \Delta(\boldsymbol{f}_\mathrm{s}) \cdot C_k(-1, 0, \boldsymbol{f}_\mathrm{s}) = \Delta(\boldsymbol{f}_\mathrm{s}) \cdot C_k(0, 0, \boldsymbol{f}_\mathrm{s}). \tag{C.21}$$

The bilinear transfer function $C_k(0, 0, \boldsymbol{f}_\mathrm{s})$ is constant for all $\boldsymbol{f}_\mathrm{s}$ and represents the total intensity measured by detector segment k in absence of a specimen.

By defining the contrast transfer functions for the real and imaginary parts of the specimen

$$\begin{aligned} T_r^{(k)}(\boldsymbol{f}_\mathrm{s}) &= C_k(-1, 0, \boldsymbol{f}_\mathrm{s}) + C_k(0, 1, \boldsymbol{f}_\mathrm{s}) \\ T_i^{(k)}(\boldsymbol{f}_\mathrm{s}) &= C_k(-1, 0, \boldsymbol{f}_\mathrm{s}) - C_k(0, 1, \boldsymbol{f}_\mathrm{s})\,, \end{aligned} \tag{C.22}$$

we can write Eq. C.19 as

$$S_k(\boldsymbol{f}_\mathrm{s}) = \Delta(\boldsymbol{f}_\mathrm{s})\, C_k(0, 0, \boldsymbol{f}_\mathrm{s}) + H_r(\boldsymbol{f}_\mathrm{s})\, T_r^{(k)}(\boldsymbol{f}_\mathrm{s}) + \mathrm{i}\, H_i(\boldsymbol{f}_\mathrm{s})\, T_i^{(k)}(\boldsymbol{f}_\mathrm{s})\,. \tag{C.23}$$

C.2 Derivation of Transfer Function Properties

In this section we will derive properties and symmetries of the transfer functions introduced in Sec. C.1, which will play a key role in the further derivation of the reconstruction method of Sec. C.3.

The bilinear transfer functions are defined as

$$C_k(m,n,\boldsymbol{f}_\mathrm{s}) = \int \mathrm{d}^2\boldsymbol{f}\, R_k(\boldsymbol{f})\, P_\mathrm{o}(m\boldsymbol{f}_\mathrm{s} - \boldsymbol{f})\, P_\mathrm{o}^*(n\boldsymbol{f}_\mathrm{s} - \boldsymbol{f})\,, \tag{C.24}$$

and the contrast transfer functions as

$$\begin{aligned} T_r^{(k)}(\boldsymbol{f}_\mathrm{s}) &= C_k(-1,0,\boldsymbol{f}_\mathrm{s}) + C_k(0,1,\boldsymbol{f}_\mathrm{s}) \\ T_i^{(k)}(\boldsymbol{f}_\mathrm{s}) &= C_k(-1,0,\boldsymbol{f}_\mathrm{s}) - C_k(0,1,\boldsymbol{f}_\mathrm{s})\,. \end{aligned} \tag{C.25}$$

Assuming that the **detector response functions** are **real** $R_k(\boldsymbol{f}) = R_k^*(\boldsymbol{f})$ we can show that

$$\begin{aligned} C_k(0,1,\boldsymbol{f}_\mathrm{s}) &= \int \mathrm{d}\boldsymbol{f}\, R_k(\boldsymbol{f})\, P_\mathrm{o}(-\boldsymbol{f})\, P_\mathrm{o}^*(\boldsymbol{f}_\mathrm{s} - \boldsymbol{f}) \\ &= C_k(0,-1,-\boldsymbol{f}_\mathrm{s}) \\ &= \left[\int \mathrm{d}\boldsymbol{f}\, R_k(\boldsymbol{f})\, P_\mathrm{o}^*(-\boldsymbol{f})\, P_\mathrm{o}(\boldsymbol{f}_\mathrm{s} - \boldsymbol{f})\right]^* \\ &= C_k^*(1,0,\boldsymbol{f}_\mathrm{s}) \\ &= C_k^*(-1,0,-\boldsymbol{f}_\mathrm{s})\,. \end{aligned} \tag{C.26}$$

Commonly, the detector response functions are real, so this is a rather general correct than limiting assumption. This results in the following property for the real contrast transfer function

$$\begin{aligned} T_r^{(k)}(\boldsymbol{f}_\mathrm{s}) &= C_k(-1,0,\boldsymbol{f}_\mathrm{s}) + C_k(0,1,\boldsymbol{f}_\mathrm{s}) \\ &= C_k(-1,0,\boldsymbol{f}_\mathrm{s}) + C_k^*(-1,0,-\boldsymbol{f}_\mathrm{s}) \end{aligned} \tag{C.27}$$

and

$$\begin{aligned} T_r^{(k)*}(-\boldsymbol{f}_\mathrm{s}) &= C_k^*(-1,0,-\boldsymbol{f}_\mathrm{s}) + C_k(-1,0,\boldsymbol{f}_\mathrm{s}) \\ &= T_r^{(k)}(\boldsymbol{f}_\mathrm{s})\,, \end{aligned} \tag{C.28}$$

and similarly for the imaginary part transfer function,

$$\begin{aligned} T_i^{(k)}(\boldsymbol{f}_\mathrm{s}) &= C_k(-1,0,\boldsymbol{f}_\mathrm{s}) - C_k(0,1,\boldsymbol{f}_\mathrm{s}) \\ &= C_k(-1,0,\boldsymbol{f}_\mathrm{s}) - C_k^*(-1,0,-\boldsymbol{f}_\mathrm{s}) \end{aligned} \tag{C.29}$$

and

$$\begin{aligned} T_i^{(k)*}(-\boldsymbol{f}_\mathrm{s}) &= C_k^*(-1,0,-\boldsymbol{f}_\mathrm{s}) - C_k(-1,0,\boldsymbol{f}_\mathrm{s}) \\ &= -T_i^{(k)}(\boldsymbol{f}_\mathrm{s}). \end{aligned} \tag{C.30}$$

This means that the real part contrast transfer functions $T_r^{(k)}$ are conjugate symmetric, while the imaginary part transfer functions $T_i^{(k)}$ are conjugate antisymmetric.

Assuming the **pupil** P_o is **real**, then the contrast transfer functions will be real as well (the detector response is always real). In this case, the real part transfer functions $T_r^{(k)}$ are symmetric, and the imaginary part transfer functions $T_i^{(k)}$ are antisymmetric.

In the case of a **symmetric detector configuration**, where each detector segment k has an opposite segment $\bar{k}$ such that $R_k(\boldsymbol{f}) = R_{\bar{k}}(-\boldsymbol{f})$, then

$$C_{\bar{k}}(-1,0,\boldsymbol{f}_\mathrm{s}) = \int \mathrm{d}\boldsymbol{f}\, R_{\bar{k}}(\boldsymbol{f})\, P_\mathrm{o}(-\boldsymbol{f}_\mathrm{s} - \boldsymbol{f})\, P_\mathrm{o}^*(-\boldsymbol{f}).$$

Through a variable transformation $\boldsymbol{f} \to -\boldsymbol{f}$, the integral over the whole frequency plane will stay the same:

$$C_{\bar{k}}(-1,0,\boldsymbol{f}_\mathrm{s}) = \int \mathrm{d}\boldsymbol{f}\, R_k(\boldsymbol{f})\, P_\mathrm{o}(-\boldsymbol{f}_\mathrm{s} + \boldsymbol{f})\, P_\mathrm{o}^*(\boldsymbol{f}).$$

If the **pupil** is **centrosymmetric** such that $P_\mathrm{o}(\boldsymbol{f}) = P_\mathrm{o}(-\boldsymbol{f})$, then

$$\begin{aligned} C_{\bar{k}}(-1, 0, \boldsymbol{f}_\mathrm{s}) &= \int \mathrm{d}\boldsymbol{f}\, R_k(\boldsymbol{f})\, P_\mathrm{o}(\boldsymbol{f}_\mathrm{s} - \boldsymbol{f})\, P_\mathrm{o}^*(-\boldsymbol{f}) \\ &= C_k(-1, 0, -\boldsymbol{f}_\mathrm{s}). \end{aligned} \tag{C.31}$$

The contrast transfer functions successively become

$$\begin{aligned} T_r^{(\bar{k})}(\boldsymbol{f}_\mathrm{s}) &= C_{\bar{k}}(-1, 0, \boldsymbol{f}_\mathrm{s}) + C_{\bar{k}}^*(-1, 0, -\boldsymbol{f}_\mathrm{s}) \\ &= C_k(-1, 0, -\boldsymbol{f}_\mathrm{s}) + C_k^*(-1, 0, \boldsymbol{f}_\mathrm{s}) \\ &= T_r^{(k)}(-\boldsymbol{f}_\mathrm{s}) \\ &= T_r^{(k)*}(\boldsymbol{f}_\mathrm{s}) \end{aligned} \tag{C.32}$$

and

$$\begin{aligned} T_i^{(\bar{k})}(\boldsymbol{f}_\mathrm{s}) &= C_{\bar{k}}(-1, 0, \boldsymbol{f}_\mathrm{s}) - C_{\bar{k}}^*(-1, 0, -\boldsymbol{f}_\mathrm{s}) \\ &= C_k(-1, 0, -\boldsymbol{f}_\mathrm{s}) - C_k^*(-1, 0, \boldsymbol{f}_\mathrm{s}) \\ &= T_i^{(k)}(-\boldsymbol{f}_\mathrm{s}) \\ &= -T_i^{(k)*}(\boldsymbol{f}_\mathrm{s}). \end{aligned} \tag{C.33}$$

Hence, for opposite detector segments in the case of a centrosymmetric pupil, the real part transfer functions $T_r^{(k)}$ are complex conjugates and the imaginary part transfer functions $T_i^{(k)}$ are negated and complex conjugates (if the pupil is symmetric). If in addition the **pupil** is **real**, then the real part transfer functions are identical for opposite segments, and the imaginary part transfer functions are opposite in sign.

For a **symmetric individual segment** k meaning $R_k(\boldsymbol{f}) = R_k(-\boldsymbol{f})$ and a **symmetric pupil**,

$$C_k^*(-1, 0, -\boldsymbol{f}_\mathrm{s}) = \int \mathrm{d}\boldsymbol{f}\, R_k(\boldsymbol{f})\, P_\mathrm{o}(\boldsymbol{f}_\mathrm{s} - \boldsymbol{f})\, P_\mathrm{o}^*(-\boldsymbol{f})$$

and now use $P_\mathrm{o}(\boldsymbol{f}) = P_\mathrm{o}(-\boldsymbol{f})$

$$= \int \mathrm{d}\boldsymbol{f}\, R_k(\boldsymbol{f})\, P_\mathrm{o}(-\boldsymbol{f}_\mathrm{s} + \boldsymbol{f})\, P_\mathrm{o}^*(\boldsymbol{f})$$

transform variables $\boldsymbol{f} \to -\boldsymbol{f}$; and use $R_k(\boldsymbol{f}) = R_k(-\boldsymbol{f})$

$$\begin{aligned} &= \int \mathrm{d}\boldsymbol{f}\, R_k(\boldsymbol{f})\, P_\mathrm{o}(-\boldsymbol{f}_\mathrm{s} - \boldsymbol{f})\, P_\mathrm{o}^*(-\boldsymbol{f}) \\ &= C_k(-1, 0, \boldsymbol{f}_\mathrm{s}). \end{aligned} \tag{C.34}$$

By comparing with this result with Eq. C.30, we see that for a symmetric segment the imaginary part transfer function $T_i^{(k)}$ is zero!

C.3 Fourier Filtering Reconstruction Derivation

C.3.1 Error Minimization

The starting point for the derivation of reconstruction through the Fourier Filtering Method is a best guess for the specimen function we hope to retrieve:

$$\widehat{H}(\boldsymbol{f}) = \sum_k W_k(\boldsymbol{f})\, S_k(\boldsymbol{f})\,. \tag{C.35}$$

This best guess $\widehat{H}$ contains the measured signals S_k weighted by filtering functions W_k, where it is the objective to derive analytical expressions for these filtering functions. Note, that in the following we drop the subscript $_\mathrm{s}$ for the scan displacement from the frequency variable because all quantities (specimen, pupil and detector response) must be calculated on the same frequency space.

Now we consider the root mean square (RMS) error of a hypothetical reconstruction through this best guess

$$\epsilon = \int \mathrm{d}\boldsymbol{f}\, \underbrace{\left\langle \left| \widehat{H}(\boldsymbol{f}) - H(\boldsymbol{f}) \right|^2 \right\rangle}_{G}, \tag{C.36}$$

where the expectation value $\langle\rangle$ averages over many measurements of the noisy data S_k. For an optimal reconstruction this RMS has to be minimized. integrand G of Eq. C.36 is real and greater than or equal to zero for all spatial frequencies $\boldsymbol{f}$. Therefore, we can disregard the frequency dependence and the integral in the minimization process and consider the integrand G by itself, which is

$$
\begin{aligned}
G &\equiv \left\langle \left| \widehat{H} - H \right|^2 \right\rangle \\
&= \left\langle \left| \sum_l W_l \, S_l - H \right|^2 \right\rangle \\
&= \left\langle \left(\sum_l W_l \, S_l - H \right) \left(\sum_m W_m^* \, S_m^* - H^* \right) \right\rangle
\end{aligned}
\qquad \text{(C.37)}
$$

We decompose the function W_k into their real $W_k^{(r)}$ and imaginary $W_k^{(i)}$ parts in order to take the partial derivative for the minimization process. The partial derivatives of the integrand G are given by

$$
\begin{aligned}
\frac{\partial G}{\partial W_k^{(r)}} &= \left\langle S_k \left(\sum_m W_m^* \, S_m^* - H^* \right) + S_k^* \left(\sum_l W_l \, S_l - H \right) \right\rangle \\
&= \left\langle \left[S_k^* \left(\sum_m W_m \, S_m - H \right) \right]^* + S_k^* \left(\sum_l W_l \, S_l - H \right) \right\rangle \\
&= \left\langle 2\mathcal{R} \left\{ S_k^* \left(\sum_l W_l \, S_l - H \right) \right\} \right\rangle
\end{aligned}
\qquad \text{(C.38)}
$$

$$
\begin{aligned}
\frac{\partial G}{\partial W_k^{(i)}} &= \left\langle \mathrm{i} \, S_k \left(\sum_m W_m^* \, S_m^* - H^* \right) - \mathrm{i} \, S_k^* \left(\sum_l W_l \, S_l - H \right) \right\rangle \\
&= \left\langle \mathrm{i} \left[S_k^* \left(\sum_m W_m \, S_m - H \right) \right]^* - \mathrm{i} \, S_k^* \left(\sum_l W_l \, S_l - H \right) \right\rangle \\
&= \left\langle -2\mathrm{i}\mathcal{I} \left\{ S_k^* \left(\sum_l W_l \, S_l - H \right) \right\} \right\rangle .
\end{aligned}
\qquad \text{(C.39)}
$$

To minimize the RMS we set both of these partial derivatives to zero (for all k). This means that the real *and* imaginary part of the quantity in braces $\{\}$

must be zero, or

$$\left\langle S_k^* \left(\sum_l W_l \, S_l - H \right) \right\rangle = 0 \qquad \text{for all } k \,, \tag{C.40}$$

In order to solve this expression for the filtering functions W_k, we substitute for S_k the specimen-linearized form of Eq. C.23, which we obtained through a weak specimen approximation.

Note, in the following treatment we will first omit the zero spatial frequency contribution $\boldsymbol{f} = 0$ component and therefore the Δ-term of Eq. C.23; we will consider this term in Sec. C.3.4. In addition we add a term $N_k(\boldsymbol{f})$ which describes the spectral noise of the measurement process for each detector segment k, so that the signal becomes

$$S_k(\boldsymbol{f}) = H_r(\boldsymbol{f}) \, T_r^{(k)}(\boldsymbol{f}) + \mathrm{i} \, H_i(\boldsymbol{f}) \, T_i^{(k)}(\boldsymbol{f}) + N_k(\boldsymbol{f}) \qquad \text{for } \boldsymbol{f} \neq 0 \text{ and all } k \,. \tag{C.41}$$

Furthermore, we use the expanded expression of Eq. C.13 for the specimen function, also omitting the Δ-term because we do not consider the zero frequency component for now. Taken this all together we arrive at the following expression for Eq. C.40 (for simplicity omitting the frequency dependence)

$$\begin{aligned} 0 = \Big\langle & \left(H_r^* \, T_r^{(k)*} - \mathrm{i} \, H_i^* \, T_i^{(k)*} + N_k^* \right) \times \\ & \times \left(\sum_l W_l \left(H_r \, T_r^{(l)} + \mathrm{i} \, H_i \, T_i^{(l)} + N_l \right) - (H_r + \mathrm{i} \, H_i) \right) \Big\rangle \\ & \qquad \qquad \text{for } \boldsymbol{f} \neq 0 \text{ and all } k \,. \end{aligned} \tag{C.42}$$

Expanding all the involved parenthesis gives

$$\begin{aligned}
0 = & \left\langle |H_r|^2 \, T_r^{(k)*} \sum_l W_l \, T_r^{(l)} \right\rangle + \mathrm{i} \, \underbrace{\left\langle H_r^* \, T_r^{(k)*} \sum_l W_l \, H_i \, T_i^{(l)} \right\rangle}_{=0 \ (H_r,\ H_i \text{ uncorrelated})} + \\
& + \underbrace{\left\langle H_r^* \, T_r^{(k)*} \sum_l W_l \, N_l \right\rangle}_{=0 \ (N,\ H \text{ uncorr.})} - \left\langle |H_r|^2 \, T_r^{(k)*} \right\rangle - \mathrm{i} \, \underbrace{\left\langle H_i \, H_r^* \, T_r^{(k)*} \right\rangle}_{=0 \ (H_r,\ H_i \text{ uncorr.})} - \\
& - \mathrm{i} \, \underbrace{\left\langle H_i^* \, T_i^{(k)*} \sum_l W_l \, H_r \, T_r^{(l)} \right\rangle}_{=0 \ (H_r,\ H_i \text{ uncorr.})} + \left\langle |H_i|^2 \, T_i^{(k)*} \sum_l W_l \, T_i^{(l)} \right\rangle - \\
& - \mathrm{i} \, \underbrace{\left\langle H_i^* \, T_i^{(k)*} \sum_l W_l \, N_l \right\rangle}_{=0 \ (N,\ H \text{ uncorr.})} + \mathrm{i} \, \underbrace{\left\langle H_r \, H_i^* \, T_i^{(k)*} \right\rangle}_{=0 \ (H_r,\ H_i \text{ uncorr.})} - \left\langle |H_i|^2 \, T_i^{(k)*} \right\rangle + \\
& + \underbrace{\left\langle N_k^* \sum_l W_l \, H_r \, T_r^{(l)} \right\rangle}_{=0 \ (N,\ H \text{ uncorr.})} + \mathrm{i} \, \underbrace{\left\langle N_k^* \sum_l W_l \, H_i \, T_i^{(l)} \right\rangle}_{=0 \ (N,\ H \text{ uncorr.})} + \\
& + \underbrace{\left\langle N_k^* \sum_l W_l \, N_l \right\rangle}_{=0 \text{ for } l \neq k \ (N_l,\ N_k \text{ uncorr.})} - \underbrace{\left\langle H_r \, N_k^* \right\rangle}_{=0 \ (H,\ N \text{ uncorr.})} - \mathrm{i} \, \underbrace{\left\langle H_i \, N_k^* \right\rangle}_{=0 \ (H,\ N \text{ uncorr.})} \\
& \qquad \text{for } \boldsymbol{f} \neq 0 \text{ and all } k.
\end{aligned} \tag{C.43}$$

If we assume that the noise is uncorrelated between different detector segments k, that the noise is uncorrelated with the specimen function (this is the definition of noise), and that the real and imaginary parts of the specimen are uncorrelated, we can disregard many of the cross terms as noted in the equation. We can also disregard the expectation value for all terms except the remaining noise term. Rearranging the remaining terms gives

$$\begin{aligned}0 = {}& |H_r|^2\, T_r^{(k)*} \left(\sum_l W_l\, T_r^{(l)} - 1 \right) + \\ & + |H_i|^2\, T_i^{(k)*} \left(\sum_l W_l\, T_i^{(l)} - 1 \right) + W_k \left\langle |N_k|^2 \right\rangle \qquad \text{for } \boldsymbol{f} \neq 0 \text{ and all } k\,.\end{aligned} \tag{C.44}$$

The inconspicuous assumption that real and imaginary parts of the specimen are uncorrelated is another part of the weak specimen approximation, which is discussed in Sec. 3.3.5.

C.3.2 General Filter Functions

If we multiply Eq. C.44 by $T_r^{(k)} / \left\langle |N_k|^2 \right\rangle$ and sum over all k, we obtain

$$\begin{aligned}0 = {}& |H_r|^2 \left(\sum_l W_l\, T_r^{(l)} - 1 \right) \sum_k \frac{\left| T_r^{(k)} \right|^2}{\left\langle |N_k|^2 \right\rangle} + \\ & + |H_i|^2 \left(\sum_l W_l\, T_i^{(l)} - 1 \right) \sum_k \frac{T_i^{(k)*}\, T_r^{(k)}}{\left\langle |N_k|^2 \right\rangle} + \sum_k W_k\, T_r^{(k)} \qquad \text{for } \boldsymbol{f} \neq 0\,.\end{aligned} \tag{C.45}$$

Now we define the following quantities:

$$\beta_r^{(k)} = \frac{\left\langle |N_k|^2 \right\rangle}{|H_r|^2} \qquad \beta_i^{(k)} = \frac{\left\langle |N_k|^2 \right\rangle}{|H_i|^2} \tag{C.46}$$

$$D^{(r)} = 1 + \sum_k \frac{\left| T_r^{(k)} \right|^2}{\beta_r^{(k)}} \qquad D^{(i)} = 1 + \sum_k \frac{\left| T_i^{(k)} \right|^2}{\beta_i^{(k)}} \tag{C.47}$$

$$D^{(r,i)} = \sum_k \frac{T_r^{(k)*}\, T_i^{(k)}}{\beta_r^{(k)}} \qquad D^{(i,r)} = \sum_k \frac{T_i^{(k)*}\, T_r^{(k)}}{\beta_i^{(k)}} \tag{C.48}$$

With those definitions, Eq. C.45 becomes

$$D^{(r)} \sum_l W_l\, T_r^{(l)} + D^{(i,r)} \sum_l W_l\, T_i^{(l)} = D^{(r)} + D^{(i,r)} - 1 \qquad \text{for } \boldsymbol{f} \neq 0\,. \tag{C.49}$$

Similarly, we can multiply Eq. C.44 by $T_i^{(k)} / \langle |N_k|^2 \rangle$ and sum over all k to obtain

$$D^{(i)} \sum_l W_l \, T_i^{(l)} + D^{(r,i)} \sum_l W_l \, T_r^{(l)} = D^{(i)} + D^{(r,i)} - 1 \qquad \text{for } \boldsymbol{f} \neq 0 \, . \quad \text{(C.50)}$$

We now are at a position where above Eq. C.49 and Eq. C.50 form a set of linear equations for $\sum_l W_l \, T_r^{(l)}$ and $\sum_l W_l \, T_i^{(l)}$. This can be solved to yield

$$\left.\begin{aligned} \sum_l W_l \, T_r^{(l)} &= 1 + \frac{D^{(i,r)} - D^{(i)}}{D^{(r)} \, D^{(i)} - D^{(i,r)} \, D^{(r,i)}} \\ \sum_l W_l \, T_i^{(l)} &= 1 + \frac{D^{(r,i)} - D^{(r)}}{D^{(r)} \, D^{(i)} - D^{(i,r)} \, D^{(r,i)}} \end{aligned}\right\} \qquad \text{for } \boldsymbol{f} \neq 0. \qquad \text{(C.51)}$$

By substituting this back into Eq. C.44 we have obtained a general solution for the reconstruction filters:

$$W_k = \frac{D^{(i)} - D^{(i,r)}}{D^{(r)} \, D^{(i)} - D^{(i,r)} \, D^{(r,i)}} \, \frac{T_r^{(k)*}}{\beta_r^{(k)}} + \frac{D^{(r)} - D^{(r,i)}}{D^{(r)} \, D^{(i)} - D^{(i,r)} \, D^{(r,i)}} \, \frac{T_i^{(k)*}}{\beta_i^{(k)}}$$

$$\text{for } \boldsymbol{f} \neq 0 \text{ and all } k. \qquad \text{(C.52)}$$

C.3.3 Simplified Filter Functions

The general reconstruction filters of Eq. C.52 can be further simplified by employing symmetry properties for transfer functions, which we obtained in Sec. C.2. We will assume that the pupil function is real and centro-symmetric. For the detector response we will assume that either each detector segment has a corresponding opposite segment, or in case of an individual segment that it is centro-symmetric. This covers a large range of possible detectors including the quadrant detector, dedicated segmented detectors and pixelated layouts.

The term $D^{(r,i)}$ of Eq. C.48 contains of a sum over all detector segments. Segments that are centro-symmetric have a vanishing imaginary part transfer $T_i^{(k)}$ and do not contribute to the sum. Considering opposite detector pairs k and $\bar{k}$ and assuming that both segments show the same noise spectrum, so that $\beta_{r,i}^{(k)} = \beta_{r,i}^{(\bar{k})}$ we get

$$D^{(r,i)} = \sum_{k,\bar{k}} \frac{T_r^{(k)*} \, T_i^{(k)} + T_r^{(\bar{k})*} \, T_i^{(\bar{k})}}{\beta_r^{(k)}} , \qquad \text{(C.53)}$$

where the sum is taken over all pairs of opposite detector segments k and $\bar{k}$. Using Eqs. C.32 and C.33, one obtains

$$\begin{aligned} D^{(r,i)} &= \sum_{k,\bar{k}} \frac{T_r^{(k)*}\, T_i^{(k)} - T_r^{(k)}\, T_i^{(k)*}}{\beta_r^{(k)}} \\ &= 0 \end{aligned} \tag{C.54}$$

if the transfer functions are real, corresponding to a real pupil function. Similarly, $D^{(i,r)}$ vanishes in this case. This simplifies the general expression for the reconstruction filters of Eq. C.52 significantly in the following

$$W_k = \frac{T_r^{(k)*}}{D^{(r)}\,\beta_r^{(k)}} + \frac{T_i^{(k)*}}{D^{(i)}\,\beta_i^{(k)}} \qquad \text{for } \boldsymbol{f} \neq 0 \text{ and all } k. \tag{C.55}$$

Furthermore, assuming that the noise is the same in all segments ($\beta_{r,i}^{(k)} = \beta_{r,i}$), we can substitute $D^{(r)}$ and $D^{(i)}$ back from Eq. C.47 to arrive at

$$W_k = \frac{T_r^{(k)*}}{\sum_l \left|T_r^{(l)}\right|^2 + \beta_r} + \frac{T_i^{(k)*}}{\sum_l \left|T_i^{(l)}\right|^2 + \beta_i} \qquad \text{for } \boldsymbol{f} \neq 0 \text{ and all } k\,. \tag{C.56}$$

We can use this simplified version of the reconstruction filters if we keep in mind that we need to have a real pupil, a specific detector configuration and a noise that is the same for all detector segments.

C.3.4 Zero Frequency Term

We will now consider the zero spatial frequency contribution, which has been left out of the consideration following Eq. C.40. The zero frequency term of Eq. C.23 reads $\Delta(\boldsymbol{f}_\mathrm{s})\, C_k(0,0,\boldsymbol{f}_\mathrm{s})$. For this term let us remember that $C_k(m,n,\boldsymbol{f}=0)$ is a constant independent of m and n (see Eq. C.20). Consequently,

$$C_k(0,0,\boldsymbol{f}=0) = \frac{1}{2}\, T_r^{(k)}(\boldsymbol{f}=0) \tag{C.57}$$

and

$$T_i^{(k)}(\boldsymbol{f}=0) = 0 \tag{C.58}$$

(compare Eq. C.22). Hence, this leaves for the detected signal of segment k at $\boldsymbol{f}=0$ the expression

$$S_k(\boldsymbol{f}=0) = \Delta(\boldsymbol{f}=0)\, C_k(0,0,\boldsymbol{f}=0) + H_r(\boldsymbol{f}=0)\, T_r^{(k)}(\boldsymbol{f}=0)\,. \tag{C.59}$$

Following the requirement for the weak specimen approximation of Eq. C.14 we can safely assume that the second term of Eq. C.59 is negligible compared to the term containing the Delta-function. Therefore, we can write

$$S_k(0) = \Delta(0)\,\frac{T_r^{(k)}(0)}{2}\,. \tag{C.60}$$

In Sec. 3.3 we have shown that

$$W_k(0) = \frac{2\,T_r^{(k)*}(0)}{\sum_l \left|T_r^{(l)}(0)\right|^2 + \beta_r(0)}\,. \tag{C.61}$$

Assuming that the noise average $\beta_r(0)$ is zero[1] we can substitute Eqs. C.60 and C.61 into our starting assumpption of a best specimen guess (Eq. C.35) to find that

$$\widehat{H}(0) = \Delta(0), \tag{C.62}$$

which is consistent with the definition of the specimen function from Eq. C.13 and therefore validates the filter function for the zero spatial frequency of Eq. C.61 (again assuming that $H_r(0)$ is negligible against the delta-function term). The imaginary part of the specimen function at $\boldsymbol{f} = 0$ is irrelevant, because

- due to the zero contrast transfer at $\boldsymbol{f} = 0$, one could not trust any reconstructed value anyway; and
- the $\boldsymbol{f}! = 0$ value of the specimen Fourier transform constitutes only a constant phase offset across the whole image, and we can easily (in fact, we have to) normalize the final result for a zero phase shift in the background region.

Furthermore, since in the present case no assumption regarding the pupil function or detector configuration have been made, the determined zero spatial frequency contribution filters apply for both the general and simplified cases of the filter functions.

---

[1] Remember that the zero frequency term in a Fourier transform or spectrum denotes the total value (or, with appropriate scaling, the average value) of the corresponding real space quantity; see Sec. A.2.7.

C.3.5 Phase-Only Approximation

In the following we will consider the situation of a pure phase object and the consequences on the filtering reconstruction process.

In the most rigorous form of the weak specimen approximation (where the absorption information is solely contained in h_r and the phase information in h_i) a phase-only object is characterized by $H_r = 0$, leaving the spectrum of the specimen function to be

$$H(\boldsymbol{f}) = \Delta(\boldsymbol{f}) + \mathrm{i}\, H_i(\boldsymbol{f})\,. \tag{C.63}$$

In order to derive the filter functions for this case, we will pick up the derivation of the general case of Eq. C.44 and set consequently $H_r = 0$. The minimized error expression of Eq. C.44 then becomes

$$0 = |H_i|^2\, T_i^{(k)*} \left(\sum_l W_l\, T_i^{(l)} - 1 \right) + W_k \left\langle |N_k|^2 \right\rangle \qquad \text{for } \boldsymbol{f} \neq 0 \text{ and all } k\,. \tag{C.64}$$

Going through a similar treatment as in Sec. C.3.2 we multiply above expression with $T_i^{(k)} / \langle |N_k|^2 \rangle$ and sum over all k; together with definitions for $\beta_i^{(k)}$ (Eq. C.46) and $D^{(i)}$ (Eq. C.47) we get

$$0 = \sum_l W_l\, T_r^{(l)}\, D^{(i)} - (D^{(r,i)} - 1) \qquad \text{for } \boldsymbol{f} \neq 0\,. \tag{C.65}$$

Therefore,

$$\sum_l W_l\, T_r^{(l)} = \frac{D^{(r,i)} - 1}{D^{(i)}} \qquad \text{for } \boldsymbol{f} \neq 0\,. \tag{C.66}$$

By inserting this result back into Eq. C.64 we obtain a solution for the phase only filter function

$$W_k^{\text{phase}} = \frac{1}{D^{(i)}}\, \frac{T_i^{(k)*}}{\beta_i^{(k)}} = \frac{T_i^{(k)*}}{\sum_l \left| T_i^{(l)} \right|^2 + \beta_i} \qquad \text{for } \boldsymbol{f} \neq 0 \text{ and all } k, \tag{C.67}$$

where similarly to Eq. C.56 we have use in the last step that the noise in all segments is the same. Note, that in the case of a detector with only one segment, this step does not reflect an assumption but is a completely correct statement.

The expression we found through Eq. C.67 for the phase-only filters look identical to the second term of the previously found simplified filters (Eq. C.56).

However, note that in the phase-only case the expression we found are the general filter functions, no assumptions regarding the pupil or specific detector configurations have been made.

The zero spatial frequency contribution for the phase-only filters is identical to what we have found in Sec. C.3.4.